

**RADIATION CHEMICAL STUDIES OF MICROHETEROGENEOUS
MEDIA AND THEIR ROLE IN THE
TEMPLATED SYNTHESIS OF CdSe NANOPARTICLES WITH
TUNED MORPHOLOGY AND OPTICAL PROPERTIES**

By

APURAV GULERIA

CHEM01201104001

Bhabha Atomic Research Centre, Mumbai

*A thesis submitted to the
Board of Studies in Chemical Sciences*

*In partial fulfillment of requirements
for the Degree of*

DOCTOR OF PHILOSOPHY

of

HOMI BHABHA NATIONAL INSTITUTE



March, 2015

Homi Bhabha National Institute

Recommendations of the Viva Voce Committee

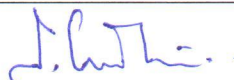
As members of the Viva Voce Committee, we certify that we have read the dissertation prepared by **Apurav Guleria** entitled **“Radiation chemical studies of microheterogeneous media and their role in the templated synthesis of CdSe nanoparticles with tuned morphology and optical properties”** and recommend that it may be accepted as fulfilling the thesis requirement for the award of Degree of Doctor of Philosophy.

Chairman – Dr. D. K. Palit



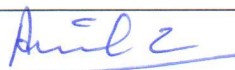
Date: 19/10/2015

Guide/Convener – Dr. Soumyakanti Adhikari



Date: 19/10/2015

External Examiner - Dr. Anil Kumar



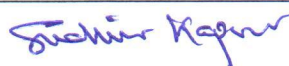
Date: 19/10/15

Member 1 – Dr. D. B. Naik



Date: 19.10.15

Member 1 – Dr. S. Kapoor



Date: 19-10-15

Member 1 – Dr. P. A. Hassan



Date: 19-10-15

External Member – Prof. A. Datta

Date:

Final approval and acceptance of this thesis is contingent upon the candidate's submission of the final copies of the thesis to HBNI.

I/~~We~~ hereby certify that I/~~we~~ have read this thesis prepared under my/our direction and recommend that it may be accepted as fulfilling the thesis requirement.

Date: October 19, 2015

Place: HBNI, Mumbai



Dr. Soumyakanti Adhikari

(Guide)

STATEMENT BY AUTHOR

This dissertation has been submitted in partial fulfillment of requirements for an advanced degree at Homi Bhabha National Institute (HBNI) and is deposited in the Library to be made available to borrowers under rules of the HBNI.

Brief quotations from this dissertation are allowable without special permission, provided that accurate acknowledgement of source is made. Requests for permission for extended quotation from or reproduction of this manuscript in whole or in part may be granted by the Competent Authority of HBNI when in his or her judgment the proposed use of the material is in the interests of scholarship. In all other instances, however, permission must be obtained from the author.

Apurav Guleria

DECLARATION

I, hereby declare that the investigation presented in the thesis has been carried out by me.
The work is original and has not been submitted earlier as a whole or in part for a degree/diploma at this or any other Institution / University.

Apurav Guleria

List of Publications arising from the thesis

Journal

1. Generation of counter ion radical ($\text{Br}_2^{\bullet-}$) and its reactions in water-in-oil (CTAB or CPB)/n-butanol/cyclohexane/water) microemulsion
Apurav Guleria, A. K. Singh, S. K. Sarkar, T. Mukherjee, and S. Adhikari
Journal of Physical Chemistry B, **2011**, *115*, 10615–10621.
2. Tuning of photoluminescence in cadmium selenide nanoparticles grown in CTAB based quaternary water-in-oil microemulsions
Apurav Guleria, S. Singh, M. C. Rath, A. K. Singh, S. Adhikari, and S. K. Sarkar
Journal of Luminescence, **2012**, *132*, 652–658.
3. Radiation induced physicochemical changes in FAP (Fluoro alkyl phosphate) based imidazolium ionic liquids and their mechanistic pathways: Influence of hydroxyl group functionalization of the cation
Apurav Guleria, A. K. Singh, S. Adhikari, and S. K. Sarkar
Dalton Transactions, **2014**, *43*, 609-625.
4. Islands of CdSe nanoparticles within Se nanofibers: A room temperature ionic liquid templated synthesis
Apurav Guleria, A. K. Singh, M. C. Rath, S. Adhikari, and S. K. Sarkar
Dalton Transactions, **2013**, *42*, 15159-15168.
5. The role of structural and fluidic aspects of room temperature ionic liquids in influencing the morphology of CdSe nano/microstructures grown *in situ*
Apurav Guleria, A. K. Singh, M. C. Rath, S. K. Sarkar, and S. Adhikari
Dalton Transactions, **2014**, *43*, 11843–11854.
6. Rapid and one-pot synthesis of self-assembled CdSe quantum dots functionalized with β -cyclodextrin: Reduced cytotoxicity and band gap engineering
Apurav Guleria, M. C. Rath, A. K. Singh, and S. Adhikari
Journal of Nanoscience and Nanotechnology, **2015**, *15*, 9341-9357.

7. Electron beam induced and microemulsion templated synthesis of CdSe quantum dots: Tunable broadband emission and charge carrier recombination dynamics
Apurav Guleria, A. K Singh, M. C. Rath, and S. Adhikari
Materials Research Express, **2015**, 2, 045006.
8. Optical properties of irradiated imidazolium based room temperature ionic liquids: New microscopic insights of the radiation induced mutations
Apurav Guleria, A. K Singh, and S. Adhikari
Physical Chemistry Chemical Physics, **2015**, 17, 11053-11061.

Conferences/Symposia

1. Generation of counter ion radicals in aqueous core of water-in-oil microemulsions and their reaction with C60 as a probe dissolved in the organic phase
Apurav Guleria, A. K. Singh, M. C. Rath, S. Adhikari, S. K. Sarkar, and T. Mukherjee; National symposia on Radiation & Photochemistry, NSRP-2011, JNV University, Jodhpur, Rajasthan, Mar 10-12, 2011 (**Best poster award**)
2. Beta-cyclodextrin (CD) functionalized CdSe quantum dots (QDs) synthesized *via* electron beam irradiation
Apurav Guleria, S. Singh, M. C. Rath, A. K. Singh and S. K. Sarkar
Trombay Symposium on Radiation & Photochemistry, TSRP-2012, BARC, Mumbai, January 4-7, 2012 (**Best poster award**)
3. Islands of CdSe Nanoparticles within Se Nanofibres synthesized in ionic liquid *via* e-beam irradiation
Apurav Guleria, S Singh, A. K. Singh, M. C. Rath, S. Adhikari, and S. K. Sarkar
Interdisciplinary Symposium on Materials Chemistry (ISMC-2012), BARC, Mumbai, December 11 – 15, 2012
4. Investigation of the effects of -OH group substitution on the radiation stability of FAP based imidazolium ionic liquids
Apurav Guleria, A. K. Singh, S. Adhikari and S. K. Sarkar

National Symposium on Radiation and Photochemistry, NSRP-2013, North Eastern Hill University (NEHU), Shillong, Meghalaya, March 20-22, 2013 (**Best poster award**)

5. Probing the structural and fluidic aspects of room temperature ionic liquid in influencing the morphology of CdSe nano/microstructures

Apurav Guleria, A. K. Singh, M. C. Rath, and S. Adhikari

International Conference on Perspectives in Vibrational Spectroscopy, (ICOPVS), Mascot Hotel, Trivandrum, Kerala, July 8-12, 2014

Others

1. Electron beam induced synthesis of CdSe nanomaterials: Tuning of shapes from rods to cubes

S. Singh, **Apurav Guleria**, M. C. Rath, A. K. Singh, S. Adhikari, and S. K. Sarkar
Materials Letters, **2011**, 65, 1815-1818.

2. Electron beam assisted synthesis of cadmium selenide Nanomaterials

M. C. Rath, **Apurav Guleria**, S. Singh, A. K. Singh, S. Adhikari, and S. K. Sarkar
AIP Conference Proceedings, **2013**, 1512, 434-435.

3. Shape evolution of CdSe nanomaterials in microheterogeneous media

S. Singh, **Apurav Guleria**, M. C. Rath, A. K. Singh, S. Adhikari, and S. K. Sarkar
Advanced Materials Letters, **2013**, 4, 449-453.

4. Radiolytic synthesis and spectroscopic investigations of CdSe quantum dots grown in cationic surfactant based quaternary water-in-oil microemulsions

S. Singh, **Apurav Guleria**, A. K. Singh, M. C. Rath, S. Adhikari, and S. K. Sarkar
Journal of Colloid and Interface Science, **2013**, 398, 112–119.

5. Sea urchin like shaped CdSe nanoparticles grown in aqueous solutions *via* electron beam irradiation

S. Singh, **Apurav Guleria**, M. C. Rath, A. K. Singh, S. Adhikari, and S. K. Sarkar
Journal of Nanoscience and Nanotechnology, **2013**, 13, 5365–5373.

6. Facile and Green Synthesis of CdSe Quantum Dots in Protein Matrix: Tuning of Morphology and Optical Properties
M. Ahmed, **Apurav Guleria**, M. C. Rath, A. K. Singh, S. Adhikari, S. K. Sarkar
Journal of Nanoscience and Nanotechnology, **2014**, 14, 5730–5742.
7. Radiation chemical studies of water-in-oil microemulsions and reaction of counter ion radicals with C60 as a probe dissolved in the organic phase
Apurav Guleria, A. K. Singh, M. C. Rath, S. Adhikari, S. K. Sarkar, T. Mukherjee
BARC News letter, Founder's day special issue, **2012**.
8. Tuning the shape of CdSe nanoparticles in water-in-oil microemulsion grown via electron beam irradiation
S. Singh, **Apurav Guleria**, M. C. Rath, A. K. Singh, S. Adhikari, S. K. Sarkar
BARC News letter, Founder day issue, **2012**.
9. Beta-cyclodextrin (CD) functionalized CdSe quantum dots (QDs) synthesized via electron beam irradiation
Apurav Guleria, S. Singh, M. C. Rath, A. K. Singh, S. K. Sarkar
BARC News letter, Founder day issue, **2013**.
10. Investigation of the effects of -OH group substitution on the radiation stability of FAP (fluoro alkyl phosphate) based imidazolium ionic liquids
Apurav Guleria, A. K. Singh, S. K. Sarkar, S. Adhikari
BARC News letter, Founder day issue, **2014**.

Apurav Guleria

DEDICATIONS

*To my loving Parents and
respected Teachers.....*

ACKNOWLEDGEMENTS

I would like to take this opportunity to thank everyone, who supported me throughout this thesis.

At the outset, I wish to begin by expressing my deepest and sincere gratitude to my guide, Dr. Soumyakanti Adhikari for his aspiring guidance, constant encouragement, and motivation. His wide knowledge and logical way of thinking and reasoning on scientific problems greatly helped me during the work. I am thankful to him for sharing his knowledge and scientific understanding during the fruitful discussions with me throughout the work.

I am privileged to thank Dr. S. K. Sarkar, Former Director, Chemistry Group for his unstinted support and encouragement. Your advice and comments have been priceless and great value for me, which played a major role in shaping my thesis work.

I would like to express my sincere regards and deepest appreciation to Dr. A. K. Singh. His invaluable constructive criticism and friendly suggestions on an academic and personal level has always been extremely helpful to me.

I am grateful to Dr. M. C. Rath, whose enthusiasm and spirited approach towards research has always been a source of inspiration to me. I take this opportunity to thank him for sharing his scientific understanding and knowledge with me.

My special thanks go to my lab mates Shalini and Mohammed Ahmed for their cooperative attitude, diversified help, and several funs which I will always cherish in my life. I am grateful to Dr. P. Mathi, Dr. J. A. Mondal and Dr. Vinu. V. Namboodiri for their moral support, stimulating discussions and constructive criticisms, which have substantially helped me in my research work.

I also gratefully acknowledge the cooperative attitude and support provided by all the members of RPCD. Their spirited research oriented approach has always been a source of inspiration and morale booster. I thank all my friends and batch mates in BARC for their

support and the wonderful moments we spent together. I greatly value their friendship and deeply appreciate their belief in me.

I would like to take this opportunity to thank LINAC staff (Shri S. A. Nadkarni, Smt. M. A. Toley, Shri S. J. Shinde, Shri B. B. Chaudhari) of RPCD, whose has immensely helped me in carrying out irradiation experiments. The facility provided by SAIF, IIT Bombay in carrying out TEM, ESI-MS and NMR measurements is thankfully acknowledged.

I am thankful and gratefully acknowledge the constant support and encouragement rendered by Dr. B. N. Jagatap, Director, Chemistry group. It gives me immense pleasure to thank the respected and distinguished members of the doctoral committee, Dr. T. Mukherjee (Former Chairman), Dr. D. K. Palit (Chairman), Dr. P. N. Bajaj (Former Member), Dr. D. B. Naik (Member), Dr. S. Kapoor (Member), Dr. P. A. Hassan (Member) and Dr. Anindya Datta (External Member) for their critical reviews and suggestions during the progress reviews and pre-synopsis presentation.

I cannot imagine my current position without the blessings of my teachers, and will always be indebted to them.

Most importantly, I owe my heartfelt gratitude to my parents for their encouragement and love. I am obliged to my brother and sister-in-law for their unrelenting support and care. Their blessings and good wishes have helped me to achieve what I am today.

Finally, I would like to express my endless thanks and appreciations to my wife, Mohini, for her support, encouragement and care.

March, 2015

Apurav Guleria

RPCD, BARC, Mumbai

CONTENTS

	Page No.
SYNOPSIS	xv
LIST OF ABBREVIATIONS	xxviii
LIST OF FIGURES	xxxix
LIST OF TABLES	Lii
Chapter 1: General introduction	1–39
1.1. Microheterogeneous systems and their importance	1
1.2. Radiation chemistry	4
1.3. Microemulsions	17
1.4. Room temperature ionic liquids (RTILs)	22
1.5. Cyclodextrins (CDs)	28
1.6. Quantum dots (QDs)	32
1.7. Outline of the thesis	38
Chapter 2: Experimental techniques	41-72
2.1. Introduction	41
2.2. Pulse radiolysis	42
2.2.1. Principle of pulse radiolysis	42
2.2.2. Linear accelerator (LINAC)	44
2.2.3. Kinetic spectrophotometer	46
2.2.4. Transient absorption measurements	48
2.2.5. Dosimeters for pulse radiolysis	49
2.2.6. Experimental data handling: The kinetic treatment	49
2.3. Cobalt-60 gamma source	52
2.4. X-ray diffraction	54
2.5. Transmission electron microscopy	57
2.6. Scanning electron microscopy	59
2.7. Steady-state UV-Vis absorption measurements	61

2.8. Steady-state photoluminescence measurements	63
2.9. Photoluminescence lifetime measurements	64
2.10. Fourier transform infrared spectrometer	68
2.11. Raman spectrometer	70
Chapter 3: Dual site for solvation of electrons and generation of counter ion radicals in CTAB based <i>water-in-oil</i> microemulsions: A pulse radiolysis study	73-93
3.1. Introduction	73
3.2. Experimental	76
3.3. Results and Discussion	78
3.3.1. Hydrated electron	78
3.3.2. Counter ion radical: Dibromide radical anion in CTAB and CPB microemulsions	83
3.3.3. Reaction of $\text{Br}_2^{\cdot-}$ radical with ABTS: A protocol for antioxidant assay for substrates insoluble in water	88
3.4. Conclusions	92
Chapter 4: Templated synthesis of CdSe quantum dots in cationic and anionic surfactant based microemulsions: Tuning of photoluminescence and their morphology	95-140
4.1. Introduction	95
4.2. Normal chemical route for the synthesis of CdSe QDs in CTAB based quaternary w/o microemulsions	97
4.2.1. Materials and Methods	97
4.2.2. Results and Discussion	99
4.3. Radiation chemical route for the synthesis of CdSe QDs in microemulsions: A rapid and one step templated approach	110
4.3.1. Materials and Methods	110
4.3.2. Results and Discussion	112

4.4. Conclusions	138
Chapter 5: Radiation stability of FAP (fluoro alkyl phosphate) based imidazolium room temperature ionic liquids: Influence of hydroxyl group functionalization of the cation	141-198
5.1. Introduction	141
5.2. Experimental	144
5.3. Results and Discussion	148
5.3.1. UV-Vis absorption studies of irradiated FAP ionic liquids	150
5.3.2. Physicochemical properties	155
5.3.3. NMR and Mass spectral studies	166
5.3.4. Hydrogen gas yields	176
5.3.5. Pulse radiolysis study	177
5.3.6. Photophysical studies	180
5.4. Conclusions	197
Chapter 6: Room temperature ionic liquids as a media for the synthesis of complex nanostructures	199-241
6.1. Introduction	199
6.2. Radiation mediated synthesis	200
6.2.1. Materials and Methods	200
6.2.2. Results and Discussion	202
6.3. Normal chemical route	221
6.3.1. Materials and Methods	221
6.3.2. Results and Discussion	221
6.4. Conclusions	240
Chapter 7: Self-assembled CdSe quantum dots functionalized with β-cyclodextrin: Reduced cytotoxicity and band gap engineering	243-279
7.1. Introduction	243
7.2. Experimental	245

7.3. Results and Discussion	248
7.3.1. Morphology and structural characterization	248
7.3.2. Optical studies	259
7.3.3. Pulse radiolysis study	275
7.3.4. Cytotoxicity study	277
7.4. Conclusions	278
Chapter 8: Summary and Outlook	281-289
References	291

Synopsis

In general, materials used in recent technology are heterogeneous and multi-component, which possess rich and complex internal structure. Coexistence of polar and apolar domains characterized by local orientational order, associated interfaces and the dynamic nature of their aggregation are some of the key features of microheterogeneous media.¹ In the recent years, significant number of photochemical and photobiological studies probing the static, dynamic and the interfacial properties of such organized assemblies could be found in the literature.^{1,2} The information obtained from such studies have found utmost relevance in the biological field for in-depth understanding of the charge transport and other related processes occurring in naturally organized assemblies. Furthermore, these complex systems have found tremendous applications in diverse fields such as drug delivery, pharmaceuticals, petroleum industry, catalysis, cosmetics, nanotechnology and organic synthesis.¹⁻³ It is worth mentioning here that many biological reactions such as plant photosynthesis illustrate the benefits of such molecular organization.

The present thesis is an exposition of the radiation and photochemical investigation of three microheterogeneous systems namely microemulsions (MEs), room temperature ionic liquids (RTILs) and cyclodextrins (CDs). Subsequently, these chemical systems were employed as host matrices for controlled synthesis and tuning the morphology and the optical properties of CdSe nanoparticles (NPs).

MEs are thermodynamically stable, isotropic and optically clear dispersions of either 'water in oil' or 'oil in water' stabilized by amphiphiles (or surfactants).³ The geometry and the charge on the polar head group of the surfactant plays an essential role in guiding

the structure, dynamics and transport behaviors of MEs. For instance, the structural composition of AOT (an anionic surfactant; sodium bis (2-ethylhexyl) sulfosuccinate) and CTAB (cationic surfactant; Cetyltrimethylammonium bromide) based MEs are markedly different from each other. Further, CTAB based *water-in-oil* (w/o) MEs possess flexible interfacial film owing to the presence of a co-surfactant and therefore exhibit greater amount of dynamism^{3, 4} as compared to that of AOT based w/o MEs, where interfacial film is quiet rigid.⁵ Thus, CTAB MEs are much more complex in terms of dynamics of the reactants as compared to AOT MEs. Majority of the reports²⁻⁶ including radiochemical studies have been carried out in AOT based w/o MEs, where it has been used as a microreactor to carry out and study the kinetics and mechanism of various chemical and biological processes. For example, the dynamics of generation, migration, recombination and solvation of electrons have been extensively probed in AOT MEs by Gratzel *et al.*,⁶ Gebicki *et al.*⁶ and others⁶ by employing mainly pulse radiolysis and flash photolysis techniques. However, the number of such studies carried out on cationic surfactant (such as CTAB) based w/o MEs is relatively unexplored.⁵

In the present thesis, an effort was made to comprehend the solvated electron properties in CTAB based w/o ME. Further, the presence of co-surfactant leading to the manipulation of interfacial properties such as polarity and rigidity was clearly reflected from the electron solvation at two regions as well as the difference in kinetics of the electrons solvated in these two locations. On the contrary, no such dual solvation of electron has been reported in case of AOT MEs.⁶ Further, the presence of counter ions in MEs has not been seriously considered in earlier radiation chemical studies. However, we

could observe and characterize the formation of dibromide radical anion, which was found to be the product of the interaction of bromide ion and hydroxyl radical. Subsequently, the possibility of a two phase reaction was illustrated.

The application areas of MEs have increased dramatically during the past decades.³⁻⁵ One such important area is the fabrication of nanomaterials.^{3, 5} Therefore, after acquainting with the CTAB w/o MEs, the same system was employed as a reaction media for the synthesis of Cadmium selenide (CdSe) NPs *via* conventional as well as radiation chemical route. Moreover, there are very few reports of the synthesis of CdSe NPs in CTAB based quaternary w/o MEs. CdSe is one of the most important members of II–VI group semiconductors with an energy band gap, E_g of 1.75 eV at 300 K and has been widely used for optoelectronic devices.⁷ Nonetheless, the role of the intrinsic structural dynamics of CTAB MEs at various W_0 (water to surfactant molar ratio) values in influencing the morphology and the associated photoluminescence (PL) behavior of CdSe NPs has been examined and described in the thesis. Meanwhile, another methodology for the synthesis of NPs was demonstrated; wherein electron beam irradiation technique was clubbed with the templated approach of MEs. This hybrid approach possesses inherent advantageous features of radiation induced technique⁸ and is relatively new for the controlled synthesis of semiconductor nanomaterials. So far, primarily metals, alloys, metal oxide NPs have been synthesized by this means.^{8, 9} Nevertheless, a comparative study was conducted wherein CdSe NPs were grown in AOT and CTAB MEs. Interestingly, profound and contrasting results were observed and have been explained

taking into account of the fundamental differences in the interfacial properties and the chemical nature of the water cores of both the MEs.

RTILs are the second microheterogeneous systems studied in the present thesis. RTILs are basically a class of low temperature molten salts (melting points below 100 °C) which are composed entirely of ions.¹⁰ Owing to their unique physicochemical properties such as high polarity, negligible vapor pressure, high ionic conductivity, wide electrochemical window and thermal stability, these fluids are finding tremendous applications in variety of areas ranging from synthesis to energy.¹⁰ In the recent past, RTILs have aroused much interest as a media in nuclear fuel cycle. However, understanding the radiation stabilities of the ILs and the underlying chemistry involved has become the most important issues for their successful use in nuclear fuel reprocessing. No surprise that several radiation stability studies on ILs have already been reported¹¹ and contributed in this endeavor. However, in the present thesis, we have performed an assortment of characterization and qualitative studies to explore the radiation stabilities of FAP (tris(perfluoroalkyl)trifluorophosphate) ILs. Amongst various ILs, imidazolium ILs with bulky FAP anion are ultra-hydrophobic and possess excellent hydrolytic stability as compared to their counterparts containing anions such as PF_6^- , BF_4^- or halogens.¹² The insignificant changes in the physicochemical properties clearly indicated the potential of the FAP imidazolium ILs to be a good solvent for various applications involving high radiation fields. Furthermore, introduction of -OH group in the alkyl side chain of the imidazolium moiety resulted into significant changes in the physical properties of these ILs on irradiation. Through transient spectroscopic studies,

we could delineate the mechanism for the radiation induced changes in the physicochemical properties of the non-hydroxyl and hydroxyl FAP ILs. In the subsequent studies, photophysical behavior of the post-irradiated FAP ILs was monitored. It was revealed that the ionic moieties in the IL undergo significant changes in their molecular arrangements. This study would be useful in gaining a comprehensive understanding of the radiation induced degradation of ILs and its mechanistic pathways.

RTILs, being considered as ‘green’ media have recently received a great deal of attention as superior media (with respect to the conventional organic solvents) for the synthesis of various nanomaterials.¹³ However, the synthesis of metal chalcogenides using *neat* ILs (as solvents) have been rarely studied that too using radiation induced techniques. Therefore, electron beam irradiation of the solutions containing cadmium and selenium precursors in *neat* RTIL (i.e. 1-ethyl-3-methyl imidazolium ethyl sulfate, [EMIM][EtSO₄]) was carried out to initiate the nucleation. Interestingly, a unique highly porous 3-D structure of entangled Selenium (Se) nanofibers along with the heterogeneous distribution of CdSe NPs grown *in situ* within this network was obtained. In the second set of experiment, CdSe NPs were synthesized in *neat* IL ([EMIM][EtSO₄]) at purely ambient conditions without perturbing its internal structure by either high energy radiation or any solvent (for dilution)/stabilizing agent. Interestingly, co-existence of anisotropic 2D sheet and flower-like 3D nanostructures was observed. Accordingly, a possible mechanism for the as obtained self-assembled anisotropic nanostructures has been provided on the basis of fluidic and the structural aspects of the IL in conjunction with the energetics of the transient morphologies involved in the process.

Recently, the directed self-assembling of primary NPs into superstructures has attracted tremendous interest because they can reveal fundamentally interesting collective physical properties with enhanced efficiencies.¹⁴ In this pretext, biomolecules such as CDs and its derivatives have been used as a host matrix for the synthesis of various organized assemblies of predominantly metal NPs.¹⁵ Having mentioned that, we have demonstrated a simple, rapid and one step method for the synthesis as well as *in situ* functionalization of CdSe quantum dots (QDs) with β -CD. It was found that the β -CD molecules cap the as grown CdSe QDs by forming a non-inclusion complex. X-ray photoelectron spectroscopy (XPS) and pulse radiolysis studies were carried out to elucidate the role of β -CD in influencing the morphology and the formation mechanism of CdSe NPs, respectively. Furthermore, the cytotoxicity studies of CdSe QDs were also carried out keeping in view of the bio-compatibility of β -CD.

With this back drop, the results obtained from the radiation and photochemical investigations of aforementioned microheterogeneous media have been described and compiled under different chapters of this thesis. A brief account of each chapter has been given below.

Chapter 1: General introduction

In the beginning, the motivation behind the research work on the microheterogeneous systems has been explained. Since, this thesis deals with the study of three microheterogeneous media namely MEs, RTILs and CDs, therefore a brief preview of their history, structural composition, dynamic peculiarities and an account of the radiation and photochemical investigations reported earlier, has been discussed. Besides, a concise

description regarding the application of microheterogeneous systems as a template for the controlled synthesis of various NPs has been provided.

Chapter 2: Experimental techniques

A brief overview of the different experimental techniques used in the current thesis has been illustrated in this chapter. The working principle of LINAC (Linear accelerator, 7 MeV) used as an irradiation source and for carrying out the pulse radiolysis experiments, has been explained. Techniques employed for the characterization of NPs such as X-ray diffraction, transmission electron microscope, scanning electron microscope have been described in detail. Basic principles of instruments used for carrying out various photophysical studies such as absorption spectrophotometer, fluorometer, infrared spectrometer, Raman spectrometer and time-correlated single photon counting (TCSPC) have also been explained.

Chapter 3: Dual site for solvation of electrons and generation of counter ion radicals in CTAB based *water-in-oil* microemulsions: A pulse radiolysis study

In this chapter, an attempt has been made to comprehend the solvated electron properties in cationic surfactant based quaternary w/o ME (i.e. CTAB/H₂O/n-butanol/cyclohexane). The questions regarding the role of the thin interfacial layer and the effect of the water pool dimensions (at different W_0 values) in the solvation dynamics of the electron has been addressed. Further, the formation of counter radical ion i.e. Br₂^{•-} was observed and characterized. Consecutively, a two phase reaction between inorganic radicals produced in the aqueous core and a molecule that is completely insoluble in water has also been discussed.

Chapter 4: Templated synthesis of CdSe quantum dots in cationic and anionic surfactant based microemulsions: Tuning of photoluminescence and their morphology

Herein, the application of MEs in the controlled synthesis of QDs has been presented *via* radiation as well conventional chemical route. The interplay of different experimental parameters involved in this work such as precursor concentration, absorbed dose and W_0 values of the MEs facilitated controlled induction of the surface/trap states and band gap engineering of the QDs. For instance, QDs with ultra small size (~ 1.7 nm) and tunable broadband light emission extending from 450 to 750 nm (maximum FWHM ~ 180 nm) were obtained, thereby conferring their potential applications in white light emitting diodes. Furthermore, a comparative study was conducted to investigate the structural and the dynamical aspects of AOT and CTAB MEs on the morphologies, photoluminescent behaviour and the charge carrier relaxation dynamics of CdSe QDs. Interestingly, profound and contrasting results were observed and have been explained.

Chapter 5: Radiation stability of FAP (fluoro alkyl phosphate) based imidazolium room temperature ionic liquids: Influence of hydroxyl group functionalization of the cation

This chapter is the compilation of the radiation stability studies of FAP based imidazolium ILs. The effect of -OH functionalization on the radiation stability of the IL was also investigated. Furthermore, an account of the photophysical studies of the post-irradiated ILs has been provided which could further supplement the comprehensive understanding of the radiation induced structural changes. Detailed discussion of the

results is presented in this chapter, which clearly indicates significant differences in the reactivity, reaction centre and the nature of the radiolytic products after a diminutive alteration in the molecular structure of the IL.

Chapter 6: Room temperature ionic liquids (RTILs) as a media for the synthesis of complex nanostructures

This chapter demonstrates the application of RTILs as a novel media for the synthesis of self-assembled superstructures of nanomaterials. CdSe NPs were grown in *neat* imidazolium based IL ([EMIM][EtSO₄]) *via* radiation as well as normal chemical route. The main objective of the present work was to examine the role of the novel structural features of IL in directing the self assembly of initially formed small nanoparticles into well-defined structures of fundamental importance. The possible mechanism behind the as obtained nanostructures has been explained in this chapter and may provide an intuitive protocol for better understanding and development of such complicated nanostructures.

Chapter 7: Self-assembled CdSe quantum dots functionalized with β -cyclodextrin (β -CD): Reduced Cytotoxicity and Band Gap Engineering

In this chapter, a rapid and one step method has been demonstrated for the synthesis as well as *in situ* functionalization of CdSe QDs with β -CD in aqueous solution. The main objectives of this work was to employ such ligands which not only passivates the NP surface but also reduces their toxicity, provide desired aqueous solubility and possess the ability to direct the self-assembling of NPs into superstructures with potentially enhanced efficiencies in their applications. Detailed discussion on the investigations carried out to

identify the forces and the binding sites involved in the complex formation between CD molecules and the QDs have been presented. Also, the effect of experimental parameters i.e. precursor and ligand concentrations, absorbed dose and dose rate on the morphology and photophysical behavior of CdSe QDs has been described.

Chapter 8: Summary and outlook

The conclusions drawn from each study are sequentially summarized in this chapter. Besides, a brief description of how the present work on the as studied microheterogeneous systems may contribute in advancing the current understanding of their structural and dynamical aspects as well as in the precise control of nanostructures grown in them, has been presented. Further, the future perspectives of the work carried out in this thesis has been discussed.

References

1. K. Kalyanasundaram, *Photochemistry in microheterogeneous systems*, Academic press Inc. (London), 1987; M. Grätzel and K. Kalyanasundaram, *Kinetics and Catalysis in Microheterogeneous Systems*, CRC Press (New York), 1991; Joseph R. Lakowicz, *Principles of Fluorescence Spectroscopy*, Springer Science (New York), 2006.
2. A.V. Barzykin, K. Seki, and M. Tachiya, *Adv. Colloid Interface Sci.*, 2001, **89-90**, 47-140; D. M. Shin, K. S. Schanze, and D. G. Whitten, *J. Am. Chem. Soc.*, 1989, **111**, 8494-8501; J. H. Fendler, *J. Phys. Chem.*, 1980, **84**, 1485–1491; S.P. Moulik and B. K. Paul, *Adv. Colloid Interface Sci.*, 1998, **78**, 99-195; D. M. Vriezema, M. C. Aragonés, J. A. A. W. Elemans, J. J. L. M. Cornelissen, A. E. Rowan, and R. J. M. Nolte, *Chem. Rev.*, 2005, **105**, 1445–1489.
3. S. P. Moulik and A. K. Rakshit, *J. Surface Sci. Tech.*, 2006, **22**, 159-186; V. T. Liveri, *Controlled Synthesis of Nanoparticles in Microheterogeneous Systems* in Nanostructure Science and Technology ed. D. J. Lockwood, Springer Science (New York), 2006; M. Fanun, *Microemulsions: Properties and Applications*, CRC Press (Taylor & Francis Group), 2009.
4. M. P. Pileni, *J. Phys. Chem.*, 1993, **97**, 6961–6973.
5. M. A. López-Quintela, C. Tojo, M. C. Blanco, L. García Riq and J. R. Leis, *Curr. Opin. Colloid Interface Sci.*, 2004, **9**, 264–278; M. López-Quintela, J. Rivas, M. Blanco, and C. Tojo, in *Nanoscale Materials*, eds. L. M. Liz-Marzán and P. V. Kamat, Springer, 2003, pp. 135–155; A. K. Ganguli, A. Ganguly, and S. Vaidya, *Chem. Soc. Rev.*, 2010, **39**, 474–485.

6. M. Wong, M. Grätzel, and J.K. Thomas, *Chem. Phys. Lett.*, 1975, **30**, 329–333; J. L. Gebicki and P. Bednarek, *J. Mol. Structure*, 2000, **555**, 227–234; J. L. Gebicki, L. Gebicka, and J. Kroh, *J. chem. soc. Faraday Trans.*, 1994, **90**, 3411–3414; M. P. Pileni, B. Hickel, C. Ferradini, and J. Pucheault, *Chem. Phys. Lett.*, 1982, **92**, 308–312.
7. C. Burda, X. Chen, R. Narayanan, and M. A. El-Sayed, *Chem. Rev.*, 2005, **105**, 1025–1102.
8. Q. Chen, X. Shen, and H. Gao, *Adv. Colloid Interface Sci.*, 2010, **159**, 32–44.
9. K. Kurihara, J. Kizling, P. Stenius, and J. H. Fendler, *J. Am. Chem. Soc.*, 1983, **105**, 2574; H. K. Wu, X. L. Xu, X. W. Ge, and Z. C. Zhang, *Radiat. Phys. Chem.*, 1997, **50**, 585; S. Kapoor, S. Adhikari, C. Gopinathan, and J. P. Mittal, *Mater. Res. Bull.*, 1999, **34**, 1333.
10. T. Welton, *Chem. Rev.*, 1999, **99**, 2071–2083; V. I. Pârvulescu and C. Hardacre, *Chem. Rev.*, 2007, **107**, 2615–2665; J. P. Hallett and T. Welton, *Chem. Rev.*, 2011, **111**, 3508–3576.
11. L. Berthon, S. I. Nikitenko, I. Bisel, C. Berthon, M. Faucon, B. Saucerotte, N. Zorz, and P. Moisy, *Dalton Trans.*, 2006, 2526–2534; M. Y. Qi, G. Z. Wu, Q. M. Li, and Y. S. Luo, *Radiat. Phys. Chem.*, 2008, **77**, 877–883; C. J. Rao, K. A. Venkatesan, B. V. R. Tata, K. Nagarajan, T. G. Srinivasan, and P. R. V. Rao, *Radiat. Phys. Chem.*, 2011, **80**, 643–649.
12. N. V. Ignatev, U. Welz-Biermann, A. Kucheryna, G. Bissky, and H. Willner, *J. Fluorine Chem.*, 2005, **126**, 1150–1159.

- 13.** Z. Li, Z. Jia, Y. Luan, and T. Mu, *Curr. Opin. Solid State Mater. Sci.*, 2008, **12**, 1–8; M. Antonietti, D. Kuang, B. Smarsly, and Y. Zhou, *Angew. Chem., Int. Ed.*, 2004, **43**, 4988–4992.
- 14.** M. Grzelczak, J. Vermant, E. M. Furst, and L. M. L. Marzan, *ACS Nano*, 2010, **4**, 3591.
- 15.** K. Palaniappan, C. Xue, G. Arumugam, S. A. Hackney, and J. Liu, *Chem. Mater.*, 2006, **18**, 1275; T. Huang, F. Meng, and L. Qi, *J. Phys. Chem. C*, 2009, **113**, 13636; H. Kochkar, M. Aouine, A. Ghorbel, and G. Berhault, *J. Phys. Chem. C*, 2011, **115**, 11364.

LIST OF ABBREVIATIONS

ABTS:	2,2'-azino-bis(3-ethylbenzothiazoline-6-sulfonic acid)
AOT:	Sodium bis(2-ethylhexyl) sulfosuccinate
ATR:	Attenuated total reflection
BGE:	Band gap emission
BMIM:	1-butyl-3-methylimidazolium
CDs:	Cyclodextrins
CdSe:	Cadmium selenide
CIE:	Commission Internationale d'Eclairage
CPB:	Cetylpyridinium bromide
CPP:	Critical packing parameter
CTAB:	Cetyltrimethylammonium bromide
EDS:	Energy dispersive X-ray spectroscopy
EMIM:	1-ethyl-3-methylimidazolium
EOHMIM:	1-(2-Hydroxyethyl)-3-methylimidazolium
ESI-MS:	Electrospray ionization-mass spectrometry
EtSO ₄ :	Ethyl sulfate
FAP:	tris(perfluoroalkyl)trifluorophosphate
FTIR:	Fourier transform infrared spectrometer
FWHM:	Full width at half maximum
GPP:	Grey per pulse
Gy:	Gray
HMIM:	1-hexyl-3-methylimidazolium

HRTEM:	High resolution TEM
IRF:	Instrument response function
JCPDS:	Joint committee on powder diffraction standards
KCNS:	Potassium thiocyanate
LET:	Linear energy transfer
LINAC:	Linear accelerator
LO:	Longitudinal optical
NF:	Nanoflake
NMR:	Nuclear magnetic resonance
OD:	Optical density
PH(3)T:	Trihexyl(tetradecyl) phosphonium
PL:	Photoluminescence
QDs:	Quantum dots
QE:	Quantum efficiency
REE:	Red edge effect
RTIL:	Room temperature ionic liquids
SAED:	Selective area electron diffraction
SEM:	Scanning electron microscope
SO:	Surface optical
TCSPC:	Time correlated single photon counting
TEM:	Transmission electron microscope
Tf ₂ N:	bis(trifluoromethylsulfonyl)amide
TGA:	Thermogravimetric analysis

TO: Transverse optical
TSE: Trap state emission
UV-Vis: Ultraviolet visible
w/o: water-in-oil
WLED: White light emitting diodes
XPS: X-ray photoelectron spectroscopy
XRD: X-ray diffraction

LIST OF FIGURES

	Page No.
Figure 1.1. Compartmentalized structure of a plant cell.	2
Figure 1.2. Distribution of ions and excited species along the track of fast electron.	11
Scheme 1.1. Time scale of events after passage of high energy radiation through water or aqueous solutions.	12
Figure 1.3. A generalized ternary phase diagram depicting various structure formations as a function of different percentage composition of the constituents.	19
Figure 1.4. Diagrammatic representation of AOT (a) and CTAB based w/o microemulsions. The molecular structures of AOT and CTAB are also shown.	20
Figure 1.5. Diagrammatic representation of the application areas of microemulsions.	21
Figure 1.6. Some examples of common cations and anions of RTILs.	24
Figure 1.7. Diagrammatic representation of the various bonding interactions co-existing in an imidazolium based RTILs.	25

Figure 1.8.	26
One snapshot from the simulation studies on imidazolium based IL ([EMIM]/[BMIM][NO ₃]) illustrating the ‘spatial heterogeneity’ present within its molecular structure. The white spheres represent the non-polar domains originating from the cationic terminal groups; while the gold and red spheres represent the cationic head Groups, and the anions, respectively.	
Figure 1.9.	27
Structure of FAP anion.	
Figure 1.10.	29
Structures and properties of CDs.	
Figure 1.11.	32
Diagrammatic illustration of the electronic band structure difference between bulk semiconductor, quantum dot and a molecule.	
Figure 1.12.	34
Splitting of electronic band structure of bulk semiconductor into discrete energy levels with the decrease in size (Quantum confinement effect).	
Figure 1.13.	36
Bulk conduction and valence band edge positions (<i>vs.</i> vacuum and SHE) and band gaps of common semiconductor materials.	
Figure 1.14.	37
Diagrammatic depiction of the radiation (e ⁻ , γ) induced synthesis of nanomaterials.	
Figure 2.1.	43
Schematic diagram of pulse radiolysis set up.	

Figure 2.2.	45
Schematic diagram of linear electron accelerator.	
Scheme 2.1.	53
Decay scheme of Cobalt-60.	
Figure 2.3.	56
Diagrammatic representation of the Bragg's law.	
Figure 2.4.	57
Basic layout of optical components in a Transmission Electron Microscope.	
Figure 2.5.	61
Basic layout of a Scanning Electron Microscope.	
Figure 2.6.	66
Layout of a TCSPC setup.	
Figure 3.1.	77
Structures of surfactants and other chemicals used.	
Figure 3.2.	79
Transient absorption spectrum of hydrated electrons at (a) 0.6, (b) 1, (c) 2, (d) 3 μ s after the electron pulse of N ₂ saturated solution of CTAB/cyclohexane/n-butanol/water with $W_0 = 20$. (O.D. = Absorbance). Inset: Decay of hydrated electron at 650 (e) and 720 nm (f) in microemulsion with $W_0 = 20$.	
Figure 3.3.	82
Decay pattern of solvated electrons at the interface (A) and in the water core (B). (C) Plot of decay constants of solvated electrons versus W_0 (d) in the water core and (e) at the interface, respectively. O.D. = absorbance.	

Figure 3.4.	84
<p>Transient absorption spectrum of dibromide anion radical of the CTAB/cyclohexane/n-butanol/water solution after electron pulse (a) N₂O saturated ($W_0 = 40$) (b) N₂ purged ($W_0 = 40$) (c) N₂ purged ($W_0 = 30$). Inset: Decay of dibromide anion radical at 360 nm at a dose of (d) 34 Gy and (e) 62 Gy in N₂-bubbled CTAB/n-butanol/cyclohexane/water microemulsion ($W_0 = 40$).</p>	
Figure 3.5.	90
<p>Transient absorption spectrum of the ABTS radical in N₂O-saturated CTAB/cyclohexane/n-butanol/water solution ($W_0 = 40$) containing ABTS (1×10^{-3} mol dm⁻³) at (a) 5, (b) 20, (c) 30, and (d) 40 μs after the electron pulse.</p>	
Figure 3.6.	91
<p>(A) Decay curve of ABTS radical in presence and absence of ascorbate. (B) Decay curve of ABTS radical in presence and absence of tocopherol. Plots of rate constant versus concentration of ascorbate (C) and tocopherol (D), respectively, for scavenging the ABTS radical.</p>	
Scheme 3.1.	93
<p>Diagrammatic representation of the findings.</p>	
Scheme 4.1.	99
<p>Diagrammatic representation of the synthesis of CdSe QDs at room temperature inside the water pool of CTAB w/o microemulsion.</p>	
Figure 4.1.	99
<p>Camera-ready pictures of CdSe sols prepared in microemulsions with $W_0 = 30$ and [stock precursor] = 50, 100, 150 mM, a) after 2 hrs, b) after 24 hrs and c) after a week from the time of mixing of the individual precursor solutions.</p>	

Figure 4.2.	100
HRTEM images (a) and (b) of CdSe nanoparticles sampled from freshly prepared sol (microemulsion of $W_0 = 20$ and [stock precursor] = 50 mM) and TEM image (c) of nanoparticles sampled from the same sol after a time period of 1 week. Inset of image (b) depicts the SAED pattern and the lattice fringes of the nanoparticles.	
Figure 4.3.	101
Optical absorption spectra of CdSe nanoparticles synthesized at RT (a) in microemulsions of $W_0 = 20, 30, 40$ and a fixed [stock precursor] = 50 mM; (b) in microemulsions of $W_0 = 20$ and [stock precursor] = 50, 100, 150 mM.	
Figure 4.4.	104
Excitation wavelength dependent PL spectra along with the absorption spectrum of CdSe nanoparticles synthesized in microemulsion with $W_0 = 20$ and [stock precursor] = 100 mM. The arrows at the absorption spectrum indicate the excitation wavelengths for the PL spectra.	
Scheme 4.2.	105
Diagrammatic representation of the photo-excitations and PL occurring in as synthesized CdSe nanoparticles in w/o CTAB microemulsions.	
Figure 4.5.	106
Room temperature PL spectra of CdSe nanoparticles synthesized in microemulsions with $W_0 = 20$ and [stock precursor] = 50, 100 and 150 mM normalized at the TS-PL peak position of 580 nm.	
Figure 4.6.	108
Room temperature PL spectra of CdSe nanoparticles synthesized in microemulsions with $W_0 = 20, 30, 40$ and [stock precursor] = 50 mM normalized at the TS-PL peak position of 580 nm.	

Figure 4.7. 113

(A) XRD patterns of CdSe QDs (synthesized in AOT microemulsions) immediately (a) and 24 hours (b) after the irradiation; (B) HRTEM image of the QDs showing the lattice fringe pattern with the interplanar distance of 0.25 nm. Inset of image (B) depicts the SAED pattern of the corresponding QDs.

Figure 4.8. 115

Absorption spectra (a) and Normalized room temperature PL spectra (b) of CdSe QDs synthesized in w/o AOT microemulsions *via* electron beam irradiation with variable absorbed radiation doses at fixed precursor concentration (20 mM) and $W_0 = 10$. Inset of plot (a): Tauc plot for the determination of band gap values (E_g). Inset of plot (b): Plot showing the excitation wavelength independent PL spectra of CdSe QDs synthesized at an absorbed dose of 25 kGy.

Figure 4.9. 119

Emission decay curve ($\lambda_{ex} = 374$ nm) along with the IRF and the best fitted curve for CdSe QDs synthesized *via* electron beam irradiation with variable absorbed doses at fixed precursor concentration (20 mM), and $W_0 = 10$.

Figure 4.10. 121

Deconvoluted PL spectra of CdSe QDs synthesized in w/o AOT microemulsions *via* electron beam irradiation with an absorbed dose of 10 kGy (a), 25 kGy (b) and 50 kGy (c) at fixed precursor concentration (20 mM) and $W_0 = 10$.

Figure 4.11.

122

Absorption spectra (a) and Normalized room temperature PL spectra (b) of CdSe QDs synthesized in w/o AOT microemulsions *via* electron beam irradiation with variable precursor concentrations at a fixed absorbed dose (25 kGy) and $W_0 = 10$. Inset of plot (a): Tauc plot for the determination of band gap values (E_g). Inset of plot (b): A representative de-convoluted PL spectrum of CdSe QDs synthesized in microemulsion of $W_0 = 10$ @ 25 kGy and precursor concentration = 30 mM.

Figure 4.12.

124

Absorption spectra (a) and Normalized PL spectra (b) of CdSe QDs synthesized in w/o AOT microemulsions *via* electron beam irradiation with variable W_0 values at a fixed absorbed dose (25 kGy) and precursor concentration (20 mM). Inset of plot (a): Tauc plot for the determination of band gap values (E_g).

Figure 4.13.

126

Camera ready picture of vials containing CdSe QDs synthesized in AOT microemulsions with variable W_0 values [$W_0 = 5$, Bluish-white color (a); $W_0 = 10$, greenish-yellow color (b); $W_0 = 15$, reddish-orange color (c)] *via* electron beam irradiation at a fixed absorbed dose (25 kGy) and precursor concentration (20 mM).

Scheme 4.3.

127

Diagrammatic representation of the electron beam assisted synthesis of CdSe QDs in the host matrix of AOT microemulsions and the PL tunability displayed by the QDs as shown in the chromaticity diagram at various experimental conditions.

Figure 4.14.

128

TEM images of CdSe QDs synthesized in AOT microemulsions with $W_0 = 5$ at different time intervals: immediately (a) and at time duration of ~ 12 hours (b) after irradiation. Images (c) and (d) represents CdSe QDs synthesized in AOT microemulsions with $W_0 = 10$ and 15 , respectively at time duration of ~ 12 hours, after irradiation. Inset in the images (b), (c) and (d) shows the corresponding size distribution plot of the nanoparticles at respective W_0 values of microemulsions. The other experimental parameters are: [precursor] = 20 mM, absorbed dose = 25 kGy.

Figure 4.15.

129

Deconvoluted PL spectra of CdSe QDs synthesized in w/o AOT microemulsions *via* electron beam irradiation with variable W_0 values i.e. 5 (a), 10 (b), 15 (c) at fixed precursor concentration of 20 mM and an absorbed dose of 25 kGy.

Figure 4.16.

130

Absorption spectra (a) and Normalized PL spectra (b) of CdSe QDs synthesized in w/o CTAB microemulsions *via* electron beam irradiation with variable W_0 values at a fixed absorbed dose (25 kGy) and precursor concentration (20 mM). Inset: Tauc plot for the determination of band gap values (E_g).

Figure 4.17.

133

Emission decay curve ($\lambda_{ex} = 374$ nm) along with the IRF and the best fitted curve for CdSe QDs synthesized *via* electron beam irradiation in CTAB and AOT microemulsions with variable W_0 values at fixed precursor concentration (20 mM) and absorbed dose (25 kGy).

Figure 4.18. 135

TEM images showing CdSe nanorods synthesized in AOT microemulsions with variable W_0 values of 5 (a); 10 (b); 15(c) *via* electron beam irradiation at a fixed absorbed dose (25 kGy) and precursor concentration of 20 mM. The images were taken at ~ 12 hours after irradiation of the sols.

Figure 4.19. 137

TEM images at different magnifications and regions of the grid showing the self-assembling of CdSe QDs (synthesized in AOT microemulsions with $W_0 = 10$, [precursor] = 20 mM @ 25 kGy) into rod shaped structures. The images were recorded at time intervals of ~ 6 hours after the electron beam irradiation.

Figure 4.20. 138

SEM images showing the transformation of globular shaped (a) CdSe nanoparticles (formed initially after the irradiation) into nanorod like structures (b). The experimental parameters are: $W_0 = 10$, [precursor] = 20 mM, absorbed dose = 25 kGy.

Figure 5.1. 144

Structures of FAP based imidazolium ILs.

Figure 5.2. 148

Picture showing the color change of [EMIM][FAP] on irradiation. Dose imparted in kGy: (a) 0, (b) 50, (c) 100, (d) 200, (e) 300, (f) 400.

Figure 5.3.	150
UV-Vis absorption spectra of pre- and post-irradiated [EMIM][FAP] (A) and [EOHMIM][FAP] (B) at various absorbed doses in kGy : 0 (a), 100 (b), 200 (c), 300 (d), 400 (e). Inset of plot (A) shows the variation of absorbance values with absorbed doses at 290 nm, where (*) & (•) represents [EMIM][FAP] & [EOHMIM][FAP] respectively.	
Figure 5.4.	151
UV-Vis absorption spectra of ILs irradiated with an absorbed dose of 100 kGy: (a) [PH(3)T][FAP], (b) [EMIM][FAP], (c) [EOHMIM][FAP], (d) [EMIM][EtSO ₄].	
Figure 5.5.	159
Shear stress <i>vs.</i> shear rate (A) and viscosity <i>vs.</i> shear rate (B) of [EMIM][FAP] prior to irradiation.	
Figure 5.6.	159
Shear stress <i>vs.</i> shear rate (A) and viscosity <i>vs.</i> shear rate (B) of irradiated (Dose \approx 100 kGy) [EMIM][FAP].	
Figure 5.7.	160
Linear fit plots showing the variation of $\ln \eta_a$ with $1/T$ for unirradiated and irradiated FAP ILs.	
Figure 5.8.	162
TGA profiles of unirradiated and irradiated (400 kGy) ILs (a) [EMIM][FAP] and (b) [EOHMIM][FAP], showing the onset decomposition temperatures T_d ($^{\circ}\text{C}$).	
Figure 5.9.	165
Cyclic Voltammograms of pre- and post-irradiated FAP ILs: (a) [EMIM][FAP], (b) [EOHMIM][FAP].	

Figure 5.10.	166
¹ H and ¹⁹ F NMR spectra of pre- and post-irradiated [EMIM][FAP].	
Figure 5.11.	167
¹ H and ¹⁹ F NMR spectra of pre- and post-irradiated [EOHMIM][FAP].	
Figure 5.12.	171
ESI (+) mass spectra of [EMIM][FAP] after irradiation to a total absorbed dose of 400 kGy.	
Figure 5.13.	173
ESI (+) mass spectra of [EOHMIM][FAP] after irradiation to a total absorbed dose of 400 kGy.	
Figure 5.14.	175
ESI (-) mass spectra of [EMIM][FAP] after irradiation to a total absorbed dose of 400 kGy.	
Figure 5.15.	178
Transient absorption spectra recorded at 3 μs after the electron pulse from neat [EMIM][FAP] (blue) and [EOHMIM][FAP] (red); dose per pulse was 12 Gy.	
Figure 5.16.	179
Transient decay in the absence and presence of oxygen for [EMIM][FAP] (A) and [EOHMIM][FAP] (B).	
Figure 5.17.	181
Fluorescence spectra of neat unirradiated (A) and post irradiated [EMIM][FAP] at various absorbed doses (in kGy) i.e. 100 (B); 200 (C); 300 (D). Inset: Plot of λ _{ex} vs. λ _{em} showing the shifts in the maximum intensity peak positions.	

Figure 5.18.	183
Fluorescence spectra of neat unirradiated (A) and post irradiated [EOHMIM][FAP] at various absorbed doses (in kGy) i.e. 100 (B); 200 (C); 300 (D). Inset: Plot of λ_{ex} vs. λ_{em} showing the shifts in the maximum intensity peak positions.	
Figure 5.19.	184
Fluorescence spectra of post-irradiated (@ 400 kGy) [EOHMIM][FAP]. Inset: Plot of λ_{ex} vs. λ_{em} showing the shifts in the maximum intensity peak positions.	
Figure 5.20.	186
FTIR spectra of neat pre- and post-irradiated [EMIM][FAP] at various absorbed doses (in kGy) i.e. 0, 100 and 400.	
Figure 5.21.	187
FTIR spectra of neat unirradiated and post-irradiated [EMIM][FAP] in different wave number regions at various absorbed doses.	
Figure 5.22.	188
FTIR spectra of neat unirradiated and post-irradiated [EOHMIM][FAP] at various absorbed doses (in kGy) i.e. 0, 100 and 400.	
Figure 5.23.	189
FTIR spectra of neat unirradiated and post-irradiated [EOHMIM][FAP] at various absorbed doses (in kGy) i.e. 0, 100 and 400.	

- Figure 5.24.** 190
FTIR spectra of unirradiated and post-irradiated [EOHMIM][FAP] showing the perturbations in the O-H stretching frequency at various absorbed doses (in kGy) i.e. 0, 100 and 400. Inset: Graph showing the Raman spectrum of unirradiated [EOHMIM][FAP] in the same frequency region as that of FTIR. Pictorial representation of –OH bonding interactions possibly existing in [EOHMIM][FAP].
- Figure 5.25.** 192
Raman spectra of neat unirradiated and post-irradiated [EMIM][FAP] (A) and [EOHMIM][FAP] (B) at various absorbed doses.
- Figure 5.26.** 193
Raman spectra of neat unirradiated and post-irradiated [EMIM][FAP] in different wave number regions at various absorbed doses.
- Figure 5.27.** 194
Raman spectra of neat unirradiated and post-irradiated [EOHMIM][FAP] in different wave number regions at various absorbed doses.
- Figure 5.28.** 195
Lifetime decay profile of neat irradiated [EMIM][FAP] (a) and [EOHMIM][FAP] (b) at various absorbed doses.
- Figure 6.1.** 201
Structure of IL, 1-ethyl-3-methylimidazolium ethylsulfate, [EMIM][EtSO₄].
- Figure 6.2.** 202
UV-Vis absorption spectra of CdSe nanoparticles synthesized in IL *via* electron beam irradiation, Dose = 10 kGy. Inset: Camera ready picture of the unirradiated IL, (a); neat IL (10 kGy), (b); IL + CdSe (10 kGy), (c).

- Figure 6.3.** 204
UV-Vis absorption spectra of Se nanoparticles synthesized in IL ([EMIM][EtSO₄]) *via* electron beam irradiation, Dose = 10 kGy.
- Figure 6.4.** 205
TEM image of the nanostructure synthesized in IL *via* electron beam irradiation, Dose = 10 kGy. Inset: SAED pattern of the fibrous and the thick black chunks.
- Figure 6.5.** 206
SEM images (a, c, e) of the nanostructures synthesized in IL ([EMIM][EtSO₄]) *via* electron beam irradiation at various regions. Adjacent images (b), (d), (f) corresponds to the EDS of the marked locations in the SEM images (a), (c) and (e) respectively.
- Figure 6.6.** 209
Raman spectra of the nanostructures synthesized in IL ([EMIM][EtSO₄]) *via* electron beam irradiation at various regions: (a) & (c) depicts the formation of CdSe nanoparticles, while (b) & (d) represents the fibrous regions (comprises of mainly Se) present in the sample.
- Figure 6.7.** 210
Raman spectrum of the Se nanoparticles synthesized in IL ([EMIM][EtSO₄]) *via* electron beam irradiation, Dose = 10 kGy.
- Figure 6.8.** 211
XRD spectrum of as grown nanostructure synthesized in IL ([EMIM][EtSO₄]) *via* electron beam irradiation before (a) and after heating the sample at 230°C for 1 hour (b). Dose = 10 kGy.

Figure 6.9.	212
SEM image of the Se nanofibers synthesized in IL ([EMIM][EtSO ₄]) <i>via</i> electron beam irradiation, Dose = 10 kGy.	
Figure 6.10.	215
TEM images of bare CdSe nanoparticles synthesized in aqueous medium <i>via</i> electron beam irradiation.	
Figure 6.11.	216
SEM images of as obtained nanostructures synthesized in IL ([EMIM][EtSO ₄]) <i>via</i> γ -irradiation, Dose = 10 kGy.	
Figure 6.12.	217
Raman spectrum of the nanostructure synthesized in IL ([EMIM][EtSO ₄]) <i>via</i> γ -beam irradiation, Dose = 10 kGy.	
Scheme 6.1.	219
Scheme showing the proposed mechanism for the nanomorphology i.e. Islands of CdSe nanoparticles within Se nanofibers obtained on electron beam irradiation of the IL ([EMIM][EtSO ₄]) containing Cd and Se precursors. Dose = 10 kGy.	
Figure 6.13.	222
UV-Vis absorption spectra of neat IL (a) and CdSe nanoparticles synthesized in IL ([EMIM][EtSO ₄]) (b). Inset: Tauc plot of $(\alpha'hv)^2$ vs. hv for the determination of band gap values (E_g).	
Figure 6.14.	224
XRD spectrum of as grown nanoparticles synthesized in IL ([EMIM][EtSO ₄]) before (a) and after heating the sample at 230 °C for 1 hour (b). The peaks marked by the star sign (★) has been identified as originated due to the presence of residual Se.	

Figure 6.15.

225

TEM (a) (Scale bar dimensions = 50 nm) and the HRTEM (b) image (Scale bar dimensions = 2 nm) of the CdSe nanoparticles synthesized in neat IL ([EMIM][EtSO₄]). Inset in the image (b) shows the lattice fringe pattern with the interplanar distance of 0.18 nm, which correspond to the (201) plane (standard value of the interplanar distance = 0.179 nm) of the hexagonal phase of CdSe.

Figure 6.16.

225

TEM images (a & b) showing the self-assembling of primary nanoparticles. Images (c) & (d) clearly illustrates the formation of sheet like superstructures as a result of self-assembling. Inset of image (d) shows the SAED pattern of the corresponding structure. The images were taken after 5 hours of the reaction.

Figure 6.17.

226

SEM images of as grown CdSe nanostructures after 5 hours of the reaction at different regions of the sample depicting the various transient stages as: globular like shape (a), nanoflake (NF) like structure (b), flower-like 3D pattern (c) and nanosheet like 2D structures (d). (Scale bar dimensions in all the images is 3 μm). Inset of image (a) shows the EDS spectrum confirming the formation of CdSe nanoparticles.

Figure 6.18.

227

SEM images of as grown CdSe nanostructures after 24 hours, showing the dual co-existence of nanosheets and nanoflowers.

Figure 6.19.

230

SEM images (at different regions with various nanoscale dimensions) of as grown CdSe nanostructures synthesized in IL ([EMIM][EtSO₄]) having 0.35 mole fraction of water. The images were taken after 5 hours of the reaction.

Figure 6.20.	231
SEM images (at different regions with various nanoscale dimensions) of as grown CdSe nanostructures synthesized in IL ([EMIM][EtSO ₄]) having 0.35 mole fraction of water. The images were taken after 24 hours of the reaction.	
Figure 6.21.	232
SEM image of as grown CdSe nanostructures synthesized in IL ([EMIM][EtSO ₄]) having 0.91 mole fraction of water. The image were taken after 5 hours of the reaction. Scale bar dimensions = 5 μm (a) and 20 μm (b).	
Figure 6.22.	233
SEM images at different nanoscale dimensions of as grown CdSe nanostructures synthesized in IL ([EMIM][EtSO ₄]) having 0.91 mole fraction of water.	
Scheme 6.2.	234
Schematic representation showing the probable intermediate stages with different nano/micro-morphologies of CdSe synthesized in IL ([EMIM][EtSO ₄]), at various time intervals and mole fractions of water.	
Figure 6.23.	235
Multi-Lorentzian fitting Raman spectrum of CdSe nanoparticles synthesized in neat IL ([EMIM][EtSO ₄]).	
Figure 6.24.	237
FT-IR spectra of neat IL (a) and IL + CdSe (b). Inset shows the IR spectra of the same in the region of 700-500 cm ⁻¹ .	
Figure 6.25.	239
Raman spectra of neat IL (a) and IL + CdSe (b). The peaks marked have been described in the text.	

Scheme 6.3.	240
Diagrammatic representation of the possible interactions of the cationic and the anionic moieties of the IL with the as grown CdSe nanoparticles.	
Figure 7.1.	248
TEM (a) and HRTEM (b) images of β -CD/QD with molar ratio of 2:1. Inset in the image (b) shows the particle size distribution. The average size was found to be ~ 2.2 nm. TEM image of β -CD/QD with molar ratio of 1:1 (c), synthesized <i>via</i> electron beam irradiation (Absorbed dose = 25 kGy @ 140 GPP).	
Figure 7.2.	251
XRD patterns of bare CdSe nanoparticles (a), β -CD/CdSe QD with molar ratio of 2:1 (b), synthesized <i>via</i> electron beam irradiation (Dose = 25 kGy @ 140 GPP).	
Figure 7.3.	252
Raman spectra of bare CdSe nanoparticles (a), β -CD/QDs with molar ratio of 2:1 (b), synthesized <i>via</i> electron beam irradiation (Dose = 25 kGy @ 140 GPP).	
Figure 7.4.	253
SEM image (a) and the corresponding EDS (b) of β -CD/CdSe nanoparticles with molar ratio of 2:1, synthesized <i>via</i> electron beam irradiation (Dose = 25 kGy @ 140 GPP). Images (c) & (d) show the presence of Cd and Se, respectively during the chemical composition mapping of the region in image (a).	
Figure 7.5.	256
FTIR spectra of β -CD (a), β -CD/CdSe with molar ratio of 2:1 (b). Absorbed Dose = 25 kGy @ 140 GPP.	

Figure 7.6.	258
Core level XPS spectra of (a) O 1s, (b) Cd 3d, and (c) Se 3d.	
Figure 7.7.	259
UV-Vis absorption spectra of β -CD/CdSe QDs with molar ratios (β -CD: QD); 1:2 (a), 1:1 (b), 2:1 (c). Inset shows the spectra with higher molar ratios (β -CD: QD); 4:1 (d), 8:1 (e), 12:1 (f). Absorbed Dose = 25 kGy @ 140 GPP.	
Figure 7.8.	261
Trend showing PL intensity of β -CD/CdSe QDs with various molar ratios (β -CD: QD) at 525 nm. $\lambda_{\text{ex}} = 420$ nm. Absorbed dose = 25 kGy @ 140 GPP.	
Figure 7.9.	263
UV-Vis absorption spectra of β -CD/CdSe QDs with molar ratio (β -CD: QD, 2:1) at various doses (@ 140 GPP); 10 kGy (a), 15 kGy (b), 25 kGy (c). Inset: Tauc plot of $(\alpha' h\nu)^2$ vs. $h\nu$ for the determination of band gap values (E_g).	
Figure 7.10.	264
Trend showing PL intensity of β -CD/CdSe QDs vs. radiation dose with molar ratio (β -CD: QD) of 2:1 at 525 nm and λ_{ex} of 420 nm. Dose rate = 140 GPP.	
Figure 7.11.	265
Room temperature PL spectra (A) and the PL Lifetime decay curve ($\lambda_{\text{ex}} = 374$ nm) (B) of β -CD/CdSe QDs with molar ratio (β -CD: QD) of 2:1 at an absorbed dose of 25 kGy @ 140 GPP.	

Figure 7.12. 267

Room temperature time resolved PL decay curve ($\lambda_{\text{ex}} = 374$ nm and $\lambda_{\text{em}} = 600$ nm) of β -CD/CdSe QDs with molar ratio (β -CD: QD) of 2:1 at various absorbed doses @ 140 GPP.

Figure 7.13. 270

UV-Vis absorption spectra of β -CD/CdSe QDs with molar ratio (β -CD: QD, 2:1) at various dose rates; 50 GPP (a), 80 GPP (b), 140 GPP (c). Absorbed dose = 25 kGy. Inset: Tauc plot of $(\alpha' \text{h}\nu)^2$ vs. $\text{h}\nu$ for the determination of band gap values (E_g).

Figure 7.14. 272

Trends showing variations in the intensities of BGE ($\lambda_{\text{em}} = 525$ nm) and TSE ($\lambda_{\text{em}} = 600$ nm) displayed by β -CD/CdSe QDs at various dose rates i.e. 50 GPP, 80 GPP and 140 GPP, keeping absorbed dose fixed as 15 kGy (A) and 25 kGy (B). Molar ratio (β -CD: QD) = 2:1. Inset shows the ratio of the intensities of BGE and TSE.

Figure 7.15. 273

Room temperature PL spectra ($\lambda_{\text{ex}} = 480$ nm) of β -CD/CdSe nanoparticles with molar ratio (β -CD: QD) of 2:1 at an absorbed dose of 1 kGy @ 10 GPP.

Scheme 7.1. 274

Electron beam mediated synthesis and the optical tunability (shown in the chromaticity diagram) displayed by β -CD/CdSe nanoparticles at various experimental conditions.

Figure 7.16.

276

Transient absorption spectra obtained from the pulse radiolysis studies of the aqueous solutions containing Cd and Se precursors along with β -CD at following experimental conditions: [Precursor] = 1 mM; [β -CD] = 2 mM; Pulse duration = 100 ns; Dose = 21 Gy.

Figure 7.17.

278

Representative Images showing the changes in the morphology of INT 407 cells exposed to β -CD, bare CdSe QDs and β -CD/CdSe QDs, respectively. The cells were incubated and monitored 24 hour post treatment using an inverted microscope.

LIST OF TABLES

	Page No.
Table 3.1. Yields of hydrated electrons in the CTAB/H ₂ O/n-butanol/cyclohexane microemulsion.	80
Table 3.2. Yields of dibromide radical anion (Br ₂ ^{•-}) in the CTAB (or CPB)/H ₂ O/cyclohexane/n-butanol microemulsion ($W_0 = 40$).	87
Table 4.1. The band gap values (eV) and the size of the CdSe nanoparticles (nm) (shown in parentheses) synthesized at room temperature as determined from the optical absorption measurements.	103
Table 4.2. Various measurements i.e. band gap values (E_g , eV), size (d, nm), FWHM (nm), emission maxima (λ_{max} , nm), QE (η , %) and average lifetime ($\langle\tau\rangle$, ns) values of CdSe QDs synthesized <i>via</i> electron beam irradiation with different combination of W_0 values, precursor concentrations and absorbed radiation dose.	117
Table 4.3. CIE chromaticity co-ordinates along with the nature of the light emitted by CdSe QDs synthesized in AOT microemulsions <i>via</i> electron beam irradiation under various experimental conditions.	126
Table 4.4. Aspect ratio of CdSe nanorods grown in AOT microemulsions with variable W_0 values <i>via</i> electron beam irradiation at a fixed absorbed dose (25 kGy) and stock precursor concentration of 20 mM.	136

Table 5.1	153
pH values of the aqueous phase of the FAP ILs on irradiation.	
Table 5.2.	157
Refractive indices (n) of FAP ILs at 25 °C at various absorbed dose levels.	
Table 5.3.	158
Physical properties of FAP ILs measured at various absorbed dose levels.	
Table 5.4.	161
Activation energy for viscous flow, E_{η} for pre- and post-irradiated FAP ILs.	
Table 5.5.	164
Electrochemical windows of pre- and post-irradiated FAP ILs.	
Table 5.6.	169
Bond dissociation energies (kJ/mol).	
Table 5.7.	176
Hydrogen gas yields from benzene and various ILs irradiated with the same absorbed dose of 54 kGy.	
Table 5.8.	182
Table showing the corresponding λ_{em} and maximum fluorescence intensity values for neat pre- and post-irradiated [EMIM][FAP] at different λ_{ex} and absorbed dose values.	
Table 5.9.	184
Table showing the corresponding λ_{em} and maximum fluorescence intensity values for neat pre- and post-irradiated [EOHMIM][FAP] at different λ_{ex} and absorbed dose values.	

Table 5.10.	196
Lifetime values for post-irradiated [EMIM][FAP] and [EOHMIM][FAP] at various absorbed doses. The values provided in the parentheses are the respective amplitudes for each times constants (T1, T2, and T3).	
Table 7.1.	262
The band gap values (E_g , eV) and the size of the CdSe QDs (nm) synthesized <i>via</i> electron beam irradiation with different molar ratios of β -CD and precursor concentrations, absorbed dose and dose rates.	
Table 7.2.	268
Emission lifetime values of β -CD/CdSe QDs synthesized <i>via</i> electron beam irradiation at different absorbed doses with fixed molar ratio of 2:1 and dose rate at 140 GPP ; $\lambda_{ex} = 374$ nm and $\lambda_{em} = 600$ nm.	
Table 7.3.	273
CIE Chromaticity x, y co-ordinates of as grown β -CD/CdSe QDs with molar ratio (β -CD: QD) of 2:1 at various experimental conditions.	

Chapter 1

General Introduction

1.1. Microheterogeneous systems and their importance

The ability of the nature to direct the self-assembly of simple molecular precursors into extremely complex biomolecules is one of the vital phenomenon for the existence as well as sustainment of the life processes. Evidently so, most of the matter surrounding us in contemporary world is heterogeneous (composites) and multi-component, possessing a rich and complex self-organized internal structure. It is quite astonishing to notice that majority of the naturally occurring biochemical reactions takes place in a confined environment and are closely interconnected to each other in such a way that the product of one reaction becomes the reactant or catalyst of the subsequent one.¹ The coupling, control and fine-tuning of many such reactions are facilitated by the existence of compartmentalized network of nanometer to micrometer-sized complex assemblies. Coexistence of polar and apolar domains characterized by local orientational order, associated interfaces and the dynamic nature of their aggregation are some of the key features of these microheterogeneous systems.¹ For instance, a cell (see Fig.1.1), which is the basic functional unit of life comprises of multiple levels of compartmentalization as a result of self-sorting of various molecular components (e.g., sugars, amino acids and fatty acids). This allows the coexistence of different functional architectures acting

Chapter 1

independently.² Many biological reactions including plant photosynthesis illustrate the benefits of such molecular organization.¹

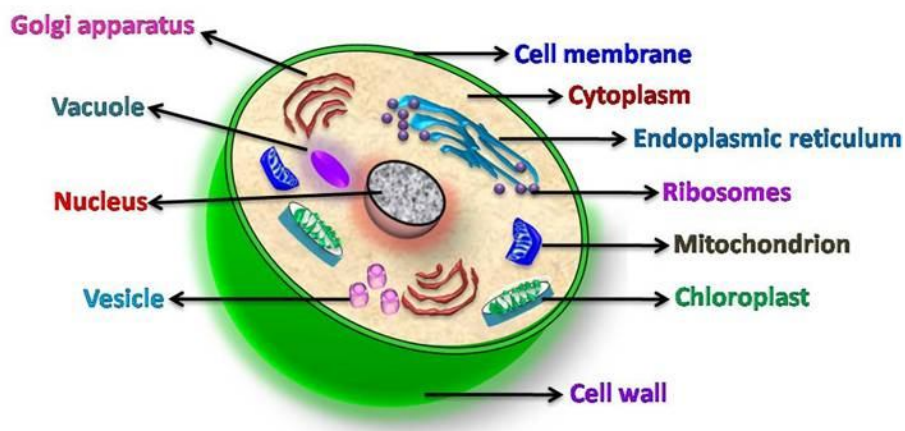


Fig.1.1. Compartmentalized structure of a plant cell.

It is a matter of fact that humans have always approached and tried to emulate the ‘mother nature’ to seek the solutions of their day to day problems. Artificial photosynthesis is one such example³ to tackle the energy crisis scenario. However, to address the core issues of the likewise problems, it is pertinent to have an estimation of a real time information as well as in-depth understanding of the fundamental processes/reactions taking place inside the confined media of naturally occurring self-organized systems. In this endeavour, researchers across the globe have and are being putting their efforts in the design and development of much simplified tailor-made nanoreactors, since construction of a cell like artificial system requires a more natural approach and is still an ultimate fantasy.² Nonetheless, these synthetic systems are structurally microheterogeneous and inherit compartmentalization and other complex functionalities such as dynamism, self-organization, self-replication and recognition,

Chapter 1

which are found in biological systems.^{1, 2} Owing to these, physicochemical properties such as surface tension, vapour pressure, viscosity, solubility, dissociation constants, reaction rates, nucleation and growth processes, stability of reactants, products and intermediates are significantly altered compared to the homogeneous systems. Therefore, in the past three decades, significant number of photochemical and photobiological studies probing the static, dynamic and the interfacial properties of such organized assemblies have been appeared in the literature.⁴ Moreover, these media can be employed as model systems to mimic the naturally occurring organized assemblies for simulating and gaining microscopic insights into various biochemical reaction mechanisms, charge transport and other related processes.^{1, 2} The information obtained from such studies has found utmost relevance in variety of areas such as energy, healthcare and synthesis.^{1, 2, 4, 5}

Some well-known examples of microheterogeneous media are micelles, microemulsions, vesicles (or liposomes), room temperature ionic liquids (RTILs), cyclodextrins (CDs), polymers and lipid membranes.^{1, 2} It is of fundamental interest as well as quite intriguing to probe the primary processes (such as electron solvation, electron transfer, free radical reactions etc.) in these media taking into account of their dissimilarities (mentioned earlier) from the homogeneous systems. Therefore, the present thesis is an attempt to carry out an exposition of the radiation and photochemical investigation of three microheterogeneous systems namely microemulsions, RTILs and CDs, which are entirely different from each other in their structure, nature of heterogeneity, composition and fluidic aspects. Subsequently, the prospects of utilizing the inherent compartmentalization of these media in the controlled synthesis and

Chapter 1

stabilization of nanomaterials were explored. For this, as a case study, cadmium selenide (CdSe) quantum dots (QDs) were grown in the host matrices of aforementioned microheterogeneous systems by radiation as well as normal chemical routes.

In the subsequent sections, an introduction of the basic radiation chemistry and its interaction with the matter (relevant to the present thesis work) has been provided followed by a brief overview of the structural composition and organizational peculiarities of as studied microheterogeneous systems (microemulsions, RTILs and CDs). Besides this, a concise description of the semiconductor QDs and their electronic structure has been discussed. Amongst various techniques, the formation mechanism of nanomaterials in case of radiation (e^- , γ) induced approach is different from the conventional ones, so a discussion accounting for its principle and related advantageous aspects is presented herein.

1.2. Radiation chemistry

Radiation chemistry is the study of the chemical effects of high energy charged particles (electrons, protons, deuterons, α -rays, etc.) and electromagnetic radiations of short wavelengths (γ -rays and X-rays) with matter.⁶ It is distinct from the photochemistry, which deals with the chemical effects produced by photons (energies of a few electron volts (eV)) in the UV-Visible region. On the other hand, in radiation chemistry, photon or a particle involved carries energies in keV to MeV range and the maximum energy deposition is generally non-selective in nature.⁶ Nevertheless, radiation chemistry, nearly a century old area of research and probably the basis of radiation biology (indirect

Chapter 1

effects), is still active in solving many contemporary problems in industry, medicine and biology.⁶

1.2.1. Interaction of high energy radiation with matter

The extent and mechanism of interaction of the ionizing radiations with the matter depends upon the nature (energy, particulate mass and charge) of the former and the electron density (atomic number) of the medium with which it interacts.⁶ Mechanisms of interaction of ionizing radiations (such as electromagnetic radiations, electrons, neutrons and heavy charged particles), which are of primary relevance in radiation chemistry are explained briefly in the following sections.

1.2.1.1. Electromagnetic Radiation

Electromagnetic radiations having wavelength less than 100 Å belong to this class of ionizing radiation and are usually called as X-rays (extranuclear origin) or γ -rays (produced from the atomic nuclei). Their interaction with the matter involves several distinct processes. The relative efficiency of each process is strongly dependent upon the energy of the photons and the atomic number (Z) of the absorbing medium. The three main processes involved are photoelectric effect, Compton scattering and pair production.

(a) Photoelectric effect: It occurs primarily when the energy of the photon is less than 100 keV. The entire photon energy (E_0) is transferred to a single atomic electron, which is then ejected from the atom with kinetic energy equal to the difference between the photon energy and the binding energy (E_b) of the electron in the atom. This type of interaction is most probable for high Z materials.

Chapter 1

(b) Compton scattering: In this process, a photon interacts with a loosely bound or free electron which as a result gets accelerated, while the photon is deflected with reduced energy. The energy of the scattered photon is related to the angle θ (angle between the scattered photon with respect to the incident one) by equation 1.1:

$$E_{\gamma} = \frac{E_0}{1 + (E_0/m_e c^2) (1 - \cos \theta)} \quad [1.1]$$

where E_0 and E_{γ} are the energies of the incident and scattered photons, respectively and $m_e c^2$ is the rest energy of the electron.

The energy of recoiled electron, $E_e = E_0 - E_{\gamma}$. This type of process predominates for photon energies between 1 and 5 MeV in high Z materials. In water, Compton interaction is the major process for photon energies from 30 keV to 10 MeV.

(c) Pair production: In this process, complete absorption of a photon with energy > 1.024 MeV may leads to a production of two particles, an electron and a positron. The energy in excess of 1.02 MeV appears as the kinetic energy of the electron and positron. The probability of pair production increases with Z of the absorber and with the photon energy.

1.2.1.2. Electrons

Electrons interact with matter by a mainly by three processes i.e. emission of electromagnetic (or bremsstrahlung) radiation, inelastic and elastic collisions. The relative importance of these processes depends mostly on the energy of the electrons and to a lesser extent on the nature of the absorbing material.

Chapter 1

(a) **Emission of bremsstrahlung radiation:** High energy electrons passing close to the nucleus of an atom are decelerated due to their interaction with the electric field of the nucleus and radiate energy as bremsstrahlung X-radiations. However, for electrons below 100 keV, bremsstrahlung emission is negligible but increases rapidly with increasing energy and is the dominant mode of energy loss in case of high Z stopping material and at electron energy between 10-100 MeV.

(b) **Inelastic collisions:** At electron energies below those at which Bremsstrahlung emission takes place, inelastic collision is the main process of interaction. The average amount of kinetic energy lost (leading to excitation and ionization) per unit length by a fast electron through Coulomb interaction with atomic electrons in a medium is defined as the specific energy loss or stopping power (S) of the medium. It can be expressed by the modified Bethe-Bloch equation, which is expressed by equation 1.2:⁷

$$S = -\frac{dE}{dx} = 2\pi N_a r_e^2 m_e c^2 \rho \frac{Z}{A} \frac{1}{\beta^2} \left[\ln \frac{\tau^2(\tau+2)}{2(I/m_e c^2)^2} + F(\tau) - \delta - 2\frac{C}{Z} \right] \quad [1.2]$$

$$\text{and, } F(\tau) = 1 - \beta^2 + \frac{\frac{\tau^2}{8} - (2\tau + 1) \ln 2}{(\tau + 1)^2}$$

where τ is the kinetic energy of the particle in units of $m_e c^2$; r_e = classical electron radius (2.817×10^{-13} cm); m_e = electron mass, N_a = Avogadro's number = 6.023×10^{23} mol⁻¹; I = mean excitation potential; Z = atomic number of absorbing medium; A = atomic weight of absorbing medium; ρ = density of absorbing medium; β = v/c of the incident particle; δ = density correction (corrects for polarization effects in the target, which reduces the stopping power since the ion's electromagnetic fields may not be at the assumed free-space values, but reduced by the dielectric constant of the target medium); C = shell

Chapter 1

correction (This shell correction term takes care of the assumption that the ion velocity is much larger than the target electron velocity)

(c) Elastic collisions: This process occurs when electrons are deflected by the electrostatic field of an atomic nucleus and is quite frequent due to the small mass of electrons. It is more probable for electrons with low energy and the target with high atomic number.

(d) Cerenkov Emission: Electrons having a velocity greater than that of light in a particular medium lose energy by emitting electromagnetic radiation, called Cerenkov radiation. This phenomenon is responsible for the blue glow observed in case of high intensity γ -sources that are stored under water.

1.2.1.3. Neutrons

Neutrons, being uncharged particle, interact almost exclusively with the atomic nuclei of the material. The main interaction processes are elastic scattering, inelastic scattering, nuclear reaction and capture. Neutrons do not produce ionization directly in matter but the products of its interactions often cause ionization and thus, produce typical radiation chemical changes. Further, these changes are similar to those caused by charged particles because the main products of neutron interactions are protons and heavy positive ions.

1.2.1.4. Heavy charged particles

Heavy charged particles (e.g. protons, deuterons, α -particles, etc.) interact with the matter in the same way as electrons i.e. by bremsstrahlung emission, inelastic and elastic collisions. However, the most important is inelastic collision, as bremsstrahlung emission occurs only at very high energies (of the order of 1000 MeV) and elastic scattering is

Chapter 1

insignificant. For a given energy, heavy charged particles have a much higher linear energy transfer (LET) than electrons due to the higher mass of the former as compared to later ones. Essentially, LET is the measure of the rate of energy deposition by an ionizing particle traversing the medium. An average LET is calculated by dividing the total energy of a particle by its path length and can be denoted as $-dE/dx$, also called as specific energy loss or stopping power and can be expressed by Bethe-Bloch equation 1.3:⁷

$$S = -\frac{dE}{dx} = 2\pi N_a r_e^2 m_e c^2 \rho \frac{Z}{A} \frac{z^2}{\beta^2} \left[\ln\left(\frac{2m_e \gamma^2 v^2 W_{\max}}{I^2}\right) - 2\beta^2 - \delta - 2\frac{C}{Z} \right] \quad [1.3]$$

where, z is the charge on the incident particle and $\gamma = 1/\sqrt{1 - \beta^2}$. Other symbols are same as defined in equation 1.2. Higher LET values initially give rise to high local concentration of primary species, which recombine in spurs to give molecular products. Thus, with heavy charged particles, the yields of molecular products are higher as compared to those obtained with low LET radiation such as electrons and γ -rays.

1.2.2. Radiation dosimetry and chemical yield

As already mentioned, in radiation chemistry, the energy of the ionizing radiation is in keV to MeV range, while the radiation field is generally expressed as fluence. Basically, it is a measure of the number of particles or photons entering a sphere of unit cross sectional area.^{6, 7} When a material is exposed to a radiation field, the energy deposited depends on the nature of radiation, its energy and on the nature and composition of material. The quantity to measure the amount of energy absorbed by the irradiated material is termed as dose and is essential in radiation chemical studies. The energy deposited in unit mass of the material can be measured as eV g⁻¹ or ergs g⁻¹. The SI unit for the absorbed dose is Joule per kilogram (J Kg⁻¹), which is expressed as Gray (Gy).

Chapter 1

Dose can also be measured in Rad, which is 100 ergs g^{-1} and is related to Gray as: 1 Gray = 100 Rads. Radiation chemical yields are expressed in terms of G-values, where

$$G = \frac{\text{number of species formed/destroyed}}{100 \text{ eV}}$$

SI unit of G value is mol J^{-1} , which is equivalent to $9.65 \times 10^6 \text{ molecules (100 eV)}^{-1}$. Hence, G-values reported originally in terms of number of species per 100 eV can be converted to SI units by multiplying by 1.036×10^{-7} .

1.2.3. Distribution of energy and primary products

In radiation chemistry, the energy deposition takes place non-uniformly in the medium, so that the initial products are also distributed inhomogeneously till the process of diffusion takes place.^{6, 7} The spatial and temporal distribution of energy and radiolysis products in the medium is discussed briefly in this section.

Track is the path of energetic charged particle along which the energy is deposited. The ionization and excitation events take place within 10^{-16} s. On an average, a few hundred eV is transferred to the medium per inelastic collision. This is mostly in the form of kinetic energy of secondary electrons, which can further produce ionization and excitation by colliding with molecules in the immediate vicinity. Thus, all the excited and ionized species produced in a single collision by energy transfer of few hundred eVs are concentrated in a small volume. This small zone of reactive species i.e. ionized and excited species is known as “spur” (Fig.1.2). The size of the spur is decided by the energy transferred from the high energy radiation to the interacting medium. If the energy transferred is between 100-500 eV, the secondary electron can travel more distance

Chapter 1

before its energy is reduced to sub-excitation level, so that reactive species are distributed in a larger volume called as “blob”.

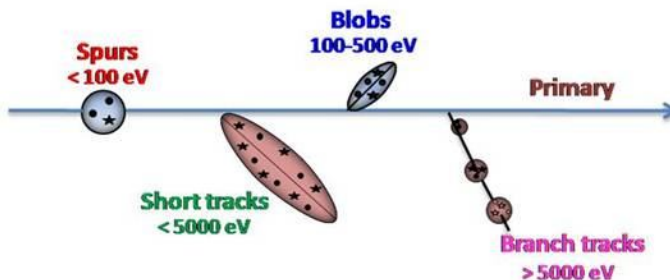


Fig.1.2. Distribution of ions and excited species along the track of fast electron.

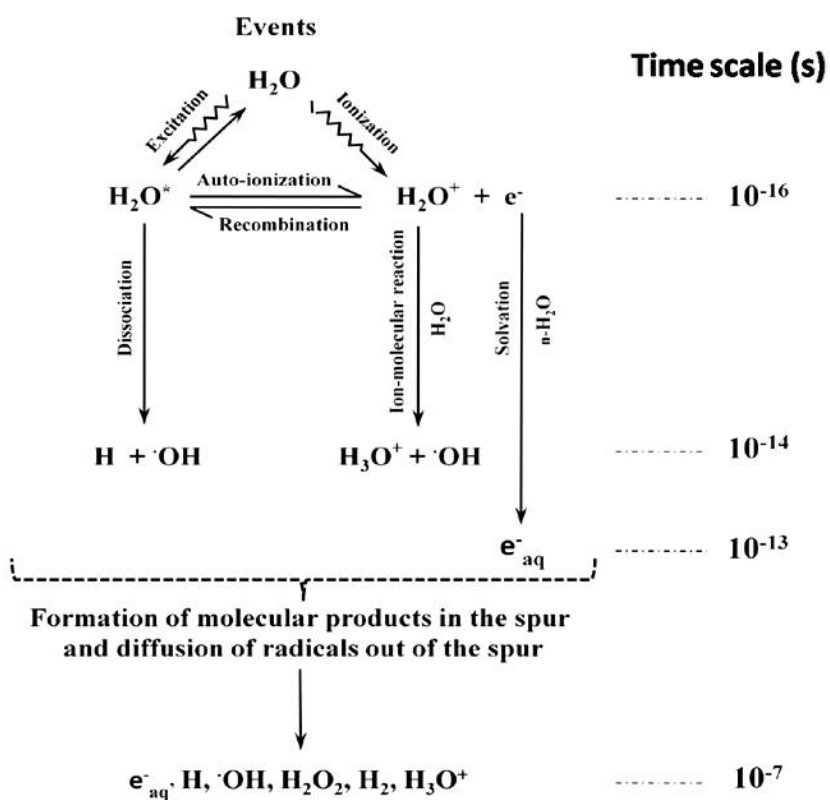
If the energy transferred is between 500-5000 eV, the secondary electrons travel much longer distance and the path followed by these electrons is called a “short track”. For still higher energy transfer, the secondary electrons themselves act as high energy particles and the path is called a “branched track”. After formation of these localized spurs, the uniform distribution of reactive species in the medium takes $\sim 10^{-7}$ s, depending upon the medium. During this time from 10^{-16} to 10^{-7} s, the initially formed ionized and excited species can undergo many reactions. In case of ionization, the released electron gets thermalized and the time taken for this also depends upon the medium. For example, in polar liquid like water, it takes place faster (10^{-13} - 10^{-14} s) as compared to that in apolar liquids such as hexane (10^{-12} s). The reactive species present after $\sim 10^{-7}$ s are distributed uniformly in the medium and are termed as “primary products”. In general, primary products in any medium can be cations, anions, electrons, radicals and excited species.

1.2.4. Radiation chemistry of water

Radiation chemistry of water and aqueous solutions has been extensively investigated and is well understood now.^{6, 8} Moreover, water is the most important component in

Chapter 1

biological systems and therefore, is of importance in radiobiology. Also, water is extensively used in nuclear reactors as coolant and moderator and thus comes in contact with reactor materials under radiation fields. Furthermore, water provides a very convenient medium of generating a variety of unstable species under well-defined conditions. The time scale of events induced by the ionizing radiations such as few MeV electrons in water or aqueous solution is shown in Scheme 1.1.



Scheme 1.1 Time scale of events after passage of high energy radiation through water or aqueous solutions.⁶

The dry electrons produced in the very early stage get trapped within water molecules in a very short time scale after thermalization process and produces hydrated/aquated electron, e_{aq}^- that actually takes part in subsequent chemical reactions. Essentially, a pre-

Chapter 1

solvated electron implies the localization of electron in a pre-existing site or cavity in the matrix without any relaxation of the surrounding solvent molecules while, solvated electron represents a state where the electron resides in an equilibrium configuration of the solvent molecules.

After the initial ionization event, the physicochemical processes are complete within $\sim 10^{-12}$ s, and the resultant species formed such as e_{aq}^- , H^\bullet , $\bullet OH$ and H_3O^+ along with any radical and molecular fragments begin to diffuse and react together to form molecular or secondary radical products (H_2 , H_2O_2). Eventually, these species undergo homogeneous distribution in the medium within $\sim 10^{-7}$ s, which is also known as ‘spur-expansion’. It is to be noted that among all these species, e_{aq}^- and H-atom are reducing while $\bullet OH$ radical is oxidizing in nature.

1.2.5. Primary yields

Primary yield is basically the quantitative estimation of the species remaining when all spur reactions are complete, i.e. in about 10^{-7} s after the ionization event. At this stage, the radiolytic changes in water can be represented by:



In principle, it is possible to measure yields of the radicals directly by using pulse radiolysis. But, in practice, only the yield of e_{aq}^- is measured by this technique because H^\bullet and $\bullet OH$ have very weak absorption in the UV region and are generally masked by those of added solutes. However, yields of H^\bullet and $\bullet OH$ can be measured by adding solutes that react to give observable products under pulse radiolysis conditions.

Chapter 1

For low LET radiations, the generally accepted values of the primary yields (per 100 eV) in the pH range 3-11 are:^{6,8}

$$g(e_{aq}^-) = g(^{\bullet}OH) = g(H_3O^+) = 2.7, g(H^{\bullet}) = 0.6, g(H_2) = 0.45, g(H_2O_2) = 0.7$$

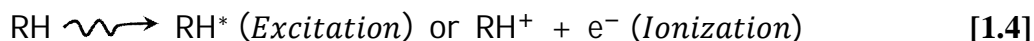
1.2.6. Radiolysis of Organic solvents

Unlike water, organic solvents (like benzene, cyclohexane, tetrahydrofuran etc.) have a lower dielectric constant and possess well defined non-dissociative excited states. As in water, the main effects of radiolysis in organic mediums are also ionization and excitation^{9, 10} however; the electrons produced in later have higher chances of geminate recombination. This is because, the thermalization distance of electron in water is few nm ($\sim 40 \text{ \AA}$), while it is much higher ($\sim 200 \text{ \AA}$) in organic solvents. Since, the probability of an electron escaping its sibling positive ion to become a free ion is $\exp(-r_c/r)$, where r is the distance at which electron becomes thermalized, while r_c is the critical distance at which the potential energy of an ion pair is equal to the thermal energy (kT). In cyclohexane, even if the electron moves away by 40 \AA from the parent cation, the escape probability is negligible whereas for water, it is almost 0.84 at the same distance.⁹

In non-polar media (RH) like cyclohexane and benzene, ion pairs are produced initially from the ionization of the solvent. As already mentioned, due to the low permittivity of these solvents, mutual Coulombic attraction results in recombination of most of these ion-pairs and formation of non-dissociative electronic excited states i.e. singlet and triplet.⁹ These solvent excited states undergo a number of photophysical processes including transfer of their excitation energy to the solute (S). The positive and negative ions arising from the solvent also interact with the solute to give the

Chapter 1

corresponding solute cation (S^+) and anion (S^-). As a result of their recombination process in the solvent cage, solute excited states (singlet and triplet) are produced indirectly. In cyclohexane, solute ion recombination is an important process, while in benzene, energy transfer is considered to be mainly responsible for solute triplet formation.⁹⁻¹¹ The aforementioned processes occurring during the radiolysis of organic solvents are represented by the equations shown below:



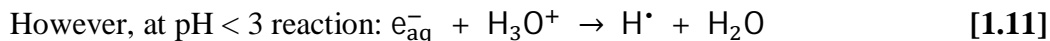
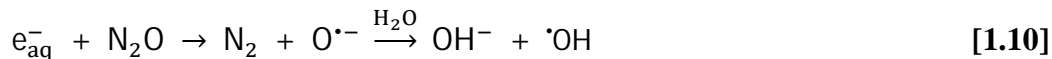
1.2.7. Generation of secondary radicals

As explained in the earlier sections, the primary species produced in the radiolysis of water contain both oxidizing and reducing radicals. However, to conduct various radiation chemical experiments, it is desirable to modify the system (under investigation) into an oxidizing or reducing medium. This can be achieved by either inter-conversion of the primary species or by converting the primary radicals into secondary radicals. In another kind of modification, the unwanted primary radicals are converted into relatively unreactive secondary radicals.

Chapter 1

1.2.7.1. Oxidizing conditions

In general, to obtain an oxidizing condition, the aqueous solutions are saturated with nitrous oxide (N₂O) gas, which converts e_{aq}⁻ to [•]OH radical.^{6,8}



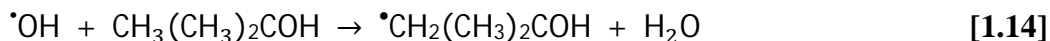
Reaction 1.11 competes with the reaction 1.10 due to which the fraction of the oxidizing radical decreases. Thus, in order to study the [•]OH radical and its reactions in acidic pH (especially < 3), solutions are saturated with oxygen (O₂). As a result, H[•] and e_{aq}⁻ reacts readily with O₂ and get scavenged from the system giving an oxidizing condition.

1.2.7.2. Reducing conditions

To obtain reducing conditions, following reactions are carried out:^{6,8}



However, these reactions are carried out only under high pH and H₂ pressure of 100 atmospheres. Therefore, an alternate and more convenient method of obtaining exclusive reducing conditions is to convert all the primary radicals into secondary reducing radicals by adding an organic solute (e.g. *tert*-butanol) to N₂ saturated aqueous solutions as shown below:



Chapter 1

1.3. Microemulsions

Microemulsions are thermodynamically stable, isotropic and optically clear dispersions of either ‘water in oil’ or ‘oil in water’ stabilized by amphiphiles (or surfactants).^{2, 5, 12, 13} The term “microemulsion” was first coined in 1959 by Schulman and his group.¹² The droplet sizes of the dispersions in microemulsions are less than 100 nm. These systems possess a well-organized internal structure. For example, considering water-*in-oil* (w/o) microemulsion, three very different microenvironments could be found i.e. a continuous medium formed by the alkane, a disperse phase formed by aqueous microdroplets, and a tensioactive film, which separates the aqueous phase from the alkane and allows solubilization to occur. Essentially, the water (dispersed phase in w/o microemulsion) confined in the cavity controls the size and shape of the microemulsion and are often characterized by W_0 , which is defined as the molar ratio of water to surfactant, $W_0 = [\text{H}_2\text{O}] / [\text{surfactant}]$. This factor has often been linearly correlated with the size of the water droplets in w/o microemulsions.^{2, 5}

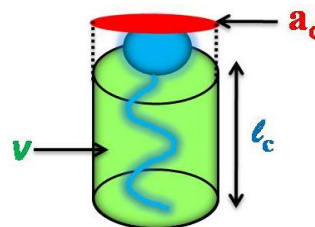
An oil-water interface has high interfacial tension ($\gamma_{o/w}$) such that the free energy of formation of interface is highly positive. It is the addition of amphiphilic compounds (generally, a surfactant) which reside at the oil-water interface and effectively lowers the interfacial tension (from 50 mN m^{-1} at the oil-water interface to the values of the order of $10^{-2} \text{ mN m}^{-1}$) leading to the spontaneous dispersion of two immiscible phases.⁵ The energetics of microemulsion formation can be expressed as:⁵

$$\Delta G = \gamma_{o/w} \Delta A - T \Delta S \quad [1.16]$$

Chapter 1

where, ΔA is the change in interfacial area, ΔS is the entropy change and $\gamma_{o/w}$ is the interfacial tension between oil and water at temperature T (Kelvin). The increase in droplet number on dispersion leads to positive ΔS . If the surfactant reduces the interfacial tension to a sufficiently low value, the energy term in equation (1.16) i.e. $(\gamma_{o/w} \Delta A)$ will be relatively small and positive, thus allowing a negative free energy change. In other words, the main driving force for the spontaneous formation of microemulsion is the lowering of interfacial tension, which eventually leads to large surface area by way of numerous droplets associated with a large change in entropy. However, microemulsion domains fluctuate in size and shape and undergo spontaneous coalescence and breakup. One of the unique factor associated with microemulsions is the presence of different structures as classified by Winsor.^{4, 5} Nevertheless, geometry of the surfactant plays an important role in predicting the type of microemulsion from the preferred curvature (of surfactant film) at the interface. And, it can be determined by calculating the surfactant packing parameter also known as critical packing parameter, CPP:^{4, 5}

$$CPP = \frac{v}{a_o \times l_c} \quad [1.17]$$



where v is the volume of the surfactant alkyl chain, a_o is the head group area and l_c is the length of the fully extended hydrocarbon chain. Surfactants with $CPP = 1$ are most likely to stabilize bicontinuous microemulsions, while surfactants with $CPP > 1$ and < 1 form w/o and o/w microemulsions, respectively. These structures can be represented in a ternary phase diagram shown in Fig.1.3.

Chapter 1

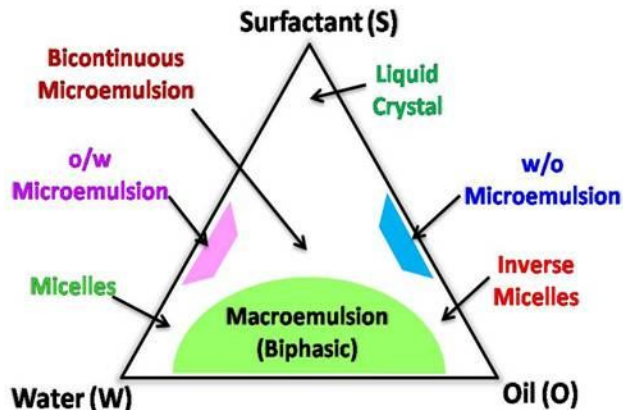


Fig.1.3. A generalized ternary phase diagram depicting various structure formations as a function of different percentage composition of the constituents.

Besides geometry, the charge on the polar head group of the surfactant (anionic, cationic, non-ionic and zwitter-ionic) is another factor to classify various microemulsions and plays an essential role in guiding the structure, dynamics and transport behaviours of microemulsions. For instance, AOT (an anionic surfactant; sodium bis(2-ethylhexyl) sulfosuccinate) and CTAB (cationic surfactant; Cetyltrimethylammonium bromide) based microemulsions are well studied and characterized systems.

Basically, CTAB based microemulsions are quaternary (comprises of 4 components i.e., surfactant, co-surfactant, oil and aqueous) in nature, while AOT based microemulsions are ternary (comprises of three components i.e. surfactant, oil, and aqueous) systems. Fig.1.4 shows the diagrammatic representation of AOT and CTAB based w/o microemulsions. CTAB being a linear chain surfactant could not fulfil the packing and thermodynamic considerations for the microemulsion formation. Hence, a co-surfactant (generally a low chain alcohols i.e. n-butanol, n-pentanol) is required to stabilize w/o microemulsions. Consequently, CTAB based microemulsions possess

Chapter 1

flexible interfacial film and therefore, exhibit greater amount of dynamism^{5, 13} as compared to that of AOT based microemulsions, where interfacial film is quiet rigid.¹⁴ This can be realized from the fact that ~ 1 in 1000 inter-droplet collisions result in an exchange of reactants in case of AOT microemulsions, whereas ~1 in 10 collisions can give rise to exchange of micellar content in case of CTAB microemulsions.^{14, 15} Thus, the CTAB based microemulsions are much more complex in terms of dynamics of the reactants as compared to that of AOT based microemulsions.

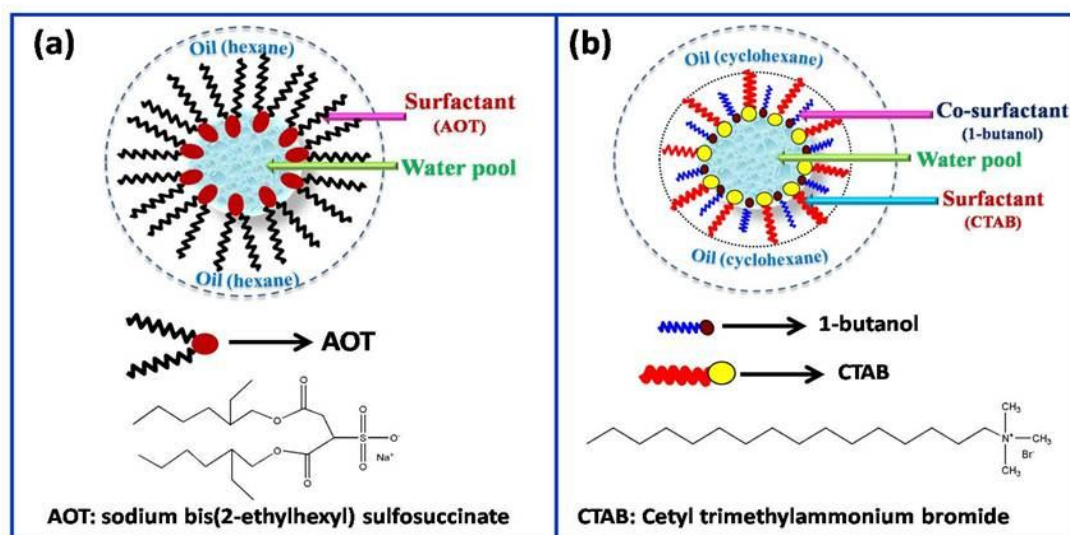


Fig.1.4. Diagrammatic representation of AOT (a) and CTAB based w/o microemulsions. The molecular structures of AOT and CTAB are also shown.

Owing to the compartmentalized molecular organization similar to that found in bioaggregates, numerous reports^{1, 2, 4, 5, 14, 15} can be found in the literature, wherein microemulsions have been used as a nanoreactor to carry out and study the kinetics and mechanism of various chemical and biological processes. In addition to that, radiochemical studies¹⁶⁻²⁰ have been carried out in these media, which could enhance our

Chapter 1

understanding of electron transfer reactions, charge separation, charge recombination and electron solvation in organized media. The nature of hydrocarbon phase, interface and the dimensions of water pool has been reported to have pronounced effect on the decay kinetics and the nature of solvated electrons.^{16, 19} However, majority of such studies have been carried out in AOT based microemulsions. While, the number of such studies carried out on microemulsions with four components (such as CTAB based) is very less. In the present thesis, an effort has been made to comprehend the solvated electron properties in CTAB based w/o microemulsion and the role of interface in influencing its kinetics has also been addressed.²¹ Furthermore, the presence of counter ions in microemulsions has not been seriously considered in earlier radiation chemical studies. However, we could observe and characterize the formation of dibromide radical anion ($\text{Br}_2^{\cdot-}$), which was found to be the product of the interaction of bromide ion and hydroxyl radical.

The application areas of microemulsions have increased dramatically during the past decades^{2, 5, 12, 13, 22} and this can be realized from Fig.1.5.

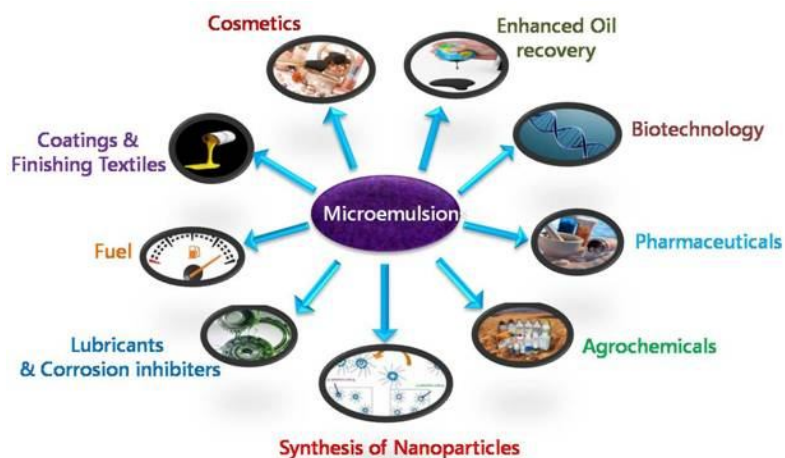


Fig.1.5. Diagrammatic representation of the application areas of microemulsions.

Chapter 1

One such important area is the fabrication of nanomaterials.^{5, 14, 22} The nanometer sized aqueous cores of the microemulsions provide an appropriate stabilized environment for controlled nucleation and growth of nanoparticles. Additionally, steric stabilization provided by the surfactant layer prevents the nanoparticles from aggregating at the later stages of growth. Reasonably so, these systems have been employed as a template for synthesizing nanoparticles of a wide class of substances including metals^{14, 23, 24} and their oxides,^{14, 25-27} bimetallic,²⁸⁻³⁰ semiconductors,^{14, 31-34} superconductors,^{35, 36} magnetic materials,³⁶⁻³⁸ biomaterials^{14, 39} and polymers.^{14, 33}

We have synthesized CdSe nanomaterials in the host matrix of CTAB and AOT based w/o microemulsions *via* conventional as well as radiation chemical route.⁴⁰⁻⁴³ The fundamental roles of the intrinsic structural dynamics of these microemulsions and the peculiarities of the synthetic techniques in influencing the morphology, surface composition and optical properties of CdSe nanomaterials have been probed in this thesis work.

1.4. Room temperature ionic liquids (RTILs)

RTILs are a class of low temperature molten salts having melting points below 100 °C.⁴⁴ The development of ILs started in 1914 and it was Paul Walden who described the synthesis and properties of the “first” IL, ethylammonium nitrate^{44, 45} (melting point = 14°C).⁴⁶ In the late 1970s, Osteryoung group⁴⁷ and Wilkes *et al.*⁴⁸ synthesized chloroaluminate melts liquid at room temperature, but these fluids suffered from their high sensitivity to atmospheric moisture. However, in 1990s, a significant milestone was achieved when the RTILs comprising of imidazolium as cation and tetrafluoroborate or

Chapter 1

hexafluorophosphate as anions were synthesized.^{44, 49} Unlike haloaluminate based ILs, this new generation of ILs was relatively resistant to hydrolysis and could be prepared, stored, and handled outside a glove box.

RTILs possess unique physicochemical properties such as high polarity, negligible vapour pressure, high ionic conductivity, wide electrochemical window and thermal stability. Owing to these, a surge in the interest of the scientific community (especially in the last two decades) can be observed from the exponential growth in the number of publications on RTILs.⁴⁴ Further, these media are often referred to as “designer” solvents. This is due to the fact that by altering the cation-anion combination, their characteristics such as hydrophobicity, miscibility (with other solvents), polarity and other physicochemical properties can be easily tuned, as desirable for a specified task.⁴⁴ According to Plechkova *et al.*,⁵⁰ pairing of all known anion and cation combinations, approximately 10^6 different ILs can be prepared. Nevertheless, till now, most of the research has been focused on RTILs with commonly used cation-anion combinations. The structures of some of these cations and anions are shown in Fig.1.6.

RTILs are entirely composed of ions; however they are different from the molten salts as the later ones have high melting temperatures. Essentially, melting point of a crystal is a synergistic effect of the cation and the anion as both influence its lattice energy. Therefore, low melting points of RTILs are result of weak inter-ionic interactions due to inefficient packing of irregularly shaped ions and diffuseness of charge.^{44, 51}

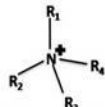
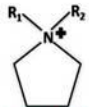
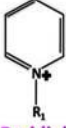
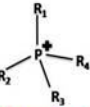
Cations		Anions
 <p>(a): Ammonium</p>	 <p>(b): Imidazolium</p>	<p>Cl^-, Br^-, I^-: Halogens</p> <p>NO_3^-: Nitrate</p> <p>BF_4^-: Tetrafluoroborate</p> <p>PF_6^-: Hexafluorophosphate</p> <p>CH_3COO^-: Acetate</p> <p>$\text{C}_2\text{H}_5\text{SO}_4^-$: Ethyl sulfate</p> <p>$\text{CF}_3\text{SO}_3^-$: Trifluoromethanesulfonate or OTf or Triflate</p> <p>$[(\text{CF}_3\text{SO}_2)_2\text{N}]^-$: bis(trifluoromethylsulfonyl) imide anion or Tf_2N^-</p>
 <p>(c): Pyrrolidinium</p>	 <p>(d): Pyridinium</p>	
	 <p>(e): Phosphonium</p>	

Fig.1.6. Some examples of common cations and anions of RTILs.

RTILs are different from the conventional organic solvents with respect to their structure and physicochemical properties (mentioned earlier). Within an IL, there are many correlation length scales present between the ion pairs which are generally less than 5 Å.⁵² These are due to a various interionic interactions⁵³⁻⁵⁵ co-existing in these fluids as a result of complex interplay of forces such as Coulombic, van der Waals (dipole-dipole, dipole-induced dipole, and dispersion), hydrogen bond, and π - π stacking interactions. A diagrammatic representation of these interactions has been shown in Fig.1.7, where 1-ethyl-3-methyl imidazolium ([EMIM]) and bis(trifluoromethylsulfonyl)amide (Tf_2N) are the cation and anion, respectively. Furthermore, a variety of experimental techniques⁵⁶⁻⁶⁰ and simulation studies⁶¹⁻⁶⁴ have revealed the presence of non-polar and polar domains in ILs. These domains have been attributed to the segregation of ions (cations or anions) containing alkyl side chains.⁵²

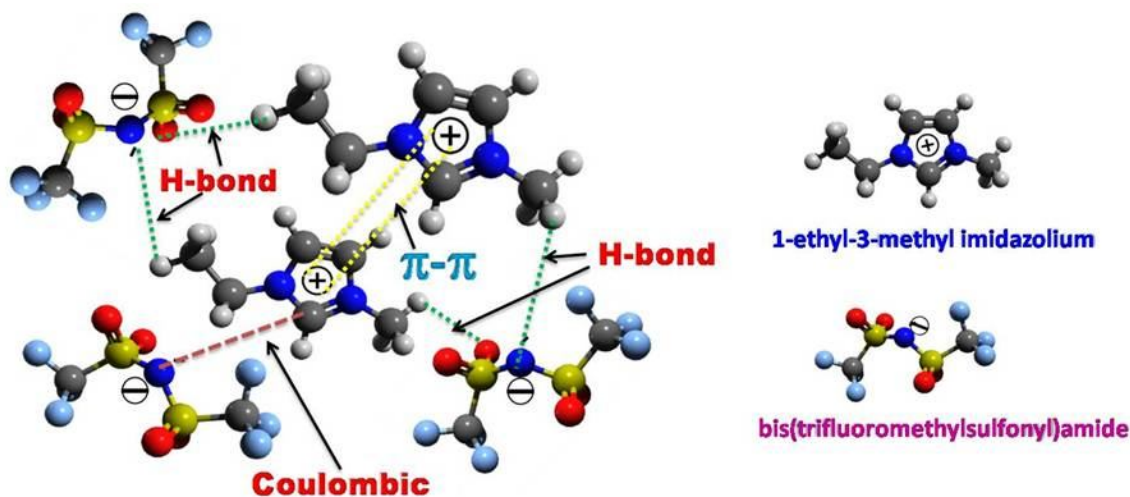


Fig.1.7. Diagrammatic representation of the various bonding interactions co-existing in an imidazolium based RTILs.

It is the existence of such nanostructures (i.e., hydrophobic and hydrophilic zones) which forms the basis of much known ‘*spatial heterogeneity*’ of RTILs.⁶¹ A snapshot illustrating this phenomenon was reported by Wang *et al.*⁶¹ in their simulation studies on imidazolium based IL ([EMIM]/[BMIM][NO₃]) and the same has been shown in Fig.1.8. Besides their structural properties, the notable feature observed in simulation studies of RTILs is so called ‘*dynamic heterogeneity*’.^{65, 66} It refers to the spatially inhomogeneous relaxation behaviour akin to that generally observed in glassy or supercooled liquids.⁶⁷ Hu *et al.*⁶⁸ with their computational calculations on 1-butyl-3-methylimidazolium hexafluorophosphate ([BMIM][PF₆]) suggested the presence of ensembles of ions with different diffusion rates.

The manifestation of this type of solvent heterogeneity is apparent in the fluorescence spectroscopy experiments reported by Samanta and co-workers.⁶⁹ It has been already mentioned that the hydrophilic or hydrophobic character of RTILs depends on the

Chapter 1

combination of the cation and the anion. The most frequently investigated ILs are based on imidazolium cations. Anions such as halides, acetate, nitrate and ethylsulfate form hydrophilic ILs, while anions i.e. hexafluorophosphate, bis(trifluoromethylsulfonyl)imide lead to hydrophobic ILs.

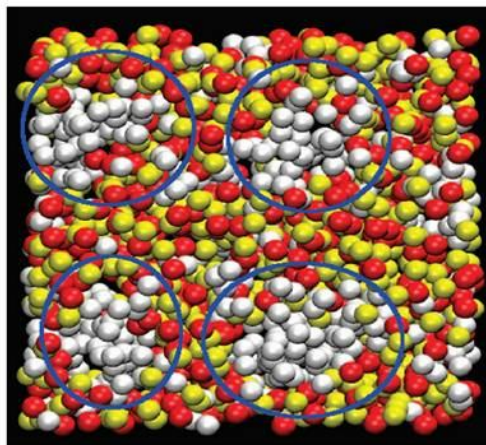


Fig.1.8. One snapshot from the simulation studies on imidazolium based IL ($[EMIM]/[BMIM][NO_3]$) illustrating the ‘spatial heterogeneity’ present within its molecular structure. The white spheres represent the non-polar domains originating from the cationic terminal groups; while the gold and red spheres represent the cationic head Groups, and the anions, respectively.⁶¹

In today’s scenario, RTILs are a rapidly expanding family of condensed-phase media with multitude of applications in synthesis, extraction, catalysis and electrochemistry.^{44, 70,}

⁷¹ However, in the recent times, RTILs have aroused much interest as new media in nuclear fuel cycle.^{72, 73} Nonetheless, understanding the radiation stabilities of the ILs and the underlying chemistry involved are some of the most important issues for their successful use in nuclear fuel reprocessing. It is therefore imperative to study the radiation chemistry of ILs, their radiolytic products and the degradation pathways. This

Chapter 1

information could aid in the development of more robust and task specific ILs with better extraction efficiency and solvent recovery. No surprise that several radiation stability studies on ILs have already been reported.⁷⁴⁻⁸⁴ Most of these studies have been carried out on imidazolium ILs having anions such as PF_6^- , BF_4^- or halogens. Essentially, these ILs have been found to be hydrolytically unstable giving off highly toxic and corrosive HF.^{44, 85} Imidazolium based ILs with bulky tris(perfluoroalkyl)trifluorophosphate (FAP) anion are ultra hydrophobic and possess excellent hydrolytic stability.⁸⁵ Fig.1.9 shows the structure of FAP anion. In the present thesis, an assortment of characterization and qualitative studies were carried out to explore the radiation stabilities of FAP ILs in the radiation doses, ranging from 50 to 500 kGy. Besides this, transient absorption studies were conducted to determine the influence and the radiolytic sensitization effects of hydroxyl group substitution on the physicochemical properties and the degradation mechanistic pathways of these ILs.

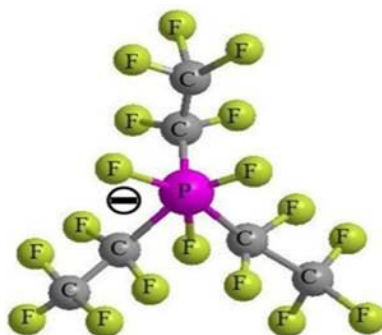


Fig.1.9. Structure of FAP anion.

It was observed that even a diminutive alteration in the molecular structure causes marked difference in the reactivity and reaction centre of the imidazolium based FAP ILs.

Chapter 1

Another area of research where RTILs have recently received a great deal of attention is their potential application as superior media (with respect to the conventional organic solvents) for the synthesis of various nanomaterials.⁸⁶⁻⁹⁸ It has already been mentioned that RTILs display a high degree of self-organization comprising of three-dimensional (3D) ionic network dominated by the electrostatic and non-covalent bonding interactions.⁵²⁻⁶⁶ Consequently, *hydrogen bond-co- π - π stacking mechanism* has been regarded as the shape directing mechanism for obtaining various anisotropic structures (tubes, wires, rods, sheets) of nanomaterials synthesized in imidazolium based ILs, by different techniques. However, the synthesis of metal chalcogenides using *neat* ILs (as solvents) that too using radiation induced techniques have been rarely studied. Therefore, taking into account the high radiation stability of imidazolium based ILs; electron beam irradiation technique was employed to initiate the nucleation process for the synthesis of CdSe nanomaterials. The main objective of this part of the thesis work was to explore & exploit the noble structural features of RTILs and the peculiarities of radiation induced techniques in synthesizing & directing the self-assembly of nanomaterials into well-defined structures of fundamental importance.

1.5. Cyclodextrins (CDs)

CDs are bucket shaped molecules comprising of glucose units (six or more) connected by α -1, 4 glycosidic linkages to form a series of oligosaccharide rings. They are produced as a result of intramolecular transglycosylation reaction from degradation of starch by cyclodextrin glucanotransferase (CGTase) enzyme.⁹⁹ The most common CDs comprise six, seven and eight glucopyranose units and are named α -, β - and γ -CD, respectively.

Chapter 1

The structures of CDs and their related properties are shown in Fig.1.10. The oligosaccharides in CDs forms a truncated cone in which the primary (1°) -OH groups (on C_6) are directed towards the narrow side or the primary face, and the secondary (2°) -OH (on C_2 and C_3) groups are projected on the wider side or the secondary face (Fig.1.10). The inner part of the cone comprises of apolar C_3 and C_5 hydrogens and ether-like oxygens. These features of CDs impart them a rigid conical molecular structure with a hydrophilic outside (can dissolve in water) and a hydrophobic apolar cavity, thereby providing a ‘*microheterogeneous environment*’.⁹⁹

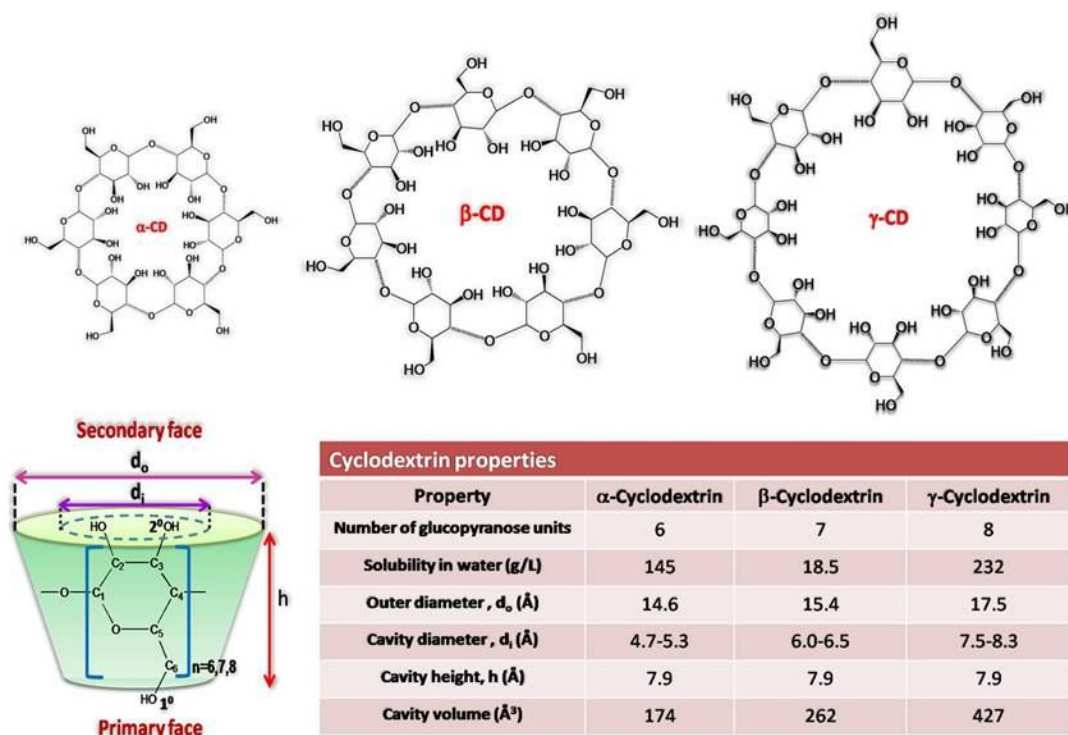


Fig.1.10. Structures and properties⁹⁹ of CDs.

The main interest in CDs lies in their ability to form inclusion complexes (host–guest complexes) with a very wide range of solid, liquid and gaseous compounds by a

Chapter 1

molecular complexation.⁹⁹⁻¹⁰² Basically, the lipophilic cavity of CD molecules provides a microenvironment into which appropriately sized non-polar moieties can enter to form inclusion complexes.¹⁰³

The predominant driving force behind this complexation has been attributed to the release of enthalpy-rich water molecules from the cavity. Consequently, water molecules are displaced by more hydrophobic guest molecules present in the solution to attain an apolar–apolar association and decrease of CD ring strain, which lead to a more stable lower energy state.⁹⁹ Amongst various CDs, β -CD is the most studied one and generally the most useful⁹⁹ too. This has been attributed to its easy accessibility and distinctive properties (such as solubility) as compared to other analogues. Essentially, the relative insolubility of β -CD has important consequences on its applications as a solution host. Nevertheless, a number of explanations have been proposed for this anomalous behaviour of β -CD.^{99, 104} First is the unfavourable enthalpy and entropy of hydration of β -CD as compare to its smaller and larger colleagues. The probable reason is that the 6 (α -CD) and 8 (γ -CD) fold symmetries of the other CDs are more compatible with the solvent cage of water. It has also been suggested that the intramolecular hydrogen bonds on the secondary face of β -CD are mainly responsible for its low solubility, thereby limiting the interaction with water. Nevertheless, it is plausibly these properties of β -CD, which has made it the most common CD in pharmaceutical formulations and, thus, probably the best studied CD in humans.⁹⁹

Self-aggregation of CDs in aqueous solutions is an important phenomenon, which has been widely investigated.¹⁰⁵ Through various scattering and microscopic techniques, it

Chapter 1

has been confirmed that native CDs can form aggregates in water with the size of about 200–300 nm.¹⁰⁶⁻¹⁰⁸ For instance, Bonini *et al.*¹⁰⁶ reported the aggregation of β -CD monomers into different shapes in water, depending on the concentration of β -CD. Further, an important observation was made wherein the critical aggregation concentration of β -CD self-aggregation in water was between 2 and 3 mM. Nevertheless, the main driving force for the self-assembly of CD molecules has been ascribed to the hydrogen bonding.^{108, 109}

CDs have been utilized in various fields such as sensing, pharmaceuticals, biochemistry, cosmetics, food, catalysis and electronics.^{99, 100} Because of their ability to link covalently or non-covalently, CDs can be used as building blocks for the construction of supramolecular complexes.¹¹⁰ Indeed, in the recent times, the self-assembling tendency of CDs has aroused a lot of interest in the field of nanoscience to fabricate and stabilize superstructures of various nanomaterials¹¹¹⁻¹¹⁸ (especially metal based) with enhanced efficiencies. Besides, various radiation chemical studies carried out on CDs have clearly showed their higher radiation stability (less than 10 % radiolytic decomposition of β -CD was found up to an absorbed dose of ~ 72 kGy) in comparison to simple saccharides.¹¹⁹⁻¹²² This ability of CDs provides them extra advantage,¹²³ which could be utilized in applications (e.g. biomedicine) having high radiation fields. Nevertheless, the radiation resistance put forth by CD has been attributed to the fact that α -D-glucose units present in CDs are joined by α -1, 4-glucosidic links and therefore, do not contain a free reducing group where radiation-induced oxidation reactions are generally dominant.¹¹⁹⁻¹²¹

Chapter 1

Taking into account of aforementioned facts, an attempt was carried out in the present thesis work to synthesize self-assembled CdSe nanoparticles functionalized with β -CD *via* electron beam irradiation technique. Specifically, this methodology is attractive from the view point of time efficiency (rapid one pot synthesis), clean chemistry (no external reducing agent is involved) and ensuring reproducibility in the synthetic protocol.

1.6. Quantum dots (QDs)

A material (usually, a semiconductor) which is size-restricted in three dimensions such that the charge carrier wave functions are confined within its volume is called a quantum dot (QD). The quantized energy levels observed in QDs lead to electronic band gap structures that are intermediate between single molecules which have a single HOMO-LUMO gap and bulk semiconductors which have continuous energy levels within bands (see Fig.1.11). QDs were discovered by A. Ekimov in a glass matrix^{124, 125} and then in colloidal solutions by L. E. Brus in 1985 (at Bell Labs)¹²⁶ while, the term "Quantum Dot" was coined by Mark Reed.¹²⁷

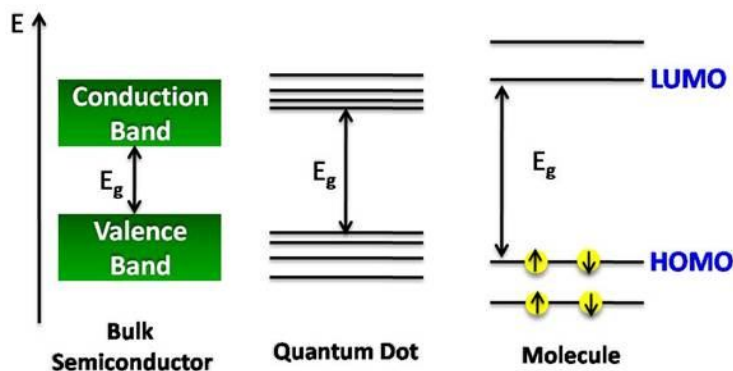


Fig.1.11. Diagrammatic illustration of the electronic band structure difference between bulk semiconductor, quantum dot and a molecule.

Chapter 1

In a bulk semiconductor, an electron excited from the valence band by the absorption of a quantum of light moves to the conduction band, leaving a positive charge (a hole). The as generated electron and the hole experience attractive Coulomb forces and can form a so called ‘exciton’. Essentially, an exciton is a state similar to a hydrogen atom. Therefore, like a hydrogen atom, it also has a Bohr radius (most probable distance from the nucleus at which an electron can be found) which is the most probable distance of the electron from the hole. Bohr exciton radius (a_B) of a semiconductor can be determined by: $a_B = \epsilon \hbar^2 / \mu_0 e^2$, where ϵ is the dielectric constant of the material, \hbar is the reduced Planck constant ($\hbar = 1.0545 \times 10^{-34}$ J s), μ_0 is the reduced mass of an exciton ($\mu_0 = (m_e \times m_h)/(m_e + m_h)$), m_e is the effective mass of an electron, m_h is the effective mass of a hole, e is the charge of an electron (1.6×10^{-19} coulomb).

An exciton is delocalized within the bulk crystal lattice. However, when the physical size of the semiconductor material is reduced such that its size becomes comparable to or smaller than the Bohr exciton radius, the continuous energy bands split into discrete energy levels (see Fig.1.12).¹²⁸ This state, wherein the space for the movement of excitons gets restricted is called as ‘quantum confinement’. In case of QDs, the confinement is strong as their size is $\leq a_B$. For instance, considering the case of CdSe, the size of its QDs should be less than or equal to 5.6 nm (Bohr exciton radius of bulk CdSe) for any confinement effects to be observed.¹²⁹ Electrons in QDs occupy discrete energy levels in a similar way as they do in atoms. For these reasons, QDs are also called as artificial atoms. Therefore, the situation of an electron in a QD can be compared with that

Chapter 1

of a particle in a box (quantum mechanics problem of a particle-in-a-box), wherein the energy of different states is dependent on the length of the box.

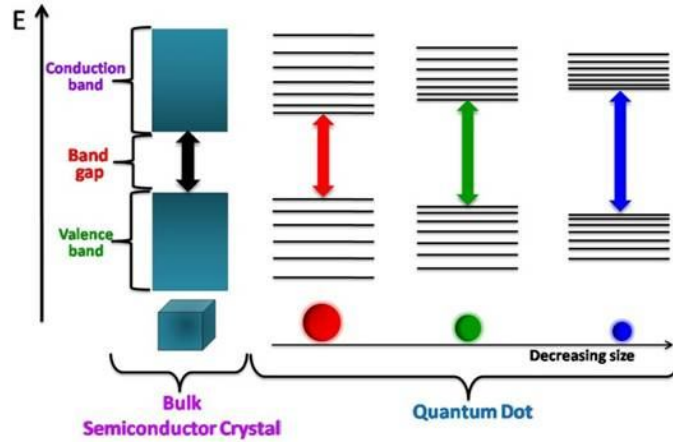


Fig.1.12. Splitting of electronic band structure of bulk semiconductor into discrete energy levels with the decrease in size (Quantum confinement effect).

Brus, by his effective mass approximation model¹³⁰ showed the relation between the particle size with the band gap energy of a semiconductor QD i. e. E_g (QD):

$$E_g(\text{QD}) = E_g(\text{bulk}) + \frac{\hbar^2}{8R^2} \left(\frac{1}{m_e} + \frac{1}{m_h} \right) - \frac{1.8 e^2}{4\pi\epsilon R} \quad [1.18]$$

where, E_g (bulk) is the bulk band gap energy of the semiconductor, 'R' is the QD radius (nm), m_e and m_h are the effective mass of electron and hole, respectively and ϵ is the dielectric constant of the material. The second term in equation 1.18 represents the particle-in-a-box quantum localization energy and has $1/R^2$ dependence; the third term with $1/R$ dependence represents the Coulomb energy. The major consequence of the quantum confinement effect is an increase of the apparent band gap with decrease of the particle size. Thus, the optical and other physical and chemical (e.g., oxidation-reduction) properties of semiconductor nanoparticles become sensitive to the size and shape of the

Chapter 1

particles. These drastic changes in properties governed by the reduction of particle size inspired and attracted tremendous interest of various researchers to develop advanced techniques and methodologies for the synthesis of different semiconductor based nanomaterials, which could be used in multitude of applications such as optoelectronics,¹³¹⁻¹³⁸ sensing,¹³⁹⁻¹⁴¹ bio-labelling,¹⁴²⁻¹⁴⁴ and catalysis.^{145, 146}

In general, various techniques¹⁴⁷⁻¹⁷⁹ for the QD syntheses are categorized either as a top-down^{147, 173, 174} or bottom-up approach^{148-170, 175-179}. Top-down route use larger (macroscopic) initial structures, which can be externally-controlled by molding or etching materials into nanostructures. This approach is traditionally used by the electronics industry to manufacture integrated circuits. Ball milling^{147a} and micropatterning^{147b} techniques, such as photolithography belong to this category. While, vapour-phase methods comprises of techniques such as molecular beam epitaxy (MBE),^{171, 172} chemical vapour deposition (CVD).^{173, 174} However, incorporation of impurities (into the QDs) and structural imperfections by patterning are major disadvantages with these processes.^{147c}

In contrast to top-down method, bottom-up approach seek to have smaller (usually molecular) components built up into more complex assemblies. Using the principle of bottom-up approach, different methods for the synthesis of colloidal QDs include: microemulsion route,^{14, 23-39} sol-gel,¹⁴⁸⁻¹⁵¹ hot solution decomposition,¹⁵²⁻¹⁵⁶ sonochemical,^{157, 158} electrochemical,^{159, 160} photochemical^{161, 162} and radiation chemical route.^{163-170, 175-179}

In the present thesis, CdSe QDs were synthesized by normal and radiation chemical routes. CdSe is one of the most important member of II–VI group semiconductors with an

Chapter 1

energy band gap of 1.75 eV (see Fig.1.13);^{128, 129} synchronizes well with the solar energy spectrum thus, providing a sort of model system to study the effect of morphology and surface composition on the optoelectronic properties of similar compounds. Nevertheless, in the normal chemical route, the synthesis was carried out at ambient conditions without involving any external stabilizing or reducing agents.

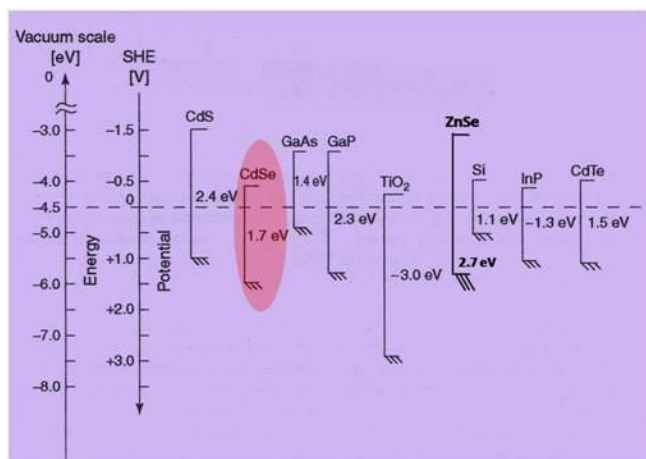


Fig.1.13. Bulk conduction and valence band edge positions (vs. vacuum and SHE) and band gaps of common semiconductor materials.¹⁸⁰⁻¹⁸²

In another methodology, nanoparticles synthesis was carried out by clubbing the electron beam irradiation technique with the templated approach of aforementioned microheterogeneous media. This hybrid approach is relatively new for the controlled synthesis of semiconductor nanomaterials and the interplay of different experimental parameters (precursor concentration, absorbed dose, dose rate and other variable structural features of microheterogeneous systems) leads to complex morphologies and interesting photophysical properties of CdSe QDs. So far, primarily metals, alloys, and metal oxide NPs have been synthesized by this means.¹²³ The as employed methodology possesses inherent advantageous features, which are as follows: (a) fast and efficient

Chapter 1

without involvement of rigorous conditions (such as high temperature, pressure, inert atmosphere, and toxic reducing agents), (b) potential for the commercial scale production of nanoparticles, since irradiation can be carried out in the common industrial accelerator plants generally used for sterilizing medical kits and other items, (c) does not require any external reducing agents as electron is itself a very strong reducing species ($E_{\text{red}} = -2.9 \text{ V}$) and (d) electron beam can also be used for tailoring the size of nanomaterials by controlling the dose and irradiation time. Diagrammatic depiction of the radiation induced synthesis of nanomaterials is shown in Fig.1.14.

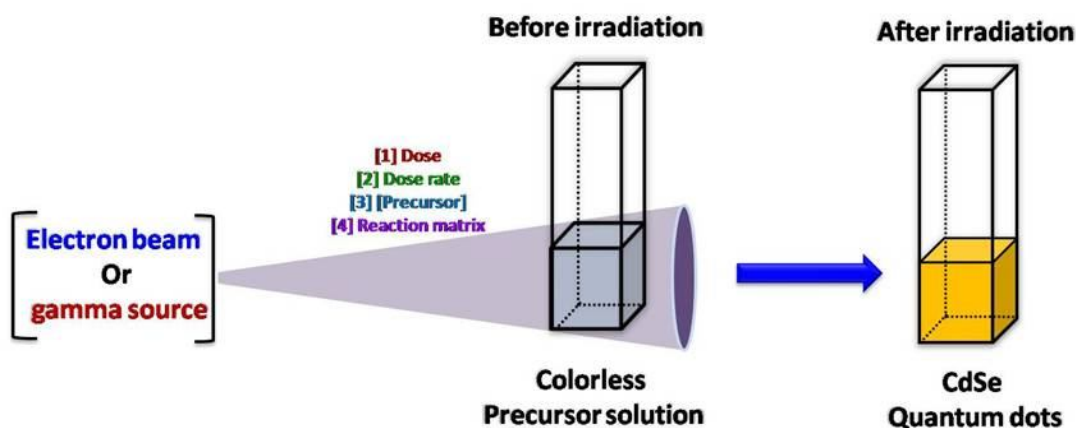


Fig.1.14. Diagrammatic depiction of the radiation (e^- , γ) induced synthesis of nanomaterials.

Essentially, in the radiation induced synthetic technique, the synthesis of the nanoparticles proceeds *via* reaction of the solvated electrons, e_{SOLV}^- or other reducing free radical species (depending on the host matrix, solvent etc.) with the precursor ions. This process differs from the mechanism in routine chemical methods. Besides, the yield of e_{SOLV}^- plays an important role in the growth kinetics of nanoparticles and depends primarily on the reaction medium.^{123, 163-170, 175-179}

1.7. Outline of the thesis

The as discussed versatility and relevance of microheterogeneous systems in contemporary life in the previous sections itself provides the explanation about the motivation behind the research work carried out on these media. Considering the structural and dynamical similarities of microheterogeneous systems with those of naturally occurring bioaggregates, the investigations carried out on these media are of fundamental interest as well as essential for the in-depth understanding of the various basic processes occurring in the later. Apart from that, the compartmentalized as well as self-assembling tendency of microheterogeneous media offers a lot of promising perspectives in the realm of nanoscience and nanotechnology. In the successive chapters, the experimental techniques employed in the current thesis work followed by an account of the radiation and photochemical investigations of microemulsions, RTILs and CDs and their application in the synthesis of CdSe QDs have been explained in detail.

In **Chapter 2**, a brief overview of the different experimental techniques used in radiation and photophysical investigation of the microheterogeneous systems have been provided. Techniques employed for the characterization of nanoparticles and to carry out various photophysical studies have been described in detail.

In **Chapter 3**, radiation chemical investigations of the solvated electron in CTAB based quaternary w/o microemulsions have been described. Also, generation of counter ion radicals and its reactions in the same system are explained.

In **Chapter 4**, the application of microemulsions in the controlled synthesis of CdSe QDs has been presented *via* radiation as well conventional chemical route. Further, the

Chapter 1

influence of the structural and the dynamical aspects of AOT and CTAB microemulsions on the morphologies, photoluminescent behaviour and the charge carrier relaxation dynamics of CdSe QDs have been described.

Chapter 5 deals with the compilation of the radiation stability studies of FAP based imidazolium ILs. The effect of –OH functionalization on the radiolytic degradation of the IL was also investigated. Various physical and chemical characterization studies followed by the photophysical investigations were performed on the irradiated ILs to determine the radiation induced effects. Pulse radiolysis studies carried out to delineate the mechanism for the radiation induced changes in hydroxyl and non-hydroxyl FAP ILs have also been described.

Chapter 6 demonstrates the application of RTILs as a novel media for the synthesis (by radiation as well as normal chemical route) of self-assembled superstructures of nanomaterials. The possible mechanism behind the as obtained complex nanostructures has been explained in this chapter.

In **Chapter 7**, β -CD functionalized CdSe QDs were synthesized *via* electron beam irradiation. Band gap engineering, cytotoxicity studies of QDs and the binding sites involved in the complex formation between CD molecules and the QDs have been presented.

The conclusions drawn from each study are sequentially summarized in **Chapter 8**. A brief description of the future perspectives of the work carried out in this thesis has also been given.

Chapter 2

Experimental Techniques

2.1. Introduction

As discussed in the previous chapter, the main objective of the thesis was to contribute and enhance the hitherto basic understanding of the fundamental processes related to electron, charge transfer and other free radical reactions in the entirely different microheterogeneous environments of microemulsions, RTILs and CDs. Further, their role as a template in the controlled synthesis for morphological and optical tuning of nanomaterials was explored. Therefore, a brief overview of the different experimental techniques used in radiation and photophysical investigation of the microheterogeneous systems and the as grown CdSe QDs has been provided in this chapter.

Radiation chemical processes involve intermediates/transient species, which are reactive and persist only for very short time periods. Identification and characterization of such species (and their reactions) require a sophisticated instrumentation with ability for real time monitoring of their transient behavior. Pulse radiolysis is one such popular technique used for generating and characterizing the free radical and reactive intermediates. In the present thesis work, Linear accelerator (LINAC) with an energy of 7 MeV was used as an irradiation source for facilitating radiation stability studies as well as for the synthesis of CdSe nanoparticles. A kinetic spectrophotometer was coupled with LINAC for carrying out the pulse radiolysis. The working principle along with the optical

Chapter 2

layout of this facility has been explained in this chapter. In some experiments, γ -irradiation (sourced from Cobalt-60) of the samples was also carried out in the synthesis of nanoparticles to investigate the effect of dose rate. Techniques employed for the characterization of nanoparticles such as X-ray diffraction (XRD), transmission electron microscope (TEM), scanning electron microscope (SEM) have been described in detail. Basic principles of instruments used for carrying out various steady state and time resolved photophysical studies such as absorption spectrophotometer, fluorometer, infrared spectrometer, Raman spectrometer and time-correlated single photon counting (TCSPC) have also been explained.

2.2. Pulse radiolysis

2.2.1. Principle of pulse radiolysis

In pulse radiolysis, the system under investigation is generally irradiated with an intense pulse of electrons to generate a significant concentration of transient species. The resulting transient species/free radicals are monitored online by a suitable physical techniques such as optical absorption, conductivity, electron spin resonance and fluorescence.^{9, 183, 184} Typically, electron pulse width should be an order of magnitude shorter than the half-life of the reaction with sufficiently high energy to produce an adequate concentration of chemical species in the irradiated sample. A schematic of pulse radiolysis set up employed in the present thesis work is shown in Fig.2.1.

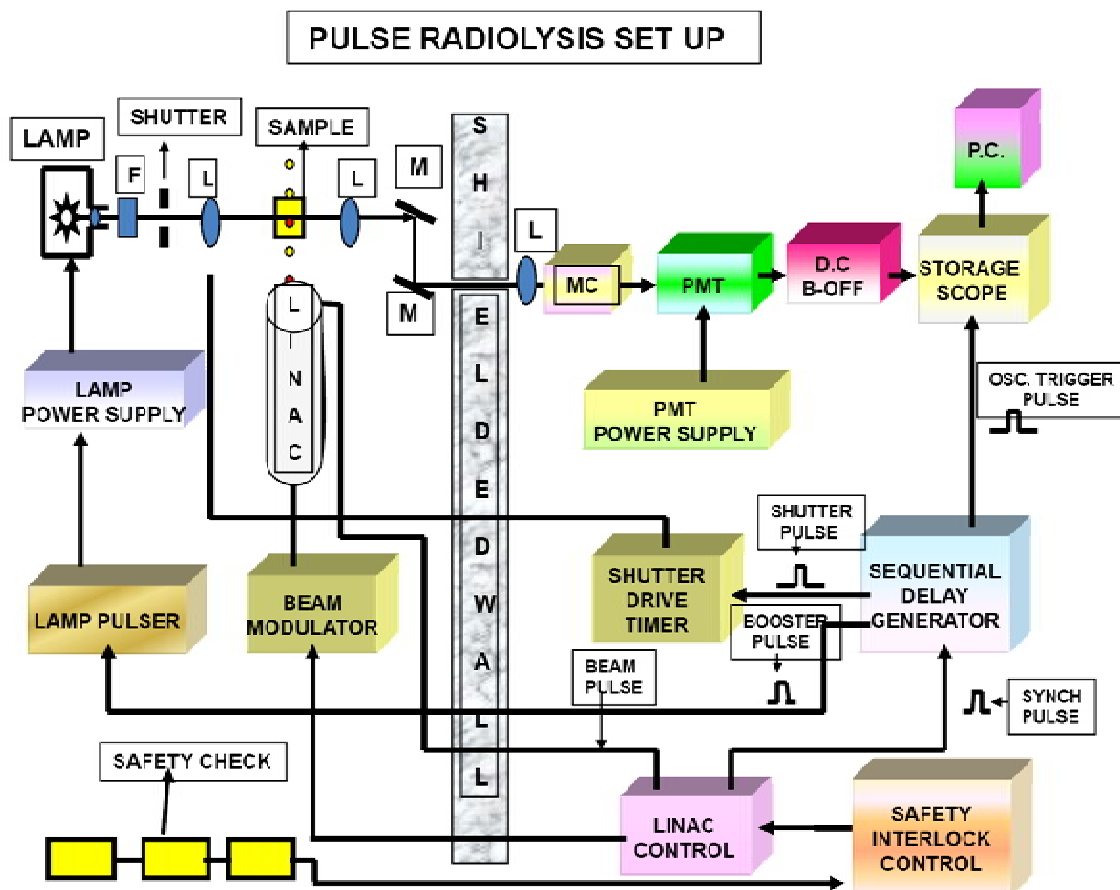


Fig.2.1. Schematic diagram of pulse radiolysis set up.

Herein, the sample solutions are taken in a quartz cuvette (1cm × 1 cm) and are kept at a distance of ~12 cm from the titanium electron beam window, where the beam diameter is ~ 1 cm. The sample solutions are then irradiated with 7 MeV electron pulse sourced from a LINAC. Subsequently, a collimated light beam from a pulsed 450 W Xenon arc lamp is used to monitor the transient changes in the absorbance of the irradiated solution. The transmitted (after passing through the sample cell) light beam is then directed to the spectrophotometer through a tunnel in the wall by making use of fused silica lenses and mirrors coated with aluminum on the front surface. The light beam is finally focused on the entrance slit of a monochromator, on the exit slit of which a

Chapter 2

photomultiplier (PMT, model no. Hamamatsu R 955) is fixed. PMT signal is then fed into a storage oscilloscope from which traces are transferred to a computer. It is to be noted that the accelerator, the sample cell and the monitoring light source are housed in a shielded cave with 1.5 m thick concrete wall and roof (shown in Fig.2.1). Details of the LINAC and kinetic spectrophotometer are given in the following sections.

2.2.2. Linear accelerator (LINAC)

Accelerator is the main component of the pulse radiolysis technique^{9, 185} and its function is to impart high energy to a particle (usually an electron in radiation chemical studies), which is then directed towards the sample under investigation. In the present pulse radiolysis set up, a linear electron accelerator has been used as the source of 7 MeV energy electron pulses (Fig.2.2). It was obtained from Viritech Ltd., U.K. The components of this machine are discussed in brief as follows.

Electron gun: A tungsten electrode in the form of a pellet is continuously heated by electrons from the filament of the gun kept at a potential of -6.0 KV (DC) with respect to the cathode. The cathode potential is varied for 2 μ s at amplitude of 43 KV. As a result of this, 2 μ s electron pulse of energy 43 KeV is generated in the system initially. This electron pulse is focused into a deflector chamber with the help of electromagnetic lenses before it enters into a cylindrical wave guide.

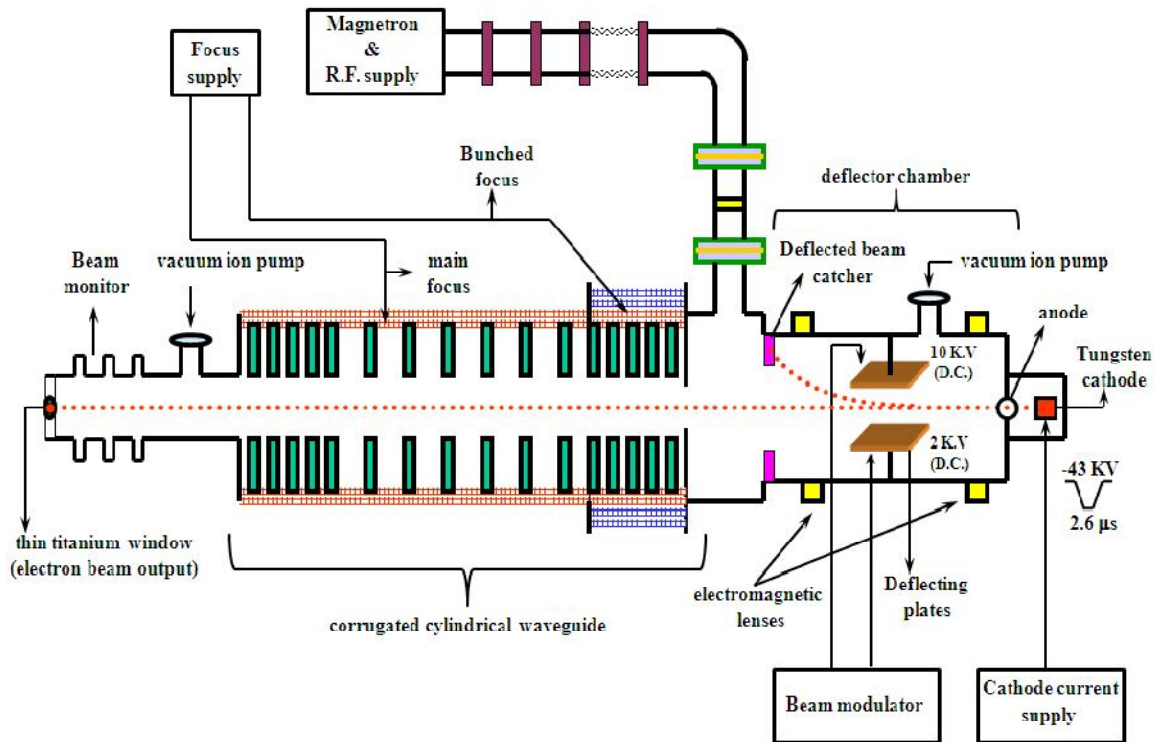


Fig.2.2. Schematic diagram of linear electron accelerator.

Wave guide: A magnetron with 3 GHz frequency and 1.8 MW peak power produces a synchronous traveling R.F. (radio frequency) field of $2 \mu\text{s}$ pulse width. The electrons produced in the electron gun assembly are allowed to enter into the wave guide in a phase synchronous with the R.F. field, wherein the electrons are accelerated in vacuum to a final energy of 7 MeV. A well-defined uniform beam of accelerated electrons are obtained after focusing by electromagnetic coils and comes out from the wave guide through a titanium window with mean diameter of $\sim 2 \text{ mm}$. Electron pulses of various widths from 5 ns to $2 \mu\text{s}$ with peak current ranging from 1.56 A to 70 mA can be produced by this machine. The nano-second pulses are obtained with the help of deflector plates placed between the anode of the electron gun and the corrugated wave guide. The

Chapter 2

43 KeV electrons emitted from the electron gun are deflected and collected by a beam catcher.

Working of the LINAC facility

A pulse generator, which is preset at 50 pulses per second (pps) triggers the R.F. pulses. The beam divider ratio is kept normally at 3 such that for every third R.F. pulse, one electron pulse is available for acceleration. The electron pulse is delayed by 600 ns to synchronize it with peak portion of the RF pulse. Further, a pulse from the pulse generator of the accelerator triggers a sequential delay pulse generator (SDPG), which then sequentially activates an electromechanical shutter, a Xenon arc lamp pulse power supply (to boost the analyzing light intensity for monitoring the fast events) and an oscilloscope. Shutter, under normal working condition is kept open for 50 ms. As the oscilloscope is triggered by a pulse from the SDPG, the pre-trigger information ranging for a duration of 600 ns to 1 μ s prior to the arrival of the electron pulse is used to mark the monitoring level as well as the incident light intensity (I_0). Fine adjustments in SDPG with respect to time allows the electron pulse and its effect to be recorded on the flat portion of the boosted lamp profile, during which time the output of the analyzing light remains steady. The dose imparted to the sample is varied either by defocusing the beam or by suitable adjustment of the filament to the cathode bombardment current.

2.2.3. Kinetic spectrophotometer

The time resolved studies in the current pulse radiolysis set up have been conducted by monitoring the variations in the absorbance of the sample solutions. The different components of the analyzing set-up consist of:

Chapter 2

(i) **Xenon arc lamp as the analyzing light source (white light continuum):** Its effective output range is wide i.e. extends from 250 to 850 nm. Secondly, for getting a good signal to noise (S/N) ratio the output light intensity of Xenon arc lamp is stable and can be boosted (20-70 times) for experimental requirements. On the contrary, commonly used continuous band light is not suitable for these purposes.

(ii) **Electromechanical shutter:** To prevent the photodecomposition of the samples as well as the fatigue of the detector during the passive mode, an electromechanical shutter is placed between the lamp and the sample holder (Fig.2.1). The shutter is synchronized in such a way that it opens just prior to boosting of the analyzing light and remains open for a period which covers the subsequent events like arrival of electron pulse and generation of transient species.

(iii) **Sample cuvette:** A square quartz cell of 1 cm × 1 cm path length is placed in its holder such that on one face it receives the electron beam and the analyzing light beam crosses the electron beam at right angles at the center of the cell.

(iv) **Monochromator:** The usable range of the as employed monochromator extends from 180 to 850 nm. Slit width of this monochromator can be continuously varied from 0.01 to 6.0 mm and corresponding band width of 0.1 to 19.8 nm. The analyzing light beam after passing through the sample cell is focused on the entrance slit of the monochromator.

(v) **Detector:** A PMT having a spectral response in the working range of 200-900 nm was used for detection. The output current of the PMT is converted to a voltage signal by a load resistor connected across its anode and ground. With a load resistor of 500 Ω , the

Chapter 2

overall rise time of detection is 75 ns. Thus, only the events of duration longer than this time period can be studied by using the detector.

(vi) Back-off device: Its function is to compensate constant (-ve DC) output of the PMT (I_0) before the arrival of the electron pulse.

(vii) Transient digitization: An oscilloscope is used for this purpose. The PMT output is fed to the vertical amplifier of the oscilloscope. The time base of the storage scope is triggered externally by a signal (derived from the accelerator) synchronous with the electron beam pulse.

2.2.4. Transient absorption measurements

The intensity of light transmitted through the cell (containing sample solution) after electron beam irradiation is given as:

$$I = I_0 10^{(-\epsilon cl)} \quad [2.1]$$

where, I_0 is the intensity of light transmitted just prior to the electron pulse, c is the molar concentration of the species formed in the sample, ϵ is the molar extinction coefficient and l is the path length of the light. Because of the proportionality between V and I , the PMT output voltage just prior to and after the pulsed irradiation are related as

$$V = V_0 10^{(-\epsilon cl)} \quad [2.2]$$

The quantity $\epsilon \cdot c \cdot l$ is called as optical density or absorbance (A) of the transient species and at any given time, it can be expressed as equation 2.3.

$$A = \log(V_0/V) \quad [2.3]$$

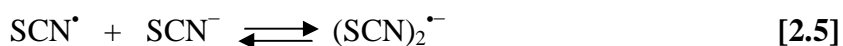
Due to the time-dependence of the concentration of the transient species produced by electron pulse, I and V will be time-dependent. Hence, A will also be time dependent. It

Chapter 2

is this time-dependence of V that is monitored with a digital oscilloscope and subsequently processed to obtain the kinetic information.

2.2.5. Dosimeters for pulse radiolysis

In pulse radiolysis experiments, thiocyanate dosimeter is commonly used to measure the absorbed dose per pulse. It is an aerated aqueous 0.01 mol dm⁻³ potassium thiocyanate (KCNS) solution. The species such as e⁻_{aq} and H-atom generated upon electron beam irradiation of the sample solution are scavenged by the dissolved oxygen. Therefore, the hydroxyl ([•]OH) radical oxidizes SCN⁻ ions to produce (SCN)₂^{•-} radicals, shown in reactions below.



The radiation dose is estimated from the maximum absorbance (A) of the radical (SCN)₂^{•-} at 475 nm. The G-value and the extinction coefficient (ε) of this radical is reported to be 3.3 per 100 eV of absorbed dose and 7600 dm³ mol⁻¹ cm⁻¹, respectively at 475 nm.¹⁸⁶ From the measured A, the absorbed dose per pulse (D) is computed from the following equation:

$$D = \frac{9.648 \times 10^6 \Delta OD}{G \cdot \epsilon \cdot \ell \cdot \rho} \text{ Gy} \quad [2.6]$$

where, ℓ and ρ are path length of the light and density of the solution, respectively.

2.2.6. Experimental data handling: The kinetic treatment

The analysis of the data (related to the spectroscopic, kinetic, and redox properties of the transient species) obtained after the pulse radiolysis experiments is the vital part of these radiation chemical studies. In general, first and second order kinetic processes are

Chapter 2

observed, while complex behavior (where both the first and second order processes occur simultaneously) is less frequently encountered. For data processing, the oscilloscope trace is first transferred to the PC and then analyzed by using sophisticated software packages. Different methods of data processing are explained in brief.

(i) First order processes

When a reacting species 'A' follows first order kinetics such that



The rate of reaction, $-d[A]/dt$ is proportional to the concentration of A:

$$-d[A]/dt = k[A] \quad [2.8]$$

where, k is the rate constant has dimension of time^{-1} . Examples of this type of reactions are, rearrangement in an isolated excited species, intramolecular transformations etc.

A bimolecular reaction can also show a first order kinetics if one of the reactant is present in large excess:



The rate equation for the above reaction can be written as:

$$-\frac{d[A]}{dt} = k_s[A][B] = k_\phi[A] \quad [2.10]$$

where, k_ϕ is the pseudo-first-order rate constant with dimension time^{-1} and the second order specific rate constant k_s has a unit of $(\text{concentration} \times \text{time})^{-1}$. On integrating equation (2.10) between time limits 0 to t gives

$$\ln[A]_t - \ln[A]_0 = -k_\phi t \quad [2.11]$$

The term $[A]_t$ and $[A]_0$ refer to the concentrations at time 't' and at the beginning of the reaction, respectively. The observed rate constants are plotted against concentration of

Chapter 2

reactant in excess and the slope of the plot gives the bimolecular rate constant k_s for the reaction of species A with B.

(ii) Second order processes

For a bimolecular reaction of single transient species reacting with itself, showing second order kinetics such as



The corresponding rate equation for the above reaction (2.12) is

$$-d[A]/dt = 2k[A]^2 \quad [2.13]$$

On integrating between time limits 0 to t ,

$$\frac{1}{[A_t]} - \frac{1}{[A_0]} = 2.k.t \quad [2.14]$$

For 'A' absorbing at the monitoring wavelength, equation (2.14) can be written as:

$$\frac{1}{OD_t} - \frac{1}{OD_0} = \left(\frac{2.k}{\epsilon.l}\right)t \quad [2.15]$$

where, OD_t represents the absorbance due to reactant 'A' at any time t . The absolute rate constant $2k$ for this second order process can be obtained from the plot of $1/OD_t$ vs t . The slope of this plot is related to the rate constant by the relation (2.16).

$$2k = slope (\epsilon.l) \quad [2.16]$$

(iii) Competition kinetics

For many transients formed in the pulse radiolysis experiments, the wavelength for monitoring is not in a convenient range of the spectrum as the substrates also absorb in the same region. In those cases, competition kinetics method is used wherein another

Chapter 2

species is monitored which are having suitable spectral characteristics. If R^\bullet is the radical generated during the radiolysis, then



Then the probability that radical ' R^\bullet ' will react with solute 'A' is given as $\frac{k_A[A]}{k_A[A]+k_B[B]}$

where, k_A and k_B are the corresponding rate constant for the reaction of the radical with A and B and [A] and [B] are respective concentrations. In terms of the radiation chemical yield of the product, G_{P_A} and the reacting radical, G_{R^\bullet} .

$$\frac{1}{G_{P_A}} = \frac{1}{G_{R^\bullet}} + \left(\frac{k_B[B]}{G_{R^\bullet} \cdot k_A[A]} \right) \quad [2.19]$$

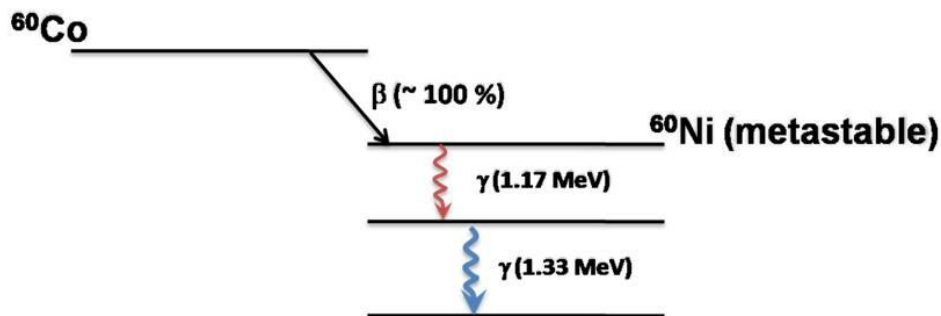
The plot of $\left(\frac{1}{G_{P_A}} \right)$ vs. $([B]/[A])$ is a straight line with an intercept = $\frac{1}{G_{R^\bullet}}$ and a slope = $\frac{1}{G_{R^\bullet}} \left(\frac{k_B}{k_A} \right)$, from which rate constant (k_A) can be calculated.

2.3. Cobalt-60 gamma source

Cobalt-60 (^{60}Co) is the most commonly used source for γ -irradiation and is prepared by neutron irradiation of Cobalt metal (^{59}Co) ^{60}Co emits two γ -rays of 1.17 and 1.33 MeV (scheme 2.1) per disintegration and it has a half life ($t_{1/2}$) of 5.27 years.⁶



The particular γ -source used in the experiments delivers a dose rate of ~20 Gy per minute.

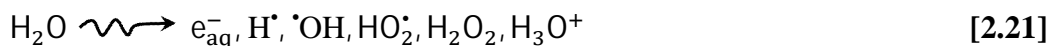


Scheme 2.1 Decay scheme of Cobalt-60.

2.3.1. Dosimetry for Cobalt-60 gamma source

Fricke dosimetry was used for the measurement of dose rate available in ^{60}Co γ -source.¹⁸⁷

The reaction involved is the radiation induced oxidation of Fe^{2+} ion to Fe^{3+} ion at low pH in the presence of oxygen. The standard dosimeter contains $1 \times 10^{-3} \text{ mol dm}^{-3}$ ferrous ammonium sulfate, $1 \times 10^{-3} \text{ mol dm}^{-3}$ NaCl (to take care of the impurities so that the solution can be prepared with normal distilled water) in 0.4 mol dm^{-3} H_2SO_4 and is saturated with air. Small variation in the concentration of the reagents does not affect the response of the dosimeter. However, due to slow oxidation, the solution should not be stored for more than few days. Reactions involved on exposure to γ -radiations are as follows:



Chapter 2

Thus the final product is Fe^{3+} and its yield is given by

$$G(\text{Fe}^{3+}) = 3g(\text{H}\cdot) + g(\cdot\text{OH}) + 2g(\text{H}_2\text{O}_2) = 15.5 \quad [2.27]$$

Ferric ion exhibit maximum absorption at 304 nm, therefore its formation can be measured on comparing the absorbance of the irradiated and unirradiated dosimeter solutions at the same wavelength (304 nm). From the as measured OD of Fe^{3+} ion, the absorbed dose (D) can be measured by the following relation:

$$D = \frac{9.648 \times 10^6 \Delta \text{OD}}{G \cdot \epsilon \cdot l \cdot \rho} \text{ Gy}$$

where, ΔOD is the change in absorbance of the dosimeter solution before and after irradiation. G is the yield (number of molecule formed per 100 eV) of ferric ions due to irradiation, ϵ is the extinction coefficient of ferric ions at 304 nm ($2201 \text{ dm}^3 \text{ mol}^{-1} \text{ cm}^{-1}$ at 25°C , has large temperature coefficient of 0.7 % per $^\circ \text{C}$), ρ is the density (1.024 g cm^{-3}) of the dosimeter solution, l is the path length in cm. Therefore, the dose rate can be determined once the absorbed dose is measured. The highest dose that an air saturated Fricke dosimeter solution can register reliably is 500 Gy.

2.4. X-ray diffraction

X-rays are electromagnetic radiation with typical photon energies in the range of 100 eV - 100 keV. These radiations are used to produce the diffraction pattern (in material science) because their wavelength (λ) is typically the same order of magnitude (1–100 Å) as the spacing (d) between planes in the crystal. Due to this reason, X-rays are ideally suited for probing the structural arrangement of atoms and molecules in a wide range of materials. Further, the energetic X-rays can penetrate deep into the materials and provide information about the bulk structure.^{188, 189} Therefore, X-ray diffraction (XRD) is one of

Chapter 2

the most important tools for the fingerprint characterization of crystalline materials and the determination of their structure. The database maintained by Joint Committee on Powder Diffraction Standards (JCPDS), International Centre for Diffraction Data (ICDD) provides information on unit cell dimensions for phase identification of a crystalline material.

In the realm of nanoscience, XRD is a widely used technique for aforesaid purposes. A typical XRD experimental set-up requires an X-ray source, sample under investigation and a detector to pick up the diffracted X-rays. The X-rays are generally produced by bombarding high-speed electrons on a metal target in a sealed X-ray tube. The most commonly used metal is copper as it can be kept cool easily due to its high thermal conductivity.

In crystal structures, atoms are arranged in regular and repeating order. Therefore, X-rays incident on the sample undergo diffraction and form either constructive or destructive interferences, according to the interplanar spacing or distance between planes. When the path difference between two scattered X-ray (Fig.2.3) beams is equal to an integer number of wavelength, they will constructively interfere, which is known as Bragg's condition:

$$n\lambda = 2d \sin \theta \quad [2.28]$$

where, n is the integer number, λ is the wavelength of incident X-rays, d is the interplanar spacing, and θ is the scattering angle. Therefore, from equation 2.28, the inter-planar spacing and lattice constants of crystal structures are determined.

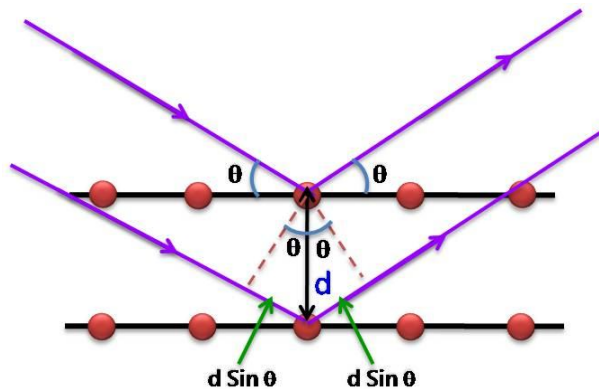


Fig.2.3. Diagrammatic representation of the Bragg's law.

In an X-ray diffractometer, a convergent beam strikes the sample and the intensity of the diffracted rays is measured as a function of diffraction angle, 2θ . The full width at half maximum (FWHM) of the peak can be used to calculate the mean crystallites sizes in the sample by using the Scherrer equation:¹⁹⁰

$$D_{hkl} = \frac{k\lambda}{B_{hkl} \cos \theta} \quad [2.29]$$

where, D_{hkl} is the crystallite size in the direction perpendicular to the lattice planes, hkl are the Miller indices of the planes being analyzed, K is a numerical factor frequently referred to as the crystallite-shape factor, λ is the wavelength of the X-rays, B_{hkl} is the FWHM of the X-ray diffraction peak in radians and θ is the Bragg angle. In the absence of detailed shape information, $K = 0.9$ is a good approximation.¹⁹⁰

In the present thesis work, XRD measurements were recorded on a Phillips X-ray diffractometer, model PW 1710 system, using a monochromatic Cu $K\alpha$ source ($\lambda = 1.54$ Å). The instrument was well calibrated using standard samples before any measurements.

Chapter 2

2.5. Transmission electron microscopy

Transmission electron microscope (TEM) is one of the most powerful tools to study nanomaterials. It not only gives a direct evidence for the formation of nanostructures, but is also routinely used for the characterization (determining shape, size, and crystal structure) of nanomaterials.¹⁹¹

In a TEM, electrons are usually generated by a process known as thermionic emission from a filament, usually of tungsten or lanthanum hexaboride (LaB_6).¹⁹² The electrons are then accelerated by an electric potential (high voltage in the range of 100 kV and 400 kV) and focused by electrostatic and electromagnetic lenses onto the sample (Fig.2.4).

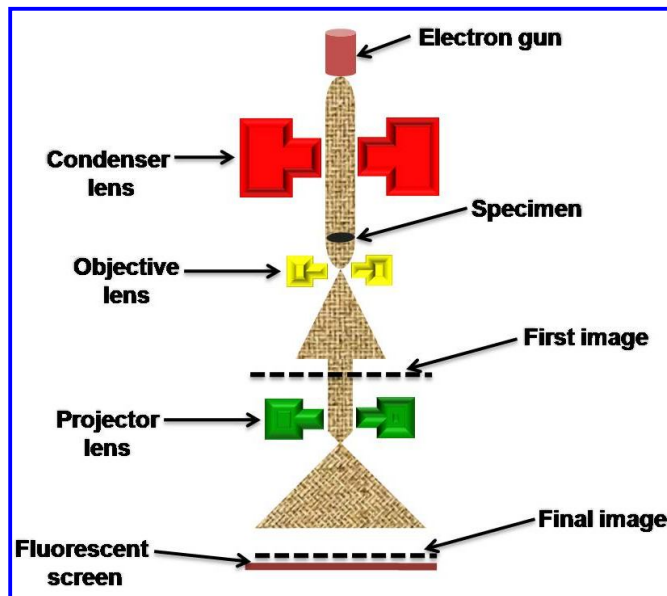


Fig.2.4. Basic layout of optical components in a Transmission Electron Microscope.

The vacuum in different parts of a standard TEM ranges from 10^{-4} to as high as 10^{-7} Pa. The main reason for such low pressures is to increase the mean free path of the electron gas interaction. Typically, a TEM consists of three stages of lensing which

Chapter 2

include condenser lenses, the objective lenses, and the projector lenses. The condenser lenses are responsible for primary beam formation, while the objective lenses focus the beam that comes through the sample itself. The projector lenses expand the beam onto the phosphor screen or other imaging device, such as film. The transmitted beam containing information about electron density, phase and periodicity is used to form an image. Since, the observed image depends not only on the amplitude of the beam, but also on the phase of the electrons. Therefore, different imaging methods attempt to modify the electron waves exiting the sample in a form that is useful to obtain information with regards to the sample. Phase effects are often ignored at lower magnifications, however in case of higher resolution measurements; the images are formed by utilizing the differences in phase of electron waves, which is caused by specimen interaction.¹⁹³

With high resolution TEM (HRTEM), in addition to the size and shape of nanoparticles, information about their internal structure (i.e. lattice fringes, which are important for the analysis of crystal structure, interplanar spacing, stacking faults, and dislocations) can be determined. In addition, selective area electron diffraction (SAED) measurements can be carried out in a TEM, which provides information about whether the material is single crystal or polycrystalline. Also, the phase of the nanoparticle can be estimated from the interplanar spacing determined from the SAED pattern.

The sample preparation for TEM imaging of nanoparticles is usually carried out by putting the drops of the solution (containing nanoparticles) on a grid, while allowing the solvent to evaporate. Usual grid materials are copper, molybdenum, gold or platinum.

Chapter 2

Standard carbon coated copper grids of size 3.05 mm diameter with a mesh size of 200 (74 μm) was used in the current thesis experiments. The TEM measurements were carried out on model number CM200, PHILIPS with operating voltage range from 20-200 kV and resolution of 2.4 \AA , while HRTEM images were acquired on FEI, TECNAI-F30.

2.6. Scanning electron microscopy

Analogous to TEM, scanning electron microscopy (SEM) is an essential tool for characterization of nanomaterials. Both the techniques use electron beams for imaging the samples. However, the former (TEM) is based on transmitted electrons, while the working principle of later one (SEM) is based on scattered electrons.^{194, 195} SEM provides important information about the sample's surface topography and composition.

In a typical SEM, an electron beam is thermionically emitted from an electron gun, usually fitted with a tungsten filament cathode. Tungsten is normally used in thermionic electron guns because it has the highest melting point and lowest vapor pressure of all metals, thereby allowing it to be heated for electron emission. The electron beam having energy ranging from 0.2 keV to 40 keV is focused by collimating and focusing lenses to a narrow spot of the order of nanometers in diameter on the specimen surface. This beam is scanned in a rectangular raster over the specimen and the intensities of various signals created by interactions between the beam of electrons and the specimen are measured. As a result of interaction of the primary electron beam with the sample, the energy exchange results in the reflection of high-energy electrons by elastic scattering, emission of secondary electrons by inelastic scattering and the emission of electromagnetic radiation, each of which can be detected by specialized detectors. The most common imaging mode

Chapter 2

collects low-energy (<50 eV) secondary electrons (SE) that are ejected from the k-shell of the specimen atoms by inelastic scattering interactions with beam electrons. Due to their low energy, these electrons originate within a few nanometers from the sample surface¹⁹⁵ and are detected by a type of scintillator-photomultiplier system. In another mode, backscattered electrons (BSE) are detected. BSE consist of high-energy electrons originating in the electron beam that are reflected or back-scattered by the specimen elastic scattering interactions. Since, heavy elements (high atomic number) backscatter electrons more strongly than light elements (low atomic number), and therefore appear brighter in the image and used to detect contrast between areas with different chemical compositions. Additionally, as already mentioned, the X-rays are produced by inelastic collisions of the incident electrons with the electrons in the discrete orbitals (shells) of atoms in the sample. As the excited electrons return to lower energy states, they yield X-rays that are of a fixed wavelength (that is related to the difference in energy levels of electrons in different shells for a given element). Thus, characteristic X-rays are produced for each element in the sample. And, this forms the basis of energy dispersive X-ray spectroscopy (EDS) and has been widely employed for determining the composition of the samples. A basic layout of a SEM is shown in Fig.2.5.

A crucial aspect of SEM sample characterization is that the sample must dissipate charge. For conducting materials on a conductive substrate, this requirement is easily met. However, a thin layer of conducting material such as carbon, gold, or some other metal/alloy is coated on the electrically insulating samples.

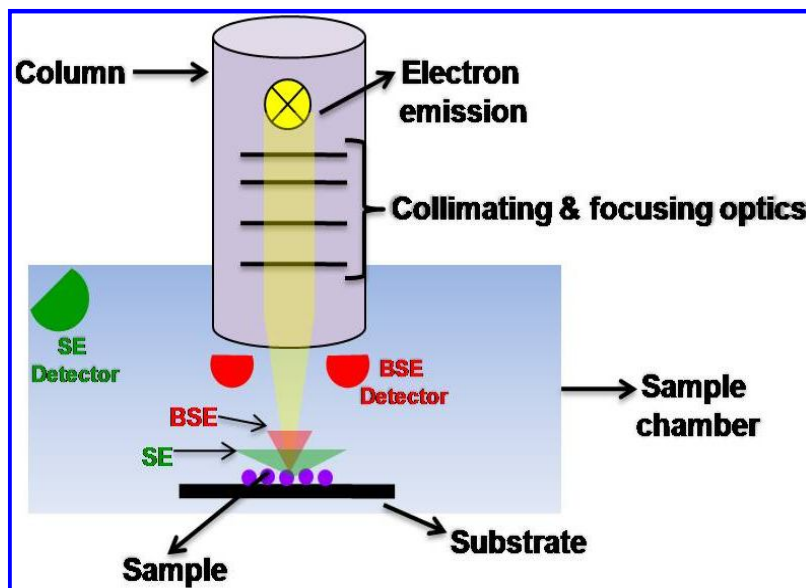


Fig.2.5. Basic layout of a Scanning Electron Microscope.

Surface and morphological characterization of nanoparticles synthesized in the present thesis work were carried out on JEOL JSM-T330 SEM. The compositional analysis for the samples was performed with energy dispersive X-ray spectrometer, an accessory of SEM. The preparation of samples for SEM and EDS analysis were carried out by putting a drop of solution containing nanoparticles on a Silicon wafer, and subsequently allowing the solvent to evaporate.

2.7. Steady-state UV-Vis absorption measurements

Since the absorption of ultraviolet or visible radiation by a molecule/compound leads to transition among their electronic energy levels, it is also often called as electronic spectroscopy. Spectrophotometers are used for the quantitative measurement of the absorption or transmission of UV-Vis light by a sample as a function of wavelength. The working principle of the spectrophotometer is based on the Beer-Lambert's law which

Chapter 2

states that the absorbance of a solution is directly proportional to the concentration of the absorbing species in the solution and the path length^{196, 197}

$$A = \log\left(\frac{I_0}{I}\right) = \epsilon cl \quad [2.30]$$

where, A is the measured absorbance in Absorbance Units (AU), I_0 is the intensity of the incident light at a given wavelength, I is the transmitted intensity, l the path length through the sample, c the concentration of the absorbing species and ϵ is a constant known as the molar absorptivity or extinction coefficient. The sample solution is generally taken in a quartz cell. The basic parts of a spectrophotometer are a light source, a holder for the sample, a diffraction grating in a monochromator or a prism to separate the different wavelengths of light, and a detector. A spectrophotometer can be either single beam or double beam. In a single beam instrument, all of the light passes through the sample cell. I_0 must be measured by removing the sample. In a double-beam instrument, the light is split into two beams before it reaches the sample. One beam is used as the reference; the other beam passes through the sample. The reference beam intensity is taken as 100% Transmission (or 0 Absorbance), and the measurement displayed is the ratio of the two beam intensities.

Ground-state optical absorption measurements were carried out on a JASCO V 650 UV-Visible spectrophotometer. It is a double-beam spectrophotometer with a PMT detector. Typical wavelength range is 190-900 nm. The light sources used in this instrument are Deuterium lamp (range: 190 to 350 nm) and a Halogen lamp (range: 330 to 900 nm).

2.8. Steady-state photoluminescence measurements

Photoluminescence (PL) spectroscopy is a contactless, nondestructive method to probe the electronic structure of materials. Light (in UV-Vis range) is directed onto a sample, where it is absorbed and imparts excess energy into the material in a process called photo-excitation. Following excitation, electrons within a material move into permissible excited states. When these electrons return to their equilibrium states, the excess energy is released by various relaxation processes, which may include the emission of light (a radiative process) or may not (a non-radiative process). The energy of the emitted light (PL) relates to the difference in energy levels between the two electron states involved in the transition between the excited state and the equilibrium state. Observation of PL at certain energy can be viewed as an indication that the excitation event had populated an excited state associated with this transition energy. Fluorescence and phosphorescence are forms of PL and observed at lower energy than absorption (the excitation energy).^{1c, 196}

PL measurements were carried out using a spectrofluorometer. In a typical fluorescence (emission) measurement, the excitation wavelength is fixed and the detection wavelength region is specified, while in a fluorescence excitation measurement, the detection wavelength is fixed and the excitation wavelength is varied across a region of interest. The light from an excitation source passes through a filter or monochromator, and strikes the sample. A proportion of the incident light is absorbed by the sample, and some of the molecules in the sample fluoresce. The fluorescent light is emitted in all directions. Some of this fluorescent light passes through a second filter or monochromator

Chapter 2

and reaches a detector, which is usually placed at 90° to the incident light beam to minimize the risk of transmitted or reflected incident light reaching the detector.

In the present thesis work, steady-state fluorescence measurements (excitation spectra or emission spectra) were carried out using a Hitachi model F-4500 fluorescence spectrometer. The instrument uses a xenon lamp (150 W; continuous) as an excitation source and R-928F (Hamamatsu) PMT as the photodetector. Sample is taken in a quartz cuvette of dimensions 1 cm × 1 cm and the fluorescence is collected and measured in a perpendicular direction with respect to the direction of the excitation beam. The wavelength range covered in the present instrument is 220 to 800 nm, while the resolution is 1 nm.

The PL quantum efficiency (QE) of a sample solution was determined based on the comparative method by using equation (2.31):^{1c}

$$\Phi_S = \Phi_R \frac{A_S}{A_R} * \frac{OD_R}{OD_S} * \left(\frac{n_S}{n_R}\right)^2 \quad [2.31]$$

where, ‘ Φ_S ’ and ‘ Φ_R ’ are the quantum yields of sample and reference, respectively, ‘A’ is the integrated PL intensity, ‘OD’ is the optical density, and ‘n’ is the refractive index. The excitation wavelength was chosen on the basis, where the OD values of both the sample and the reference matched with each other.

2.9. Photoluminescence lifetime measurements

Absorption of an appropriate photon energy follows a chain of photophysical events, such as internal conversion or vibrational relaxation (loss of energy in the absence of light emission), fluorescence, intersystem crossing (from singlet state to a triplet state), and

Chapter 2

phosphorescence.^{1c, 196, 198} Each of these processes occurs with a certain probability, characterized by decay rate constants (k) and the average length of time τ for the set of molecules to decay from one state to another can be expressed as: $\tau = 1/k$. This average length of time is called the mean lifetime or simply lifetime. The lifetime of photophysical processes vary significantly from tens of femtoseconds for internal conversion to nanoseconds for fluorescence and microseconds or seconds for phosphorescence.^{1c, 198} Moreover, fluorescence lifetime can be sensitive to a great variety of internal factors defined by the fluorophore structure and external factors that include temperature, polarity, and the presence of fluorescence quenchers. Therefore, fluorescence (or PL) lifetime measurements are essential to obtain information regarding the kinetics and dynamics of various photophysical processes as well as their mechanism involved in the deactivation of the excited fluorophores. The versatility of the fluorescence lifetime method allows its application in diverse areas of study, including materials science, aeronautics, agriculture, forensics, biology, and medicine.

At present, most of the time-domain measurements in the nanosecond to picosecond time scales are performed using time-correlated single-photon counting technique (TCSPC). The working principle of TCSPC is described as follows. Basically, it is a technique with well defined (Poisson) statistics, and is not affected by the changes in source intensity.^{1c, 199} It makes use of a pulsed excitation source such as a laser or a flash lamp, which excites the sample, while the detection system monitors the time difference between the excitation pulse and the first fluorescence photon from the sample. However, for TCSPC, the conditions are adjusted so that less than one photon is detected per laser

Chapter 2

pulse.^{1c} In fact, the detection rate is typically 1 photon per 100 excitation pulses. The layout of a typical TCSPC set up is shown in Fig. 2.6. The experiment starts with the excitation pulse, one part of which is used to excite the sample kept in the sample chamber and the other part of the light pulse is directed to a start PMT. The signal at the start PMT generates a START pulse and is then routed through a constant function discriminator (CFD), which accurately measures the arrival time of the pulse. This signal is passed to a time-to-amplitude converter (TAC), which generates a voltage ramp that increases linearly with time on the nanosecond time scale. In the second channel, pulse used to excite the sample results in the emission of photons and is detected by STOP PMT. The arrival time of the signal is accurately determined using a CFD, which sends a signal to stop the voltage ramp.

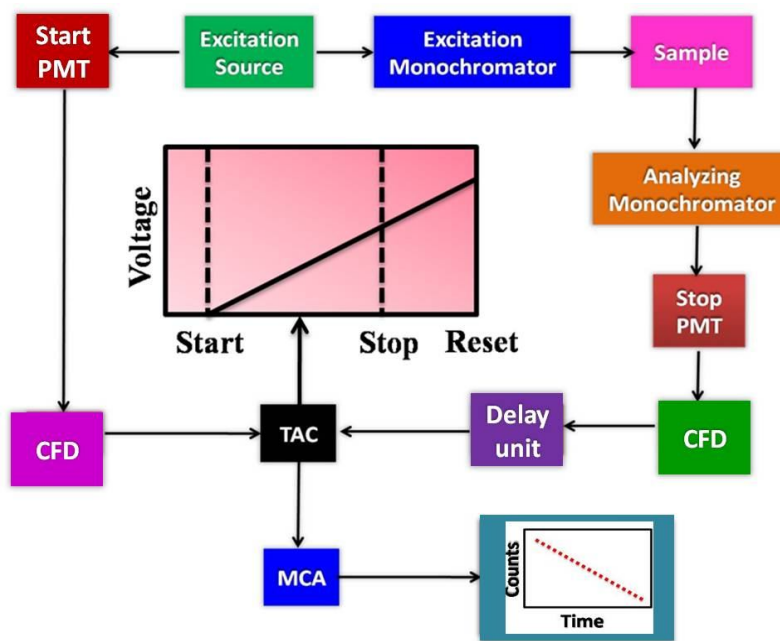


Fig.2.6. Layout of a TCSPC setup.

Chapter 2

The TAC now contains a voltage proportional to the time delay (Δt) between the excitation and emission signals. This voltage level is then fed to the input of a Multichannel Analyzer (MCA) through an Analog-to-Digital Converter (ADC). The ADC generates a numerical value proportional to the height of the TAC output pulse and thus selects the corresponding memory address (channel) in the MCA, where a single count is added up. The above cycle (from the triggering of the pulsed excitation light source to the data storage in the MCA) is repeated for a large number of times and such events are binned to form a histogram of counts versus channel number (time). During experiment, the data collection rate is kept very low i.e. <0.02 photons/excitation pulse. The histogram represents the decay of the excited state convoluted with the instrument response function.

PL lifetime measurements were carried out by using a TCSPC instrument (model: IBH, UK). Both diode laser and LED are used as excitation source. The instrument response function (IRF) of the setup was measured by collecting the scattered light from a TiO_2 suspension in water. An emission polarizer is used before collection optics and PL decay profile is recorded at magic angle (54.7°) polarization with respect to excitation light (source as diode laser). The fluorescence collected at the magic angle is free from any anisotropy components and represents the actual total fluorescence intensity decay. The as obtained decay curves were analyzed and fitted by using a non-linear least square analysis supported by instrument fitting program of IBH DAS 6.2 software:

$$I(t) = \sum_{i=1}^n \alpha_i e^{-t/\tau_i} \quad [2.32]$$

Chapter 2

where, $I(t)$ is the time-dependent emission intensity, τ_i are the decay times and ' α_i ' represent the amplitudes of the components at $t = 0$, and n is the number of decay times. The goodness of the fit was judged by the reduced χ^2 value, which should be close to 1 and weighted residuals should be randomly distributed about the zero line for the whole range of the data channels used in the decay analysis.

2.10. Fourier transform infrared spectrometer

In Infrared spectroscopy (IR spectroscopy), IR radiation (range covering near, mid and far IR regions: 1 to 1000 microns) is passed through a sample. Some of the IR radiation is absorbed by the sample and some of it is passed through (transmitted). The resulting spectrum represents the molecular absorption and transmission, creating a molecular fingerprint of the sample. Like a fingerprint, no two unique molecular structures produce the same infrared spectrum. This makes infrared spectroscopy useful for several types of analysis.^{200, 201} Nevertheless, the fundamental requirement for IR activity, leading to absorption of IR radiation is that there must be a net change in dipole moment during vibration of a molecule or the fundamental group under study.

In general, nowadays, Fourier transform infrared spectrometer (FTIR) is employed to record the vibration spectra of the samples. Typical units of frequency used in IR spectra are reciprocal centimeters (sometimes called wavenumbers), with the symbol cm^{-1} . The original infrared instruments were of the dispersive type, where one wavelength at a time passes through the sample. On the contrary, in FTIR, the information at all frequencies is collected simultaneously, improving both speed and signal-to-noise ratio. This is also known as " Fellgett's advantage " or the " multiplex advantage ".²⁰² Another is called

Chapter 2

"Jacquinot's throughput advantage", which refers to the higher optical throughput obtained in FTIR and leads to a better signal-to-noise ratio. Essentially, a very simple optical device called an interferometer is employed in FTIR, which produces a unique type of signal called as an interferogram. This signal can be measured very quickly and has all of the infrared frequencies "encoded" into it. Because the measured interferogram signal cannot be interpreted directly, therefore a means of "decoding" the individual frequencies is required. This can be accomplished *via* a well-known mathematical technique called the Fourier transformation (equation 2.33):

$$f(\nu) = \int_{-\infty}^{\infty} f(t)e^{-i2\pi\nu t}dt \quad [2.33]$$

where, t is the time and ν is the frequency.

In the present thesis work, FTIR spectra of the samples were recorded in an IR Affinity-1 spectrometer with a resolution of $\sim 1 \text{ cm}^{-1}$. Attenuated total reflection (ATR) based sampling technique was used during the measurements. ATR based FTIR is based on measuring the changes that occur in a totally internally reflected IR beam when it comes into contact with a sample. A beam of IR light is passed through the ATR crystal in such a way that it reflects at least once off the internal surface in contact with the sample. An IR beam is directed onto an optically dense crystal (diamond in the present work) with a high refractive index at a certain angle. The internal reflection forms an evanescent wave, which extends beyond the surface of the crystal into the sample held in contact with the crystal. The penetration depth into the sample is typically between 0.5 to 5 μm , with the exact value being determined by the wavelength of light, the angle of incidence and the indices of refraction for the ATR crystal and the medium being

Chapter 2

probed.^{203, 204} In regions of the IR spectrum, where the sample absorbs energy, the evanescent wave will be attenuated or altered. The attenuated energy from each evanescent wave is passed back to the IR beam, which then exits the opposite end of the crystal and is passed to the detector in the IR spectrometer. The system then generates an infrared spectrum. For reliable measurements, there must be good contact between the sample and the crystal surface.

2.11. Raman spectrometer

When a sample is irradiated with an intense monochromatic light source (usually a laser), most of the radiation is scattered by the sample at the same wavelength as that of the incoming laser radiation in a process known as Rayleigh scattering. However, a small proportion of the incoming light i.e. approximately one photon out of a million is scattered at a wavelength that is shifted from the original laser wavelength. This shift, either to the higher (anti-Stokes shift) or towards the lower frequency (Stokes shift) with respect to the excitation frequency is called as Raman scattering effect.²⁰⁵⁻²⁰⁷ Raman scattering is an example of inelastic scattering because of the energy and momentum transfer between the photons and the molecules during the interaction. Rayleigh scattering is an example of elastic scattering, the energy of the scattered Rayleigh scattering is of the same frequency (wavelength) as the incoming electromagnetic radiation. The fundamental requirement for Raman effect to be observed is that the net change in bond polarizability associated with the vibration must be non-zero, as shown below.

The dipole moment, P , induced in a molecule by an external electric field, E , is proportional to the field, equation 2.34.

Chapter 2

$$P = \alpha E \quad [2.34]$$

The proportionality constant, α is the polarizability of the molecule. The polarizability measures the ease with which the electron cloud around a molecule can be distorted. The induced dipole emits or scatters light at the optical frequency of the incident light wave. Raman scattering occurs only when a molecular vibration results into a net change in the polarizability, which can be expressed as:

$$\frac{\delta\alpha}{\delta Q} \neq 0 \quad [2.35]$$

where, Q is the normal coordinate of the vibration.

If a molecule has a center of symmetry, vibrations which are Raman-active will be silent in the infrared, and vice versa. This is called as the rule of mutual exclusion in centrosymmetric molecules. Typical strong Raman scatterers are moieties with distributed electron clouds, such as carbon-carbon double bonds. The pi-electron cloud of the double bond is easily distorted in an external electric field. Bending or stretching the bond changes the distribution of electron density substantially, and causes a large change in induced dipole moment.²⁰⁸

Raman spectral studies were carried out using a micro-Raman spectrometer (STR-300, SEKI Technotron, Japan). A fiber coupled 532 nm CW diode pumped solid state laser (DPSS, gem532, Laser Quantum) having an excitation power of approximately 50 mW at the source was initially passed through a band pass filter (532 nm), and directed on the sample *via* microscope (Make: Olympus). The Raman scattered light was collected by the same objective lens and passed through a fiber coupled to a 300 mm focal length imaging spectrograph (Action series SP2300i, 1200 groove/mm) and was detected by a

Chapter 2

thermo-electric cooled (-75°C) charge coupled device (CCD) detector (Pixis 256 CCD camera, Princeton Instruments). The spectrograph was calibrated using the 520.5 cm^{-1} line from silicon wafer. For recording the Raman spectra, samples (liquid as well as solid) were taken on a glass slide and used for carrying out the Raman spectral studies.

Chapter 3

Dual site for solvation of electrons and generation of counter ion radicals in CTAB based *water-in-oil* microemulsions: A pulse radiolysis study

3.1. Introduction

Organized assemblies are regarded as novel reaction media for which in-depth understanding of the electrons and electron transfer processes is pertinent (discussed in Chapter 1). In four components w/o microemulsions, the surfactant and cosurfactant molecules form a spherical shell with a polar core, where water can reside at various concentrations. These core shell structures are dispersed homogeneously in liquid hydrocarbons. As a result, the whole system behaves as a transparent, isotropic, and thermodynamically stable solution of water-in-oil. The water, confined in the cavity controls the size and shape of the micelle, and thus, the reverse micelles or microemulsions are often characterized by the W_0 value, which is defined as the mole ratio of water to surfactant, $W_0 = [\text{H}_2\text{O}] / [\text{surfactant}]$.

Because of the compartmentalization of reactants into polar and non-polar regions, yet within the reaction zone, the microemulsions have become important in its wide applicability in synthesis. Detailed reviews on organic synthesis²⁰⁹ and nanoparticle

Chapter 3

synthesis^{13, 14, 210} in microemulsions are available in the literature. Numerous examples are there in this regard including very recent work on synthesis of specialized materials in microemulsions.²¹¹ In two phase reactions, the ionic reactants are extracted by a phase transfer catalyst from the aqueous phase to the organic phase where the reactions take place.²¹² The phase transfer catalysts are of environmental concern, and carrying out these sorts of reactions in microemulsions is convenient and more environment friendly. It has been mentioned earlier that the water pools in the reverse micelles mimic the water pockets that are often found in various bioaggregates such as proteins, membranes, and mitochondria.¹ A variety of molecules have been studied in such systems, and it had been shown that the enzymes incorporated in the aqueous core of the reverse micelles were protected against denaturation.²¹³ Free radical reaction of β -carotene in the microemulsion system was found to generate retinol which otherwise is an enzymatic process.²¹⁴ Recently, it has been reported that DNA can be readily dissolved into microemulsions stabilized by an anionic surfactant (AOT).²¹⁵ These authors found that for $W_0 = 44.4$, with the increase in DNA concentration, the water droplets become progressively more spherical and monodisperse. The local DNA concentrations in this condition attain values as high as those naturally observed in biological organelles.

CTAB has been used as a surfactant for making reverse micelles and microemulsion for several important studies reported earlier.¹⁵ CTAB does not form reverse micelles in alkanes in the absence of a cosurfactant, and only in presence of medium chain length primary alcohols, such as 1-butanol, 1-pentanol, or 1-hexanol, formation of CTAB microemulsion in alkane is possible.²¹⁶ The characterization of this microemulsion which

Chapter 3

includes size and shape,²¹⁷ water core radius, aggregation number,²¹⁸ thickness of the interface and ion concentration at the interface^{218, 219} are well studied. The hydrodynamic radius of a system (CTAB/1-pentanol/cyclohexane/water) similar to the one used in the present study, was reported to vary from 2.4 to 11.4 nm as W_0 increases from 5 to 40, and it is not significantly affected by a change in the cosurfactant.²¹⁶ Of late, it has been demonstrated that, in the CTAB/1-pentanol/cyclohexane/water system, with the increase in water content, the packing parameter decreases which eventually leads to an increase in interfacial fluidity.²²⁰ In such a situation, reactions which involve both water core and the interface might be favored.

A variety of studies in the past^{16, 19, 213b, 221} have made noteworthy contributions to the understanding of the electron processes in reverse micelles and microemulsions. Kinetic evidence had shown earlier that the location of the probes in reverse micelles plays an important role in their reactivities.²²² In o/w (benzene/water) microemulsions, Wu *et al.*¹⁸ have observed that the rate constants for the addition of e_{aq}^- and the $\cdot OH$ radical to benzene are in agreement with those in aqueous solutions. The hydrated electrons have been studied earlier using pulse radiolysis and near IR spectroscopic measurements in reverse micellar systems of Brij30, mixture of AOT and Brij30, and AOT doped with PEG.¹⁶ These authors have demonstrated that, even though hydrated electrons could probe the polar core of the reverse micelles, it is difficult to formulate a simple relation between characteristics of the hydrated electron and the properties of reverse micelles. A report on the yield of hydrated electrons in the cationic microemulsion composed of CTAB/water/1-pentanol/cyclohexane also exists in the literature.²⁰ However, in a

Chapter 3

microemulsion, counter ion radical species and their involvement in the redox processes have not been reported till date.

Thus, in the present work, we attempted to look for three important physicochemical aspects of w/o microemulsion. In addition to revisiting the properties of hydrated electron and its decay pattern in the CTAB microemulsion system, our intention was to examine whether counter ion radical species could be observed in the small water pockets. If observed, what could be their reactivity with molecules dissolved in the aqueous phase of the microemulsion? Finally, we wished to study the two phase reaction between radicals produced in the aqueous core and a molecule that is completely insoluble in water. Each of these points would be demonstrated in this Chapter. We will discuss here, how the interface of the microemulsion competes with the water pool in the solvation of dry electrons produced in the oil phase. Clear difference in kinetic behaviour of the two types of solvated electrons as observed in this study could unfold the physical nature of the interface. Further, it will be clearly shown that the bromide ions present in the water pocket are capable of interfering in redox processes occurring in this media.

3.2. Experimental

3.2.1. Chemicals and microemulsion preparation:

CTAB, Cetylpyridinium bromide (CPB), 2,2'-azino-bis-(3-ethylbenzothiazoline-6-sulfonic acid) diammonium salt (ABTS), ascorbic acid, and tocopherol were from Aldrich. All of the surfactants were recrystallized before use. CTAB was recrystallized twice from ethanol.^{223a} CPB was purified by washing with acetone 5 times.^{223b} ABTS, tocopherol, and ascorbic acid were used as received. All other chemicals were of

Chapter 3

3.3. Results and Discussion

3.3.1. Hydrated electron

Hydrated electrons are formed in a microemulsion from two sources.^{16, ref 19, 213b, 221} One is the scavenging of excess electrons produced in the oil phase by water pools. The scavenging process is very fast and completed during the electron pulse. The other source of hydrated electrons is the direct radiolysis of water pools. The transient absorption spectra obtained in the pulse radiolysis of a microemulsion containing CTAB /H₂O/*n*-butanol/cyclohexane solutions bubbled with nitrogen are shown in Fig.3.2. The hydrated electron spectra at different times after the electron pulse was obtained from a solution with $W_0 = 20$ (as represented in this figure), where two peaks at 650 and 720 nm are visible. The later is the typical hydrated electron spectrum one expects in pure aqueous solution. The interesting observation is another absorption maximum at 650 nm, which is even more intense than the usual peak at 720 nm at longer times. This absorption peak can be attributed to electrons solvated in the interface of the reverse micelle. By calculating the effective packing parameter of the *n*-pentanol/CTAB/*n*-hexane/water microemulsion system, Giustini *et al.*^{217a} have shown that, in the dispersed phase, not only the CTAB and water but, 1-pentanol is also present. Besides, it is also reported that solvated electrons in long chain alcohols give rise to an absorption peak at around 630-650 nm.^{217b}

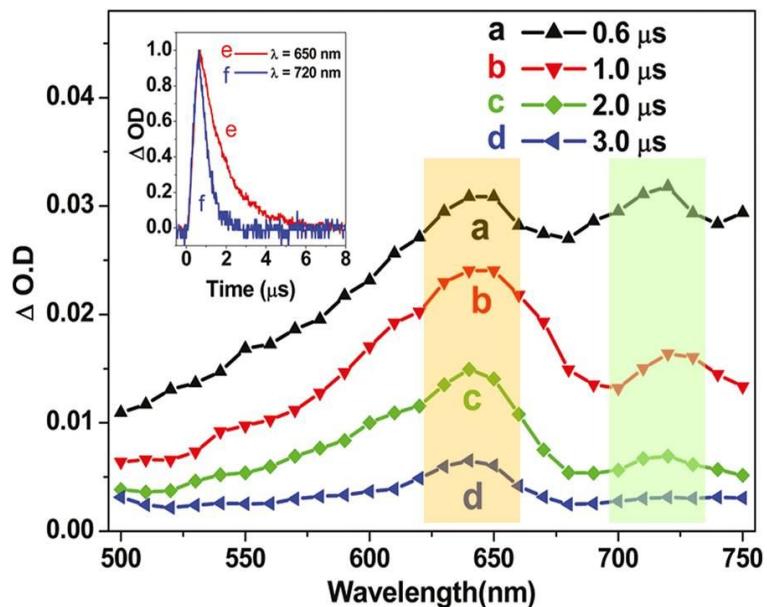


Fig.3.2. Transient absorption spectrum of hydrated electrons at (a) 0.6, (b) 1, (c) 2, (d) 3 μs after the electron pulse of N_2 saturated solution of CTAB/cyclohexane/n-butanol/water with $W_0 = 20$. (O.D. = Absorbance). Inset: Decay of hydrated electron at 650 (e) and 720 nm (f) in microemulsion with $W_0 = 20$.

In the present microemulsion system, as 1-butanol is present in the interface, the absorption peak at 650 nm is ascribed to the electrons solvated in this region. Moreover, in another study it had been shown that dual sites of solvation is possible in microemulsion containing sodium lauryl sulfate (NaLS)/ H_2O /1-pentanol/cyclohexane.¹⁹ The hydrated electron spectrum obtained from solutions with $W_0 = 30$ and 40 are similar (not shown here) but show higher yield of hydrated electrons (Table 3.1).

It must be noted that the yield of solvated electrons at the interface shows a higher value with an increase in water content of the system. However, it has also been observed that, at the end of the electron pulse, the absorption due to the electrons solvated in the interfacial

Chapter 3

region becomes lower and that for the water core becomes higher as the water content of the system is increased showing bulk-water-like behavior at higher W_0 . The electrons at the interface decay slower than the ones in the water pool. Thus, at a particular W_0 , due to slower decay, the yield of solvated electrons at the interface might show a higher value at longer times.

Table 3.1: Yields of hydrated electrons in the CTAB/H₂O/n-butanol/cyclohexane microemulsion

W_0 (CTAB system)	G(e _{aq} ⁻) at 650nm	G(e _{aq} ⁻) at 720nm
10	0.45	0.504
20	0.708	0.731
30	0.738	0.733
40	0.789	0.736

Note: The yields were calculated assuming the extinction coefficient of solvated electrons in the microemulsion system is same as that in pure water.

Further, as the solvated electrons have broad absorption spectra, the absorption at 650 nm would always have some contribution from that at 720 nm. Consequently, quantitative assessment in the properties of these two types of electrons would always have a contribution from the other. The inset of Fig.3.2 represents the decay of solvated electrons at 650 and 720 nm, respectively, in the microemulsions ($W_0 = 20$). It is seen that the decay of the hydrated electron in these systems is faster than that in pure aqueous solution. Nonetheless, the decay of hydrated electron at 720 nm is faster than that at 650 nm. The half-life values calculated from this trace are ~ 1 and ~ 1.6 μs (in the microemulsions with $W_0 = 20$) at 720 and 650 nm, respectively. On the contrary, the half-life of the electron was reported to be 12 μs as measured at 720 nm in an anionic

Chapter 3

microemulsion with $W_0 = 16$.¹⁹ The anionic nature of the charged surfaces in the NaLS system makes the electrons more stable. Moreover, the reactivity of hydrated electrons with the CTAB micelle is higher than that with NaLS,^{221h} which makes the half-life of hydrated electrons greater in the later system.

In microemulsions, the decay of hydrated electrons follows a kinetic equation, and by carrying out the reaction of solutes with hydrated electrons, it is possible to characterize these organized systems.²²² In an early report, we could determine the water pool radius and location of probes in NaLS/H₂O/1-pentanol/cyclohexane w/o microemulsion system.^{221e} However, intrinsic decay of the hydrated electron should be reasonably slow to obtain the parameters with accuracy. Unfortunately, in the present case, it is very difficult to characterize the system by following electron decay because of the short life of the hydrated electron itself. Moreover, it is worth mentioning here that Gebicki and Maciejewska^{16e} have already shown that it is impossible to get a pure hydrated electron spectrum in the microemulsion system with low water content.

It can be seen from Fig.3.3 that the decay of solvated electron at the interface is slower than that in water core. This reveals that the electrons are more stabilized and are well separated with other electrons when they are solvated in the interfacial region. The decay of electrons solvated in the water core is not dependent on W_0 , whereas that in the interface varies with W_0 . When the electron decay at the interface in microemulsions with different water content is compared, a faster decay is observed with an increase in W_0 .

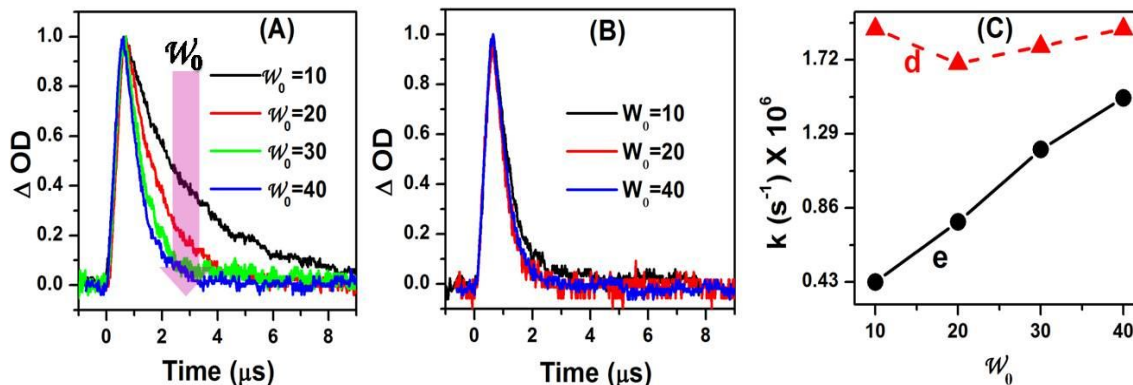


Fig.3.3. Decay pattern of solvated electrons at the interface (A) and in the water core (B). (C) Plot of decay constants of solvated electrons versus W_0 (d) in the water core and (e) at the interface, respectively. O.D. = absorbance.

It has already been mentioned in the introduction that with the increase in water content an increase in interfacial fluidity was observed in an earlier study.²²⁰ In the present case, due to the increase in interfacial fluidity with the increase in W_0 , the mobility of electrons solvated in this region increases, and so, the escape of these electrons into the water core might also be favored. All of this would lead to an increase in the interaction between the electrons present in the interface and also with those that exist in the water core. Another interesting point to be noted is that the decay rates of electrons solvated in the water core are not significantly different at various W_0 values. This is due to the cationic interface which makes the interaction between the aquated electron (e_{aq}^-) faster, and also the time window of our measurement may not be appropriate to differentiate the decay patterns of e_{aq}^- in this particular media.

Solvated electrons could not be observed in the CPB microemulsion in the present experiments. Gratzel *et al.*²²⁴ had earlier reported about the trapping of hydrated electrons by a cetyl pyridinium chloride (CPCI) micelle. According to these authors, the reaction

Chapter 3

proceeds with a bimolecular rate constant of $7 \times 10^9 \text{ dm}^3 \text{ mol}^{-1} \text{ s}^{-1}$. The electron adduct of pyridinium cation was seen to have a shoulder at around 355 nm in its broad absorption spectrum. Assuming an aggregation number of 95, it had also been found that the second order rate constant for the reaction of e_{aq}^- with the CPCl micelle to be more than $1 \times 10^{12} \text{ dm}^3 \text{ mol}^{-1} \text{ s}^{-1}$. These authors rationalized the extraordinarily high rate constant for this reaction by taking into account the electrical properties of the micellar double layer. In comparison to this rate constant, CTAB micelles react with hydrated electrons with a bimolecular rate constant of $9.2 \times 10^5 \text{ dm}^3 \text{ mol}^{-1} \text{ s}^{-1}$.²²⁴ Thus, from the data available in the literature and arguments provided therein, it is not surprising that we could not observe the hydrated electron in the CPB w/o microemulsion.

3.3.2. Counter ion radical: Dibromide radical anion in CTAB and CPB microemulsions

The absorption spectrum in the shorter wavelength region is quite different than that observed and reported earlier in reverse micellar systems.^{16, 221} We have observed another species absorbing in the region 300-430 nm with a maximum around 365 nm (Fig.3.4). The absorption at this wavelength decays much slower than at 720 and 650 nm. Other than an electron, the primary radicals that can be formed in the water pool, are the $\cdot\text{OH}$ radical and $\cdot\text{H}$ atom. Both the radicals absorb in the far UV and have very low extinction coefficients. The possibility of the absorption maximum at 360 nm cannot be accounted for by either of these radicals or radicals formed from cyclohexane. Thus, it can be assumed that a secondary radical is generated in the water pool.

Chapter 3

The bromide ion distribution in CTAB w/o microemulsion has been demonstrated earlier by chemical trapping technique.^{219b, 225} The bromide ion concentrations at the interface and water pool were shown to be as high as 7.0 and 6.0 mol dm⁻³, respectively, at $W_0 = 10$ in the CTAB/*n*-dodecane/CHCl₃/water microemulsion, and with an increase in W_0 from 10 to 40, the bromide ion concentrations decrease to 3.0 and 0.19 mol dm⁻³ at the interface and water pool, respectively.^{219b}

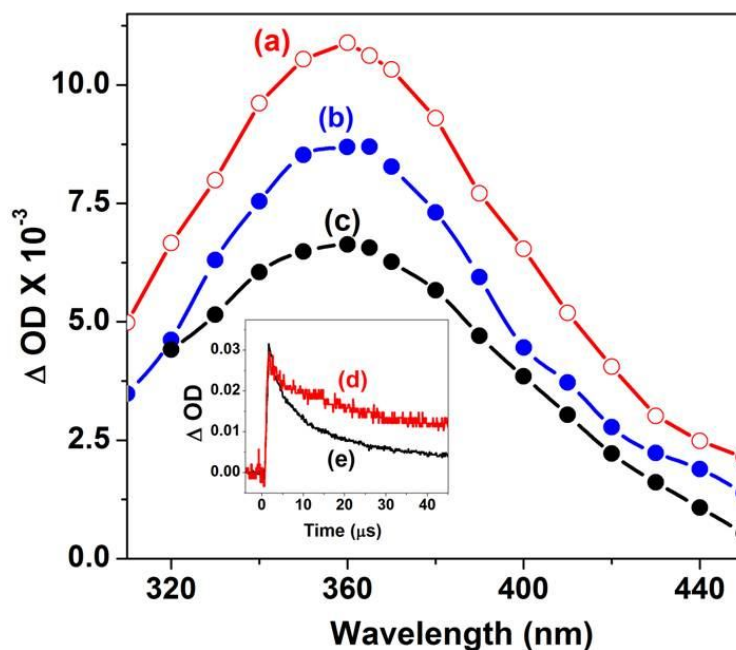


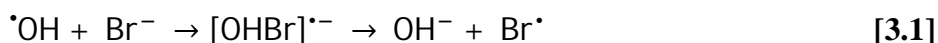
Fig.3.4. Transient absorption spectrum of dibromide anion radical of the CTAB/cyclohexane/*n*-butanol/water solution after electron pulse (a) N₂O saturated ($W_0 = 40$) (b) N₂ purged ($W_0 = 40$) (c) N₂ purged ($W_0 = 30$). Inset: Decay of dibromide anion radical at 360 nm at a dose of (d) 34 Gy and (e) 62 Gy in N₂-bubbled CTAB/*n*-butanol/cyclohexane/water microemulsion ($W_0 = 40$).

In the CTAB/isooctane/*n*-hexanol/water reverse micellar system, the bromide ion concentration in the water pool was calculated to be 1.91 and 0.29 mol dm⁻³ at $W_0 = 12$ and 44, respectively.²²⁵ The later system is closer to that used in the present study, and

Chapter 3

therefore, it is reasonable to assume a bromide ion concentration of about 2 mol dm^{-3} in the water pools at $W_0 = 10$. Direct radiolysis of water in the core of these reverse micelles produces $\cdot\text{OH}$ radicals.²⁰ Molar concentration of bromide ions in the water pool are expected to scavenge these $\cdot\text{OH}$ radicals and produce dibromide radical anion ($\text{Br}_2^{\cdot-}$).

In a N_2O -saturated aqueous solution containing bromide ion, the following well established reactions occur after the electron pulse:²²⁶



The rate constant for the formation of $\text{Br}_2^{\cdot-}$ radical is $1.2 \times 10^9 \text{ dm}^3 \text{ mol}^{-1} \text{ s}^{-1}$. In our experiments, the radical formation was complete just at the end of the pulse, and therefore, the rate constant could not be determined at such a high concentration of bromide ion. The dibromide radical anion thus produced has a strong absorption in the wavelength range of 300–500 nm ($\lambda_{\text{max}} = 360 \text{ nm}$).^{226a} In the present case, the absorption spectrum matches well with that reported earlier for dibromide radical anion in aqueous solution.

The $\text{Br}_2^{\cdot-}$ radical in pure aqueous solution decays by a second order process with a rate constant of $3.3 \times 10^9 \text{ dm}^3 \text{ mol}^{-1} \text{ s}^{-1}$ and so a first half-life of ca. 0.2 ms.^{226b} We have also observed a second order decay of the radical as is evident from the inset of Fig.3.4. The decay at 360 nm becomes faster with an increase in dose from 34 to 62 Gy because of an increase in the concentration of the radical at higher dose. The calculated first half-life is $\sim 40 \mu\text{s}$, which is faster compared to bulk aqueous solution (200 μs).

The faster decay of $\text{Br}_2^{\cdot-}$ radical in the microemulsion can be attributed due to the close proximity of the interacting radicals in a small water pool. Another important point

Chapter 3

is that the yield of $\text{Br}_2^{\bullet-}$ radical is increased when the solution is saturated with N_2O (Fig.3.4 and Table 3.2). The yield of the $\bullet\text{OH}$ radical increases in the presence of N_2O by a scavenging process of hydrated electron by the gas through the following reaction:



In this context, it is worth mentioning that $\text{Br}_2^{\bullet-}$ radical formation and its dismutation reaction was observed earlier in the CTAB micelle. However, the observations were made in an aqueous solution of 0.02 mol dm^{-3} NaBr and $0.005 \text{ mol dm}^{-3}$ CTAB.²²⁷ Consequently, the radicals were generated from the added bromide ion of NaBr and not from the counter ion of the CTAB. In the present case, the as calculated G-value of $\text{Br}_2^{\bullet-}$ ($G(\text{Br}_2^{\bullet-})$) by assuming the extinction coefficient of $\text{Br}_2^{\bullet-}$ to be same as that in bulk water is 0.27 per 100 eV at $W_0 = 40$, N_2 bubbled. We have also observed that that the yield of $\text{Br}_2^{\bullet-}$ radicals does not change with added bromide ion ($0.005 \text{ mol dm}^{-3}$) in the solution. Therefore, the yield of the $\bullet\text{OH}$ radical in the water pool corresponds to that of the observed $\text{Br}_2^{\bullet-}$ radicals. Another way to measure the $\bullet\text{OH}$ radical yield experimentally is to use KSCN at a concentration of 0.05 mol dm^{-3} in the water pool and measuring absorption at 475 nm due to $(\text{SCN})_2^{\bullet-}$ radical. The rate constant for the reaction of $\bullet\text{OH}$ radical with SCN^- is $1.4 \times 10^{10} \text{ dm}^3 \text{ mol}^{-1} \text{ s}^{-1}$ and that with Br^- is $1.2 \times 10^9 \text{ dm}^3 \text{ mol}^{-1} \text{ s}^{-1}$.²²⁸ At $W_0 = 10$, if the concentration of Br^- is assumed to be 1.9 mol dm^{-3} in the water pool, about 30% of the $\bullet\text{OH}$ radical are expected to react with SCN^- . It is not feasible to scavenge the entire $\bullet\text{OH}$ radical in the water pool unless the concentration of SCN^- reaches a value of $16.28 \text{ mol dm}^{-3}$ in the water pool. Indeed, we could not succeed in

Chapter 3

observing measurable absorption due to $(\text{SCN})_2^{\cdot-}$ radicals with KSCN concentration of 0.05 mol dm^{-3} in the water pool.

Table 3.2: Yields of dibromide radical anion ($\text{Br}_2^{\cdot-}$) in the CTAB (or CPB)/ H_2O /cyclohexane/*n*-butanol microemulsion ($W_0 = 40$)

Sr. No.	Co-surfactant and other alcohol	G($\text{Br}_2^{\cdot-}$), N_2 - bubbled		G($\text{Br}_2^{\cdot-}$), N_2O saturated	
		CTAB ME	CPB ME	CTAB ME	CPB ME
1	1-Butanol	0.27	0.56	0.29	0.48
2	1-Pentanol	0.25	0.53	0.30	0.53
3	1-Hexanol	0.30	0.59	0.36	0.52
4	1-Butanol and 0.07 mol dm^{-3} methanol	0.29	0.58	0.25	0.57
5	1-Butanol and 0.5 mol dm^{-3} methanol	0.30	0.59	0.31	0.54
6	1-Butanol and 1.0 mol dm^{-3} methanol	0.31	0.67	0.24	0.61
7	1-Butanol and 0.07 mol dm^{-3} ethanol	0.25	0.59	0.29	0.49
8	1-Butanol and 0.5 mol dm^{-3} ethanol	0.31	0.59	0.25	0.55
9	1-Butanol and 1.0 mol dm^{-3} ethanol	0.20	0.66	0.24	0.55

Note: The yields were calculated assuming the extinction coefficient of $\text{Br}_2^{\cdot-}$ radical in the microemulsion system is same as that in pure water.

From the aforesaid results, it is now clear that the free bromide ions present in the system as dissociated counter ions are capable of scavenging all of the $\cdot\text{OH}$ radicals produced in the water pool after irradiation. The yield of $\text{Br}_2^{\cdot-}$ radical in CTAB and CPB microemulsion using different cosurfactants and also in presence of other alcohols are shown in Table 3.2. It is evident that the cosurfactant does not have any significant role in the yield of the counter ion radical. Methanol and ethanol are known scavengers of the $\cdot\text{OH}$ radicals and are expected to be present in the water core in addition to the dispersed

Chapter 3

phase. However, it is clear from the table that these alcohols are not able to scavenge the $\cdot\text{OH}$ radicals, and thus, the yield of the $\text{Br}_2^{\cdot-}$ radical is unchanged up to a concentration of 1 mol dm^{-3} of the alcohols in the microemulsions. The yield of $\text{Br}_2^{\cdot-}$ radical in the CPB microemulsion is always higher as compared to that in the CTAB systems. This anomaly is due to the overlapping absorption of the electron adduct of the pyridinium cation of the CPB and the $\text{Br}_2^{\cdot-}$ radical.²²⁴

It may be recalled from the last section that the observed half-life of the hydrated electron in the CTAB microemulsion is much lower compared to that in the SDS system and also in pure water. It is known that the bimolecular rate constant of e_{aq}^- with $\text{Br}_2^{\cdot-}$ is $1.3 \times 10^{10} \text{ dm}^3 \text{ mol}^{-1} \text{ s}^{-1}$.^{226b} Therefore, the interaction with the $\text{Br}_2^{\cdot-}$ radical should also be accounted for besides the presence of charged interface, for the faster decay of the hydrated electron in the CTAB microemulsion system.

3.3.3. Reaction of $\text{Br}_2^{\cdot-}$ radical with ABTS: A protocol for antioxidant assay for substrates insoluble in water

After the characterization of $\text{Br}_2^{\cdot-}$ radical, its reactions with the solute dissolved in the aqueous phase of the microemulsion was studied. For this purpose, ABTS was used. Essentially, the ABTS radical assay (employing the technique of kinetic spectroscopy) is a standard method to determine antioxidant activity of different samples of unknown composition and contents.²²⁹ These samples are generally herbal extracts obtained in different organic solvent systems. The ABTS radical is also known as a reference system for electron transfer kinetic studies where the free radical is considered as the one electron oxidant.²³⁰ Thus, the reactivity of unknown or speculated radicals can be determined from

Chapter 3

the formation of the strongly absorbing ABTS radical. As an example, peroxy radicals of glycine and vaniline radicals have been known to be reactive toward the ABTS dianion to form the ABTS \cdot^- radical.²³¹ In a pulse radiolysis study, generation of the ABTS radical in aqueous solution involves scavenging of the primary radicals ($\cdot\text{OH}$) by azide ion (N_3^-) producing azidyl radical ($\text{N}_3\cdot$), which in turn generates ABTS radical, if present in the solution. This radical shows its absorption maxima at 415, 645 and 734 nm.²³² By following the decay of this radical at any of these wavelengths in the presence of known antioxidant such as vitamin C, one can form a standard curve. Looking at the change in the decay pattern in presence of an extract and determining the decay constant of the ABTS radical, it is trivial to fit the value in the standard curve and determine the antioxidant efficiency in terms of the ascorbate equivalent. However, problems arise when the substrate is not water-soluble. Mixing of a very low amount of these non-polar solvent extracts with aqueous solution obviously makes the whole system optically non-transparent and inappropriate for kinetic spectrophotometric analysis. Even for alcohol soluble substrates, it becomes difficult to test the radical scavenging efficacy because the alcohols scavenge primary radical ($\cdot\text{OH}$). In the present investigation, we intended to observe ABTS radical *via* the reaction of ABTS with the $\text{Br}_2\cdot^-$ radical in the first step. The ABTS radical formation and its transient absorption spectrum are shown in Fig.3.5. Similar to that in aqueous solution, it shows absorption maxima at 650 and 745 nm within 5 μs after the electron pulse. The radical is formed with a bimolecular rate constant of $1.18 \times 10^9 \text{ dm}^3 \text{ mol}^{-1} \text{ s}^{-1}$. Under such experimental conditions, it should be possible to study the ABTS radical scavenging process with the molecules soluble in solvents with

Chapter 3

wide polarity assortment. For instance, we have considered tocopherol (water insoluble) and ascorbate (water-soluble) as scavengers of this radical. Fig.3.6, panels A and B, show the decay of the ABTS radical at 645 nm in the presence and absence of different concentrations of ascorbate and tocopherol, respectively.

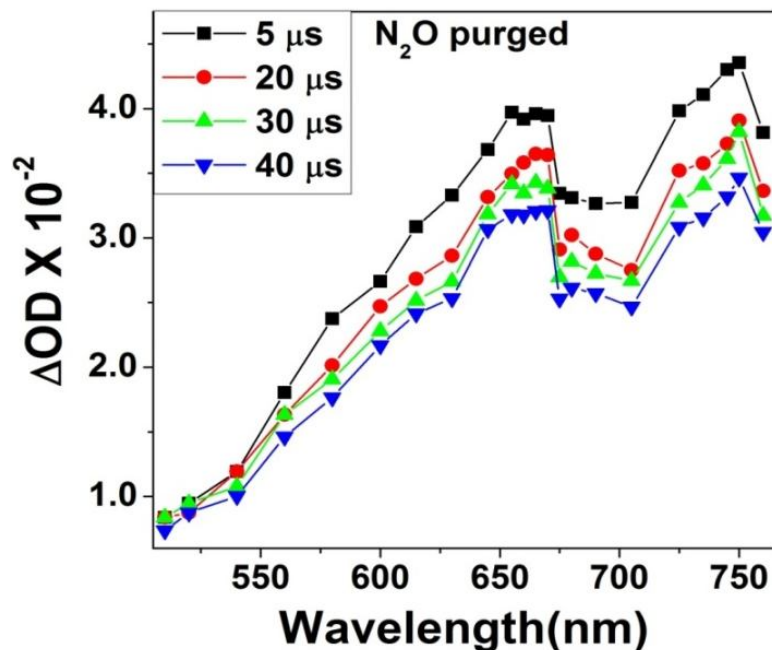


Fig.3.5. Transient absorption spectrum of the ABTS radical in N_2O -saturated CTAB/n-butanol/cyclohexane/water microemulsion ($W_0 = 40$) containing ABTS ($1 \times 10^{-3} \text{ mol dm}^{-3}$) at (a) 5, (b) 20, (c) 30, and (d) 40 μs after the electron pulse.

It is clearly seen that with an increase in the scavenger concentrations, the decay of the ABTS radical becomes faster. By plotting the decay constant versus concentration of ascorbate and tocopherol, we have determined the bimolecular rate constant for the reactions and also standard curves have been constructed (Fig.3.6). The bimolecular rate constants for the reaction of $ABTS^{\bullet-}$ radical with ascorbate and tocopherol are 1.6×10^7 and $4.6 \times 10^7 \text{ dm}^3 \text{ mol}^{-1} \text{ s}^{-1}$, respectively. The obvious reason for the higher reactivity of

Chapter 3

ascorbate compared to tocopherol is the location of these molecules in the microemulsion. Ascorbate being water-soluble, it resides in the water core, where the reacting radical is produced whereas, tocopherol may reside both in the oil phase as well as at the interface, the reaction of which involves diffusion of $ABTS^{\bullet-}$ radical to or through the interface.

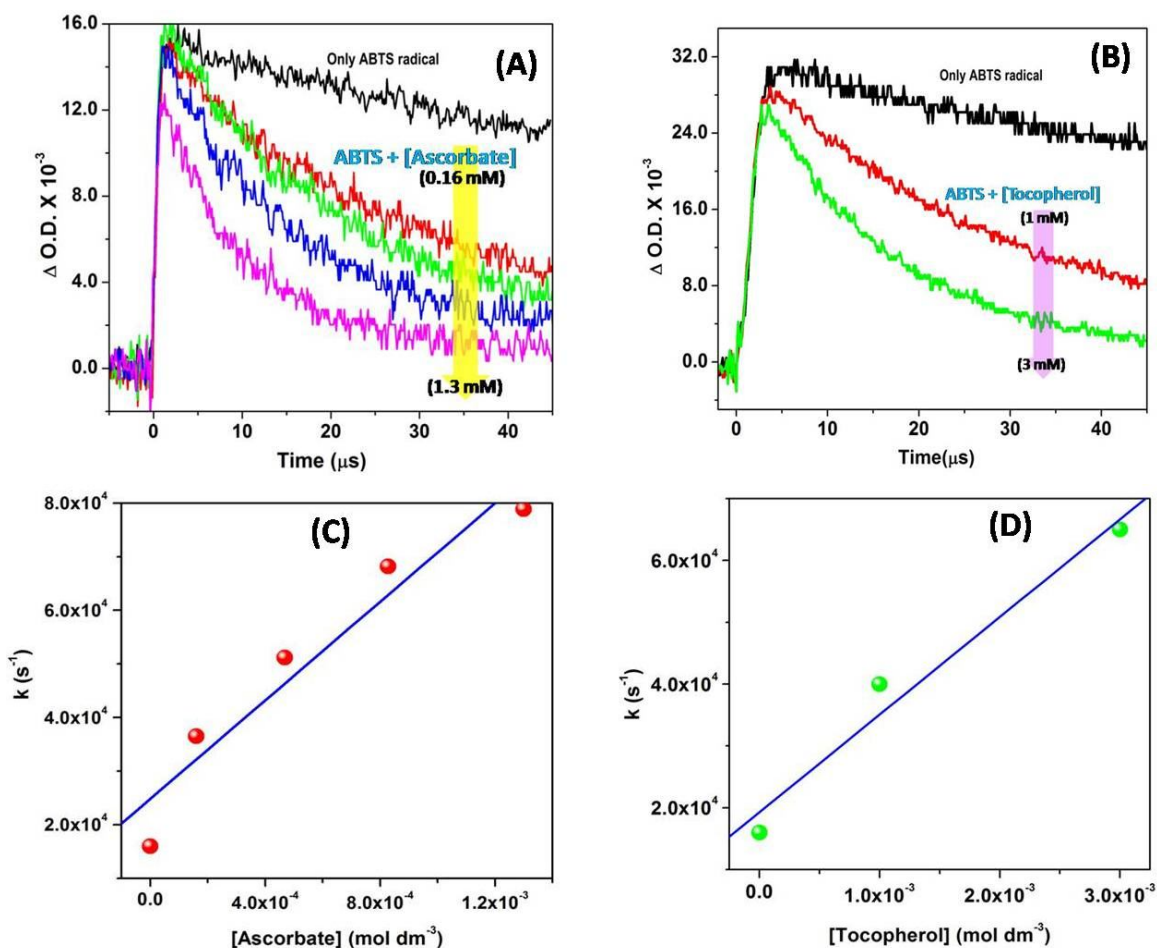


Fig.3.6. (A) Decay curve of ABTS radical in presence and absence of ascorbate. (B) Decay curve of ABTS radical in presence and absence of tocopherol. Plots of rate constant versus concentration of ascorbate (C) and tocopherol (D), respectively, for scavenging the ABTS radical.

Thus, it is demonstrated in this study that a two phase reaction can occur in the microemulsion without the use of phase transfer catalyst. It must be pointed out that the

Chapter 3

initial yield of the ABTS radical is dependent on the concentrations of ascorbate or tocopherol. With the increase in concentration of ascorbate or tocopherol, the probability of scavenging the primary and/secondary radicals ($\cdot\text{OH}$ and $\text{Br}_2\cdot^-$) progressively increases leading to a lower yield of ABTS radical.

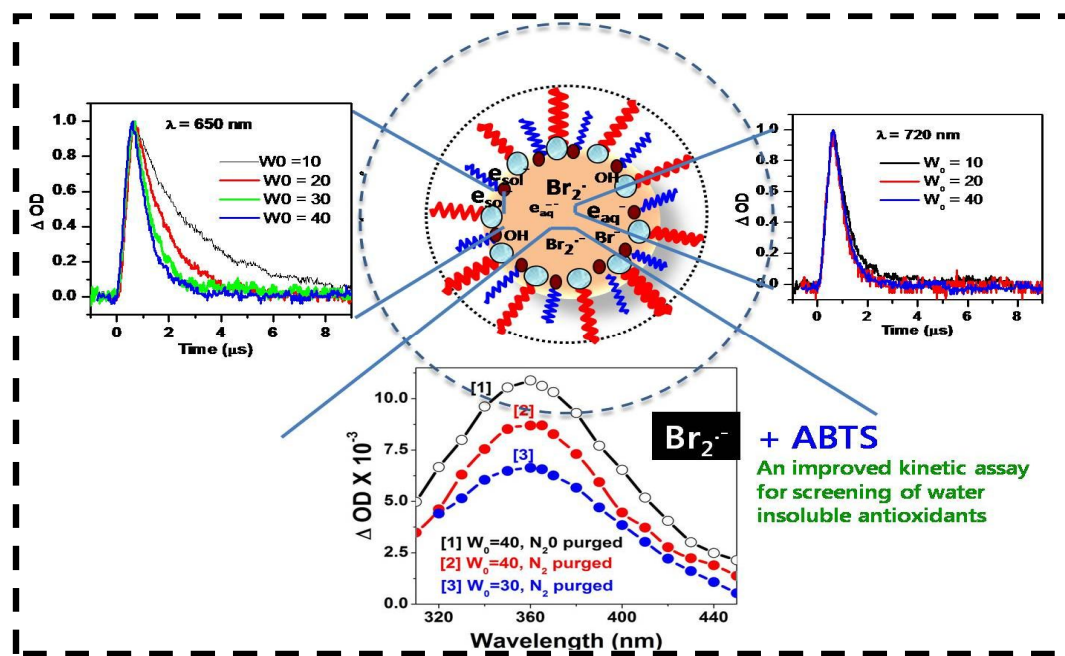
In the next step, by following the decay of the ABTS radical in presence of different concentrations (mg/ml) of extracts, it would be possible to obtain the vitamin E or C equivalent antioxidant capacity of any water-soluble/insoluble extracts or mixtures of compounds.

3.4. Conclusions

In summary, the hydrated electrons could be observed in a w/o CTAB/H₂O/n-butanol/cyclohexane microemulsion. The lifetime of the hydrated electron is shorter than that compared to aqueous solution as well as in an anionic microemulsion. The electrons are more stabilized at the interface as compared to that in the water core. The decay rate constant of the electrons solvated in the interface can provide information about the rigidity in that region. To the best of our knowledge, generation of the counter ion radical ($\text{Br}_2\cdot^-$) in both of the CTAB and CPB microemulsions have not been reported earlier in any of the pulse radiolysis studies. In addition, it has been demonstrated that two phase reaction occurring between radicals produced in the aqueous core and a molecule that is completely insoluble in water was possible. ABTS radicals were also generated in the water pool and its reaction with molecules soluble in either phase in the CTAB microemulsion could be observed. The spinoff of this result is a significant improvement in the established kinetic protocol involving the ABTS radical for free radical scavenging

Chapter 3

and antioxidant activity assay, which is now applicable to molecules soluble in solvents with a wide assortment of polarities. Scheme 3.1 illustrates the diagrammatic representation of the findings of this work.



Scheme 3.1. Diagrammatic representation of the findings.

Chapter 4

Templated synthesis of CdSe quantum dots in cationic and anionic surfactant based microemulsions: Tuning of photoluminescence and their morphology

4.1. Introduction

The application areas of microemulsions in the contemporary life have increased during the past decades.^{2, 5, 12, 13, 22} One such important area is the controlled synthesis of nanomaterials.^{5, 14, 22} There are a wide range of techniques based on physical^{147, 233, 234} and chemical methods,¹⁴⁸⁻¹⁶² which have been developed for the preparation of nanomaterials. Among all the chemical methods, the microemulsion based synthetic technique is one of the most versatile and reproducible one, that allows control over the size and yield of nanoparticles with a narrow size distribution.²³⁵ Essentially, the water droplets inside the microemulsion act as a nanoreactor and provide a suitable environment for controlled nucleation and growth. The size of the core of these media can also be controlled by changing the water to surfactant ratio i.e. W_0 values.

The synthesis of semiconductor nanoparticles and QDs has received extensive research interest in the recent years due to their morphology dependent optical and electronic properties.^{130, 236} Owing to these promising functions and properties, colloidal

Chapter 4

semiconductor nanocrystals have found numerous potential applications in optoelectronics,¹³⁵ catalysis,^{131, 149} sensing,¹³⁹⁻¹⁴¹ and bio-labeling.^{142, 144} As discussed in the introduction, CdSe, a group II–VI semiconductor, has medium band gap energy ($E_g = 1.75$ eV), thereby provide a sort of model system to study the effect of morphology and surface composition on the optoelectronic properties of similar compounds. This is one of the important aspects in the synthesis/growth of the semiconductor nanomaterials *vis-à-vis* their applications.

After acquainting with the CTAB w/o microemulsions, the same system (CTAB/1-butanol/water/cyclohexane) was employed as a reaction media for the synthesis of CdSe QDs *via* normal as well as radiation chemical route. It is to be mentioned here that significant number of reports²³⁷ are available in the literature regarding the synthesis of CdSe nanostructures in anionic surfactant (mainly AOT) based w/o microemulsions. On the contrary, there are very few studies on the application of CTAB microemulsions for the templated synthesis of CdSe nanoparticles. This part of the present thesis is focused on two main objectives. The first one was to probe the role of the intrinsic structural dynamics of CTAB microemulsions at various W_0 values in influencing the morphology and the associated photoluminescent behavior of the CdSe QDs. The second objective was to investigate the effect of the fundamental differences in the structural and dynamical aspects of the AOT and CTAB microemulsions in directing the morphology, and the photophysical behavior of the QDs. Furthermore, the inherent features of the employed techniques on the optical properties of CdSe nanoparticles were also examined.

Chapter 4

Based on these objectives, the work carried out in this part of the thesis has been divided and described under two sections i.e. (i) Normal and (ii) Radiation chemical routes for the controlled synthesis of CdSe QDs in the host matrices of the w/o microemulsions.

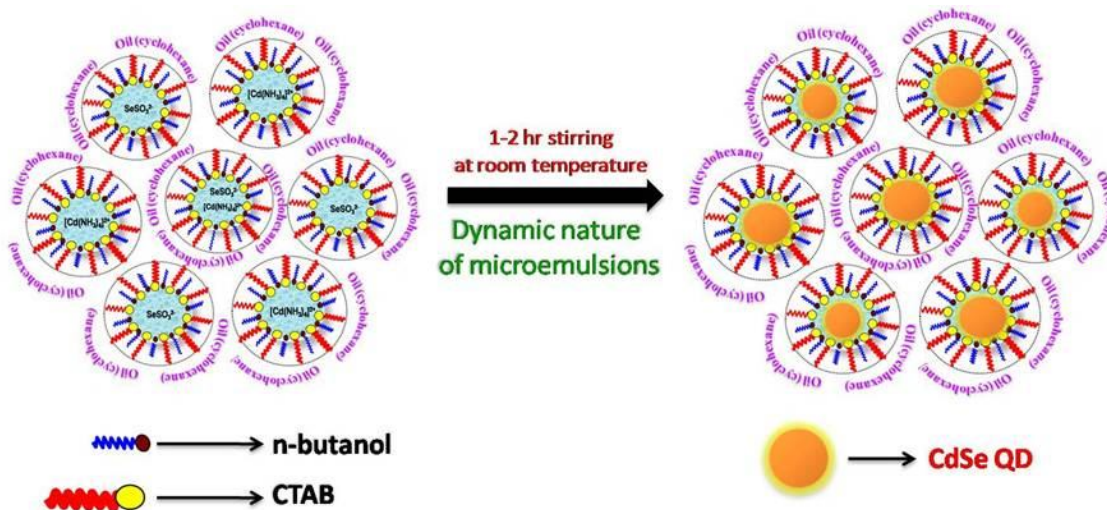
4.2. Normal chemical route for the synthesis of CdSe QDs in CTAB based quaternary w/o microemulsions

4.2.1. Materials and Methods

High purity chemicals, cyclohexane, n-butanol (spectroscopic grade), cadmium sulphate (CdSO_4), sodium sulphite (Na_2SO_3) and selenium (Se) powder were obtained from Sigma-Aldrich and used without any further purification. CTAB, was purchased from Sigma-Aldrich, was re-crystallized twice from ethanol.²¹ The stock solution of the Cadmium precursor i.e. ammoniated cadmium sulfate ($\text{Cd}[\text{NH}_3]\text{SO}_4$) with a concentration of 200 mM was prepared as follows.⁴⁰ 1.04 g of CdSO_4 was taken in a 25 ml flask and dissolved in 15 ml of nanopure water. Subsequently, 25 % ammonia solution was added to it with the appearance of a milky white color till the solution turned colorless and transparent. The total volume of the solution was made to 25 ml with nanopure water. This particular stock solution of Cd precursor was utilized to prepare different concentrations and can be called as solution A. The stock precursor solution for Se i.e. sodium selenosulphate (Na_2SeSO_3) was prepared by refluxing the solution containing 1g Se powder and 10 g Na_2SO_3 in 50 ml nanopure water at 70°C for 7 hours.⁴⁰ This solution can be called as B.

Chapter 4

After preparing the stock solutions of precursors (A & B) with different concentrations (50, 100 and 150 mM), the synthesis of the CdSe QDs was carried out by the following procedure. 0.1 M CTAB was added to cyclohexane and 1-butanol was added to this solution to achieve a 1-butanol/CTAB ratio of 5:1.²¹ Different volumes of aqueous solution containing equimolar precursors of Cd and Se i.e. solution A and B, respectively, were added to this system to obtain W_0 values of 20, 30 and 40. For example, preparing a 10 ml microemulsion of $W_0 = 20$, requires 360 μl of aqueous solution containing a mixture of solution A and B. Similarly, for preparing microemulsions (of 10 ml volume) with W_0 values of 30 and 40 requires aqueous solution of volume 540 and 720 μl , respectively. Subsequently, the as prepared microemulsions containing the precursor solutions inside the water pool were continuously stirred for about 1-2 hrs at room temperature. Since, microemulsions are dynamic in nature, inter-droplet collisions lead to the reaction between the precursors.^{235, 238} The colorless microemulsion transformed into greenish yellow or light orange color after stirring, depending on the experimental parameters, and this sol was used for further studies. Scheme 4.1 shows the diagrammatic representation of the synthesis of CdSe QDs inside the CTAB w/o microemulsions.



Scheme 4.1 Diagrammatic representation of the synthesis of CdSe QDs at room temperature inside the water pool of CTAB w/o microemulsion.

4.2.2. Results and Discussion

4.2.2.1. Growth of CdSe nanoparticles in microemulsion and TEM microscopy

The microemulsions ($W_0 = 30$) containing the precursor solutions turned greenish yellow color after stirring for about 2 hrs at room temperature. The camera-ready pictures of the sols prepared in microemulsions are shown in the Fig.4.1.

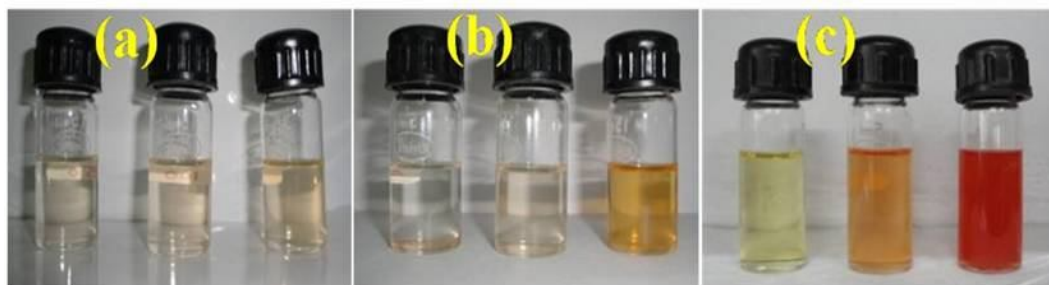


Fig.4.1. Camera-ready pictures of CdSe sols prepared in microemulsions with $W_0 = 30$ and [stock precursor] = 50, 100, 150 mM, **a)** after 2 hrs, **b)** after 24 hrs and **c)** after a week from the time of mixing of the individual precursor solutions.

Chapter 4

It was observed that the color of the sols were different for different concentration of precursors. It has been previously reported by our group that the mixture of the as employed precursors lead to the formation of CdSe.²³⁹ Nonetheless, it can be anticipated here that the CdSe nanoparticles would be formed inside the water pool of the microemulsions, as the precursors are in the aqueous phase.^{240, 241} The HRTEM images recorded from a freshly prepared CdSe nanoparticle sol in microemulsion of $W_0 = 20$ with [precursor] = 50 mM is shown in Fig.4.2a and b. The image in the inset of Fig.4.2b clearly shows the lattice fringes of CdSe nanoparticles, while the SAED pattern indicates their polycrystalline nature. Fig.4.2c shows the TEM image of CdSe nanoparticles sampled from the same sol after a time period of 1 week.

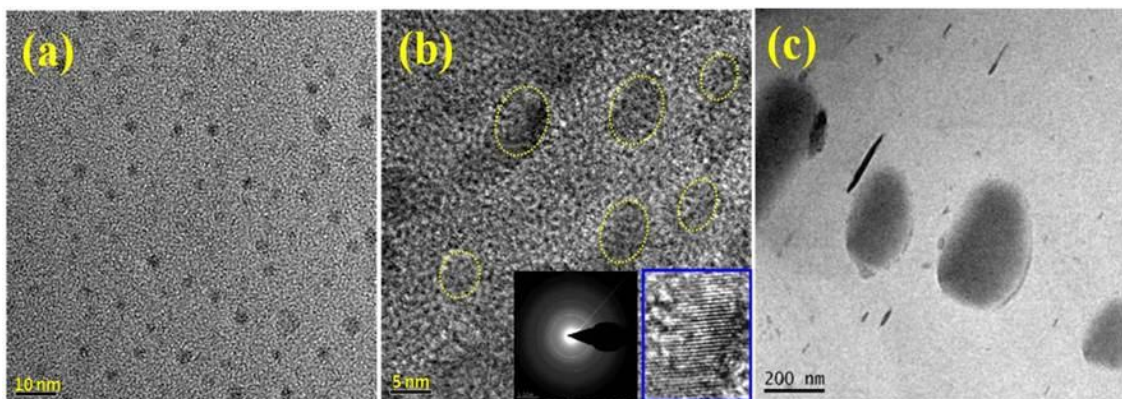


Fig.4.2. HRTEM images (a) and (b) of CdSe nanoparticles sampled from freshly prepared sol (microemulsion of $W_0 = 20$ and [stock precursor] = 50 mM) and TEM image (c) of nanoparticles sampled from the same sol after a time period of 1 week. Inset of image (b) depicts the SAED pattern and the lattice fringes of the nanoparticles.

It can be observed from the image Fig.4.2c that with aging, the CdSe QDs in the microemulsions exist in rather associated form instead of completely separated from each other, which could be due to the dynamic nature of the microemulsions.¹³

Chapter 4

4.2.2.2. UV-visible absorption spectroscopic study

The room temperature optical absorption spectra of the sols were recorded after 24 hrs of preparation and are shown in Fig.4.3.

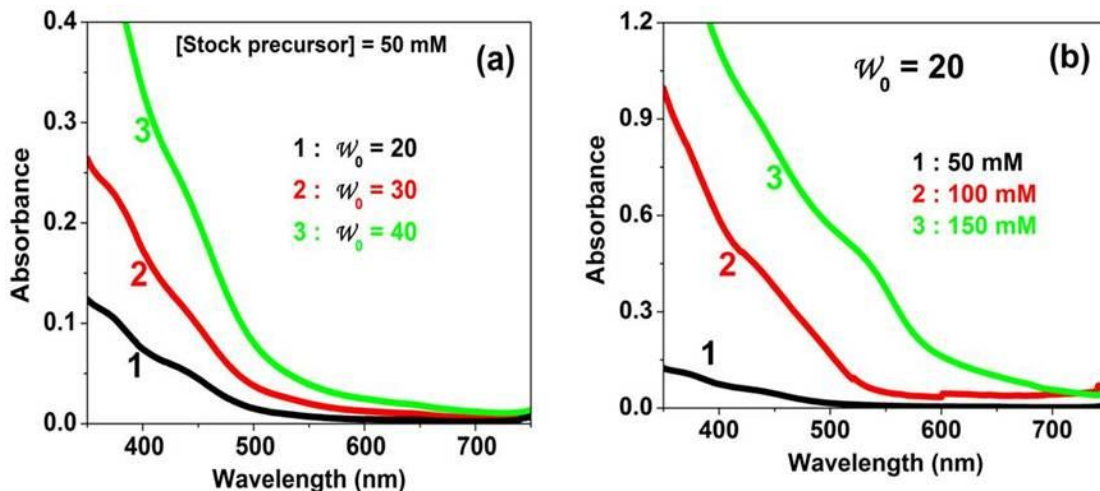


Fig.4.3. Optical absorption spectra of CdSe nanoparticles synthesized at RT (a) in microemulsions of $W_0 = 20, 30, 40$ and a fixed [stock precursor] = 50 mM; (b) in microemulsions of $W_0 = 20$ and [stock precursor] = 50, 100, 150 mM.

It is a well established fact that the dimensions of the water pools are directly proportional to the W_0 values.^{235, 238} Contrary to this, no significant shift in the excitonic peak position with the increase in the W_0 values of microemulsions for a fixed precursor concentration was observed (Fig.4.3a). However, a red shift can be noticed in the excitonic peak position with the increase in precursor concentration for a fixed W_0 value (Fig.4.3b). The band gap (E_g) values (listed in Table 4.1) were determined from the Tauc plot of $(\alpha' h\nu)^2$ vs. $h\nu$, as CdSe is a direct band gap semiconductor. The symbol ' α ' represents the term, ' αc ' where ' α ' is the absorption coefficient and ' c ' is the concentration of the CdSe QDs. The values of ' α ' were determined from the absorbance

Chapter 4

values, by using the relation, $\alpha c = (2.303A) / l$, where A is the absorbance value and 'l' is the optical path length (10 mm). The term 'hv' represents the photon energy. The average size of the nanoparticles was determined from these E_g values using equation (4.1), which is the representation of the modified effective mass approximation model, as proposed by Brus (discussed in the introduction).²⁴² Since, the excitonic peak is widely blue shifted from the bulk band gap value of CdSe (1.75 eV implies $\lambda = 714$ nm), which is an indication of strong confinement, the coulomb interaction between the electron and hole can be neglected.²⁴³ The average sizes of the primary nanoparticles estimated using modified Brus equation (4.1) have been listed in Table 4.1:

$$E_g = E_g(0) + \frac{\alpha}{d^2} \quad [4.1]$$

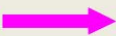
where, $\alpha = 3.7$ eV nm², $E_g(0) = 1.75$ eV, d = particle size (nm) and E_g = band gap value in eV. It can be seen that the size of initially formed CdSe nanoparticles are 2 to 3 nm in diameter within the water pool of the microemulsion. Furthermore, the variation of the size of the primary CdSe nanoparticles with the W_0 values is very less (Table 4.1).

However, contradictory results are present in the literature regarding the ability to control the particle size by varying the water pool size in CTAB microemulsions. Zhang *et al.*²⁴⁴ prepared nanoparticles of size ranging from 4 to 8 nm with increasing W_0 values from 5.01 to 24.45 thus, indicating that the w/o microemulsion droplet can be utilized as a nanoreactor to restrict the growth of nanoparticles. On the other hand, Agastiano *et al.*²⁴¹ and others²⁴⁵ have shown that the size of the nanoparticles seems to be poorly correlated with the aqueous droplet dimension (i.e. W_0 values) in the quaternary microemulsion. Moreover, the dynamic nature of the CTAB microemulsions and the inefficient capping

Chapter 4

by the surfactant are the probable reasons for the association of the nanoparticles with each other.¹³ The TEM images of the nanoparticles sampled from the freshly prepared sol (shown in Fig.4.2a & b) and that from a week old sol (shown in Fig.4.2c) clearly support the above statement.

Table 4.1 The band gap values (eV) and the size of the CdSe nanoparticles (nm) (shown in parentheses) synthesized at room temperature as determined from the optical absorption measurements.

W_0 	20	30	40
[precursor] (mM)			
50 	2.78 (1.8)	2.62 (2.0)	2.46 (2.2)
100	2.46 (2.2)	2.38 (2.3)	2.35 (2.4)
150	2.35 (2.4)	2.27 (2.5)	2.16 (2.8)

4.2.2.3. Photoluminescence (PL) study

4.2.2.3.1. Photo-excitation wavelength dependent photoluminescence

The steady-state PL spectra from the as prepared CdSe sols were recorded at room temperature. The excitation wavelength dependence PL spectra of one of the CdSe sols prepared in the microemulsion with $W_0 = 20$ and [stock precursor] = 100 mM, is shown in Fig.4.4. It can be seen that the nanoparticles exhibit two distinct PL bands, one with the peak position at 500 nm and the other with the peak position at 580 nm. The PL band with the peak at 500 nm gets converted to another band with the peak at 580 nm upon increasing the excitation wavelength from 380 to 480 nm, under identical conditions. This clearly indicates that with decrease in the excitation photon energy, the red shifted PL band dominates.

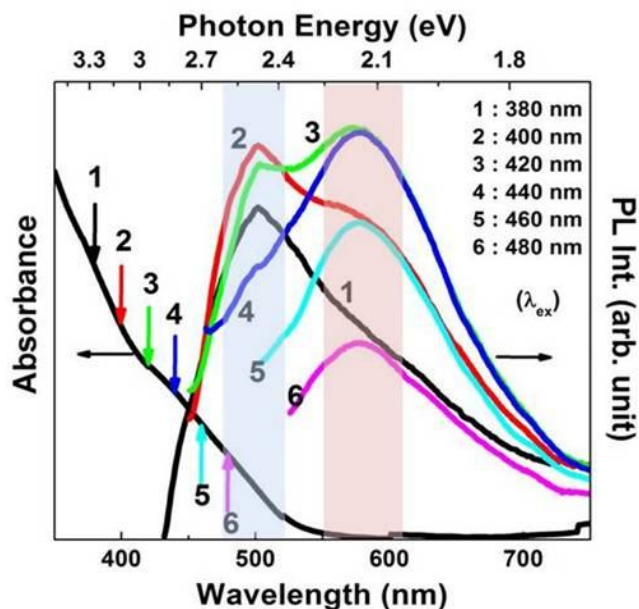
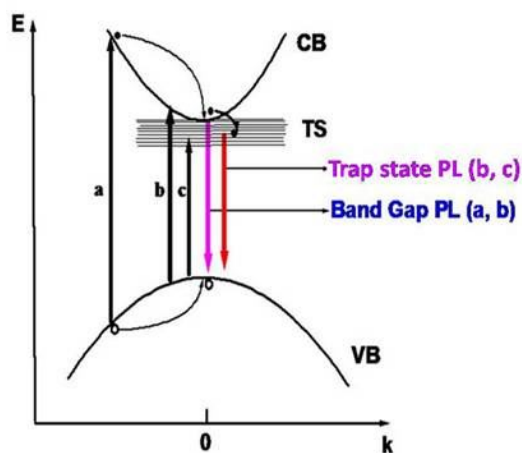


Fig.4.4. Excitation wavelength dependent PL spectra along with the absorption spectrum of CdSe nanoparticles synthesized in microemulsion with $W_0 = 20$ and [stock precursor] = 100 mM. The arrows at the absorption spectrum indicate the excitation wavelengths for the PL spectra.

The present observation could not be correlated to the size distribution of the CdSe nanoparticles, as the average size of the primary nanoparticles was about 3 nm without much variation (see Fig.4.2a). It is to be mentioned here that, this observation is quite different from the earlier study reported by Chandrasekharan *et al.*,^{237b} where the emission maximum shifts from 490 to 610 nm upon increasing the W_0 value of the AOT microemulsion with a drastic reduction in the emission intensity at 490 nm. The PL band with the peak at 500 nm was assigned to the band gap PL (BG-PL) due to its close proximity from the excitonic absorption peak. The PL band with the peak at 580 nm can be attributed to the trap state PL (TS-PL) due to the large Stokes shift between the exciton absorption and the PL peak position. Based on these observations, a model for the photo-

Chapter 4

excitation and the de-excitation processes occurring in these nanoparticles has been proposed, as shown in Scheme 4.2. When the energy of the excitation photon (**a**) is more than the band gap energy (E_g), then BG-PL dominates. When it is less than that of the E_g value i.e. (**c**), TS-PL predominates. However, for the excitation photon energy (**b**) close to the E_g value, both BG-PL as well as TS-PL appears with different proportions. Also, the overall PL intensity for this excitation photon energy was found to be higher.



Scheme 4.2: Diagrammatic representation of the photo-excitations and PL occurring in as synthesized CdSe nanoparticles in w/o CTAB microemulsions.

Thus, the tuning of the magnitude of either of the bands is possible in these nanoparticles. As it is shown in the Scheme 4.2, the BG-PL is obtained through the photo-excitation channels 'a' and 'b', whereas the TS-PL is obtained through the photo-excitation channels 'b' and 'c'. The PL quantum efficiency (PLQE) of the CdSe nanoparticles was determined by using the standard reference, quinine sulfate ($\Phi = 0.55$) dissolved in 0.5 M sulfuric acid and was found to be ~ 18 %.

Chapter 4

4.2.2.3.2. Precursor concentration dependent photoluminescence

The PL from the as synthesized CdSe nanoparticles in microemulsions with different W_0 values and precursors concentration was also recorded at room temperature. Fig.4.5 shows the PL spectra ($\lambda_{\text{ex}} = 420$ nm and normalized at the TS-PL peak position of 580 nm) measured from the CdSe sols synthesized in microemulsions with a fixed $W_0 = 20$ and different [stock precursor] = 50, 100 and 150 mM.

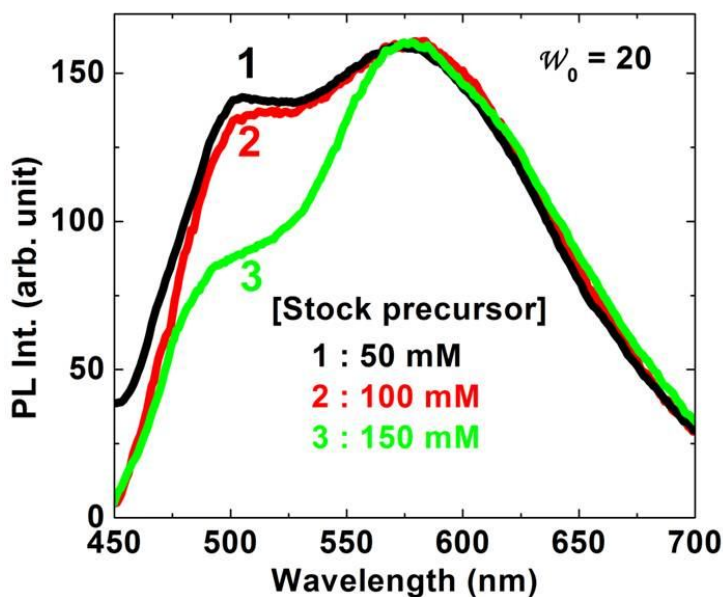


Fig.4.5. Room temperature PL spectra of CdSe nanoparticles synthesized in microemulsions with $W_0 = 20$ and [stock precursor] = 50, 100 and 150 mM normalized at the TS-PL peak position of 580 nm.

It was observed that the magnitude of the BG-PL band does not change much with increasing the concentration from 50 to 100 mM but at 150 mM, we can see a drastic decrease in the band gap emission peak (at 500 nm), while the magnitude of the TS-PL increases with the increase in the precursor concentrations. This variation in the intensities of band gap and trap state emission peaks with the increase in the precursor

Chapter 4

concentration could be attributed to the increase in the number of unsaturated selenium vacancies on the surface of CdSe nanoparticles. Although, equimolar precursors of cadmium and selenium were used, but due to the highly dynamic nature¹³ of microemulsions, it is possible that selenium rich surfaces reside on the CdSe nanoparticles, as here the capping agent is CTAB which is a cationic surfactant. Further support for this argument lies in the broad emission spectra (Fig.4.5), which usually originates due to the selenium vacancies.^{237b, 246} Thus, the magnitude of the PL bands could be tuned by controlling the concentration of the precursors used for the synthesis of nanoparticles.

4.2.2.3.3. Water pool size dependent photoluminescence

In another set of experiments, the CdSe sols were synthesized in microemulsions with different $W_0 = 20, 30$ and 40 and a fixed [stock precursor] = 50 mM. The PL spectra measured from these sols at room temperature with the excitation wavelength at 420 nm, normalized at the TS-PL peak position of 580 nm are shown in the Fig.4.6. It was observed that both the BG-PL and TS-PL bands were clearly visible in case of $W_0 = 20$. However, for the other two W_0 values, either of one is only prominent. BG-PL was more prominent for $W_0 = 30$ whereas, TS-PL was more predominant in case of $W_0 = 40$. The exact reason for this particular behavior is not clear.

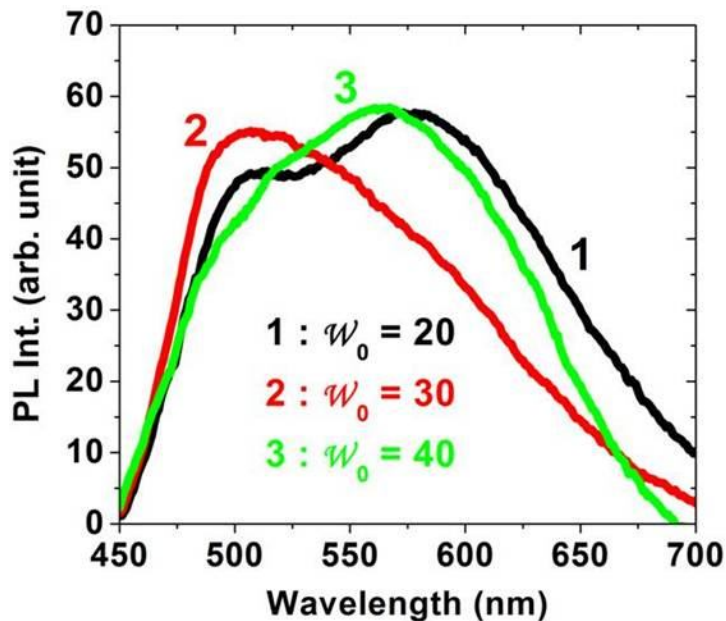


Fig.4.6. Room temperature PL spectra of CdSe nanoparticles synthesized in microemulsions with $W_0 = 20, 30, 40$ and [stock precursor] = 50 mM normalized at the TS-PL peak position of 580 nm.

However, as seen from Table 4.1, the size of the CdSe nanoparticles poorly correlates with the dimensions of the water pool (i.e. W_0 values) in CTAB microemulsions. Therefore, the observed trend in the PL properties of CdSe nanoparticles with the W_0 values could probably be attributed to the variation in the shape of the nanoparticles.^{236b, 247} It is well established that the shape of water droplets in the CTAB microemulsions turns from spherical to cylindrical at very low water content.^{237a, 248} Essentially, the hydrophilic groups of surfactant molecules reassemble in order to maximize their contact with water, resulting into the formation of cylindrical droplets. As the water content increases, the preference for the cylindrical shape decreases. This is due to an increased hydrophilicity in the system, which favors the presence of relatively smaller sized water droplets separately instead of staying together. Therefore, the shape of water droplets

Chapter 4

changes with the volume ratio of oil to water. Nevertheless, the same phenomenon has been envisaged during the synthesis of CdSe nanoparticles in CTAB based microemulsions *via* electron beam radiation, where the shape of nanoparticles changed from rods-to-cubes-to-spheres, on increasing the W_0 values from 10 to 40.⁴¹ Thus, the two PL peaks (Fig.4.6) exhibited by CdSe nanoparticles synthesized in the CTAB microemulsion with $W_0 = 20$ may be due to their anisotropic shape.

Cantele *et al.*²⁴⁹ on the basis of their calculation on semiconductor ellipsoidal QDs explained that the decrease in the degree of symmetry as well as the anisotropy effect can rupture the degeneracy leading to the splitting of the excited states of cylindrical or ellipsoidal shapes. In the present case, with the change in the W_0 value from 20 to 30, the BG-PL becomes more prominent. The most probable reason behind this could be the decrease in the shape anisotropy. The other contributing factor could be the better optimization of the parameters (such as water content and the surfactant-nanoparticles interactions) in terms of droplet shape and effective capping, which are resulting in predominantly band gap originated emission. While, in case of $W_0 = 40$, the TS-PL was found to be the major contributor in the emission spectra of nanoparticles (Fig.4.6). At such high W_0 values, the interfacial film rigidity decreases and so, the intermicellar collisions would be more in that case, resulting in higher mass transfer between the droplets. At this stage, it can be anticipated that the surfactant may not be able to effectively cap the nanoparticles thereby, leading to the enhancement in the trap states as well as increase in the size polydispersity of the nanoparticles. Hence, the combination of these factors could be assigned for the broad emission observed for nanoparticles

Chapter 4

synthesized in microemulsion with $W_0 = 40$. Similar observations were obtained for the other concentrations of the precursors.

4.3. Radiation chemical route for the synthesis of CdSe QDs in microemulsions: A rapid and one step templated approach

In this methodology, CdSe QDs were synthesized inside the water pool of AOT based w/o microemulsions *via* electron beam irradiation technique (high dose rate). This hybrid approach possesses inherent advantageous features of radiation induced technique (discussed in Chapter-1) and is relatively new for the controlled synthesis of semiconductor nanomaterials. The interplay of different experimental parameters such as precursor concentration, absorbed dose and W_0 values of microemulsions were found to have interesting consequences on the morphology, PL, surface composition and carrier recombination dynamics of as grown QDs. Besides, the fundamental roles of the chemical nature of water pool and the interfacial fluidity of AOT microemulsions in influencing the photophysical properties of QDs were investigated by carrying out the similar study in CTAB based microemulsions.

4.3.1. Materials and Methods

AOT was obtained from Sigma-Aldrich. Other chemicals used were same as in the first part and are described in section 4.2.1. The precursors employed for the synthesis of CdSe QDs are same in the present methodology as employed in the earlier one i.e. $\text{Cd}[\text{NH}_3]\text{SO}_4$ and Na_2SeSO_3 . However, the procedure for the preparation of their stock solutions in this particular case is slightly different in the sense that *tert*-butanol (1 M) was added to the precursor solutions of cadmium (labeled as solution A) and selenium

Chapter 4

(labeled as solution B). The purpose of adding *tert*-butanol was to scavenge the OH[•] radicals generated in the water pool of the microemulsion during the irradiation of the sample solutions. For preparing the microemulsion, 0.1 M AOT was added to hexane followed by the addition of aqueous solutions containing equimolar precursors of Cd and Se i.e. Solution A and B, respectively. Different volumes of required aqueous solutions were added to this system to obtain microemulsions with various W_0 values. The procedure for preparing CTAB based microemulsions have been explained earlier in section 4.2.1.

Various experimental parameters such as precursor concentration effect, W_0 value of the microemulsions (AOT and CTAB) and radiation dose were varied and their effect on the morphology and the photophysical properties of the as synthesized QDs were investigated. The microemulsions containing the precursors were freshly prepared and de-aerated by purging with N₂ just before the electron beam irradiation (7 MeV, FWHM = 2 μs, from LINAC) in each case. The absorbed dose per pulse was kept at 140 Gy and the samples were irradiated with repetitive electron pulses at 12 Hz.

The colorless microemulsion solutions immediately transformed into light green/or orange color after the irradiation, depending on the experimental parameters, which indicated the formation of CdSe QDs and this sol was used for carrying out the optical studies. It is to be noted that the microemulsions are highly complex and dynamic systems, so all the optical measurements reported herein were carried out after 15 minutes and within 1-2 hours of the irradiation to facilitate better consistency and reliability in the results of various set of experiments. For carrying out other characterization studies (i.e.

Chapter 4

SEM, XRD), the QDs were extracted from the microemulsion by breaking its structure on adding 5-10 drops of ethanol. Subsequently, the solution became turbid and was centrifuged to 9000 rpm. The precipitates were collected and washed for at least 3 times with nanopure water and ethanol.

4.3.2. Results and Discussion

4.3.2.1. Characterization and formation mechanism

Fig.4.7A shows the typical XRD patterns of as synthesized CdSe QDs (in AOT microemulsions), immediately and at a time interval of 24 hours after electron beam irradiation. The spectrum recorded immediately after the irradiation shows a broad and noisy spectrum, which makes it difficult to identify the phase of the QDs. However, diffraction peaks consistent with the hexagonal structure (JCPDS file no. 08-0459) of CdSe could be seen in the XRD spectrum recorded at time duration of 24 hours after the irradiation. The lattice planes corresponding to the respective peaks have been marked in the spectrum.

HRTEM image showing the lattice fringes of as grown QDs have been shown in Fig.4.7B. The interplanar distance was found to be 0.25 nm, which matches well with the standard value of the interplanar distance of 0.255 nm for (102) plane of the hexagonal phase of CdSe. Furthermore, the appearance of rings in the SAED pattern (inset of image B) clearly indicates the polycrystalline nature of the as grown QDs.

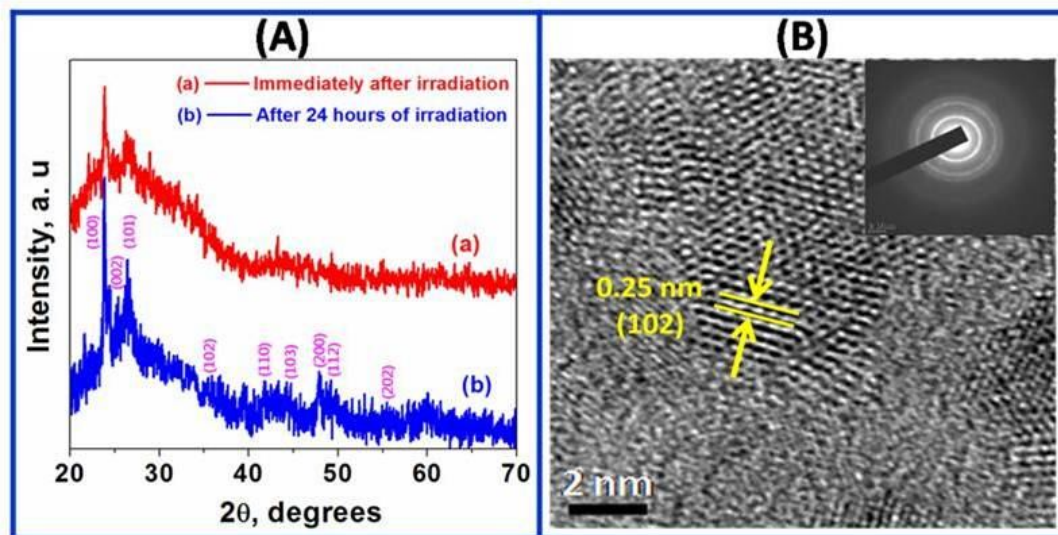
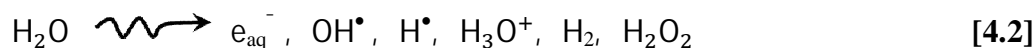


Fig.4.7. (A) XRD patterns of CdSe QDs (synthesized in AOT microemulsions) immediately (a) and 24 hours (b) after the irradiation; (B) HRTEM image of the QDs showing the lattice fringe pattern with the interplanar distance of 0.25 nm. Inset of image (B) depicts the SAED pattern of the corresponding QDs.

The plausible mechanism for the formation of the QDs in the host matrix of AOT microemulsions has been discussed as follows. The water pool of the microemulsion acts as a nanoreactor, comprising of Cd and Se precursors. It is to be noted that the formation of CdSe QDs took place only when the microemulsions containing the precursors were irradiated with the electron beam. Essentially, radiation-induced synthesis of nanomaterials in the aqueous phase is mainly preceded by the radiolysis of water.³⁻⁵ It is well known that the radiolysis of water generates three major primary radical species such as e_{aq}^- (aquated electron), OH^\bullet and H^\bullet . Amongst these, e_{aq}^- and H^\bullet are reducing, while OH^\bullet is oxidizing in nature. Since, the H^\bullet and OH^\bullet are scavenged by adding *tert*-butanol ($CH_3(CH_3)_2COH$) to the aqueous phase therefore, the e_{aq}^- with a high redox potential ($E_{red} = -2.9$ V) reduces the precursor ions thereby, resulting in the formation of nanoparticles.

Chapter 4

The radiolytic synthesis of CdSe nanoparticles in pure aqueous solutions has been previously reported by our group.⁵ The probable radiolytic reactions taking place during the formation of CdSe nanoparticles are mentioned below.



The radiolysis of oil phase (hexane in the present case) also generates electrons, which are scavenged by the water pool to form e_{aq}^- ²²⁻²⁴



Such reactions taking place in the water pool of the microemulsions eventually lead to the formation of CdSe nanoparticles. Subsequently, the microemulsion itself acts as a shell for stabilizing these nanoparticles.

4.3.2.2. Optical studies

A systematic set of experiments were carried to fix the optimum dose of irradiation for the synthesis and it was observed that an absorbed dose of ~ 25 kGy is sufficient for a complete transformation of precursor reactants into CdSe QDs. However, samples were irradiated with different absorbed doses to investigate its effect on the morphology and optical properties of the QDs.

4.3.2.2.1. Dose effect

While investigating the dose effect, the W_0 value of the microemulsions and the precursor concentration were kept constant at 10 and 20 mM, respectively and the imparted dose

Chapter 4

was varied from 10 to 50 kGy. Fig.4.8a shows the absorption spectra of the sols irradiated at different radiation doses. No absorption was observed in case of unirradiated sols in the region 400-700 nm, which rules out the formation of CdSe QDs, whereas appearance of excitonic peaks can be clearly seen in the absorption spectra of irradiated sols.

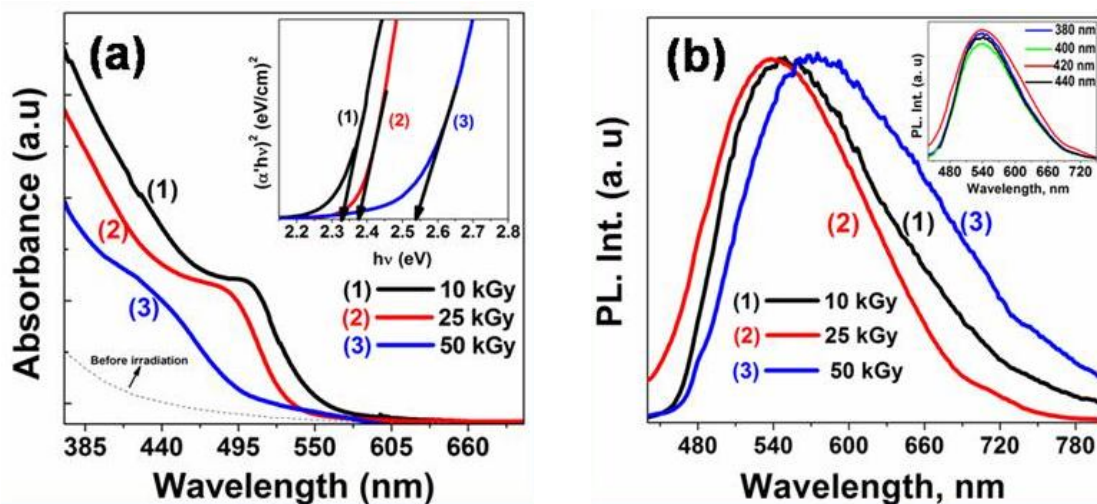


Fig.4.8. Absorption spectra (a) and Normalized room temperature PL spectra (b) of CdSe QDs synthesized in w/o AOT microemulsions via electron beam irradiation with variable absorbed doses at fixed precursor concentration (20 mM) and $W_0 = 10$. Inset of plot (a): Tauc plot for the determination of band gap values (E_g). Inset of plot (b): Plot showing the excitation wavelength independent PL spectra of CdSe QDs synthesized at an absorbed dose of 25 kGy.

The blue-shift in the excitonic peak with the increase in the absorbed dose indicates the decrease in the size of QDs. The band gap (E_g) values (listed in Table 4.2) were determined from the Tauc plot shown in the inset of Fig.4.8a. The average size of the QDs was estimated from these E_g values using equation (4.1). Essentially, the droplets of microemulsions are kinetically unstable and involve continuous inter-droplet collisions followed by the mass transfer/or exchange in between them.^{4d, 250} This dynamic exchange

Chapter 4

of material on one hand facilitates the growth process to take place after the nucleation stage induced by the electron beam irradiation; while on the other hand, it may lead to the changes in the particle size at different intervals of time. Nevertheless, the estimated sizes (listed in Table 4.2) unambiguously illustrates the trend in their sizes and band gap energy values, as all the measurements were carried out within the particular time frame (mentioned in the experimental section) to ensure the reproducibility and the reliability of the results. It can be clearly seen from Table 4.2 that the size of the QDs decreases with the increase in the absorbed dose. The observed trend can be explained on the basis that at higher absorbed doses, more number of nucleation centers are formed, which leads to the retardation of growth process. Similar results regarding the effect of dose on the size of the nanoparticles have been reported earlier by various researchers.^{251, 252}

The corresponding PL spectra of the CdSe QDs reflecting the effect of absorbed dose has been shown in Fig.4.8b. Interestingly, contrary to the absorption spectra, the as usual blue shift in the peak (with the decrease in the size of the QDs) is not emulated in the PL spectra. Although, there is a slight blue shift in the peak (see emission maxima values provided in Table 4.2) with increasing the absorbed dose from 10 to 25 kGy. But, there is a significant red shift in the peak position of the PL spectra on further increasing the dose to 50 kGy. This clearly indicates that the emission predominantly originates from the defects/trap states, as the surface states-assisted emission is independent (or has poor correlation) of the size of the QDs.²⁵³

Chapter 4

Table 4.2: Various measurements i.e. band gap values (E_g , eV), size (d , nm), FWHM (nm), emission maxima (λ_{max} , nm), QE (η , %) and average lifetime ($\langle \tau \rangle$, ns) values of CdSe QDs synthesized via electron beam irradiation with different combination of W_0 values, precursor concentrations and absorbed radiation dose.

S. No	Sample	Absorbed dose, kGy	Precursor conc., mM	Band gap value, E_g (eV)	Estimated size, nm	Emission maximum, λ_{max}	FWHM, nm	Quantum efficiency, η	Average lifetime, $\langle \tau \rangle$ ns
1	$W_0 = 5$, AOT ME	25	20	2.96	1.74	501	145	~ 9 %	44.1 ($\chi^2 = 1.1$)
2	$W_0 = 10$, AOT ME	10	20	2.32	2.52	548	122	~ 6 %	18.5 ($\chi^2 = 1.2$)
		25	10	2.48	2.23	535	126	-	-
		25	20	2.36	2.44	542	147	~ 8 %	37.7 ($\chi^2 = 1.1$)
		25	30	2.18	2.89	580	179	-	-
		50	20	2.54	2.15	569	169	~ 2 %	73.7 ($\chi^2 = 1.2$)
3	$W_0 = 15$, AOT ME	25	20	2.15	3.00	583	155	~ 4 %	25.6 ($\chi^2 = 1.1$)
4	$W_0 = 5$, CTAB ME	25	20	2.75	1.91	522	154	~ 0.2 %	2.7 ($\chi^2 = 1.3$)
5	$W_0 = 10$, CTAB ME	25	20	2.62	2.05	584	192	~ 0.8 %	6.8 ($\chi^2 = 1.2$)
6	$W_0 = 15$, CTAB ME	25	20	2.58	2.09	573	190	~ 1.1 %	8.2 ($\chi^2 = 1.1$)

Furthermore, it is to be noted here that the PL spectra is quite broad and extends from 450-800 nm region. The FWHM values were determined and have been listed in Table 4.2. In general, such broadening in the PL spectra of QDs can be rationalized by: (i) polydispersity in the size distribution²⁵⁴ or (ii) polydispersity in the density and the nature of distribution of trap/defect states leading to various recombination paths for the photogenerated carriers in the QDs.^{253b, 255} Even though, the contribution of the first factor

Chapter 4

cannot be completely ruled out, as grown CdSe QDs exhibits emission spectra with peak shifts independent of the excitation wavelength (shown in the inset of Fig.4.8b). Also, the polydispersity in this particular case was found to be only ~ 15 % (from TEM measurements, discussed later), which further suggests the major role of trap/defect states in the broadening of the PL spectra.

The quantum efficiencies (QEs) of the QDs synthesized with different absorbed doses were calculated and are listed in Table 4.2. As can be observed that the QDs synthesized with the optimum dose of 25 kGy exhibited highest QE of ~ 8 % followed by those synthesized with an absorbed dose of 10 kGy (~ 6%). This decline in the QE could be due to the insufficient amount of absorbed dose employed for the synthesis of QDs. Further, the least QE (~ 2 %) was obtained in case of QDs synthesized with the highest absorbed dose of 50 kGy. This could be due to the enhancement in the participation of non-radiative relaxation processes owing to the rise in density of the trap/defects of the QDs synthesized at higher absorbed doses. Therefore, it is imperative to optimize the absorbed dose for the synthesis of good quality nanomaterials.

The charge carrier dynamics of the QDs synthesized with different absorbed doses was investigated by measuring the time resolved PL decay using TCSPC at room temperature. The excitation and emission wavelengths were fixed at 374 and 550 nm, respectively. The PL decay curves of as synthesized QDs exhibited multi-exponential (tri-exponential) behavior (shown in Fig.4.9), which were analyzed and fitted using equation (4.7):

$$I(t) = a_1 e^{-t/\tau_1} + a_2 e^{-t/\tau_2} + a_3 e^{-t/\tau_3} \quad [4.7]$$

Chapter 4

where, $I(t)$ is the time-dependent emission intensity, 'a' is the amplitude, and ' τ ' is the lifetime. The average PL lifetime ($\langle\tau\rangle$) values were deduced using equation (4.8) and have been listed in Table 4.2. The corresponding χ^2 (represents the goodness of fit) values have been provided within the parentheses.

$$\langle \tau \rangle = \frac{\tau_1 a_1 + \tau_2 a_2 + \tau_3 a_3}{a_1 + a_2 + a_3} \quad [4.8]$$

Such multi-exponential behavior of the CdSe QDs is widely known and has been reported earlier.²⁵⁶ Although, most of these reports attribute such behavior to the diverse recombination paths owing to the varying degree of size, shape, surface defects/energy traps between the individual nanocrystals. However, the origin and the explanation for this multi-exponential behavior still remain unclear and is currently a subject of debate.

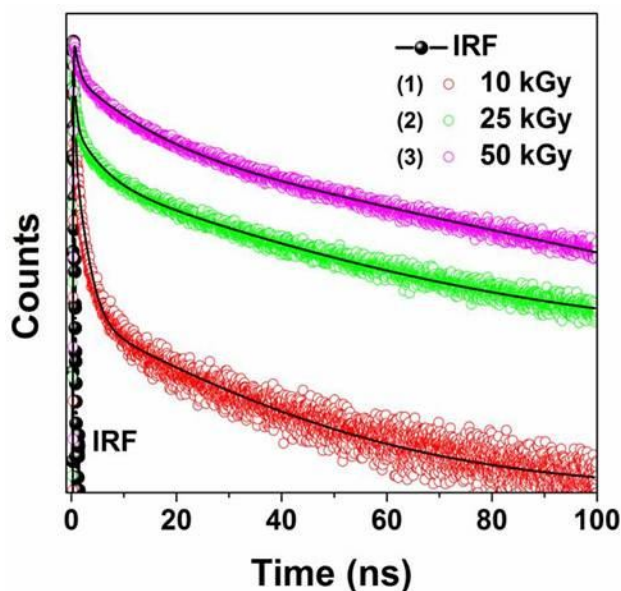


Fig.4.9. Emission decay curve ($\lambda_{ex} = 374 \text{ nm}$) along with the IRF and the best fitted curve for CdSe QDs synthesized via electron beam irradiation with variable absorbed doses at fixed precursor concentration (20 mM), and $W_0 = 10$.

Chapter 4

Nevertheless, the average lifetime values ($\langle\tau\rangle$) listed in Table 4.2 does provide an assessment about the excitonic dynamics and the nature of distribution of surface/trap states of as-grown CdSe QDs at various absorbed doses. The average lifetime representing the excitonic recombination increases with the enhancement in the radiation dose, which further substantiates the predominant contribution of trap/defect states in the photoluminescent behavior of the QDs (broadening of the PL spectra as well as the decline in the quantum efficiency) at higher absorbed doses. Indeed, this can be realized on deconvoluting the PL spectra of the QDs synthesized at different doses. Fig.4.10 shows the deconvoluted emission spectra at various doses. It can be noticed that at higher absorbed dose (25 kGy), the emission spectra in addition to the band gap emission (peak at 513 nm) comprises of contributions from defect/trap states. The nature of these trap states can be appraised from the appearance of peaks at 569 nm and 638 nm, which are widely shifted from the excitonic peak position and have been assigned to be originated from the shallow and deep trap states, respectively. Similarly, the broadening of the PL spectra obtained at dose of 50 kGy can be attributed to the principal contribution from the trap states.

These observations support the multi-exponential behavior of the QDs as well as the longer PL lifetime decay accompanied by the low quantum yields at higher absorbed doses. Nevertheless, it is being emphasized here that this aspect of the controlled induction of the surface/trap can contribute to the better understanding of the role of trapping sites on the dynamics of charge recombination processes, which eventually governs the efficiency of solar cell devices.^{256d}

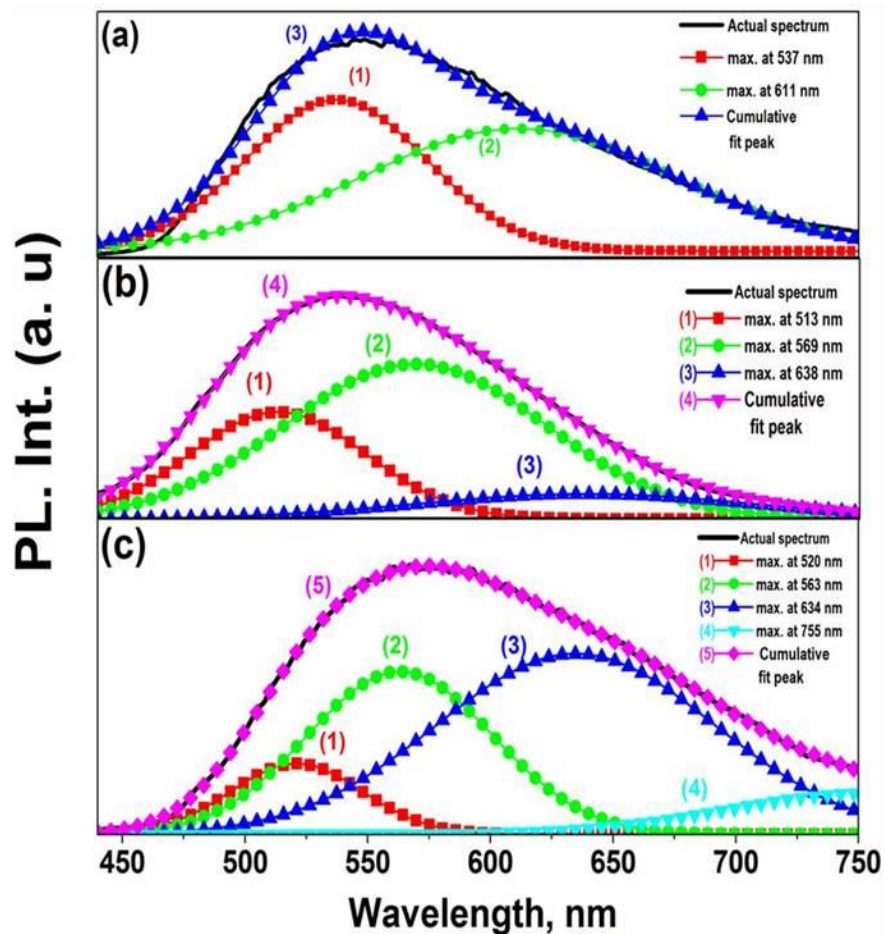


Fig.4.10. Deconvoluted PL spectra of CdSe QDs synthesized in w/o AOT microemulsions via electron beam irradiation with an absorbed dose of 10 (a), 25 (b) and 50 kGy (c) at fixed precursor concentration (20 mM) and $W_0 = 10$.

4.3.2.2.2. Concentration effect

Fig.4.11a shows the absorption spectra of irradiated sols with different precursor concentrations. The excitonic peak position red shifted with the increase in precursor concentration, which indicates an increase in the size of QDs.

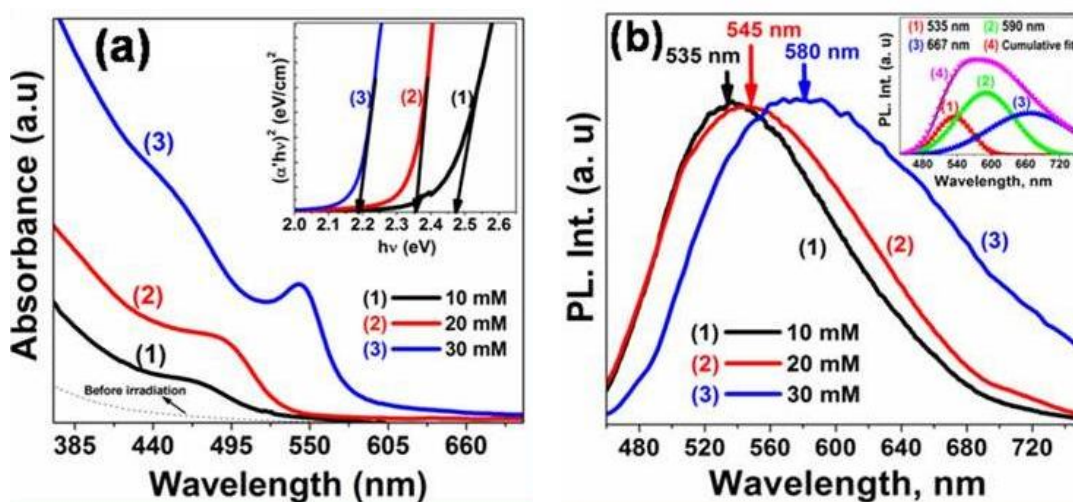


Fig.4.11. Absorption spectra (a) and Normalized room temperature PL spectra (b) of CdSe QDs synthesized in w/o AOT microemulsions via electron beam irradiation with variable precursor concentrations at fixed absorbed dose (25 kGy) and $W_0 = 10$. Inset of plot (a): Tauc plot for the determination of band gap values (E_g). Inset of plot (b): A representative de-convoluted PL spectrum of CdSe QDs synthesized in microemulsion of $W_0 = 10$ @ 25 kGy and precursor concentration = 30 mM.

The band gap (E_g) values were determined from the Tauc plot (inset of Fig.4.11a) and the average sizes (listed in Table 4.2) of the QDs were estimated by using equation (4.1). Similar type of experiment (precursor concentration was varied keeping other parameters constant) was performed in our earlier work⁴³ wherein the CdSe QDs were synthesized in CTAB based w/o microemulsions. It was found that the excitonic peak shift was nominal with an increase in the precursor concentration and the same was correspondingly reflected in the size values of the QDs. Such contrasting observations in the two cases (AOT and CTAB w/o microemulsions) could be explained on the basis of the interfacial rigidity/or fluidity. It has been mentioned earlier (in the introduction) that contrary to the AOT microemulsions, the CTAB microemulsions are more dynamic and flexible in

Chapter 4

nature, which lead to the distribution of the primary nanoparticles, thereby minimizing the effect of precursor concentration in the later case.

The PL spectra of the QDs demonstrating the effect of precursor concentration have been shown in Fig.4.11b. It could be seen that the PL peak position shifts to the red side with an increase in the precursor concentration, which is in agreement with the QDs size variation as was indicated by the absorption spectral studies. However, this increase in the average size of the QDs was also accompanied with higher FWHM values (listed in Table 4.2). The peak position was found to be independent of the excitation wavelength. Unlike other synthetic methodologies, large amount of energy is dumped within a small fraction of time in the electron beam irradiation technique (e.g. only a time duration of 15 seconds is required for imparting a dose of 25 kGy). Consequently, it could lead to the formation of large amount of nuclei instantaneously. The small nuclei at this juncture possess high surface energy (involving unsatisfied valencies/or dangling bonds and surface defects) and subsequently leading to aggregation followed by the growth process. Moreover, higher precursor concentrations would be accompanied by correspondingly higher amount of nucleation in the present scenario. Apparently, the growth process would lead to various amounts and types of defects including surface as well as deep trap states. This is indicated by deconvoluting the PL spectrum of QDs (synthesized by employing precursor concentration of 30 mM) shown in the inset of Fig.4.11b. The peak 1 (535 nm) represents band gap emission, while peaks 2 (590 nm) and 3 (667 nm) could be attributed due to the defects involving surface as well as deep trap states. Therefore, the broadening in the PL spectra (with increase in the precursor concentration) could be attributed to the

Chapter 4

differences in the density and distribution of trap states accompanied by a possible contribution from the polydispersity in the particle size.

4.3.2.2.3. W_0 effect

It is one of the most important parameters to characterize and manipulate the water pool size as well as the fluidity of the interface of microemulsions (as discussed in Chapter 1). Considering this, the W_0 values of the microemulsions were varied from 5 to 15, while keeping the precursor concentration and absorbed dose constant at 20 mM and 25 kGy, respectively. Fig.4.12a shows the absorption spectra of the irradiated sols representing the significant red shift in the excitonic peak position (of CdSe QDs) with the subsequent increase in the W_0 values of the AOT microemulsions. This indicates an increase in the average size of the QDs, which was determined by using the Brus equation (4.1).

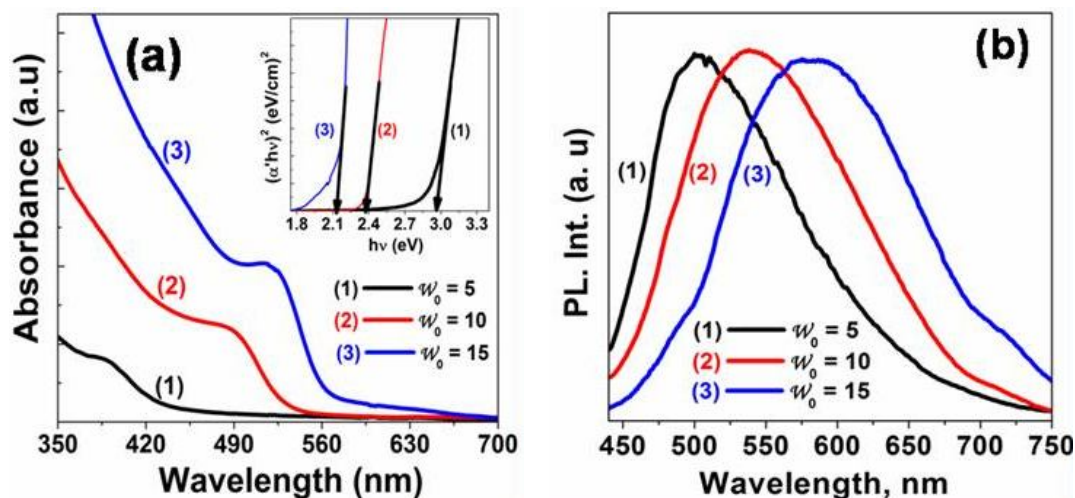


Fig.4.12. Absorption spectra (a) and Normalized PL spectra (b) of CdSe QDs synthesized in w/o AOT microemulsions via electron beam irradiation with variable W_0 values at fixed absorbed dose (25 kGy) and precursor concentration (20 mM). Inset of plot (a): Tauc plot for the determination of band gap values (E_g).

Chapter 4

The band gap (E_g) and the average size values of the QDs as determined are listed in Table 4.2. It is to be mentioned here that the QDs synthesized in microemulsion with $W_0 = 5$ were found to be ultrasmall (i.e. $d \sim 1.7$ nm). Moreover, the excitonic peak in this particular case appeared at ~ 400 nm, which is very close to the band-edge absorption peak (408 nm) of ultrasmall CdSe nanocrystals reported by Dukes *et al.*²⁵³ Generally, ultrasmall nanocrystals are defined as those which are having a diameter of less than 2 nm.^{253, 257} Such nanomaterials have recently become an active area of research as they own very interesting properties (that differ considerably from those of larger nanocrystals) such as quantized (sequential) growth,²⁵⁸ size-independent emission spectrum^{253, 257} and white light emission.²⁵⁹

In analogy with the absorption spectral measurements, the PL peak positions also red shifted with the subsequent variation in the W_0 values of the microemulsions (see Fig.4.12b). In fact, the observed tunability in the PL spectra can be realized from the periodic variation of ~ 40 nm in the maximum peak positions (listed in Table 4.2) with the step wise increase in the W_0 values from 5 to 15. This can be clearly visualized from the photos of the CdSe QDs taken in a UV chamber, as shown in Fig.4.13.

Indeed, the as displayed tunability in the photoluminescent behavior of these QDs clearly signifies their potential applications in light emitting devices (especially, white light emitting diodes i.e. WLEDs).

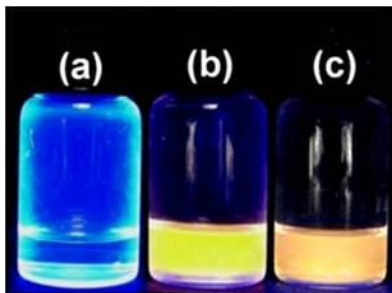


Fig.4.13. Camera ready picture of vials containing CdSe QDs synthesized in AOT microemulsions with variable W_0 values [$W_0 = 5$, Bluish-white color (a); $W_0 = 10$, greenish-yellow color (b); $W_0 = 15$, reddish-orange color (c)] via electron beam irradiation at fixed absorbed dose (25 kGy) and precursor concentration (20 mM).

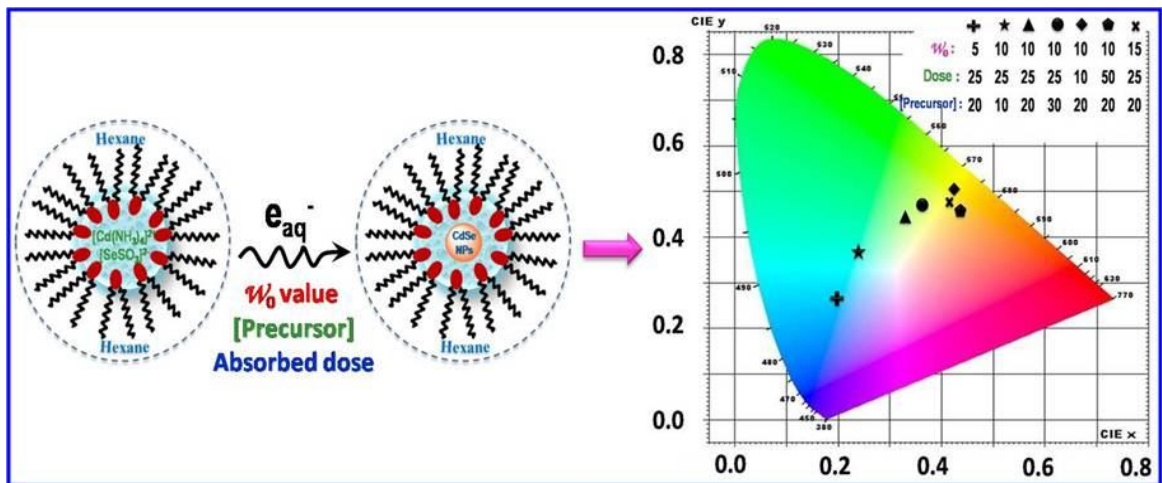
The nature of the light emitted by as grown QDs under various conditions has been listed in Table 4.3 along with their respective CIE (Commission Internationale d'Eclairage) x, y co-ordinates.

Table 4.3: CIE chromaticity co-ordinates along with the nature of the light emitted by CdSe QDs synthesized in AOT microemulsions via electron beam irradiation under various experimental conditions.

S. No	Sample	Absorbed dose, kGy	Precursor conc., mM	CIE x, y co-ordinates	Remarks
1	$W_0 = 5$, AOT ME	25	20	0.20, 0.27	Blue-white light
2	$W_0 = 10$, AOT ME	25	10	0.25, 0.38	Cyan light
		25	20	0.34, 0.44	Green-yellow light
		25	30	0.37, 0.46	Yellow-green light
		10	20	0.44, 0.49	Yellow-orange light
		50	20	0.43, 0.45	Orange-yellow light
3	$W_0 = 15$, AOT ME	25	20	0.42, 0.46	Yellow light

Chapter 4

The electron beam mediated synthesis of CdSe QDs has been represented in Scheme 4.3 along with the chromaticity diagram illustrating the optical tunability achieved by varying the different experimental parameters.



Scheme 4.3: Diagrammatic representation of the electron beam assisted synthesis of CdSe QDs in the host matrix of AOT microemulsions and the PL tunability displayed by the QDs as shown in the chromaticity diagram at various experimental conditions.

However, the QE of the QDs was found to decrease with the increase in the W_0 values, (see Table 4.2) and the highest QE of ~ 9 % was obtained for QDs synthesized in microemulsion with $W_0 = 5$, while it decreases to ~ 4 % in case of microemulsion with $W_0 = 15$. The polydispersity in size distribution was found to be ~ 12 % for $W_0 = 5$, which slightly increased to ~ 15 % and ~ 16 % for higher W_0 values of 10 and 15, respectively (size distribution plots shown in the inset of Fig.4.14). Thus, the main reason for the above decline in QE (with increase in the W_0 values) has been attributed to the increase in the number of trap/defects states.

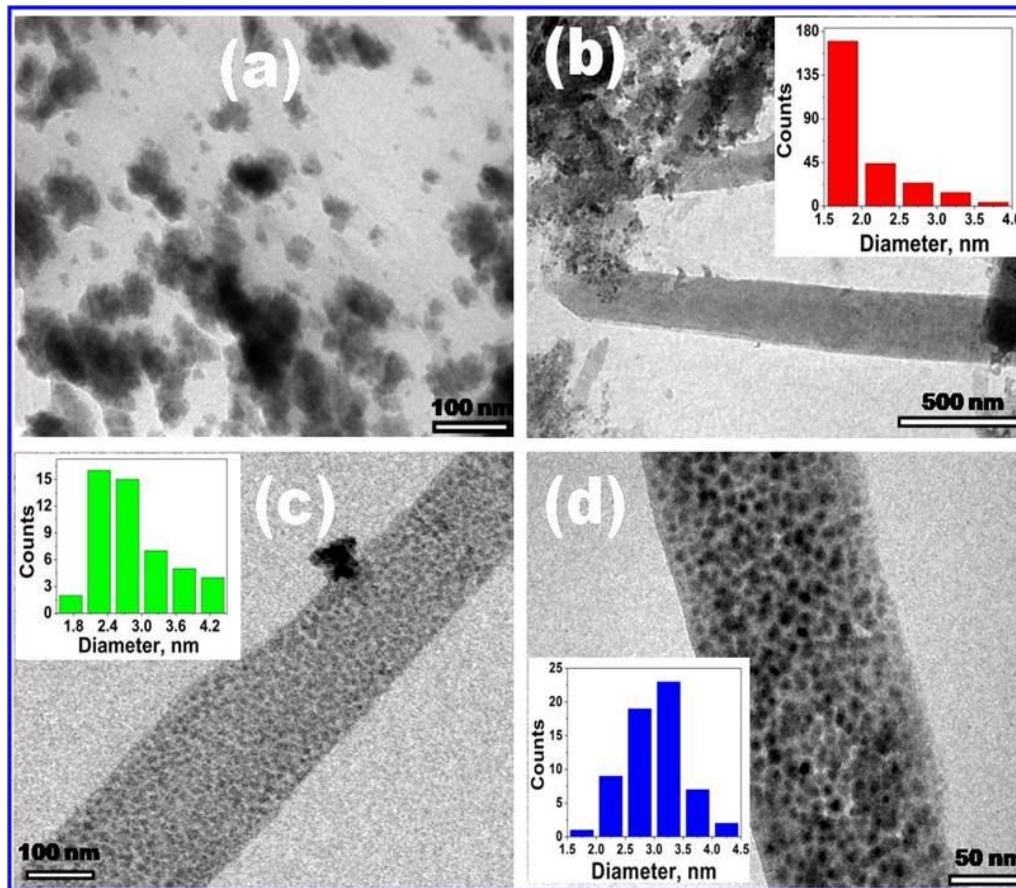


Fig.4.14. TEM images of CdSe QDs synthesized in AOT microemulsions with $W_0 = 5$ at different time intervals: immediately (a) and at time duration of ~ 12 hours (b) after irradiation. Images (c) and (d) represents CdSe QDs synthesized in AOT microemulsions with $W_0 = 10$ and 15 , respectively at time duration of ~ 12 hours, after irradiation. Inset in the images (b), (c) and (d) shows the corresponding size distribution plot of the nanoparticles at respective W_0 values of microemulsions. The other experimental parameters are: [precursor] = 20 mM, absorbed dose = 25 kGy.

In fact, the increase of defects (at higher W_0 values) comprising of energetically distributed trap states (i.e. shallow and deep) could be substantiated from the appearance of several peaks in the deconvoluted PL spectra (shown in Fig.4.15) at higher wavelength regions.

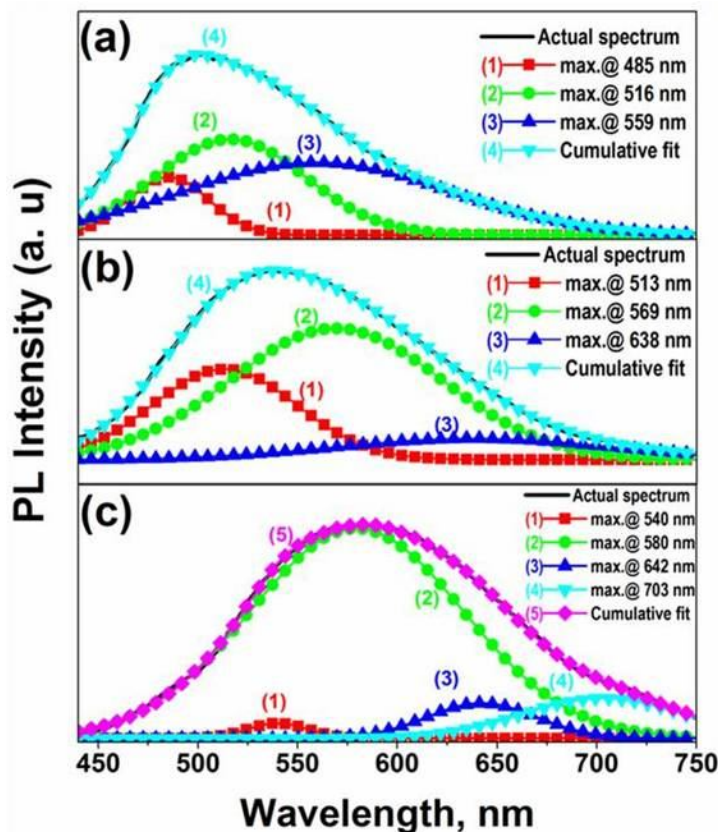


Fig.4.15. Deconvoluted PL spectra of CdSe QDs synthesized in w/o AOT microemulsions via electron beam irradiation with variable W_0 values i.e. 5 (a), 10 (b), 15 (c) at fixed precursor concentration of 20 mM and absorbed dose of 25 kGy.

Basically, at higher W_0 values, the rigidity of the interface decreases, thereby resulting into the increased inter-droplet exchange of material.^{4d, 250} Under such conditions, the augmented amount of trap/defects and the polydispersity in the size distribution of the QDs could be anticipated. This is further evidenced from the increasing trend of the FWHM values (obtained from the PL spectra and have been listed in Table 4.2) for the QDs synthesized in microemulsions with higher W_0 values.

However, contrary to the AOT microemulsions, the QDs size (as well as the photoluminescent properties) and the W_0 value was poorly correlated in case of CTAB

Chapter 4

based quaternary w/o microemulsions, as reported earlier.^{40, 43} Similar results were observed by Curri *et al.*²⁴⁵ and others²⁴¹ in which the size of semiconductor nanoparticles could not be correlated well with the aqueous droplet dimension (represented by the W_0 value) of quaternary microemulsions. Fig.4.16a clearly shows the marginal changes in the excitonic peak positions with the subsequent increase in the W_0 values (of CTAB microemulsions), especially above $W_0 = 5$. This can be further realized from the band gap energy values (determined from the Tauc plot, shown in the inset of Fig.4.16a) and the estimated average size (using equation 4.1) of the QDs listed in Table 4.2. Analogous to the absorption behavior, minor shift was observed in the peak positions of the PL spectra (shown in Fig.4.16b) with variation in the W_0 values of CTAB microemulsions. These observations clearly reflect the difference in the interfacial rigidities of the two microemulsion systems.

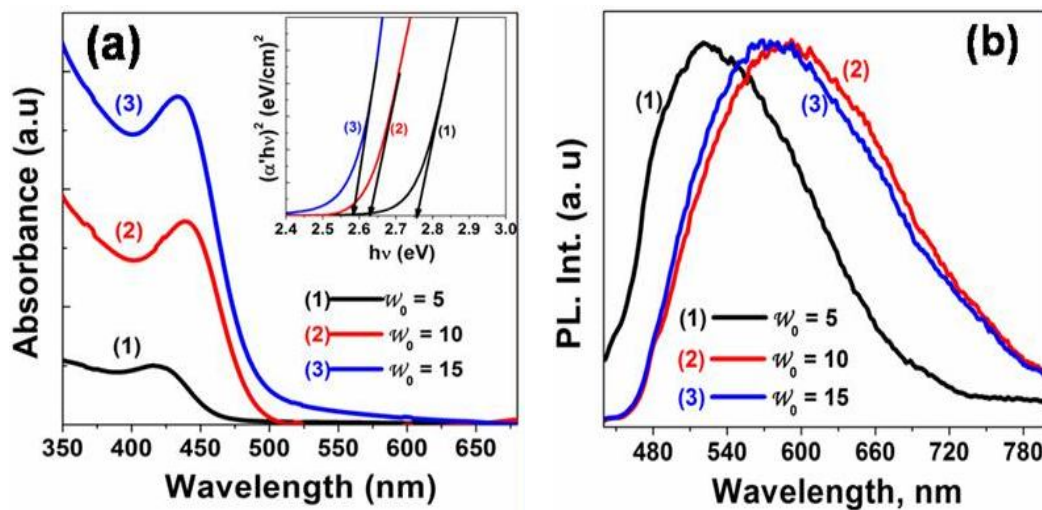


Fig.4.16. Absorption spectra (a) and Normalized PL spectra (b) of CdSe QDs synthesized in w/o CTAB microemulsions via electron beam irradiation with variable W_0 values at fixed absorbed dose (25 kGy) and precursor concentration (20 mM). Inset: Tauc plot for the determination of band gap values (E_g).

Chapter 4

On comparing the same W_0 values, the FWHM values (see Table 4.2) determined from the PL spectra of the QDs synthesized in CTAB microemulsions are higher than those in case of AOT microemulsions. Considering the negligible excitonic peak shifts with the increase in the W_0 values, the polydispersity in the size distribution cannot be the predominant factor behind the higher FWHM values (obtained in case of CTAB microemulsions), as has also been explained earlier.⁴³ However, polydispersity in the density and distribution of the trap/defect states in CdSe QDs synthesized in CTAB microemulsions might be assigned as the main rationale behind the broadening of the PL spectra. Keeping aside the case of $W_0 = 5$, the estimated average size of the QDs grown in CTAB microemulsions was found to be less than the average size of QDs synthesized in AOT microemulsions. Therefore, the amount of surface states would be more in the former case. Further, it was observed that after 24 hours, agglomeration of the QDs (synthesized *via* electron beam irradiation) takes place in CTAB microemulsions, thereby rendering them less stable. On the other hand, no such phenomenon was noticed in case of CdSe QDs grown in AOT microemulsions. One of the most striking differences between the QDs synthesized in CTAB and AOT microemulsions is their QEs. The QDs synthesized in the former case shows poor QE, as can be seen from Table 4.2. At this stage, it is important to point out the differences in the molecular structures of CTAB and AOT (shown in Chapter 1). The former one is linear and require a cosurfactant to form microemulsions, while later has a branched double-chained structure which facilitates molecules to pack together to form microemulsions without the involvement of any cosurfactant. Taking into account of QEs, it can be anticipated that the nanosized

Chapter 4

templating cages present in AOT microemulsions provide better encapsulation for the QDs as compared to those of CTAB based microemulsions. Furthermore, it is to be mentioned that unlike the case of AOT microemulsions, the QE of the QDs grown in CTAB microemulsions increases with increase in the W_0 values. This indicates towards the difference in compositions (or the chemical nature) of the water pool environments prevailing in the CTAB and the AOT microemulsions. In CTAB microemulsions, the bromide ion (Br^-) being the counter ion resides inside the water pool with high molar concentrations, thereby acting as a quencher.²¹ This is also regarded as heavy ion effect and results in lower quantum yields.^{1, 260} Therefore, the observed increase in the QEs of the QDs (synthesized in CTAB microemulsions) with the W_0 values could be explained from the fact that the concentration of bromide ions and their proximity from the QDs would be relatively lower at larger water pool sizes.

Apart from the quantum yields, the heavy atom halides (mostly bromide and iodide) have also been reported to shorten the lifetime of fluorophores.¹ Indeed, a very profound and contrasting influence was observed wherein the average lifetime values, $\langle\tau\rangle$ exhibited by the QDs synthesized in case of CTAB microemulsions were found to be at least 3 times lower (considering same W_0 values) as compared to those grown in AOT microemulsions. To the best of our knowledge, the contrasting influence of cationic and anionic surfactant based microemulsions on the PL lifetime of CdSe QDs has not been reported earlier. Fig.4.17 shows the emission decay curves ($\lambda_{\text{ex}} = 374 \text{ nm}$) for CdSe QDs synthesized in CTAB and AOT microemulsions with variable W_0 values at fixed precursor concentration (20 mM) and absorbed dose (25 kGy).

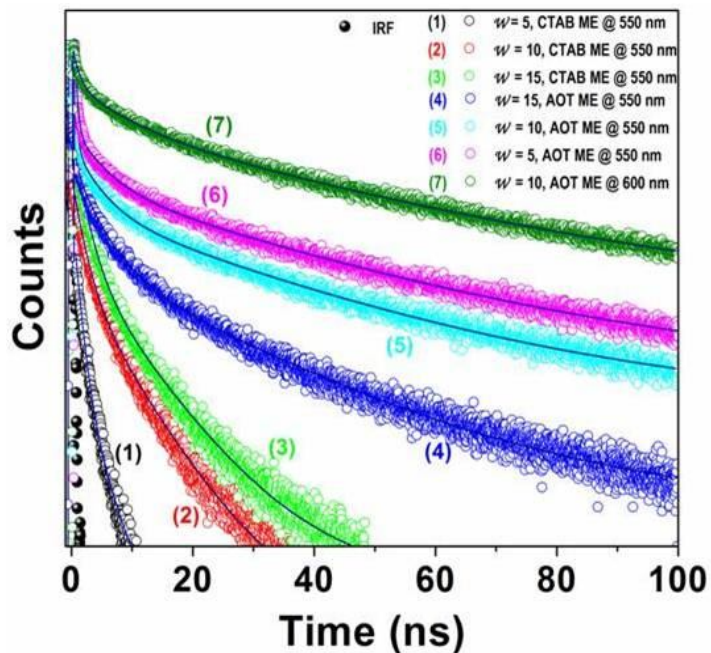


Fig.4.17. Emission decay curve ($\lambda_{ex} = 374$ nm) along with the IRF and the best fitted curve for CdSe QDs synthesized via electron beam irradiation in CTAB and AOT microemulsions with variable W_0 values at fixed precursor concentration (20 mM) and absorbed dose (25 kGy).

The PL decay curves exhibited multi-exponential behavior and were analyzed using equation (4.7). The average lifetime values ($\langle\tau\rangle$) have been listed in Table 4.2. A good correlation between the lifetime and the QE of the QDs was observed. CdSe QDs with high QEs synthesized in either of the microemulsions were found to have higher average PL lifetime values. The QDs synthesized in AOT microemulsions with $W_0 = 5$ had smallest size, highest QE and longest lifetime of 44.1 ns. Since, the QDs were ultrasmall and the presence of surface states can be realized from the deconvoluted PL spectrum shown in Fig.4.15a. Evidently, the long PL lifetime could be attributed to the surface state assisted recombination process of charge carriers.^{261, 262} However, QDs synthesized

Chapter 4

at higher W_0 values (of AOT microemulsions) exhibit lower QEs indicating the enhancement in the non-radiative relaxation processes, which further resulted in shorter PL lifetime (as compared to the case of AOT microemulsion with $W_0 = 5$). Apart from this, the PL decay trace recorded at 600 nm showed much slower PL decay ($\langle\tau\rangle = 74$ ns) as compared to that measured at 550 nm ($\langle\tau\rangle = 37.7$ ns). Evidently, this shows the higher contribution of surface states in the relaxation dynamics, since the band edge charge carrier recombination rate is faster than that taking place at surface states.^{261, 263} Nevertheless, the shortest PL lifetime, $\langle\tau\rangle = 2.7$ ns was observed in case of QDs grown in CTAB microemulsions with $W_0 = 5$. On increasing the W_0 values, the PL lifetime was found to increase (Fig.4.17) (see Table 4.2). Similar to the trends of QEs (for the QDs grown in CTAB microemulsions), the PL lifetime behavior can be explained primarily on the basis of the halide ion effect (discussed earlier).

Furthermore, as indicated from the absorption spectra, the variation in the W_0 values of AOT microemulsions was found to have substantial influence on the morphology of the CdSe QDs. TEM images recorded at later stages of the growth process revealed the formation of nanorods, as shown in Fig.4.18. The aspect ratio of the rods was determined and has been listed in Table 4.4. It is to be mentioned here that the values presented represents the average aspect ratio of many such rods examined during the TEM measurements. So, the nanorods shown in Fig.4.18 may appear to have different aspect ratios.

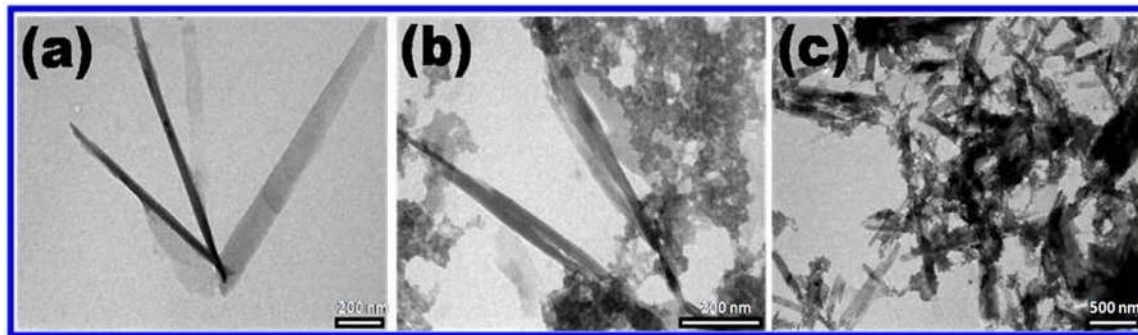


Fig.4.18. TEM images showing CdSe nanorods synthesized in AOT microemulsions with variable W_0 values of 5 (a); 10 (b); 15(c) via electron beam irradiation at fixed absorbed dose (25 kGy) and precursor concentration of 20mM. The images were taken at ~ 12 hours after irradiation of the sols.

Nonetheless, the aspect ratio of the nanorods decreases with the increase in the W_0 values of AOT microemulsions. The reason for this observation is probably the following. Microemulsions formed of ionic surfactants undergo structural transitions from *rod-to-sphere* as a function of water content and thus, the water pool size.^{14c, 15, 264} At lower W_0 values (generally for W_0 values ≤ 10), the amount of free water is negligible or very less, which enables the ionic surfactants to re-orient themselves into cylindrical or rod shapes in order to acquire maximum contact with the aqueous polar phase. While, cylindrical (or rod) to spherical shape transition takes place for higher W_0 values (generally for W_0 values ≥ 10) as the amount of free water in the water pool increases, which is further accompanied by the subsequent rise in the bulk water characteristics. Similar type of shape tuning from *rods-to-cubes-to-spheres* has been reported⁴⁰ by our group during the synthesis of CdSe QDs in CTAB based microemulsions on increasing the W_0 values (from 10 to 40).

Chapter 4

Table 4.4: Aspect ratio of CdSe nanorods grown in AOT microemulsions with variable W_0 values via electron beam irradiation at fixed absorbed dose (25 kGy) and stock precursor concentration of 20 mM.

S. No	AOT MEs	Aspect ratio
1	$W_0 = 5$	20 ± 2
2	$W_0 = 10$	13 ± 1
3	$W_0 = 15$	7 ± 1

Another interesting aspect is the initial formation of quasi-spherical QDs, which self-assemble into nanorods. This was evident from the TEM and SEM images of the QDs recorded at different time intervals. The TEM image shown in Fig.4.14a illustrates the formation of quasi-spherical shaped CdSe QDs (synthesized in AOT microemulsions with $W_0 = 5$; [precursor] = 20 mM@ 25 kGy) and was recorded immediately after the electron beam irradiation. The image shown in Fig.4.14b was recorded after ~ 12 hours of irradiation and represents the self-assembling of primary QDs into rod like anisotropic structures. Similar growth mechanism was observed in case of other W_0 values. Fig.4.19 shows the TEM images at different magnifications and regions of the grid demonstrating the self-assembling of CdSe QDs.

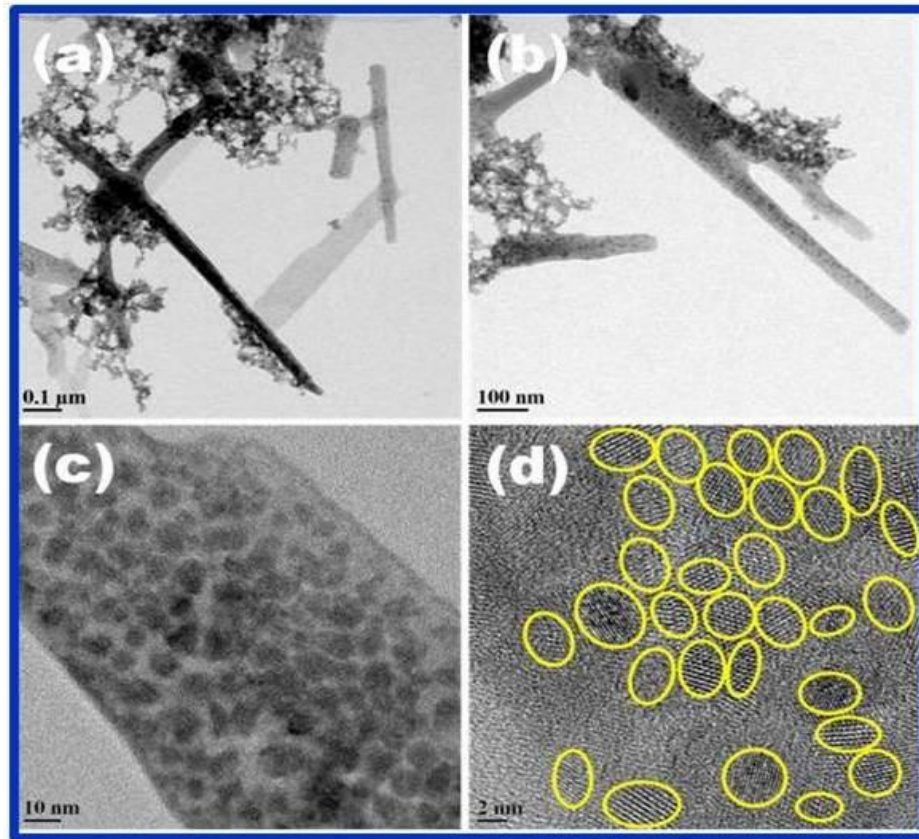


Fig.4.19. TEM images at different magnifications and regions of the grid showing the self-assembling of CdSe QDs (synthesized in AOT microemulsions with $W_0 = 10$, $[precursor] = 20 \text{ mM}$ @ 25 kGy) into rod shaped structures. The images were recorded at time intervals of ~ 6 hours after the electron beam irradiation.

Some more TEM images of nanorods comprising of CdSe QDs have been provided in Fig.4.14 c & d. Apart from these, SEM images shown in Fig.4.20 further confers the aforementioned transformation of quasi-spherical shaped (or globular shaped, image (a)) CdSe QDs into nanorod-like structures (image (b)).

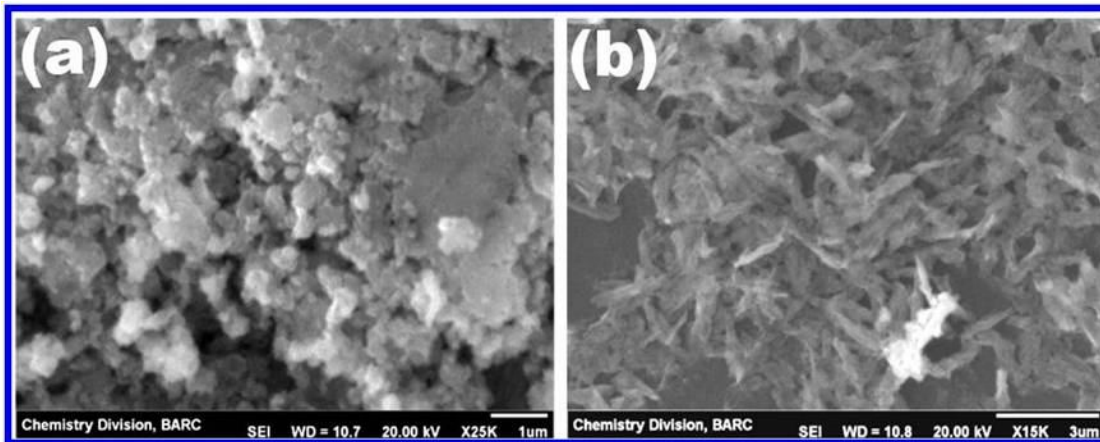


Fig.4.20. SEM images showing the transformation of globular shaped (a) CdSe nanoparticles (formed initially after the irradiation) into nanorod like structures (b). The experimental parameters are: $W_0 = 10$, [precursor] = 20 mM, absorbed dose = 25 kGy.

4.4. Conclusions

CdSe nanoparticles were synthesized in CTAB based quaternary w/o microemulsions under purely ambient conditions without any external reducing/stabilizing agents. It was observed that the water pool dimensions have poor correlation with the size of the as grown nanoparticles. However, photoluminescent properties of the nanoparticles were found to vary with the W_0 values of the CTAB microemulsions. This was attributed to the probable variation in the shape of the nanoparticles. The nanoparticles exhibited excitation wavelength dependent PL spectra and the ratio of BG-PL and the TS-PL could be tuned by varying the precursor concentrations and the W_0 values. On the contrary, the PL properties displayed by CdSe nanoparticles synthesized in CTAB based microemulsions *via* electron beam irradiation technique were predominantly originated from the trap states. A comparison between the two methodologies (i.e. normal and

Chapter 4

radiation chemical routes) for the synthesis of CdSe nanoparticles in CTAB microemulsions has been shown below.

NORMAL chemical route	RADIATION chemical route
1. Both BG-PL and TS-PL were observed	1. Predominantly TS-PL was observed
2. Excitation wavelength dependent PL spectra was obtained	2. Excitation wavelength independent PL spectra was obtained
3. Slower approach & requires 2-3 hours	3. Very fast; synthesis can be done in seconds

The comparative study conducted to investigate the influence of the structural and dynamical aspects of AOT and CTAB microemulsions on the morphology and photophysical properties of the CdSe QDs showed profound and contrasting results, as shown below.

CdSe QDs synthesis in CTAB microemulsions	CdSe QDs synthesis in AOT microemulsions
1. Poor correlation between the size of the QDs and the W_0 values	1. Good correlation between the size of the QDs and the W_0 values
2. Less stable and weakly photoluminescent; Maximum QE, $\eta \sim 1\%$	2. Relatively more stable and photoluminescent; Maximum QE, $\eta \sim 9\%$
3. Ultrasmall QDs (size < 2 nm) could be grown but difficult to stabilize due to agglomeration.	3. Blue light emitting ultrasmall QDs obtained and stabilized
4. Average PL lifetime less	4. Average PL lifetime values are relatively more

The interplay of different experimental parameters such as precursor concentration, absorbed dose, W_0 values and nature of the surfactant of the microemulsions facilitated the maneuvering of the morphology, PL, surface composition and carrier recombination

Chapter 4

dynamics of as grown CdSe QDs. Taking into account of the broad PL spectra, the as grown QDs may have potential applications in WLEDs, which can also be realized from their CIE x, y co-ordinates. Apart from this, the less reported fundamental role of the chemical nature of water pools (i.e. nature of surfactant and its counter ions) and the interfacial fluidity of microemulsions in influencing the photophysical properties of QDs has been illustrated in this chapter. These results emphasize the judicious selection of the host matrix (or the template) in the synthesis of QDs.

Chapter 5

Radiation stability of FAP (fluoro alkyl phosphate) based imidazolium room temperature ionic liquids: Influence of hydroxyl group functionalization of the cation

5.1. Introduction

Room temperature ionic liquids (RTILs) are a rapidly expanding family of condensed-phase media with important applications in synthesis, extraction, catalysis and electrochemistry.^{44a, 71, 265, 266} These liquids are also known as ‘designer solvents’, since by changing the cation-anion combination, it is possible to synthesize task-specific ILs for a multitude of applications. In the present context, ILs as solvents provide great opportunities for studying the kinetics of solvated as well as dry electrons, electron transfer reactions, and so on. As has been discussed in Chapter 1 that in the recent times, the RTILs have aroused much interest in nuclear fuel reprocessing.⁷⁴ Understanding the radiation stabilities of the ILs, and the underlying chemistry involved becomes the most important issue for their successful use in fuel reprocessing. Several radiation stability studies on ILs have already been reported. For example, Allen *et al.*⁷⁵ have primarily assessed the effects of α -, β - and γ -radiation on the hydrophilic RTILs such as [BMIM] NO₃, [EMIM] Cl and [HMIM] Cl. It was reported by these authors that even though ~1%

Chapter 5

of the samples undergo radiolytic degradation up to an exposure dose of 400 kGy, the ILs exhibit darkening in color with an increase of optical absorbance. Berthon and co-workers investigated the radiation stability of the hydrophobic imidazolium based ILs containing anions such as $[\text{PF}_6]^-$, $[\text{NTf}_2]^-$ and $[\text{N1444}]^+$ (where, $[\text{N1444}]^+$ is the methyl tributylammonium cation).^{76, 77} These authors proposed possible degradation schemes of the RTILs based on the NMR and ESI-MS analyses. Meanwhile, Qi *et al.* and Yuan *et al.* investigated the influence of γ -radiolysis on imidazolium based fluoroanions such as $[\text{PF}_6]^-$ and $[\text{BF}_4]^-$ using spectroscopic methods along with differential scanning calorimetry (DSC).⁷⁸⁻⁸⁰ Bartels *et al.*²⁶⁷ have determined the yields of hydrogen gas in the irradiated imidazolium, pyridinium and phosphonium based ILs. Very recently, Dhiman *et al.*²⁶⁸ have investigated the radiolytic production of molecular hydrogen in aromatic and aliphatic ILs irradiated with γ -rays, proton and helium ions to determine the functional dependence of the yield (of hydrogen) on particle track structure. The effect of commonly used anions i.e. NTf_2^- , Trifluoromethanesulfonate (TfO^-), PF_6^- and BF_4^- on the radiochemical stability of imidazolium based ILs under γ -irradiation was investigated by G. Le Rouzo and co-workers.⁸¹ Jagadeeswara Rao *et al.*⁸² had reported the influence of radiations on the rheometric and electrochemical properties of some halide and NTf_2^- based ILs. Yuan *et al.*^{83, 269} have shown the radiation induced darkening of IL $[\text{BMIM}][\text{NTf}_2]$ and subsequent decoloration on adding different oxidants. These authors have also employed the same IL (taking into account its high hydrophobicity) for extracting Sr^{2+} from the aqueous solution and further identified the radiolytic products of this particular IL.

Chapter 5

From all these aforesaid studies, it becomes evident that the imidazolium based ILs containing fluoroanions such as PF_6^- , BF_4^- and NTf_2^- are more stable than the corresponding halides, and also possess unique properties desired for the nuclear fuel reprocessing. However, ILs containing PF_6^- and BF_4^- , have been reported to decompose in the presence of water, giving off highly toxic and corrosive HF. Commonly used ILs containing $[\text{PF}_6]^-$ (hydrophobic) are hydrolytically unstable, especially at elevated temperature.^{85 a & b, 270} On the contrary, ILs with the bulky FAP anion are ultra hydrophobic.^{85a} Thus, these ILs also offer lower risk for accumulation in waterways or in the biosphere. Also, these ILs exhibit high electrochemical stability comparable with that of NTf_2^- and recently reported bis[bis(pentafluoroethyl)phosphinyl] imide anion (FPI) based ILs.^{85a, 270d} The electrochemical window for FAP ILs can span up to 7 V,^{85a} much higher than that of tetrafluoroborates. Having such unique properties, FAP based ILs are expected to provide an intriguing opportunity for their use in nuclear fuel reprocessing and in space technologies. However, for such applications, it is essential to examine the effect of radiations on their physicochemical properties. It is interesting to note that reports on radiation chemical studies of FAP based ILs are missing in the vast literature discussed already, dealing with different ILs.

In the present study, we have performed an assortment of characterization and qualitative studies to explore the radiation stabilities of FAP based ILs in the absorbed doses, ranging from 50 to 500 kGy. Pulse radiolysis experiments were carried out to determine the transient species and their kinetic behavior on radiolysis. [EMIM][FAP] was chosen as the representative member of this new class of ILs. Besides, we seek to

Chapter 5

atmosphere) to avoid any exposure of the ILs to the moisture. The impurities such as halides were less than 0.1%. It is also supported by the fact that the ILs were colorless and transparent. Other chemicals such as acetonitrile, ethanol, and acetone, used for carrying out various measurements were obtained from SDFCL, Mumbai, with highest purity. Nanopure water (conductivity, $0.06\mu\text{S cm}^{-1}$) was obtained from a Millipore water purifying system.

5.2.2. Instrumentation: The ILs were irradiated with a 7 MeV electron beam (FWHM $\sim 2 \mu\text{s}$) obtained from LINAC, in conjugation with pulse radiolysis system, as described in Chapter 2. The absorbed dose per pulse was kept at 160 Gy and the samples were irradiated with repeated pulses @ 50 pulses per second accounting for a cumulative dose ranging from 50 to 500 kGy. The electron pulse used for carrying out the pulse radiolysis experiments was 500 ns, while the dose per pulse was kept as 12 Gy. High purity ($>99.9\%$) N_2 was used for purging solutions as per requirement. The physicochemical measurements such as density, viscosity and refractive index of the samples were carried out at $25^\circ\text{C} \pm 0.5^\circ\text{C}$ and are described below with their respective instrumental specifications. The instruments employed for carrying out photophysical (i.e. UV-Vis absorption, fluorescence, PL lifetime) and vibrational studies (FTIR and Raman) have been described in Chapter 2.

5.2.2. a. Density measurement: Density of the ILs was measured with an Anton Paar DMA-5000M vibrating-tube densimeter.

5.2.2. b. Conductivity and Electrochemical studies: The conductivity measurement of the ILs was carried out with Con1500 Conductivity meter from Eutech Instruments.

Chapter 5

Cyclic voltammetric studies were conducted on an Autolab cyclic voltameter (Model 70909) employing a three-electrode system using glassy carbon electrode as the working electrode and a Pt wire auxiliary and quasi-reference with a scan rate of 50 mV/sec. The samples were purged with high purity N₂ gas for 10 minutes before measurements.

5.2.2. c. Refractive Index studies: RX-50000 Atago Refractometer was used for refractive index measurements. The apparatus was calibrated by measuring the refractive index of Millipore quality water ($n_D = 1.3330$).

5.2.2. d. Viscosity: Viscosity and Rheometric studies were carried out on Anton Paar Physica MCR 101 Rheometer with double gap measuring cylinder geometry. Stress-strain studies were carried out at four different temperatures ranging from 25 to 50°C. Shear rate was varied from 1 to 100 s⁻¹.

5.2.2. e. Thermo-gravimetric analysis: Thermal stability studies of the ILs were carried out on a Mettler Toledo (TG/DSC STAR^c) thermal analysis system. About 10-15 mg of the sample was weighed into alumina crucibles and measurements were taken in N₂ atmosphere (gas flow, 50 ml/min.), at a heating rate of 20°C/min., from 30 to 900°C.

5.2.2. f. pH measurements were carried out on a digital pH meter procured from LabIndia using Model pico. Instrument was well calibrated at pH 4.0, 7.0 and 9.0 using standard Buffer solutions.

5.2.2. g. Mass Spectrometric studies: The ESI (Electrospray ionization)-mass spectrometry (MS) measurements were carried out using model 410 Prostar Binary LC with 500 MS IT PDA Detectors of Varian Inc, USA. The mass spectrometry measurements were recorded both in positive and negative mode over a mass range of m/z

Chapter 5

from 50 to 1000. The nebulizing gas pressure (N_2) was set to 35 psi, while the flow rate of the nitrogen drying gas was set as 5 L min^{-1} . Needle voltage, Spray shield voltage, and Capillary voltage were 5000, 600 and 80 V, respectively, in positive mode (ESI⁺) and -5000, -600 and -80 V, respectively, in negative mode (ESI⁻). Spray chamber temperature was maintained at 50°C . Skimmer 1 voltage was set within the range 20–80 V while the skimmer 2 voltage was kept constant at 10 V. Samples were diluted to 10^4 times with acetonitrile and infused, using a syringe infusion pump (Cole Parmer) at a flow rate of $90 \mu\text{L h}^{-1}$. For MS_n experiments, helium was used as collision gas.

5.2.2. h. NMR studies: ^1H NMR spectra were recorded with a Bruker Ac-200 (200 MHz) instrument while ^{19}F NMR spectral studies were carried out with a Mercury Plus 300 MHz NMR spectrometer, Varian, USA. Samples were diluted with anhydrous DMSO (Dimethyl sulfoxide). The chemical shift scale was calibrated with DMSO (2.42 ppm) and trichloro-fluoro-methane, CFCl_3 (0 ppm) for ^1H and ^{19}F NMR, respectively. CFCl_3 was used as an external standard for ^{19}F NMR. The ^1H and ^{19}F NMR spectral features of the unirradiated FAP ILs are provided below.

(a) **[EMIM][FAP]**

^1H NMR (DMSO- d_6 , 200 MHz) δ [ppm]: 1.42 (t, $J = 7.4 \text{ Hz}$, 3H); 3.84 (s, 3H); 4.20 (q, $J = 7.4 \text{ Hz}$, 2H); 7.65 (s, 1H); 7.73 (s, 1H); 9.14 (s, 1H)

^{19}F NMR (DMSO- d_6 , 300 MHz) δ [ppm]: -43.0 (dm, PF); -80.14 (m, CF_3); -81.72 (m, 2CF_3); -86.0 (dm, PF_2); -115.84 (dm, CF_2); -116.32 (dm, 2CF_2); $^1J_{\text{P,F}} = 891 \text{ Hz}$; $^1J_{\text{P,F}} = 906 \text{ Hz}$; $^2J_{\text{P,F}} = 106 \text{ Hz}$

Chapter 5

(b) [EOHMIM][FAP]

^1H NMR (DMSO- d_6 , 200 MHz) δ [ppm]: 3.73 (t, $J = 4.8$ Hz, 2H); 3.85 (s, 3H); 4.20 (t, $J = 5.4$ Hz, 2H); 5.09 (s, -OH); 7.65 (s, 1H); 7.69 (s, 1H); 9.09 (s, 1H)

^{19}F NMR (DMSO- d_6 , 300 MHz) δ [ppm]: -43.0 (dm, PF); -80.14 (m, CF_3); -81.72 (m, 2CF_3); -86.35 (dm, PF_2); -115.84 (dm, CF_2); -116.32 (dm, 2CF_2); $^1J_{\text{P,F}} = 891$ Hz; $^1J_{\text{P,F}} = 906$ Hz; $^2J_{\text{P,F}} = 106$ Hz

5.2.2. i. Gas Chromatographic studies: The gas chromatograph used was DHRUVA GC 2006 model (Chromatography & Instruments Company, Baroda, India). Hydrogen gas of 99.999% purity from Ultra Pure Gases (I) Pvt. Ltd. was used as standard for the estimation.

5.3. Results and Discussion

Colorless and transparent ILs ([EMIM][FAP] and [EOHMIM][FAP]) became yellow to orange to red, with an increase in the absorbed dose. However, the ILs were still transparent, and devoid of any insoluble visible mass even at an absorbed dose of 500 kGy. The photos of the pre- and post-irradiated ILs depicting the evolution of color can be seen in Fig.5.2.

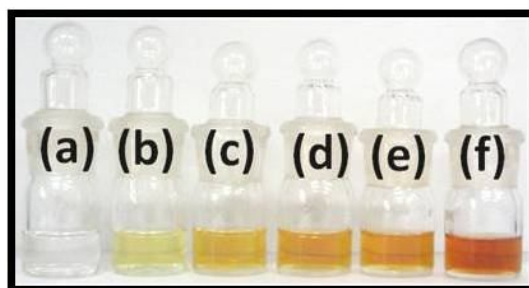


Fig.5.2. Picture showing the color change of [EMIM][FAP] on irradiation. Dose imparted in kGy: (a) 0, (b) 50, (c) 100, (d) 200, (e) 300, (f) 400.

Chapter 5

Above 200 kGy, pungent white fumes were observed, which could be due to HF gas formation, as it caused corrosion of glass container (especially, in case of [EOHMIM][FAP]) after keeping the irradiated ILs for about 8 months. However, release of some other gases (F_2 , H_2) along with the HF cannot be ruled out. Such fumes have also been observed in earlier studies, where fluoro anion based imidazolium ILs were exposed to higher absorbed doses.^{78, 80} Nonetheless, the darkening in color and fume emission on irradiation at higher dose (> 200 kGy) was more in case of [EOHMIM][FAP]. It suggests that the hydroxyl group is not only enhancing the radiolytic degradation of cationic part but also making the FAP anion further susceptible to decomposition as indicated by more release of pungent white fumes. In order to determine the species (cationic or anionic) responsible for the color evolution of post-irradiated FAP ILs, two more ILs were subjected to irradiation up to a dose of 100 kGy. These were [EMIM][EtSO₄] (having the same cationic moiety as in case of [EMIM][FAP]) and trihexyl(tetradecyl) phosphonium FAP, [PH(3)T][FAP] (having the same anionic moiety as in case of [EMIM][FAP]). On irradiation, [EMIM][EtSO₄] showed similar color change as was in the case of [EMIM][FAP] at an equivalent dose of 100 kGy but [PH(3)T][FAP] remained colorless. From this observation, we infer that the degradation products of the imidazolium cation are responsible for the color darkening of the irradiated FAP ILs. It must be mentioned here that the color observed in [EMIM][EtSO₄] and [EMIM][FAP] were similar but much more darker in the former case, which shows the influence of anionic moiety on their radiolytic degradation behavior. Yet, the vital question to be answered for the proposed

Chapter 5

potential application of FAP is the extent and mechanism of degradation of FAP ILs possessing unique physicochemical properties.

5.3.1. UV-Vis absorption studies of irradiated FAP ionic liquids

Prior to recording the UV-Vis absorption spectra, all the samples were diluted 100 times with acetonitrile to avoid the saturation level (observed using both 10 mm & 1 mm path lengths) occurring due to their intense color. Acetonitrile was used as diluents because of its miscibility with FAP ILs and negligible absorption above 200 nm. Besides, the blank correction was done with acetonitrile before recording any absorption measurements. Typical optical absorption spectra of irradiated and unirradiated FAP ILs are shown in Fig.5.3.

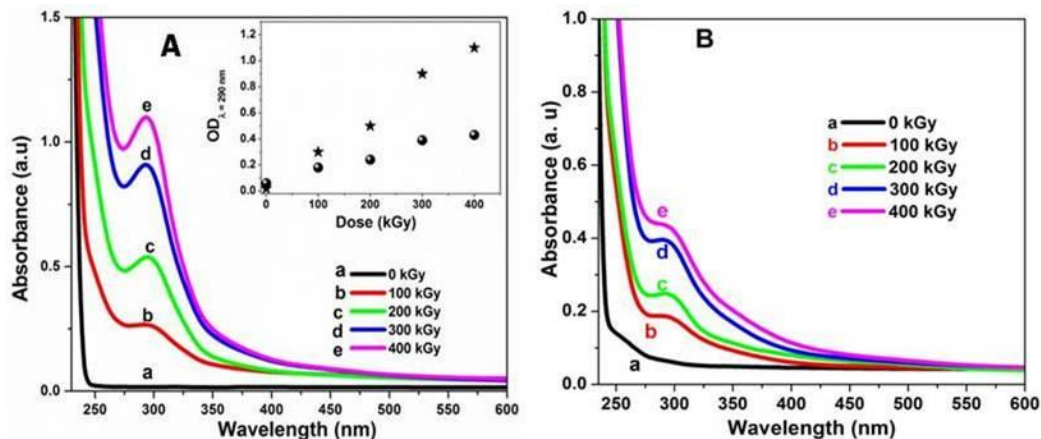


Fig.5.3. UV-Vis absorption spectra of pre- and post-irradiated [EMIM][FAP] (A) and [EOHMIM][FAP] (B) at various absorbed doses in kGy : 0 (a), 100 (b), 200 (c), 300 (d), 400 (e). Inset of plot (A) shows the variation of absorbance values with absorbed doses at 290 nm, where (*) & (•) represents [EMIM][FAP] & [EOHMIM][FAP] respectively.

An absorption maximum at around 290 nm appears on irradiation for both the FAP ILs, showing an increase in the absorbance with increase in the absorbed dose (inset of

Chapter 5

Fig.5.3). In our earlier discussion, we tried to emphasize that the emergence of color on irradiation is due to the radiolytic products formed from the decomposition of the imidazolium cation. However, the absorption peak around 290 nm could be due to the radiolytic products of the imidazolium cation as well as from the degradation products of FAP anion. To determine the origin of the absorption peaks, UV-Vis absorption spectra of irradiated ILs i.e. [EMIM][EtSO₄] (same cationic moiety as [EMIM][FAP]) and [PH(3)T][FAP] (same anionic moiety as [EMIM][FAP]) were recorded and has been shown in Fig.5.4.

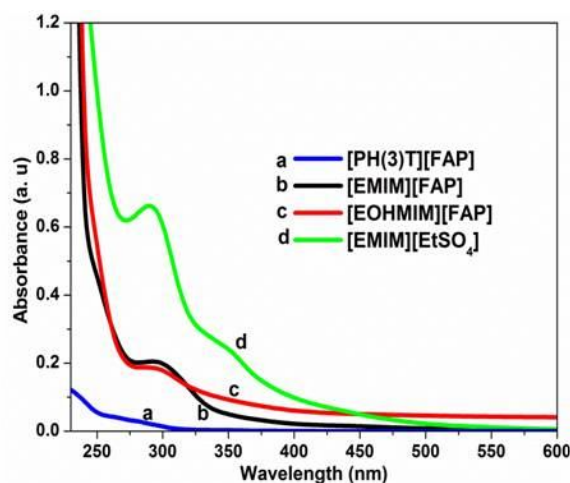


Fig.5.4. UV-Vis absorption spectra of ILs irradiated with an absorbed dose of 100 kGy: (a) [PH(3)T][FAP], (b) [EMIM][FAP], (c) [EOHMIM][FAP], (d) [EMIM][EtSO₄].

On irradiation, [EMIM][EtSO₄] showed the similar absorption spectra as [EMIM][FAP], while no significant changes were observed for [PH(3)T][FAP]. Therefore, the radiolytic products of the imidazolium cation are responsible for the emergence of color as well as the peaks observed in the optical absorption spectra of the irradiated ILs as shown in Fig. 5.3. But, it is very difficult to determine precisely the

Chapter 5

species responsible for the evolution of color in irradiated ILs, as a large number of radiolytic products are formed in very low yields on irradiation (observed from NMR and mass studies, discussed later). However, the most probable reasons for the color evolution of the imidazolium based ILs is due to the formation of oligomeric species as well as radiolytic products containing multiple bond order groups through various radical intermediates of imidazolium cation. Some of these products have been identified in the mass and vibrational studies. Nonetheless, depending on the dose imparted, several species including imidazolium radicals are generated through deprotonation, dealkylation and carbene formation.^{76, 271} Spin density results show that^{271a} the unpaired electron is localized in the region comprised by central carbon (C-2) and the two nitrogen atoms. Therefore, imidazolium originated radical species are highly vulnerable to undergo oligomerization, as shown by Shkrob.²⁷² Further, C-2 position of imidazolium cation is acidic ($pK_a = 21-22$)^{85b} in nature and prone to deprotonation to form a stabilized carbene. Indeed, washing the irradiated ILs with nanopure water (pH 6.8) yields an aqueous phase with lower pH values as compared to that obtained in case of unirradiated ILs. The pH measurements were carried out to determine the formation of the acidic products in the ILs after irradiation. The ILs (1 ml, both unirradiated as well as irradiated) were mixed with the nanopure water (4 ml) in a beaker and stirred for 2 minutes. Consequently, separation of the water layer from the ILs was visible due to the ultra hydrophobic nature of these ILs. The acidic products (if any) generated on irradiation are expected to diffuse in to the aqueous phase, which could be extracted using a separating funnel. The pH of this aqueous phase was measured and the data has been shown in Table 5.1. It further

Chapter 5

indicates that the formation of acidic products (such as HF) in the irradiated ILs. However, their amount appeared to be much higher in case of hydroxyl group containing IL ([EOHMIM][FAP]) than the non-hydroxyl one ([EMIM][FAP]), as indicated by the trend in the pH values.

Table 5.1: pH values of the aqueous phase of the FAP ILs on irradiation

Sample	0 kGy	400 kGy
Aqueous phase of [EMIM][FAP]	6.22	4.38
Aqueous phase of [EOHMIM][FAP]	5.82	3.11

These arguments are well supported by various reports on the oligomeric species of imidazole and its derivatives.²⁷³ According to these studies, oligomeric products of imidazole derivatives are chromophoric in nature having high molar extinction coefficient (ϵ) of the orders of $10^4 \text{ dm}^3 \text{ mol}^{-1} \text{ cm}^{-1}$ and exhibit similar optical absorption spectral features as in the present case of irradiated ILs. The products formed from the dimerization reaction of carbene of imidazole derivatives also exhibit dark red color.²⁷⁴ Therefore, one of the probable reasons for the appearance of peaks in the absorption spectra of post-irradiated FAP ILs can be ascribed to π - π^* transition that originates from the radiolytic products derived from the imidazolium cation, similar to the case of imidazole led oligomeric species.²⁷⁵ Besides this, the appearance of two more shoulder peaks at around 390 and 495 nm in the absorption spectra for irradiated FAP ILs probably indicates the formation of higher molecular weight radiolytic products, which might include higher order oligomeric species but certainly with very low yields. However, absorption peaks in post-irradiated [EOHMIM][FAP] were much broader at 290 nm along with a long tail extending up to 600 nm.

Chapter 5

From the similar optical absorption spectral features of [EMIM][FAP], [EOHMIM][FAP] and [EMIM][EtSO₄], it appears that the imidazolium cation and the anion are two separate, weakly coordinating entities, as similar observations has been reported previously^{85a, 276} on the basis of conductivity and X-ray photoelectron spectroscopic studies (XPS), respectively. As mentioned earlier that the darkening in color of [EMIM][EtSO₄] was much greater in comparison to that in FAP based imidazolium ILs at similar absorbed dose, which clearly indicates the higher amount of decomposition in the former case. Considering this, it appears that the FAP anion is playing a role in strengthening the radiation resistance of the IL. Essentially, the FAP anion due to its larger effective molar volume (226.020 cm³ mol⁻¹) than the imidazolium cation (100.017 cm³ mol⁻¹),²⁷⁷ occupies more space, thus might be acting as a protector for the cationic moiety. While, in case of [EMIM][EtSO₄], effective molar volume of [EtSO₄] anion is 90.681 cm³ mol⁻¹,²⁷⁷ which is less than that of its cationic part. Comparing the effective molar volume of all the fluorinated as well as other halide based anions,²⁷⁷ FAP anion shows the largest effective molar volume i.e. FAP⁻ > NTf₂⁻ > EtSO₄⁻ > PF₆⁻ > BF₄⁻ > NO₃⁻ > Cl⁻. Even though, the molecular volume cannot be considered as a determinant for the radiation stability, but the present results and the literature clearly reflect a good correlation between the molecular volume of the anions, and the radiation stability of their associated ILs. Nevertheless, quantitative estimates of the protective effects of the anions towards cation damage have been rationalized on the basis of the electron counts of the anions relative to the total (cation and anion) electron count. In fact, the estimation of the radiation resistance put forth by various anions (with the same

Chapter 5

cation) was quantitatively explained on the basis of their fractional stopping powers by Le Rouzo *et al.*⁸¹ It was found that the relative degradation of the imidazolium cation reflects the influence of the anion in the following order: $\text{Tf}_2\text{N}^- < \text{TfO}^- < \text{PF}_6^- < \text{BF}_4^-$. Similarly, the fractional stopping power of the anions (in the present work) has been calculated to be 0.78, 0.76, 0.52 for [EMIM][FAP], [EOHMIM][FAP] and [EMIM][EtSO₄], respectively. Further, assuming the same cation (as used in the present work, i.e. EMIM), the fractional stopping powers of the anions studied earlier⁸¹ were calculated as 0.69, 0.54, 0.53, 0.40 for Tf_2N^- , TfO^- , PF_6^- and BF_4^- , respectively. Thus, it is anticipated that FAP based imidazolium ILs would exhibit somewhat better radiation stability amongst the aforementioned anions. However, the presence of functional groups on the cationic moiety i.e. hydroxyl group, which is capable of undergoing hydrogen bonding with the FAP anion can influence its radiation stability by encouraging the abstraction of fluorine based radicals i.e. F^\bullet , CF_3^\bullet , $\text{CF}_3\text{CF}_2^\bullet$ and the same can further attacks the cationic moiety thereby enhancing the radiolytic degradation.

5.3.2. Physicochemical Properties

5.3.2.1. Refractive index

The refractive index of any medium is related to its polarizability and/ or dipolarity.^{278a} In case of RTILs, the refractive index holds an immense relevance, as it can be used to calculate the molar refraction, which in turn may provide essential information regarding the molar free volumes of the ILs. An interesting observation is that the FAP anion due to its larger effective molar volume ($226.020 \text{ cm}^3 \text{ mol}^{-1}$) than the imidazolium cation ($100.017 \text{ cm}^3 \text{ mol}^{-1}$),²⁷⁷ would occupy more space. While, in case of [EMIM][EtSO₄],

Chapter 5

effective molar volume of [EtSO₄] anion is 90.681 cm³ mol⁻¹,²⁷⁷ which is less than that of its cationic part. Numerous reports are available in which molar free volume has been used to determine the solubility of gases in ILs.^{278 b-f} Molar free volume (V_f) of any medium can be calculated as follows:

$$V_f = V_m - R_m \quad [5.1]^{279a}$$

where, V_m is the molar volume while R_m represents molar refraction. V_m of IL can be calculated from the ratio of its molecular weight (M) and the experimental density (ρ). Whereas, the R_m values of ILs can be determined by using Lorenz-Lorentz equation^{279b} given as:

$$R_m = \left(\frac{n^2 - 1}{n^2 + 2} \right) V_m \quad [5.2]$$

where, n is the refractive index. It is to be mentioned here that equation (5.2) is generally applied in case of isotropic fluids comprising of spherical non-interacting particles, while ILs are non-isotropic fluids (microheterogeneous in nature). Nonetheless, such correlations have yielded correct values of refractive indices as reported in earlier studies.^{278b, 279 a, c, d} The refractive index values of the FAP ILs prior to and after irradiation at various doses are shown in Table 5.2. Although, the changes in the refractive index values for both the ILs are nominal, but tender important information regarding their structural integrity on irradiation. The molar volume and free molar volume of pre- and post-irradiated [EMIM][FAP] are higher than that of [EOHMIM][FAP]. The trend is reverse in case of molar refraction values (R_m). After irradiation, the molar free volume decreases for both the ILs and the decrease is more in case of [EOHMIM][FAP] as compared to [EMIM][FAP]. This result possibly indicates

Chapter 5

that the number of radiolytic products formed in the case of hydroxyl FAP IL is more than that for the non-hydroxyl IL.

Table 5.2: Refractive indices (n) of FAP ILs at 25°C at various absorbed dose levels

S. No.	Dose (kGy)	[EMIM][FAP]				[EOHMIM][FAP]			
		n	V_m $\text{cm}^3 \cdot \text{mol}^{-1}$	R_m $\text{cm}^3 \cdot \text{mol}^{-1}$	V_f $\text{cm}^3 \cdot \text{mol}^{-1}$	n	V_m $\text{cm}^3 \cdot \text{mol}^{-1}$	R_m $\text{cm}^3 \cdot \text{mol}^{-1}$	V_f $\text{cm}^3 \cdot \text{mol}^{-1}$
1	0	1.36886	325.91	73.512	252.39	1.37775	324.77	74.831	249.93
2	100	1.36882	-	-	-	1.37821	-	-	-
3	200	1.36894	-	-	-	1.37824	-	-	-
4	300	1.36919	325.87	73.562	252.30	1.37847	324.60	74.919	249.68
5	400	1.36925	-	-	-	1.37841	-	-	-
6	500	1.36931	-	-	-	1.37852	-	-	-

A higher yield of the radiolytic products causes a decrease in molar free volume (but increase in the density, discussed in the following section) and its implication can also be observed in the increase in their refractive indices at higher absorbed doses.

5.3.2.2. Density

Density is probably the most widely studied physical property of RTILs, because of its high significance and experimental accessibility.²⁸⁰ The density of ILs are found to be dependent on the bulkiness and molecular weight of the cationic and anionic moieties.^{279c,}²⁸¹ However, radiolysis of FAP ILs did not exhibit much impact on their densities even at very high radiation fields as shown in Table 5.3. Though, [EOHMIM][FAP] showed little variation in its density when irradiated up to a dose of 300 kGy. This nominal variation in the density of [EOHMIM][FAP] reflects the possible distortions in its molecular structure at higher doses.

Chapter 5

Table 5.3: Physical properties of FAP ILs measured at various absorbed dose levels

FAP IL	Dose (kGy)	Density, (g/cc)	Viscosity, cP	Onset Temp., T _d (°C)
[EMIM][FAP]	0	1.7065 1.7092 ^{282a} 1.7077 ^{282b}	57 60 ^{282b}	361 300 ^{85a, 270c}
	100	-	52	-
	300	1.7067	-	-
	400	-	59	360
[EOHMIM][FAP]	0	1.7618	177	301
	100	-	174	-
	300	1.7627	-	-
	400	-	179	283

**Density and Viscosity measurements were carried out at 25°C.*

5.3.2.3. Viscosity and Rheometric studies

Viscosity, η of RTILs is of immense importance considering their applications mainly in the field of electrochemistry, catalysis, synthesis and as a solvent for extraction such as in spent nuclear fuel reprocessing.²⁸³ Generally, ILs are viscous in nature and a variety of them exhibit viscosities in the range of 66-1110 cP at 20-25°C,⁴⁴ which is 1-3 orders of magnitude higher than most of the conventional molecular solvents. Essentially, viscosity of the ILs is a function of shape, size, molar mass and symmetry of both the cationic and anionic moieties.^{44d} Table 5.3 shows the viscosity of the tested ILs at various absorbed doses measured at 25°C. The minimal variations in the viscosities at higher absorbed doses indicate modest structural degradation of these ILs.

Chapter 5

Rheometric studies

Keeping in view of the wide applicability, rheological properties of irradiated ILs are an important parameter. To carry out such studies, the effect of the shear rate on shear stress and viscosity was determined to examine whether the liquid is Newtonian or not (Fig.5.5 and Fig.5.6). For a Newtonian liquid, the plot of shear stress versus shear rate follows linearity, while its viscosity must be independent of shear rate.

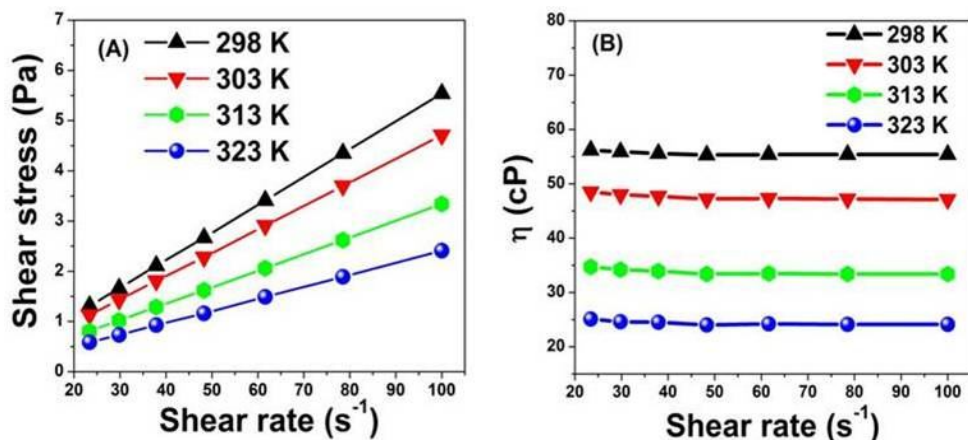


Fig.5.5. Shear stress vs. shear rate (A) and viscosity vs. shear rate (B) of [EMIM][FAP] prior to irradiation.

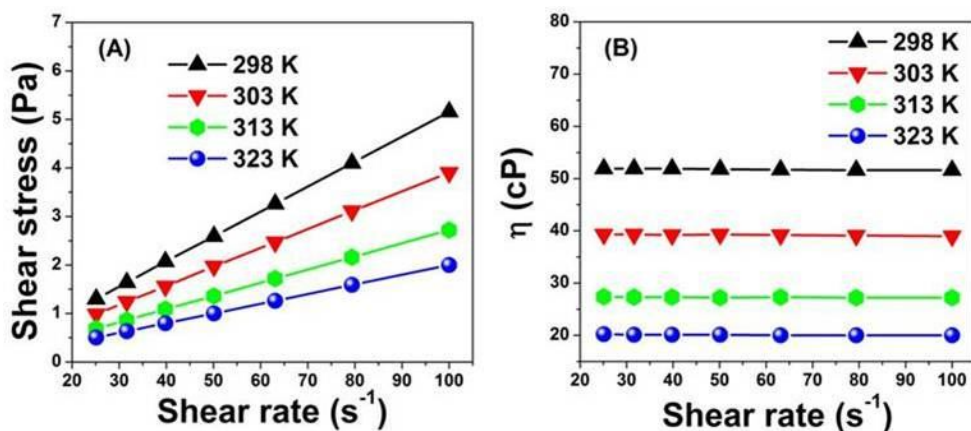


Fig.5.6. Shear stress vs. shear rate (A) and viscosity vs. shear rate (B) of irradiated (Dose \approx 100 kGy) [EMIM][FAP].

Chapter 5

Similar trends were observed for pre- and post-irradiated [EOHMIM][FAP]. This indicates that both the ILs exhibit Newtonian behavior before and after irradiation. Besides, it was also noticed that the viscosities of both the ILs decrease with increase in temperature. Subsequently, this data comprising the temperature assisted change in viscosity was used to determine the activation energy, E_η for viscous flow using the Arrhenius type equation, known as Guzman-Andrade law:^{44d, 80, 82}

$$\ln \eta_a = \ln \eta_\infty + E_\eta/RT \quad [5.3]$$

where, η_a is the apparent viscosity (or viscosity), E_η is the activation energy for viscous flow (J/mol), R is the gas constant ($8.314 \text{ J mol}^{-1} \text{ K}^{-1}$) and T is the absolute temperature (K). The variation of $\ln \eta_a$ with $1/T$ for unirradiated and irradiated FAP ILs ([EMIM][FAP] and [EOHMIM][FAP]) has been shown in Fig.5.7.

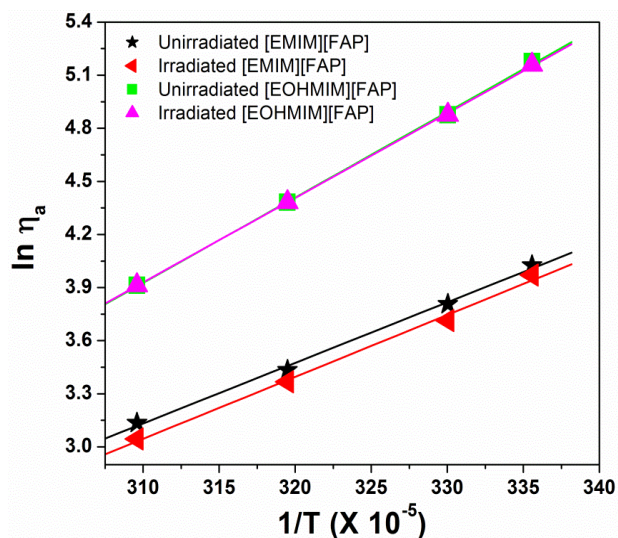


Fig.5.7. Linear fit plots showing the variation of $\ln \eta_a$ with $1/T$ for unirradiated and irradiated FAP ILs.

The activation energy of viscous flow, E_η for both the ILs (pre- and post-irradiated) has been shown in Table 5.4.

Chapter 5

Table 5.4: Activation energy for viscous flow, E_η for pre- and post-irradiated FAP ILs

FAP IL	Temperature (K)	Viscosity (cP)		Activation energy, E_η (kJ/mol)	
		Unirradiated (0 kGy)	Irradiated (≈ 100 kGy)	Unirradiated (0 kGy)	Irradiated (≈ 100 kGy)
[EMIM][FAP]	298	57	52	28.4 ± 1.1	29.1 ± 1.4
	303	45	41		
	313	32	29		
	323	23	21		
[EOHMIM][FAP]	298	177	174	40.1 ± 0.7	39.7 ± 0.4
	303	131	131		
	313	80	80		
	323	50	50		

The activation energy in presence of hydroxyl group is ~ 1.5 times higher than that of non-hydroxyl IL, which indicates that [EMIM][FAP] have better fluidic properties than [EOHMIM][FAP]. However, the activation energies do not change much for both the ILs, even on irradiation to high absorbed doses (≈ 100 kGy).

5.3.2.4. Thermal stability

Considering the application of RTILs in areas such as nuclear fuel reprocessing, as lubricants, electrolytes in fuel cells, or as heat transfer fluids, it is vital to understand the thermal behavior of irradiated RTILs. The thermogravimetric analysis, (TGA), of the unirradiated as well as irradiated FAP ILs was carried out and presented herein. The TGA curves of both the ILs have been corrected for blank and are shown in Fig.5.8. The corresponding T_d ($^{\circ}\text{C}$) values are given in Table 5.3. Onset temperatures T_d ($^{\circ}\text{C}$) were obtained from the TGA profiles by using the step tangent method.²⁸⁴

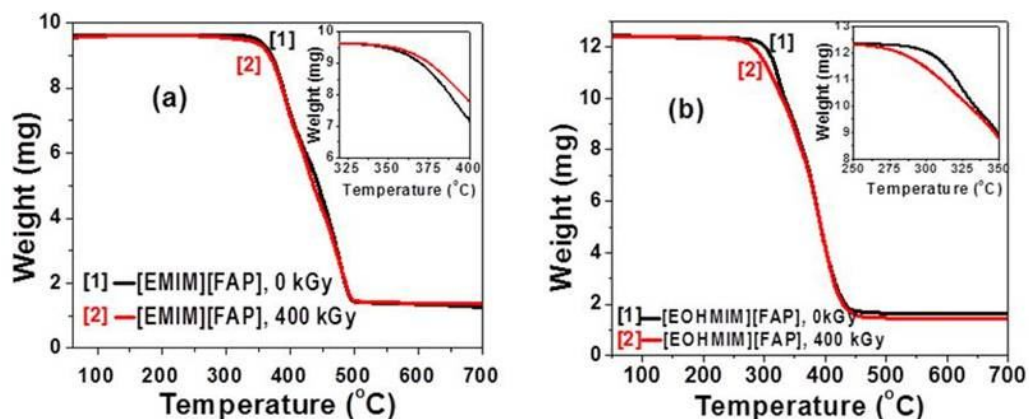


Fig.5.8. TGA profiles of unirradiated and irradiated (400 kGy) ILs (a) [EMIM][FAP] and (b) [EOHMIM][FAP], showing the onset decomposition temperatures T_d (°C).

A significant difference is noticed in the onset values reported by us and by N. V. Ignat'ev *et al.*^{85a} for [EMIM][FAP]. One possible reason for this could be that the authors therein seems to have applied the “percent loss threshold” method for the determination of $T(d)$ which is different from ours as already mentioned. In addition to this, our onset decomposition values T_d (°C) are based on fast TGA scan (20 °C/min.), and it has been shown in various reports^{280a, 285} that the TGA onset point depends on various parameters such as scan rate, gas flow rate, composition of pan/crucible used and mass of the sample, which might be reflected as difference in the reported values. The thermal stability of ILs is largely influenced by the strength of the incorporated heteroatom-carbon and heteroatom-hydrogen bonds.⁷⁰ From the earlier studies on pyrolysis of the imidazolium based salts and dealkylation of imidazole quaternary salts, it is clear that, the nucleophilicity of anion and the ability of the cation to undergo substitution (SN2) or elimination reaction have significant influence on the thermal stability of the ILs.^{280a, 286} Considering this, it might be emphasized here that the FAP anion is a poor nucleophile.²⁸⁷

Chapter 5

From the TGA profiles of unirradiated and irradiated FAP ILs (shown in Fig.5.8), we can see that there is little change in the thermal behavior of [EMIM][FAP] on irradiation, while the thermal resistance of [EOHMIM][FAP] decreases remarkably on irradiation. This can be attributed to the possible formation of the hydroxyl based nucleophilic species on irradiation, which might have paved the way for the substitution or elimination reactions leading to the reduction in the thermal stability of [EOHMIM][FAP]. This argument is in agreement with the results obtained by Glenn *et al.*²⁸⁸ in which they have reported that the thermal stability of imidazolium ILs significantly reduces in the presence of nucleophiles. Therefore, on the basis of obtained results, it can be inferred that [EMIM][FAP] is much more suitable for thermal applications than its hydroxyl functionalized counterpart.

5.3.2.5. Conductivity and Electrochemical studies

RTILs with many charge carriers per unit volume are expected to exhibit very high conductivities when these charge carriers are mobile. The solvating properties and wide electrochemical window (6-7 V) of FAP based RTILs make these materials an excellent candidates for a range of applications, including catalysis, supercapacitors and photovoltaics.^{49, 289} Thus, it is pertinent to study the conductivity behavior of these ILs after irradiation for their effective use in nuclear and space research. Moreover, the effect of functional groups has a great impact on the electrochemical properties of ILs, as can be observed from Table 5.5.

Chapter 5

Table 5.5: Electrochemical windows of pre- and post-irradiated FAP ILs

Dose (kGy)	[EMIM][FAP]				[EOHMIM][FAP]			
	Conductivity (mS.cm ⁻¹)	Cathodic potential (V)	Anodic potential (V)	Total window (V)	Conductivity (mS.cm ⁻¹)	Cathodic potential (V)	Anodic potential (V)	Total window (V)
0	3.2	-2.8	2.7	5.5	1.0	-2.4	2.3	4.7
100	3.5	-2.9	2.7	5.6	1.02	-2.8	2.3	5.1
400	3.21	-3.0	2.5	5.5	0.636	-2.9	1.9	4.8

*Conductivity measurements were carried out at 20 °C.

The conductivity of [EMIM][FAP] changes negligibly as compared to the significant decrease in the conductivity of [EOHMIM][FAP] on exposure to radiation. The parameters on which the conductivity of ILs depends are viscosity, density, ion size, ion association and mobility of ions.^{44d, 85a} But amongst all these, viscosity plays a dominating role in deciding the conductivity behavior of ILs.^{285b, 290} However, as described in earlier sections, the viscosity as well as density of these ILs remains almost constant after irradiation, so the changes in the conductivities can be attributed to the mobility of the ions, which is related to the ion pair formation or ion aggregation. The significant decrease in the conductivity of [EOHMIM][FAP] after an exposure of 400 kGy is obviously the influence of hydroxyl group, as the bonding interactions between the ionic species is appreciably different compared to [EMIM][FAP]. These interactions most likely comprises of an intermolecular hydrogen-bond network between the radiolytic products. Certainly, the hydrogen-bond network would be present among the radiolytic products of both the irradiated ILs, but much more in case of hydroxyl group containing IL; hence their transport properties can be anticipated to be more affected in the later one.

Chapter 5

The cyclic voltammograms of the post-irradiated FAP ILs are shown in Fig.5.9. The limits of the electrochemical window were recorded at current densities of 0.15 mA cm^{-2} and 0.10 mA cm^{-2} for [EMIM][FAP] and [EOHMIM][FAP], respectively.

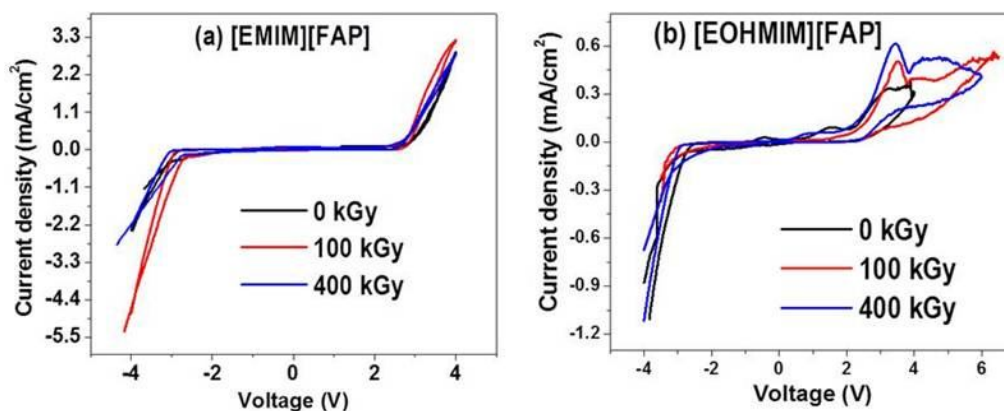


Fig.5.9. Cyclic Voltammograms of pre- and post- irradiated FAP ILs: (a) [EMIM][FAP], (b) [EOHMIM][FAP].

The large electrochemical windows of these ILs are believed to be due to the significant anodic stability of FAP anion, thus possess better resistance to oxidation.²⁹¹ The approximate cathodic and anodic limiting potential values along with the electrochemical windows of the irradiated ILs were determined from the voltammograms and has been shown in Table 5.5. On irradiation, almost no change occurs in the electrochemical window of [EMIM][FAP], while marginal variations could be observed in the case of [EOHMIM][FAP] with an increase in the absorbed dose. Nevertheless, these changes are much smaller as compared to that reported earlier^{82, 292} for the irradiated ILs containing halides, BF_4^- , PF_6^- , and NTF_2^- . On the basis of above results, [EMIM][FAP] appears to be more suitable for various electrochemical applications as compared to [EOHMIM][FAP], because the oxidation stability of later significantly drops

Chapter 5

at high absorbed dose as compared to the former. The decrease in the anodic stability of [EOHMIM][FAP] after irradiation is most probably due to the higher decomposition of the FAP anion in this IL.

5.3.3. NMR and Mass spectral studies

5.3.3.1. NMR studies

^1H and ^{19}F NMR of the pre- and post-irradiated (400 kGy) FAP ILs were recorded (shown in Fig.5.10 and Fig.5.11) to get an idea of the firmness of the cationic and anionic moieties in terms of their structural decomposition due to irradiation. The peaks at various chemical shifts (in ppm) were assigned to appropriate protons and fluorine atoms, respectively.

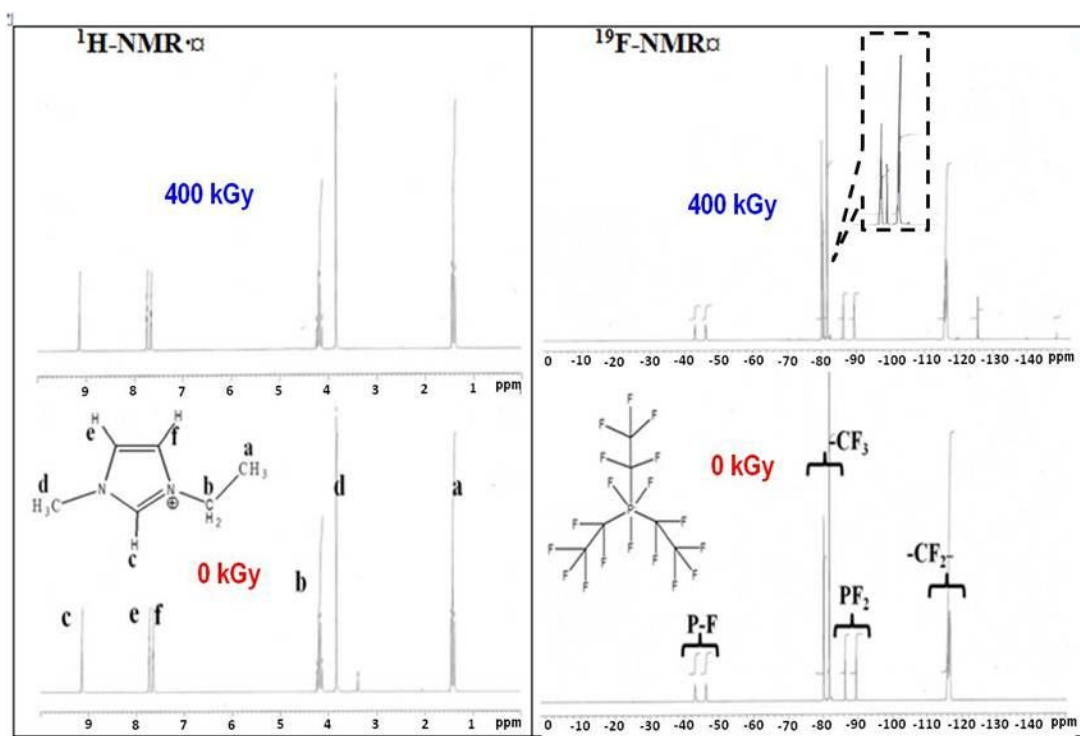


Fig.5.10. ^1H and ^{19}F NMR spectra of pre- and post-irradiated [EMIM][FAP].

Chapter 5

As can be seen, the ^1H NMR of irradiated [EMIM][FAP] (Fig.5.10) shows very little changes in the chemical shift values along with the rise of small peaks as compared to the unirradiated one. Because of very low intensity, chemical identification was very difficult for these peaks. Similar observations were noticed in the case of [EOHMIM][FAP] (Fig.5.11) on irradiation, except for peak broadening of the hydroxyl group proton accompanied by a little chemical shift from 5.09 ppm to 4.86 ppm. This chemical shift could be explained on the basis of the nature of interaction between cationic and anionic moieties present in the IL.

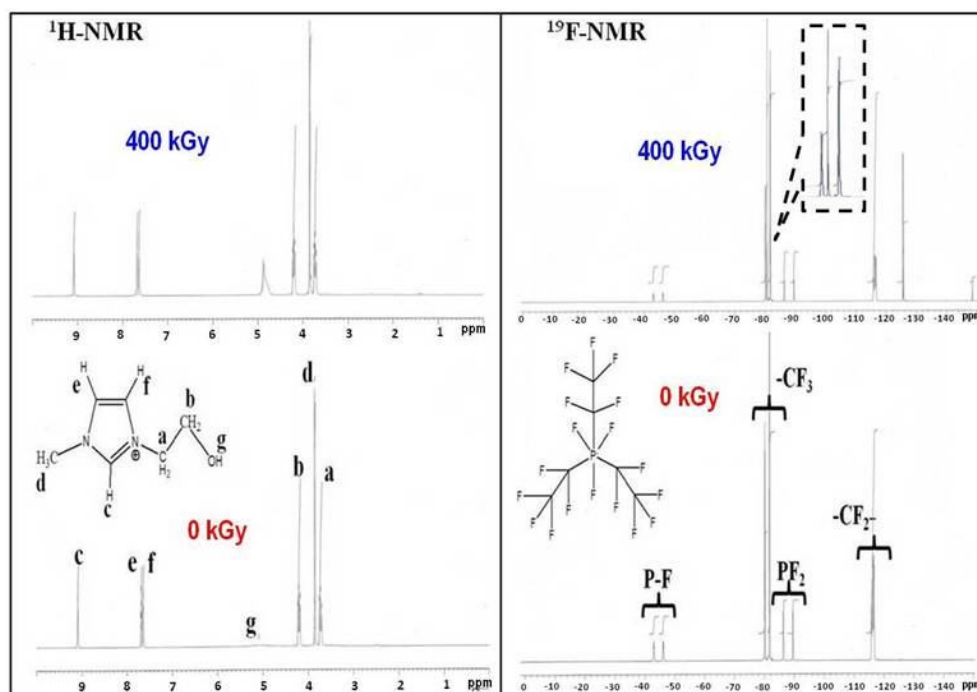


Fig.5.11. ^1H and ^{19}F NMR spectra of pre- and post-irradiated [EOHMIM][FAP].

In imidazolium based ILs, hydrogen bonding between the anions and the proton at C-2 of the imidazolium ring is one of the main interacting forces between them. Essentially, as per the conductivity measurements,^{85a} interaction of the bulkier anions such as FAP

Chapter 5

and NTf_2 with the cation is weaker as compared to the ILs in which the anions are less bulky. This is further reflected in the negligible difference in the chemical shift values corresponding to the C-2 proton in the $^1\text{H-NMR}$ spectra for both the FAP ILs (9.0 ppm in case of $[\text{EOHMIM}][\text{FAP}]$ and 9.14 ppm for $[\text{EMIM}][\text{FAP}]$).

Of late, the interaction of $[\text{EOHMIM}]^+$ and $[\text{EMIM}]^+$ with various anions was investigated using DFT calculations and NMR by Zhang *et al.*²⁹³ According to the optimized geometries obtained by them, the anions were located in front of the imidazolium ring, where the atoms carrying more negative charges were closer to proton at C-2 position in non-hydroxyl ILs ($[\text{EMIM}]^+$), whereas in $[\text{EOHMIM}][\text{FAP}]$, the anions were somewhat closer to the hydroxyl group compared to the C-2 proton. Thus, a competition exists for hydrogen bond formation with the anion between hydroxyl group and the C-2 proton. In the present case, a little decrease in the chemical shift value of the C-2 proton was observed for the hydroxyl functionalized IL. In other words, the competition for the formation of hydrogen bond between the hydroxyl group and the anion gives rise to relatively free C-2 proton in comparison to the non-hydroxyl IL. As mentioned earlier also, the chemical shift values of C-2 proton in the $^1\text{H-NMR}$ spectra of both the FAP ILs decreases feebly on irradiation. Meanwhile, the broadening along with the decrease in the chemical shift value of the peak corresponding to the hydroxyl group proton of the irradiated $[\text{EOHMIM}][\text{FAP}]$ can be attributed to the perturbation in the hydrogen bond between the hydroxyl group of the cation and the fluorine atom of the FAP anion, $\text{OH}\cdots\text{F}$. Most probably, the decrease (though nominal) in the chemical shift values of C-2 proton as well as that of the hydroxyl proton towards higher field are the

Chapter 5

indications of the alterations in the distribution and the nature of interactions accessible to the aforementioned protons due to the formation of some new species, on radiolysis of the ILs. This type of molecular restructuring and realignment of bonding interactions in post-irradiated ILs has also been observed in their photophysical studies (discussed later).

The ^{19}F NMR spectra of post-irradiated FAP ILs are shown in Fig.5.10 and Fig.5.11. A new singlet and a doublet at -80.6 ppm and -125.5 ppm, respectively can be seen in the ^{19}F NMR spectra of both the FAP ILs on irradiation. The intensity of the singlet was higher than that of doublet. Furthermore, the intensity of both the peaks were lower for [EMIM][FAP] than [EOHMIM][FAP]. The analysis of the integrated area of the peaks in case of irradiated [EOHMIM][FAP] reveals the appearance of two extra fluorine atoms. It suggests that the radiolytic product corresponding to the singlet at -80.6 ppm is most probably generated from the dissociation and rearrangement in the units of $\text{CF}_3\text{-CF}_2$ -group. Moreover, it does not contain phosphorous (P), because the F and P atoms couple each other strongly, so the presence of later would have led to appearance of a multiplet, in spite of a singlet. This argument is also well supported by the bond dissociation energies (Table 5.6).

Table 5.6: Bond dissociation energies (kJ/mol)

Bond	Dissociation energy (kJ/mol)
C-P	264
C-C	347
P-F	520
C-F	540

The energy for C-P bond dissociation is lowest thereby, the release of the $\text{CF}_3\text{-CF}_2$ -group followed by the further discharge and rearrangement of its units are expected. In

Chapter 5

case of [EOHMIM][FAP], the formation of radiolytic products containing entities like $\text{CF}_3\text{-CO-}$, $\text{-CF}_2\text{-O-}$ are possible, as the chemical shift value of the fluorine present within these lies between -70 to -90 ppm (CFCl_3 as standard).²⁹⁴ While, the doublet appearing at -125.5 ppm indicates the formation of species like -CHF_2 , $\text{-CF}_2\text{-CO-}$, as the integrated area of the doublet shows the presence of two fluorine atoms in that particular unit. However, in case of [EMIM][FAP], the peak intensities are very small and integrated area analysis does not show the presence of extra fluorine atoms, which makes it extremely difficult to precisely identify the species responsible for the peaks. Some other peaks were also appeared but, it was very complicated to identify them due to their extremely low intensities. Undoubtedly, there is a formation of number of radiolytic products on irradiation (especially in case of [EOHMIM][FAP] as compare to [EMIM][FAP]), but in much smaller amounts as supported by the mass spectral studies too.

5.3.3.2. ESI-MS study

Fig.5.12 shows the ESI mass spectra (+, positive mode) of irradiated [EMIM][FAP] at an absorbed dose of 400 kGy, while the ESI-MS of irradiated [EOHMIM][FAP] at same dose is shown in Fig.5.13. The relative intensities of the radiolytic products formed in comparison to the parent ion peaks at $m/z = 111.0$ and 127.1 in case of [EMIM][FAP] and [EOHMIM][FAP], respectively are much less. The maximum intensity of the radiolytic product formed on irradiating [EMIM][FAP] corresponds to $m/z = 229.1$, which is about 3.8 % of the parent cation peak intensity, and has been identified as $[(\text{EMIM})\text{CF}_2\text{CF}_3]^+$. The probable molecular structure of this ion has been shown in the inset of Fig.5.12.

Chapter 5

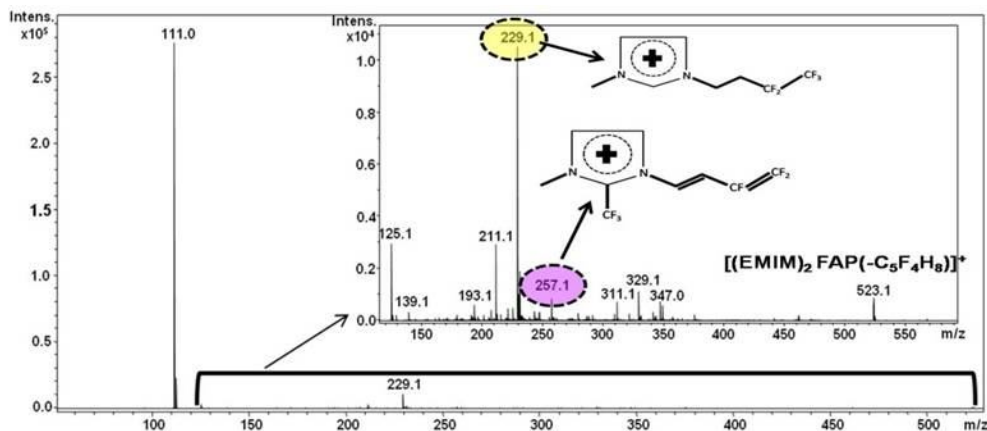


Fig.5.12. ESI (+) mass spectra of [EMIM][FAP] after irradiation to a total absorbed dose of 400 kGy.

All other peaks with various m/z values were having intensity below 1.2 % relative to the parent ion peak. However, ions with m/z values 125.1 and 667.1 were also observed in the unirradiated mass spectra of [EMIM][FAP]. The relative intensities of these peaks prior to irradiation were found to be 1.13 % and 1.46 %, respectively, with respect to the parent ion peak. After irradiation, the intensity of the peak with $m/z = 125.1$ was found to be nearly same as earlier, while the intensity for the peak with $m/z = 667.1$ decreased to 0.45 %. This suggests that the ion with $m/z = 125.1$ is an ionization product of the parent cation, while the ion with $m/z = 667.1$ is a type of adduct or a cluster, identified as a dimeric ion, $[(EMIM)_2 FAP]^+$. However, it was found to be very weak in nature since the collision energy of only 2 eV led to its dissociation into the parent ion with m/z value of 111.0, as was observed from its MS/MS spectra. The peak ($m/z =$ of 523.1, see Fig.5.12) is most probably a dimeric ion, $[(EMIM)_2 FAP(-C_5F_4H_8)]^+$ resulted due to the fragmentation of a $C_5F_4H_8$ group from the aggregate with $m/z = 667.1$. The ion peak with $m/z = 211.1$ has been identified as a dimeric species having composition,

Chapter 5

$[(EMIM)(MIM)F]^+$. On a similar note, the formation of a dimeric radical cation in combination with an anion radical has been predicted by Shkrob *et al.*²⁹⁵ Essentially, most of the identified peaks shown in Fig.5.12 were found to be originated from the radiolytic products containing the fragmented units of the FAP anion such as F, CF_3 , and C_2F_5 . Consequently, the permutation and combination of these species with that of the parent cation led to the emergence of various ion peaks with m/z values 193.1, 257.1, 311.1, 329.1 and 347.0. The ion with $m/z = 193.1$ might be attributed due to the combination of parent cation ($[EMIM]^+$) and the radical species, CH_3^\bullet and CF_3^\bullet , generated from the fragmentation of cationic and anionic moieties, respectively. The peak with $m/z = 257.1$ is most probably assigned to an ion with conjugated double bonds. The presence of such products with multiple bond order groups have also been observed in the vibrational spectral studies of these irradiated FAP ILs (discussed later). Apparently, the formation of such double bond radiolytic products could also contribute in the color evolution observed for the post-irradiated imidazolium based ILs. Moreover, recently, Wang *et al.* by means of UV-Vis analysis and density functional theory calculations proposed that the color darkening in imidazolium based IL ($[BMIm][NTf_2]$) upon irradiation originates from the formation of double bonds in the aliphatic chains of pristine organic cations (or radiolytic products of RTILs) and various associated species containing these “double bond products”.²⁹⁶

Chapter 5

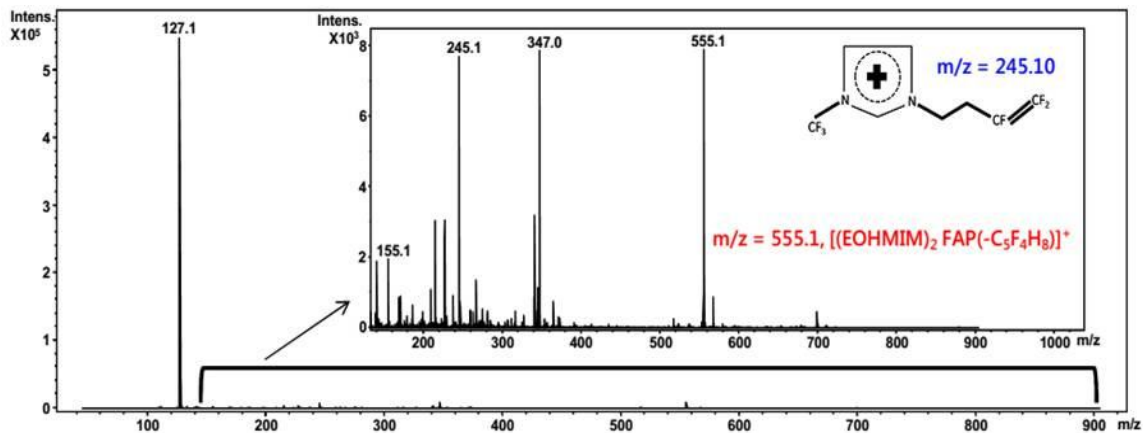


Fig.5.13. ESI (+) mass spectra of [EOHMIM][FAP] after irradiation to a total absorbed dose of 400 kGy.

The ions with m/z values 311.1, 329.1 and 347.0 appear to have the same basic structural composition with the subsequent addition of F atom. The ion peak with $m/z = 347.0$ was also observed in the ESI (+) mass spectra of irradiated [EOHMIM][FAP], as shown in Fig.5.13. This peak with $m/z = 347.0$ has been identified as the cation, [(EMIM) Y], where $Y = 2 (C_2F_5^\bullet)$. The composition of the ion with $m/z = 347.0$ was observed as $(C_{10}H_9N_2F_{10})^+$. Similarly, the composition of ion peaks with m/z values 311.1 and 329.1 has been assigned to $(C_{10}H_{11}N_2F_8)^+$ and $(C_{10}H_{10}N_2F_9)^+$, respectively. Further, there is also an evidence of the disintegration of the imidazolium cation as the ion with $m/z = 139.1$ have been identified as the recombination of the [EMIM]⁺ cation with the C_2H_5 unit, fragmented from another parent cation.

In case of irradiated [EOHMIM][FAP], the number of radiolytic species formed were much more as compared to the non-hydroxyl FAP IL. An aggregate with $m/z = 699.1$ was observed in the pre-irradiated [EOHMIM][FAP]. This has been identified as a dimeric ion, [(EOHMIM)₂ FAP]⁺, similar to the one observed in case of [EMIM][FAP] and thus,

Chapter 5

the peak corresponding to the m/z value of 555.1 is a result of fragmentation of a $C_5F_4H_8$ group from the aggregate with $m/z = 699.1$. However, the intensity of the ion peak with $m/z = 555.1$ in case of irradiated [EOHMIM][FAP] was nearly 1.5 %, while at same dose, the intensity of the ion peak with $m/z = 523.1$ in case of irradiated [EMIM][FAP] was about 0.3 %. It shows that the hydroxyl group (present in [EOHMIM][FAP] as well as in the dimeric ion with $m/z = 699.1$) being involved in the hydrogen bonding with the anion leading to the further weakening of the P- C_2F_5 bond. As shown in Table 5.6, the bond dissociation energy of P-C bond is least among other bonds, which the presence of hydroxyl group increases its susceptibility to radiolytic dissociation. Consequently, the fragmentation of C_2F_5 unit of FAP anion appears to be more vulnerable to radiolysis in case of [EOHMIM][FAP] as compared to [EMIM][FAP]. Other ion peak with intensity greater than 1.0 % was having $m/z = 245.1$ and its probable molecular structure has been shown in the inset of Fig.5.13. The degradation of parent cation was also observed in the form of ion peak with $m/z = 155.1$ and was assigned as $[(EOHMIM) X]^+$, where $X = C_2H_5$.

ESI-mass spectra of the irradiated ILs were also carried out in the negative mode to determine the structural degradation of the FAP anion. Interestingly, the ESI-MS (-, negative mode) of the irradiated [EMIM][FAP] at an absorbed dose of 400 kGy did not show much degradation, as can be observed in Fig.5.14.

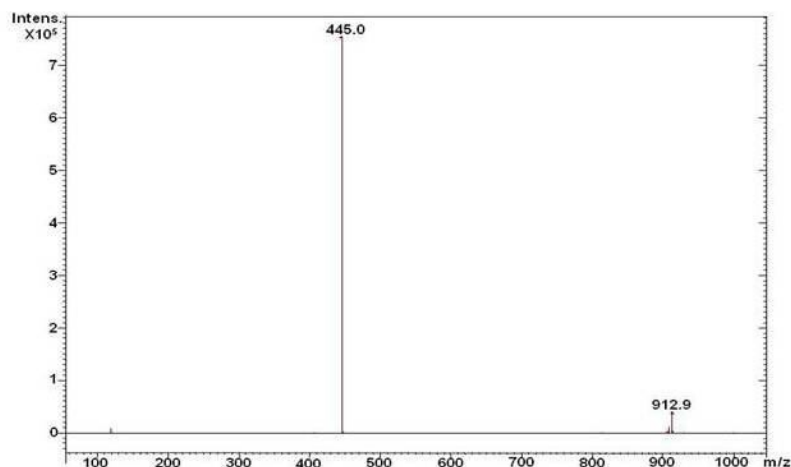


Fig.5.14. ESI (-) mass spectra of [EMIM][FAP] after irradiation to a total absorbed dose of 400 kGy.

However, an ion peak of low intensity (5.3 %) with $m/z = 912.9$ was noticed in case of irradiated [EMIM][FAP]. This ion has been identified as a cluster of two FAP anions with an imidazolium cation having a composition, $(C_{16}F_{33}P_2H_4N_2)^+$. But in case of irradiated [EOHMIM][FAP], such cluster formation was observed at lower absorbed doses. This is probably due to their dissociation into smaller fragments at high absorbed doses, which is attributed to the influence of hydroxyl group as discussed earlier. Nonetheless, the intensity of the peaks was found to be very low ($< 0.5\%$). All these observations clearly indicate the high radiation stability possessed by the FAP ILs. However, the presence of electron withdrawing hydroxyl groups in the vicinity of the umbrella of delocalized electron cloud of anionic moiety led to its distortion, thereby led to the reduction in the radiation stability. Furthermore, the ESI-MS studies of both the irradiated ILs categorically indicate the fragile nature of C_2F_5 unit of the FAP anion and this observation is in fairly good agreement with the results obtained in case of NMR studies, especially in case of [EOHMIM][FAP].

Chapter 5

5.3.4. Hydrogen gas yields

Gaseous products evolution is a crucial factor to be considered for any industrial or reactor scale application. Among various gases, hydrogen yield determination ($G(\text{H}_2)$) is one of the primary steps for the ILs to be employed in any such applications. Moreover, there are very few reports regarding the hydrogen yield determination in irradiated ILs.²⁶⁷²⁶⁸ Therefore, hydrogen yields were measured from the irradiated FAP ILs and are shown in Table 5.7.

Table 5.7: Hydrogen gas yields from benzene and various ILs irradiated with the same absorbed dose of 54 kGy.

Sample	$G(\text{H}_2)$, mol/J
Benzene	$(6.5 \pm 0.4) \times 10^{-9}$ 3.93×10^{-9} ²⁹⁷
[EMIM][FAP]	$(7.6 \pm 0.2) \times 10^{-9}$
[EOHMIM][FAP]	$(8.5 \pm 0.4) \times 10^{-9}$
[BMIM][FAP]	$(1.02 \pm 0.02) \times 10^{-8}$
[BMIM][NTf ₂]	$(1.2 \pm 0.1) \times 10^{-8}$
[BMIM][PF ₆]	$(2.3 \pm 0.1) \times 10^{-8}$

Along with the FAP ILs, benzene and other ILs were irradiated and hydrogen yields were determined to compare their radiation stabilities. Generally, aromatic compounds like Benzene possess excellent radiation stability as the excitation energy rapidly redistributes over the whole molecule instead of getting localized at a specific bonding site.²⁹⁸ As can be seen from Table 5.7, the $G(\text{H}_2)$ of [EMIM][FAP] is marginally higher than that of Benzene. However, on hydroxyl group substitution, the $G(\text{H}_2)$ increases.

Chapter 5

This observation further validates our earlier discussion, where the radiation stability of [EOHMIM][FAP] was found to be inferior as compared to [EMIM][FAP]. The hydrogen yield increases on increasing the length of alkyl chain, i.e. from [EMIM] to [BMIM] (Table 5.7). This observation has been further substantiated by the recent study on the hydrogen production in aromatic and aliphatic ILs by Dhiman and co-workers.²⁶⁸ The imidazolium ILs containing anions such as NTf₂ and PF₆ have been studied in detail earlier due to their physicochemical properties having relevance in the nuclear fuel reprocessing. Therefore, ILs with anionic moieties such as FAP, NTf₂ and PF₆ comprising same cationic unit were irradiated to a similar dose and the G (H₂) were measured. Due to the unavailability of [EMIM][NTF₂] and [EMIM][PF₆], we irradiated [BMIM][NTf₂] and [BMIM][PF₆] along with [BMIM][FAP] to compare the hydrogen yields. As can be seen from Table 5.7, the [BMIM][FAP] shows the lowest G (H₂) followed by [BMIM][NTf₂], and [BMIM][PF₆].

5.3.5. Pulse radiolysis study

Pulse radiolysis experiments were carried out to follow the kinetics and spectral characteristics of the FAP ILs. It has been observed from Fig.5.15 that the two ILs give rise to similar transients with absorption peaks at 320 nm and a weak shoulder at 370 nm. However, the absorbance at 320 nm in case of [EOHMIM][FAP] is 1.3 times higher than that in case of [EMIM][FAP]. On pulse irradiation, neat IL containing imidazolium cation²⁷¹ had been shown earlier to generate various transient species including radical cation and neutral radical of imidazole through the reaction of e⁻ (dry or solvated), H-adducts

Chapter 5

and fragmented alkyl radicals having overlapping absorptions at around 325 nm. In addition, the anion derived primary radicals also produces numerous oxidized species.

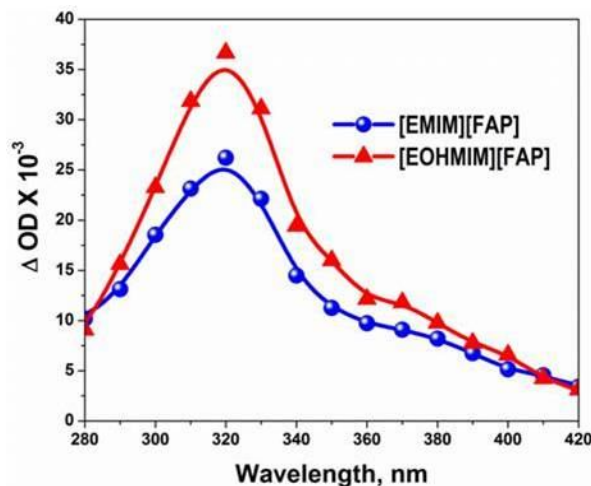


Fig.5.15. Transient absorption spectra recorded at $3\mu\text{s}$ after the electron pulse from neat $[\text{EMIM}][\text{FAP}]$ (blue) and $[\text{EOHMIM}][\text{FAP}]$ (red); dose per pulse was 12 Gy.

Even though, fascinating and challenging radiation chemistry of neat ILs is much more complex than other liquids as portrayed vividly in the recent articles by Wishart and Co-workers.²⁹⁹ In the present case, the transient absorption spectrum matches well with that reported by Behar *et al.*^{271a} for the reaction of e_{aq}^- with imidazolium cation in aqueous solution. Of course, formation and presence of other transients as discussed already are obvious. Nevertheless, the yield and chemical nature of these species are expected to be similar for both the ILs, but in reality, a clear difference could be observed in optical absorbance of the transients in the two cases. It may be mentioned here that we have also observed a faster rate of formation of the transients in case of $[\text{EOHMIM}][\text{FAP}]$ ($5.7 \times 10^6 \text{ s}^{-1}$) than that in case of $[\text{EMIM}][\text{FAP}]$ ($3.26 \times 10^6 \text{ s}^{-1}$). Considering the absorbance at 320 nm to be mostly due to (EMIM^{2+}) , and (EMIM^{\bullet}) , the electron transfer from these

Chapter 5

radicals to oxygen is not expected as reported earlier.^{271a} These authors have elucidated through *ab initio* calculation that the imidazolyl radical (here EMIM[•]) acquires a puckered ring structure, where the two nitrogen atoms and C2 are not conjugated with the C4=C5 double bond and thus, lacks the electron donating ability. Fig.5.16A shows the transient decay at 320 nm in absence and presence of oxygen for [EMIM][FAP].

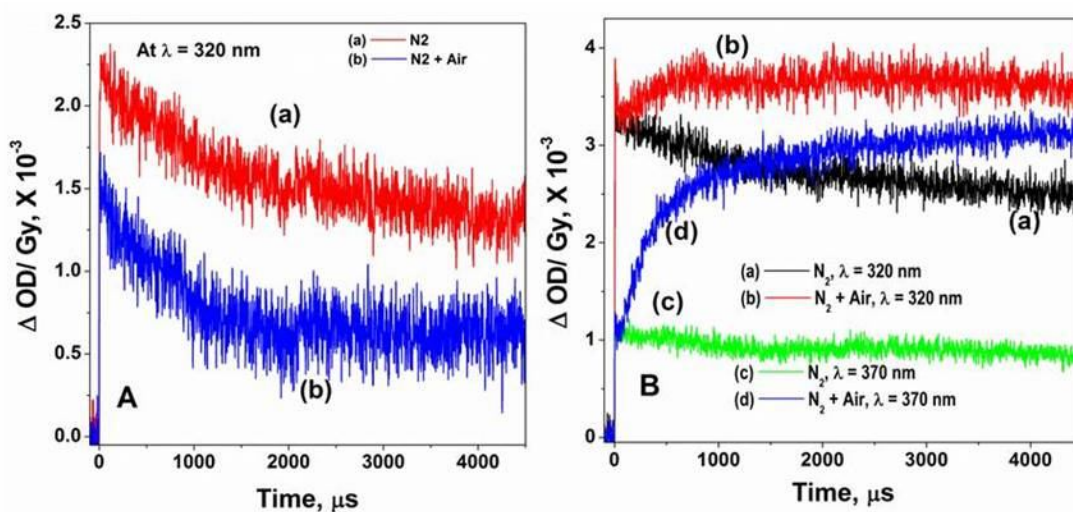


Fig.5.16. Transient decay in the absence and presence of oxygen for [EMIM][FAP] (A) and [EOHMIM][FAP] (B).

Only a reduction in the initial absorbance was observed without showing any indication of the interaction between oxygen and the radicals, which matches well with the earlier proposition. The reduction in the initial yield might be due to scavenging of alkyl radicals. Quenching of primary radicals, including e^- and e_{sol}^- may also contribute to this effect, which would produce superoxide radical. Superoxide radicals are known to be unreactive or slowly reactive with the cation of imidazolium based IL.³⁰⁰ The situation was very different in case of [EOHMIM][FAP] IL (Fig.5.16B). The transient decay has been seen to be affected by the presence of oxygen considerably and formation of a new

Chapter 5

species was evident, which was quite prominent while measuring at 370 nm. The presence of the hydroxyl group in the side chain is not expected to cause a remarkable change in the electron density and so in the structure of the imidazolium radical, such that it can transfer an electron to oxygen. Thus, we infer that in the pulse irradiated [EOHMIM][FAP] IL, formation of alkyl radical at the ethoxy side chain of the cation is quite likely. Further, addition of oxygen to this radical would form a peroxy radical, which shows a strong absorption in the wavelength region 320-370 nm. Thus, it becomes clear that the two ILs behave differently in radiation environment which has been reflected in the number and yield of products as described in the previous sections.

5.3.6. Photophysical studies

Photophysical studies of imidazolium RTILs have been investigated extensively in the recent times, which show unconventional behavior of these solvents such as excitation wavelength dependent fluorescence behavior also known as Red Edge Effect or REE.³⁰¹ This particular phenomenon has been attributed to the presence of various associated species and the inefficiency of the excitation energy-transfer between them or an incomplete solvation process. Information regarding the photophysical behavior of irradiated ILs could be useful in gaining better understanding of the radiation driven perturbations in the structure-property relationships, which eventually affects the radiolytic degradation pathways and the product distribution.

5.3.6.1. Fluorescence studies

Most interestingly, the well established excitation wavelength dependent fluorescence behavior of imidazolium ILs was found to be considerably perturbed on irradiation. The

Chapter 5

emission spectra of pre- and post-irradiated [EMIM][FAP] at different levels of absorbed dose have been shown in Fig.5.17.

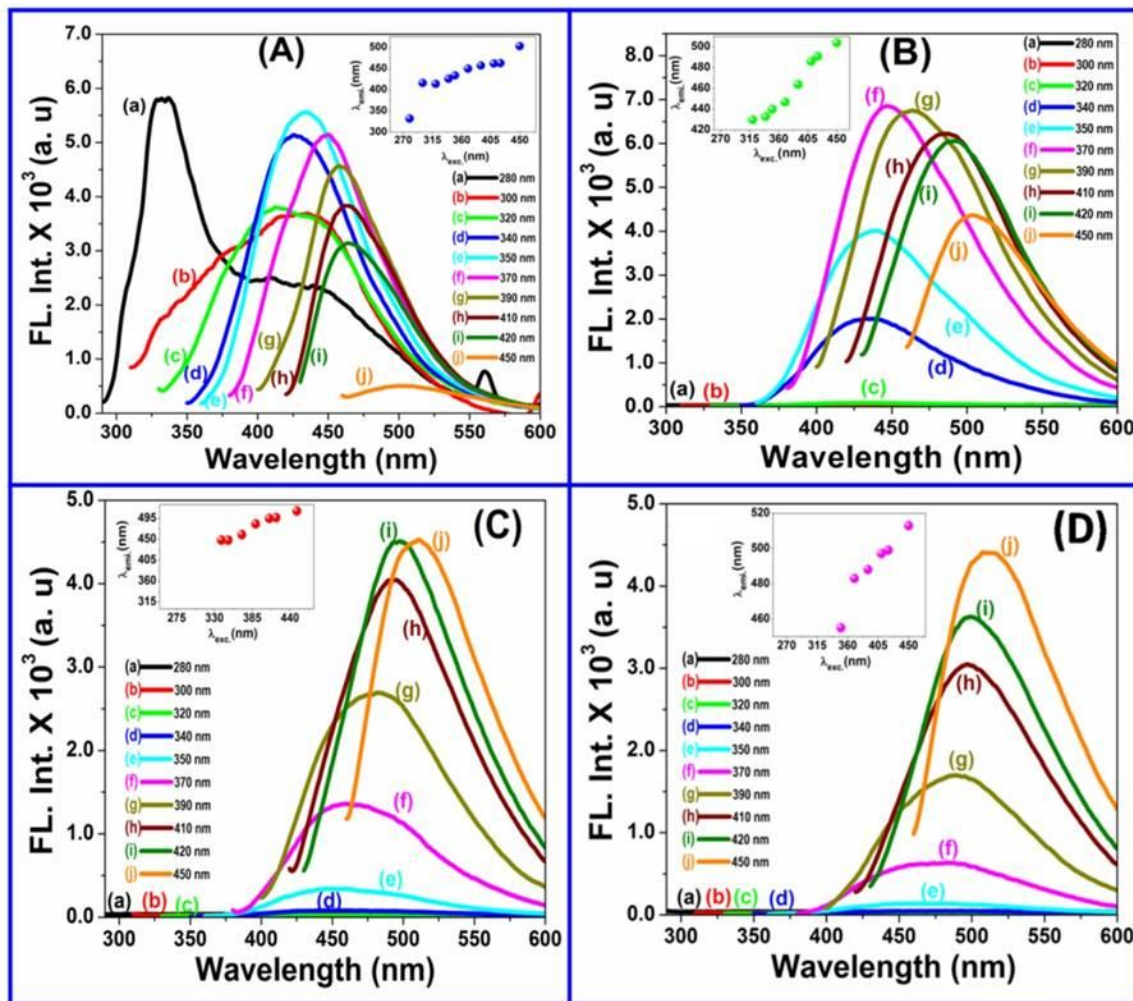


Fig.5.17. Fluorescence spectra of neat unirradiated (A) and post irradiated [EMIM][FAP] at various absorbed doses (in kGy) i.e. 100 (B); 200 (C); 300 (D). Inset: Plot of λ_{ex} vs. λ_{em} showing the shifts in the maximum intensity peak positions.

As can be seen from Fig.5.17A, the unirradiated IL shows two emission bands (at ~ 340 nm and a shoulder peak at ~ 450 nm) when excited at lower wavelength region. However, with the increase in the excitation wavelength, the two emission bands merge

Chapter 5

into single broad peak with simultaneous bathochromic shift. Surprisingly, there was subsequent quenching of fluorescence at lower excitation wavelengths after irradiation to different degrees of absorbed doses (see Fig.5.17). At the same time, the maximum emission peaks showed bathochromic shifts for higher excitation wavelengths with gradual increase in the absorbed dose. Such trends can also be envisaged from the plots of λ_{ex} vs. λ_{em} shown in the insets of emission spectra of irradiated [EMIM][FAP] IL (Fig.5.17).

For better understanding, the maximum fluorescence intensity and λ_{em} values corresponding to the respective excitation wavelengths and absorbed doses for neat [EMIM][FAP] (pre- and post-irradiated) have been tabulated in Table 5.8.

Table 5.8: Table showing the corresponding λ_{em} and maximum fluorescence intensity values for neat pre- and post-irradiated [EMIM][FAP] at different λ_{ex} and absorbed dose values.

Dose $\lambda_{exc.}$ (nm)	0 kGy		100 kGy		200 kGy		300 kGy		400 kGy	
	λ_{em} (nm)	Max. Intensity								
280	332	5823	No emission	-	No emission	-	No emission	-	No emission	-
300	416	3629	No emission	-	No emission	-	No emission	-	No emission	-
320	414	3792	430	84	No emission	-	No emission	-	No emission	-
350	434	5574	440	4014	448	340	455	136	479	69
390	457	4572	464	6750	483	2689	488	1696	492	976
410	462	3835	486	6220	495	4047	497	3049	499	1890
420	463	3140	491	6050	497	4510	499	3625	504	2305
450	503	500	504	4360	511	4526	513	4400	521	3047

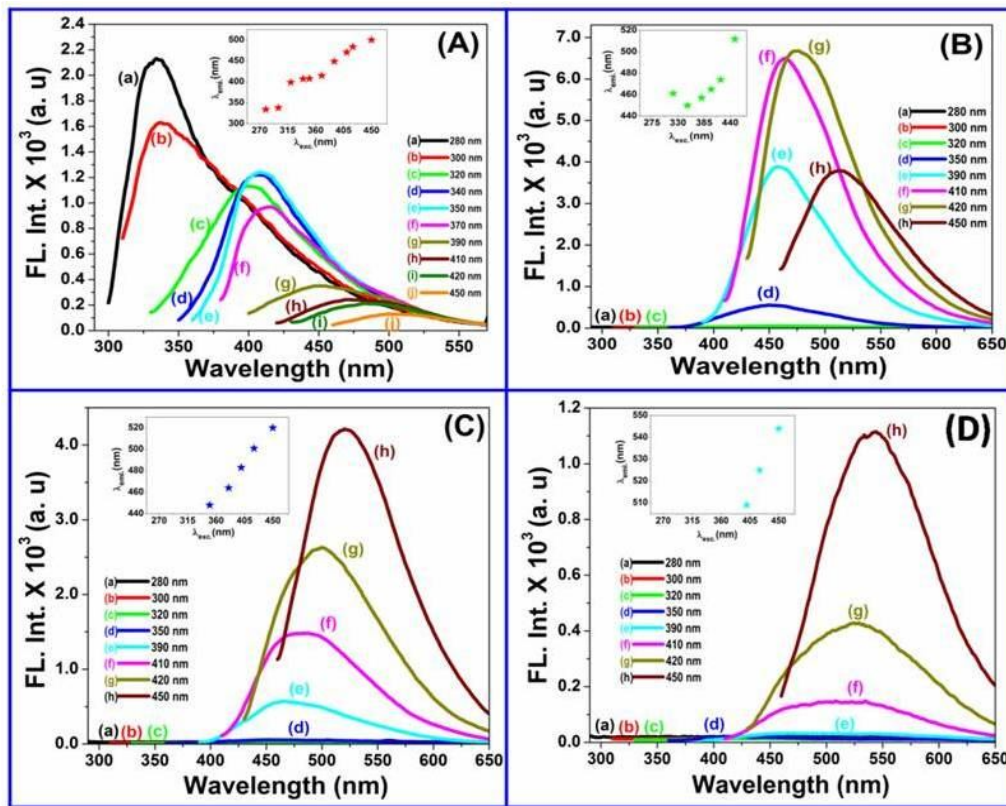


Fig.5.18. Fluorescence spectra of neat unirradiated (A) and post irradiated [EOHMIM][FAP] at various absorbed doses i.e. 100 kGy (B); 200 kGy (C); 300 kGy (D). Inset: Plot of λ_{em} vs. λ_{ex} showing the shifts in the maximum intensity peak positions.

Analogous to [EMIM][FAP], the -OH group containing IL (i.e. [EOHMIM][FAP]) displayed similar excitation wavelength dependent behavior after irradiation (see Fig.5.18). But, in [EOHMIM][FAP], the decrease in the fluorescence intensity as well as the red shift in the emission peaks were more pronounced for subsequent increase in the excitation wavelengths at higher absorbed doses. These trends can be visualized in Table 5.9.

Chapter 5

Table 5.9: Table showing the corresponding λ_{em} and maximum fluorescence intensity values for neat pre- and post-irradiated [EOHMIM][FAP] at different λ_{ex} and absorbed dose values.

Dose $\lambda_{exc.}$ (nm)	0 kGy		100 kGy		200 kGy		300 kGy		400 kGy	
	λ_{em} (nm)	Max. Intensity								
280	334	2135	No emission	-						
300	338	1626	No emission	-						
320	399	1134	461	51	No emission	-	No emission	-	No emission	-
350	408	1242	450	553	448	56	No emission	-	No emission	-
390	449	350	457	3886	464	572	No emission	-	No emission	-
410	471	243	465	6497	483	1482	509	148	No emission	-
420	484	213	474	6674	501	2626	525	429	550	50
450	500	130	512	3787	520	4214	544	1115	560	172

Considering the excitation wavelength of 450 nm and an absorbed dose of 400 kGy, it can be envisaged that the red shift (with respect to the unirradiated IL) in the emission peak was 18 nm for [EMIM][FAP], while it was 60 nm in case of [EOHMIM][FAP] (see Fig.5.19).

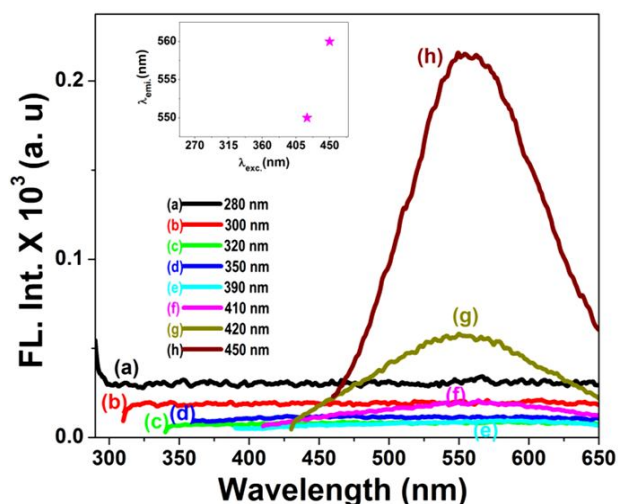


Fig.5.19. Fluorescence spectra of post-irradiated (@ 400kGy) [EOHMIM][FAP]. Inset: Plot of λ_{ex} vs. λ_{em} showing the shifts in the maximum intensity peak positions.

Chapter 5

These observations indicate the formation of higher order (in terms of conjugation and introduction of new π - π interactions) radiolytic products in [EOHMIM][FAP]. Nevertheless, as already mentioned that the excitation wavelength dependent fluorescence spectra of imidazolium ILs has been rationalized taking into consideration the existence of various associated structures of cations and anions.³⁰¹ In fact, some of the associated forms of cation and anion were observed during the mass spectrometric studies of neat unirradiated [EMIM][FAP] and [EOHMIM][FAP], as has been discussed earlier.⁸⁴ However, these ions were found to be very weak in nature since the collision energy of only 2 eV led to their dissociation into respective parent ions. Therefore, the described perturbations in the excitation wavelength dependent behavior of irradiated FAP ILs could be attributed to the irradiation induced decoupling or break down of such pre-existing different associated forms of the cations and anions (in the unirradiated IL) and simultaneously driving the formation of oligomers and other species containing multiple bond order groups. Indeed, it was substantiated by the vibrational studies (FTIR and Raman) which are discussed in the subsequent sections.

5.3.6.2. Vibrational studies

We have noticed a strong correlation between the vibrational changes and fluorescence behavior of irradiated ILs. The FTIR spectra of pre- and post-irradiated [EMIM][FAP] are shown in Fig.5.20, while Fig.5.21 represents the spectra of particular wavenumber regions with significant alterations in the amplified scale for better visibility.

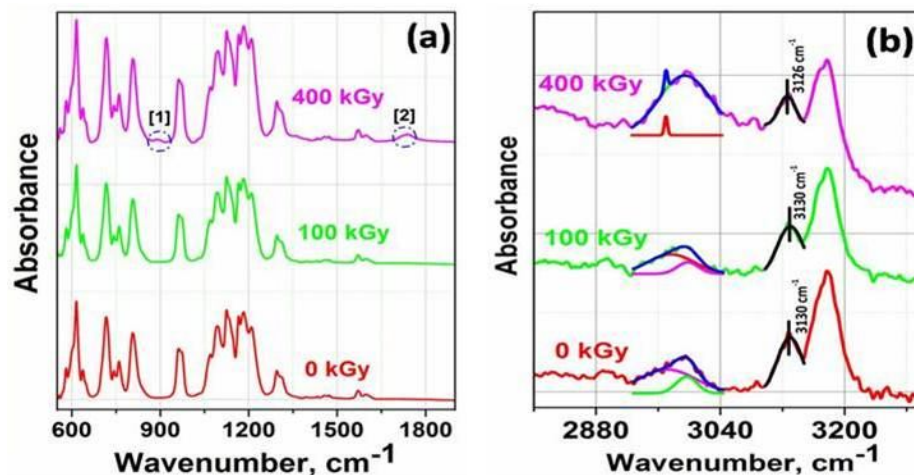


Fig.5.20. FTIR spectra of neat pre- and post-irradiated [EMIM][FAP] at various absorbed doses (in kGy) i.e. 0, 100 and 400.

Up to a dose of 100 kGy, no significant change was observed in the FTIR spectra of irradiated ILs, which reflects their radiation stability. However, at an absorbed dose of 400 kGy, following modulations were observed. The peak at $\sim 890 \text{ cm}^{-1}$ (peak marked as [1] in Fig.5.20; Fig.5.21a) has been attributed to the olefinic C-H bending vibrations, which indicates the formation of radiolytic products having vinylidene double bond ($>\text{C}=\text{CH}_2$).³⁰² The intensity of the peaks in the region $1180\text{-}1220 \text{ cm}^{-1}$ were found to increase on irradiation (for dose $\geq 100 \text{ kGy}$), which could be attributed to the formation of radiolytic products with $-\text{CF}_3$ units.³⁰³ At the same time, some perturbations in the imidazolium ring and possible dissociation (or dislocations) of the alkyl groups attached to it were noticed from the decrease in the intensity of peaks located in the region $1400\text{-}1480 \text{ cm}^{-1}$. These peaks (at $\sim 1433 \text{ cm}^{-1}$, $\sim 1457 \text{ cm}^{-1}$ and $\sim 1463 \text{ cm}^{-1}$) originates due to the ring in-plane asymmetric stretching, (N)CH₃ CN stretching, (N)CH₃ HCH symmetric bending.^{303, 304} Another absorption band centered at $\sim 1736 \text{ cm}^{-1}$ (peak marked as [2] in Fig.5.20; Fig.5.21b) signifies the formation of species with double bonds in the form of

Chapter 5

C=C, -CF=CF-, -CF=CF₂.²⁹⁶ To precisely determine the changes in the C-H bond stretching frequencies of the ethyl and the terminal methyl group attached to the side chain of the imidazolium cation, a Gaussian peak fitting was carried out in the region 2900-3000 cm⁻¹ and has been shown in the blue color in Fig.5.20b. The peaks at ~ 2996 cm⁻¹ accompanied by a shoulder at ~ 2972 cm⁻¹ (assigned to Ethyl HCH symmetric stretching)³⁰⁴ were found to be broadened and red shifted by 2-3 cm⁻¹ in post-irradiated [EMIM][FAP] (@ 400 kGy).

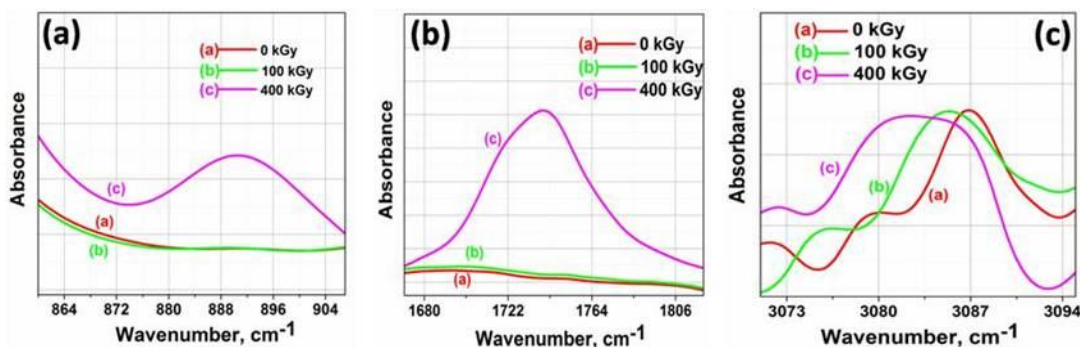


Fig.5.21. FTIR spectra of neat unirradiated and post-irradiated [EMIM][FAP] in different wave number regions at various absorbed doses.

Furthermore, a peak at ~ 3086 cm⁻¹ (for unirradiated [EMIM][FAP]) originated due to the (N)CH₃ HCH asymmetric stretching vibrations^{303c, 305} was red shifted on irradiation of the IL (shown in Fig.5.21c). Subsequently, the broadening in the peaks signifies the presence of radiolytic products mostly derived from the imidazolium cation with varying C-H bond strengths. Certainly, these variations substantiate the realignment of the intermolecular hydrogen bonding interactions among the ionic moieties. Moreover, a red shift observed in the ring NC(H)NCH (or C₂-H) vibrational frequency from 3130 cm⁻¹ to 3126 cm⁻¹ on irradiation of [EMIM][FAP] clearly shows the weakening of the respective

Chapter 5

bond.²⁶⁸ It is to be mentioned here that C-2 position of the imidazolium cation is acidic ($pK_a = 21-22$)^{85b} in nature and prone to deprotonation to form a stabilized carbene. Therefore, the weakening of the C₂-H bond on irradiation can be regarded as strong evidence supporting the vulnerability of imidazolium-derived radical species to undergo oligomerization.^{75-84, 268, 272} Consequently, this has been found to be one of the possible contributing factors behind the color evolution in irradiated imidazolium ILs.

The FTIR spectra of post-irradiated [EOHMIM][FAP] at different absorbed doses (same as in case of [EMIM][FAP]) have been shown in Fig.5.22. A blue shift in the peak frequency originated due to C-N stretching ($\sim 615 \text{ cm}^{-1}$)^{75-83, 268} was observed (Fig.5.23).

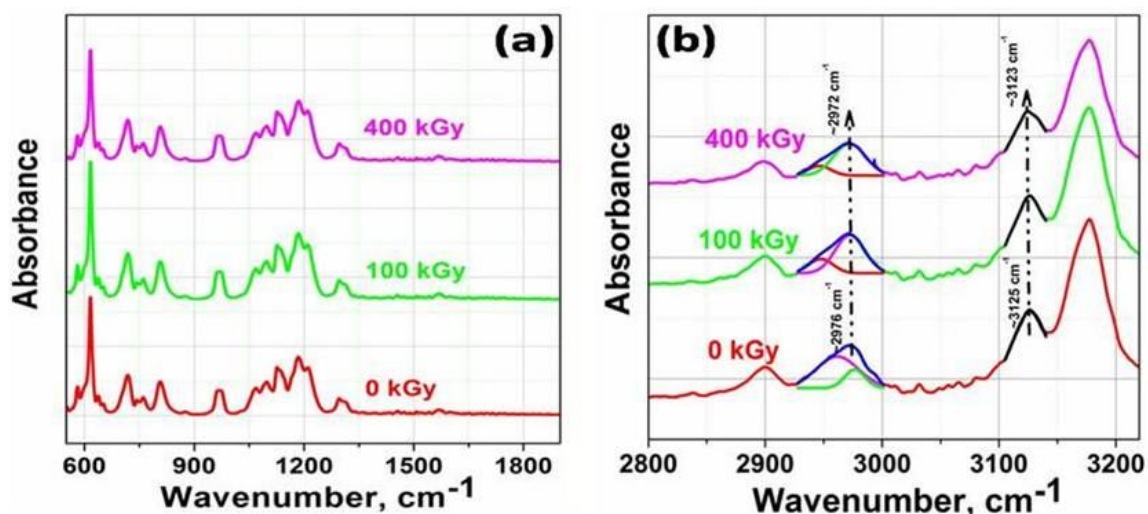


Fig.5.22. FTIR spectra of neat unirradiated and post-irradiated [EOHMIM][FAP] at various absorbed doses (in kGy) i.e. 0, 100 and 400.

Further, analogous to [EMIM][FAP], the formation of radiolytic products with multiple bond order functional groups as well as bathochromic shifts in the C-H stretching frequencies were also observed in case of post-irradiated [EOHMIM][FAP] IL.

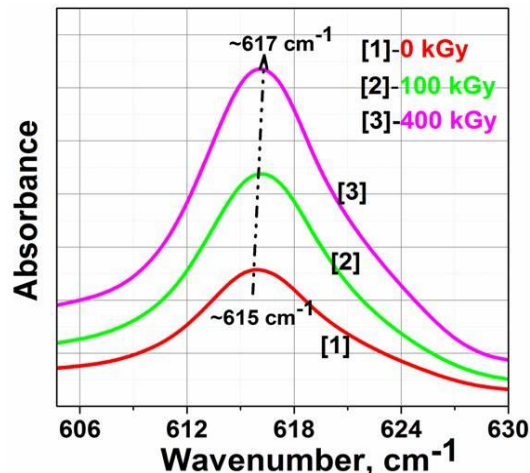


Fig.5.23. FTIR spectra of neat unirradiated and post-irradiated [EOHMIM][FAP] at various absorbed doses i.e. 0 kGy, 100 kGy and 400 kGy.

Peak at $\sim 2976 \text{ cm}^{-1}$ representing the HCH stretching vibrations in the ethoxy group (attached to ring N)^{303c, 304} of [EOHMIM][FAP] red shifted to $\sim 2972 \text{ cm}^{-1}$ on irradiation. Also, the peak at $\sim 3127 \text{ cm}^{-1}$ for the ring NC(H)NCH (or C₂-H) was found to be red shifted to 3123 cm^{-1} .²⁶⁸ The introduction of conjugation by the attachment of alkenyl groups could also be one of the probable reasons behind the observed red shift. In fact, the peaks corresponding to the formation of conjugated C=C groups were noticed in the Raman spectra of irradiated ILs (discussed in the following section). A broad shoulder centered at $\sim 3430 \text{ cm}^{-1}$ was observed in addition to a peak at $\sim 3621 \text{ cm}^{-1}$ in case of unirradiated [EOHMIM][FAP] (see Fig.5.24). These peaks were also observed in the Raman spectra of unirradiated [EOHMIM][FAP], shown in the inset of Fig.5.24. Similar type of broad feature at $\sim 3425 \text{ cm}^{-1}$ and a peak at $\sim 3598 \text{ cm}^{-1}$ have been reported recently by Katsyuba *et al.*³⁰⁶ in case of [EOHMIM][PF₆]. The former peak was assigned to the vOH of hydrogen bonded cationic clusters, while the later one was attributed to the

Chapter 5

OH stretching frequency hydrogen bonded to the F atom of the PF_6^- anion ($\nu\text{OH}\cdots[\text{PF}_6^-]$). Moreover, the νOH in case of isolated $[\text{EOHMIM}]^+$ cation has been reported to be 3690 cm^{-1} by computational analysis.³⁰⁶ Taking account of these, the peak at $\sim 3621\text{ cm}^{-1}$ has been attributed to the stretching frequency of $-\text{OH}$ hydrogen bonded to the FAP anion ($\text{Im}(\text{OH})\cdots[\text{FAP}]^-$). While the broad shoulder centered at $\sim 3430\text{ cm}^{-1}$ could be assigned to the stretching frequency of $-\text{OH}$ hydrogen bonded to the other hydroxyl groups of neighboring cations; the pre-existence of such cationic clusters have been observed and discussed earlier. The possible $-\text{OH}$ bonding interactions (discussed so far) existing in $[\text{EOHMIM}][\text{FAP}]$ has been pictorially represented in Fig.5.24.

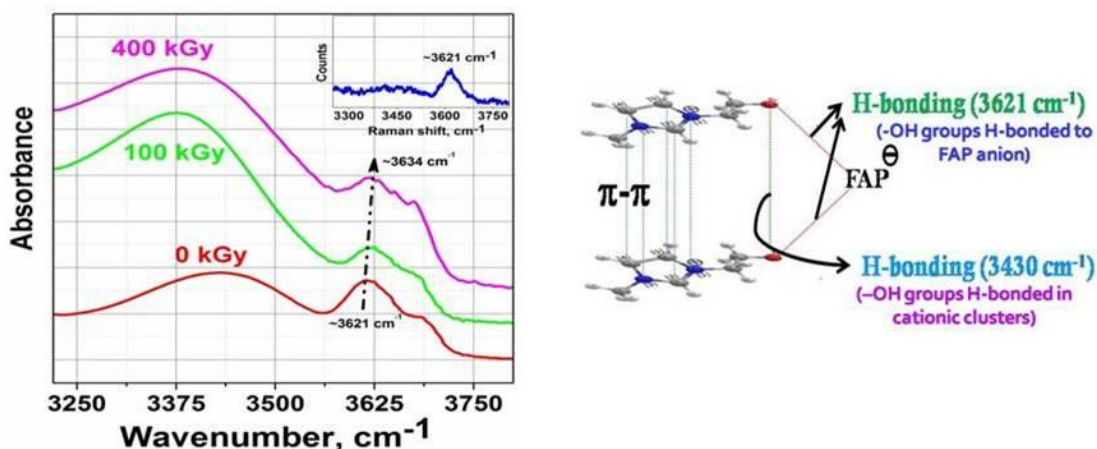


Fig.5.24. FTIR spectra of unirradiated and post-irradiated $[\text{EOHMIM}][\text{FAP}]$ showing the perturbations in the O-H stretching frequency at various absorbed doses i.e. 0 kGy, 100 kGy and 400 kGy. Inset: Graph showing the Raman spectrum of unirradiated $[\text{EOHMIM}][\text{FAP}]$ in the same frequency region as that of FTIR. Pictorial representation of $-\text{OH}$ bonding interactions possibly existing in $[\text{EOHMIM}][\text{FAP}]$.

Nevertheless, an interesting observation of a blue shift in the peak frequency from $\sim 3621\text{ cm}^{-1}$ (for unirradiated $[\text{EOHMIM}][\text{FAP}]$) to $\sim 3634\text{ cm}^{-1}$ (in post-irradiated $[\text{EOHMIM}][\text{FAP}]$) was noticed (Fig.5.24). This signifies the weakening of the hydrogen

Chapter 5

bond ($\text{Im}(\text{OH})\cdots[\text{FAP}]^-$) between the OH and the FAP anion. On the other hand, broad peak at $\sim 3430\text{ cm}^{-1}$ was red shifted to $\sim 3380\text{ cm}^{-1}$ indicating the reduction in the O-H bond strength. Apparently, it points towards the possible distribution of the O-H bond strength, which could be due to the involvement of -OH group in multiple non-covalent bonding interactions with the newly formed radiolytic species in its neighborhood. At this stage, it is important to mention that the geometry involving the orientation and the interactions of the cations and the anions in -OH group functionalized ILs is different from non-hydroxyl ILs. It has been reported earlier²⁹³ that anions are located in front of the imidazolium ring, where more negatively charged atoms are close to the alkyl groups and in particular, $\text{C}_2\text{-H}$ in all the non-hydroxyl ILs. However, the anions are somewhat above the imidazolium ring, moving close to the -OH group in case of hydroxyl containing ILs such as $[\text{EOHMIM}][\text{FAP}]$. Considering this, the aforementioned shifts in the vibrational peaks can be regarded as an important evidence for the reorientation or restructuring occurring in $[\text{EOHMIM}][\text{FAP}]$ on irradiation.

Raman spectra of irradiated FAP ILs further substantiated the FTIR studies. Baseline corrected Raman spectra of $[\text{EMIM}][\text{FAP}]$ and $[\text{EOHMIM}][\text{FAP}]$ has been shown in Fig.5.25. As can be seen, the Raman spectra of the ILs did not exhibit significant changes on irradiation up to an absorbed dose of 100 kGy. However, the analysis of the Raman spectra of the ILs irradiated at an absorbed dose ≥ 200 kGy became difficult due to the increase in the contribution of fluorescence from the radiolytic products.

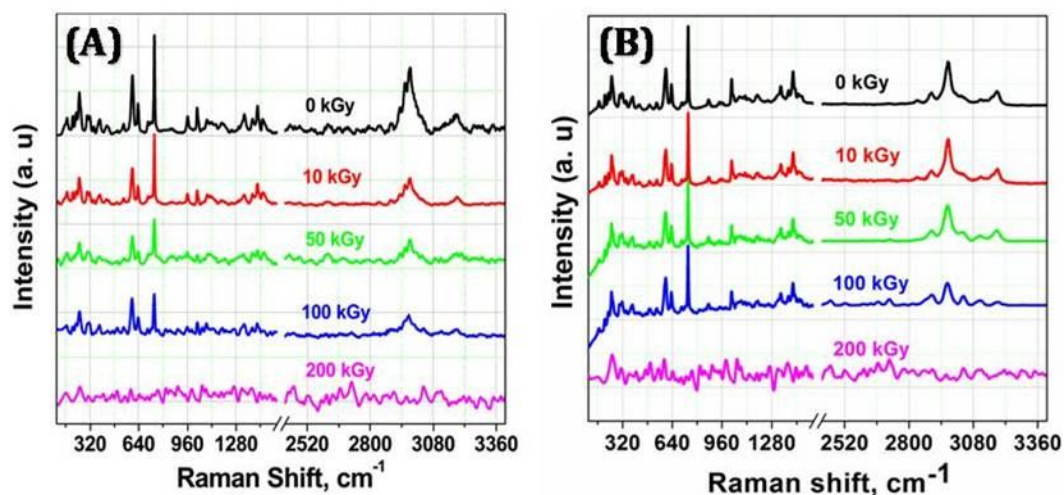


Fig.5.25. Raman spectra of neat unirradiated and post irradiated [EMIM][FAP] (A) and [EOHMIM][FAP] (B) at various absorbed doses.

Nevertheless, a red shift in the symmetric bending modes of $-\text{CF}_3$ ($\sim 742 \text{ cm}^{-1}$) as well as a new broad peak centered at $\sim 985 \text{ cm}^{-1}$ was observed for both the FAP ILs on irradiation (see Fig.5.26a & b and Fig.5.27a & b). The appearance of broad peak at $\sim 985 \text{ cm}^{-1}$ indicates the formation of radiolytic products with vinyl C-H groups.³⁰² A broad peak marked as [2] ($1050\text{-}1070 \text{ cm}^{-1}$) in Fig.5.26b is most plausibly attributed to the formation of fluoroalkanes.³⁰² Besides, in-plane bending C-H vibrational frequency (in [EMIM][FAP]) at $\sim 1088 \text{ cm}^{-1}$ red shifted to 1085 cm^{-1} on irradiation.^{303b} Furthermore, red shifts in the frequencies representing ring in-plane asymmetric stretching, CC stretching, CH_3 (N) CN stretching (from 1421 cm^{-1} to 1419 cm^{-1}) and broadening in the CH_2 (N) CN stretching vibrations ($\sim 1570 \text{ cm}^{-1}$)^{303c} was observed in Raman spectra of [EMIM][FAP] on irradiation. Similar distortions in the corresponding wavenumber regions were observed for post-irradiated [EOHMIM][FAP] (see Fig.5.27). An important observation was the appearance of peaks in the range $1600\text{-}1650 \text{ cm}^{-1}$ in both the

Chapter 5

irradiated FAP ILs and these have been assigned to the formation of radiolytic products with conjugated C=C groups (alkenyl C=C stretching).³⁰² It could be regarded as another strong signature of the formation of chromophoric species responsible for the color evolution in imidazolium based ILs on irradiation.

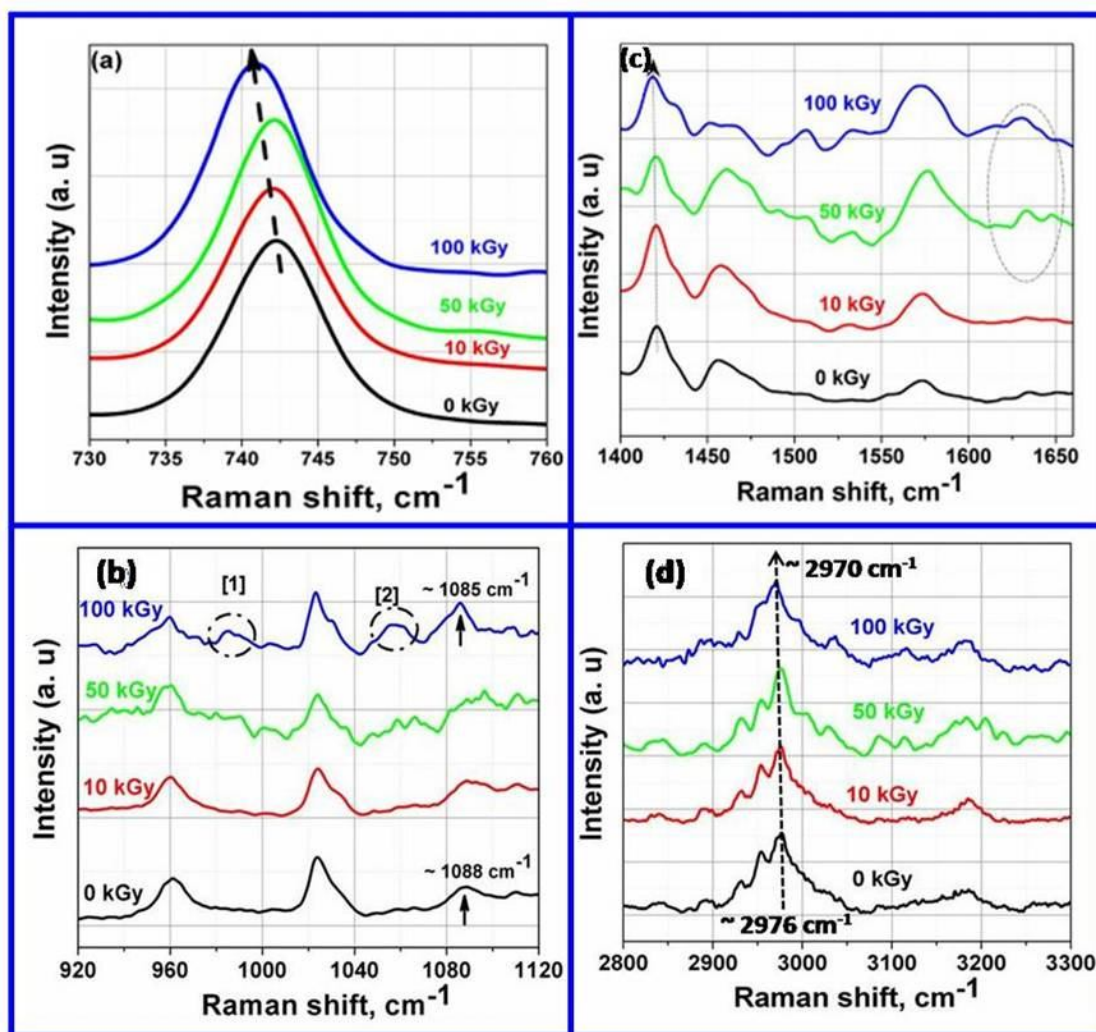


Fig.5.26. Raman spectra of neat unirradiated and post-irradiated [EMIM][FAP] in different wave number regions at various absorbed doses.

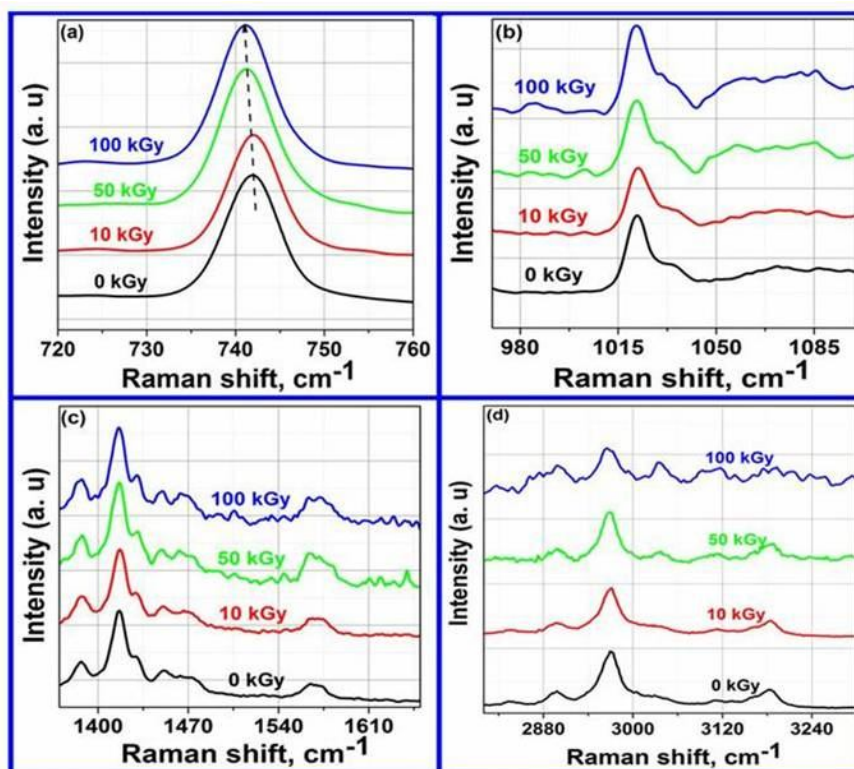


Fig.5.27. Raman spectra of neat unirradiated and post-irradiated [EOHMIM][FAP] in different wave number regions at various absorbed doses.

There have been additional strong evidences which indicate perturbations in the bonding interactions amongst the cationic and the anionic moieties and their surrounding environments. This could be observed primarily from the variations in the C-H stretching frequencies of the alkyl side chains in the region 2800-3200 cm^{-1} . For instance, in case of [EMIM][FAP], peak representing the ring CH_3 HCH symmetric stretching at $\sim 2932 \text{ cm}^{-1}$ red shifted to $\sim 2929 \text{ cm}^{-1}$ at an absorbed dose of 100 kGy.³⁰⁴ Peak at $\sim 2953 \text{ cm}^{-1}$ could be assigned to CH_2 HCH stretching frequency,³⁰⁴ which was found to be broadened at high absorbed dose (Fig.5.26d), and might be attributed to the presence of radiolytic products with variations in the C-H bond strengths. Further, a red shift (from 2976 cm^{-1} to

Chapter 5

2970 cm^{-1} @ 100 kGy) in the asymmetric stretching vibrational frequency of ethyl HCH was observed (in [EMIM][FAP]), which signifies the weakening of the respective bond.³⁰⁴ Similar red shift was observed (asymmetric stretching vibrational frequency of ethyl HCH) for irradiated [EOHMIM][FAP] (@ 100 kGy). Peak at $\sim 3180 \text{ cm}^{-1}$ representing the ring HCCH symmetric stretching³⁰⁴ broadened at higher absorbed doses in both the FAP ILs, which is a clear indication of the presence of radiolytic products derived from the imidazolium cation with varying bond strengths.

The vibrational studies hitherto categorically reflect the considerable changes in the inherent spatial correlations of the ionic species (in ILs) on irradiation.

5.3.6.3. Fluorescence lifetime studies

The influence of irradiation induced decoupling of particular pre-existing arrangements and related perturbations in the bonding interactions (amongst cationic and anionic moieties) were further observed from the fluorescence lifetime behavior of FAP ILs (shown in Fig.5.28); especially in case of -OH group containing [EOHMIM][FAP].

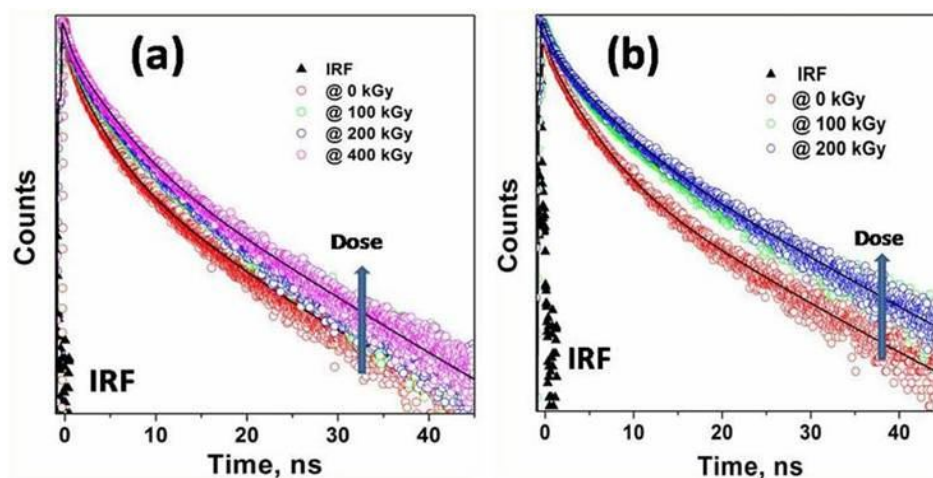


Fig.5.28. Lifetime decay profile of neat irradiated [EMIM][FAP] (a) and [EOHMIM][FAP] (b) at various absorbed doses.

Chapter 5

On irradiation, the average lifetime of [EMIM][FAP] and [EOHMIM][FAP] increases with the rise in the absorbed dose imparted however, the trend was found to be more prominent in the later case (see Table 5.10).

Table 5.10: Lifetime values for post-irradiated [EMIM][FAP] and [EOHMIM][FAP] at various absorbed doses. The values provided in the parentheses are the respective amplitudes for each times constants (T_1 , T_2 , and T_3).

Sample	Dose	T1	T2	T3	χ^2	$\langle\tau\rangle$, ns
[EMIM][FAP]	0 kGy	2.47 ns (0.42)	9.02 ns (0.50)	0.42 ns (0.08)	1.09	5.58 ns
[EMIM][FAP]	100 kGy	3.40 ns (0.39)	9.84 ns (0.51)	0.95 ns (0.10)	1.08	6.43 ns
[EMIM][FAP]	200 kGy	3.40 ns (0.41)	9.87 ns (0.51)	0.88 ns (0.08)	1.08	6.49 ns
[EMIM][FAP]	400 kGy	3.48 ns (0.41)	10.2 ns (0.52)	0.92 ns (0.07)	1.03	6.79 ns
[EOHMIM][FAP]	0 kGy	3.14 ns (0.49)	9.93 ns (0.41)	0.76 ns (0.1)	1.03	5.68 ns
[EOHMIM][FAP]	100 kGy	4.25 ns (0.40)	11.3 ns (0.48)	1.35 ns (0.13)	1.05	7.29 ns
[EOHMIM][FAP]	200 kGy	3.86 ns (0.31)	10.0 ns (0.60)	1.19 ns (0.09)	1.06	7.30 ns

The multi-exponential behavior signifies the heterogeneous nature of these media and indicates the existence of energetically distributed aggregates with different conformations, as has been reported earlier.³⁰¹ Nonetheless, the exact reason for the increasing trend in the average lifetime values of FAP ILs with higher absorbed doses is not precisely clear. However, the probable explanation could be the formation of new intermolecular hydrogen bonds and other non-covalent bonding interactions (i.e. π - π) between radiolytic products and the ionic moieties, as indicated from the vibrational

Chapter 5

studies. Consequently, enhancement in the rigidity level in the vicinity of the ions can be anticipated which eventually might have hindered the non-radiative decay processes leading to the increase in the average lifetime values observed in case of post-irradiated FAP ILs.

5.4. Conclusions

Considering the anticipated applications of RTILs, an in-depth report on the physicochemical characteristics and their changes after deposition of ionizing radiation for an important class of ILs has been presented herein. The color evolution in the imidazolium based ILs on irradiation could be rationalized through the formation of oligomeric and multiple bond order group containing radiolytic products. The significant radiation resistance put forth by FAP ILs has been correlated well with the fractional stopping power of the FAP anion, which clearly implicates it as an effective protector/shield (among various other fluoroanion based ILs) to the cation. Through pulse radiolysis studies, the influence and the radiolytic sensitization effects of the -OH group substitution on the reaction mechanistic pathways could be delineated. The insignificant variations in the physicochemical properties even at high absorbed doses clearly indicate the hidden potential of FAP based imidazolium ILs to be a good solvent for various applications involving high radiation fields. Nevertheless, the photophysical behavior of pre- and post-irradiated FAP ILs categorically points towards the considerable changes in the orientations and the molecular rearrangements of the ions on irradiation. For instance, (i) bathochromic shifts in the excitation wavelength dependent fluorescence spectra of irradiated FAP ILs, (ii) vulnerability of the C₂-H to undergo deprotonation, (iii) blue shift

Chapter 5

in the O-H stretching frequency (in case of -OH functionalized FAP IL) and (iv) the observation of vibrational peaks originated due to multiple bond order groups are some of the additional findings of this study, which could be useful in gaining a comprehensive understanding of the radiation driven degradation of ILs and its mechanistic pathways.

Chapter 6

Room temperature ionic liquids as a media for the synthesis of complex nanostructures

6.1. Introduction

RTILs have recently received a great deal of attention for the synthesis of various nanomaterials.^{87, 88, 98, 307} Various synthetic techniques have been employed for this purpose such as electrodeposition,³⁰⁸⁻³¹¹ solvothermal,^{91, 312-314} sol-gel,^{315, 316} sonication³¹⁷ and radiation induced (e⁻-beam,³¹⁸⁻³²⁰ γ -ray,^{321, 322} microwave^{93, 323}) methods.

However, the fundamental questions regarding the role of the inherent structure of the IL in directing the morphology and the growth mechanism of the nanoparticles are still unexplored. Considering the self-organized networking structure of RTILs, it would be quite intriguing to examine the potential of these solvents in the templated synthesis of self-assembled nanostructures with exciting applications. It is to be noted that the phenomenon of self-assembly of nanomaterials is one of the hot topics nowadays for its potential application mainly in the field of energy conversion and storage.^{324, 325}

This chapter describes the work on the application of RTILs as a novel media for the synthesis of self-assembled superstructures of metal chalcogenide nanomaterials. CdSe nanoparticles were synthesized in *neat* imidazolium based IL *via* radiation as well as normal chemical route. In the radiation chemical route, considering the high radiation stability of ILs (described in Chapter 5), electron beam irradiation technique was

Chapter 6

employed to initiate the nucleation process. A unique nanomorphology i.e. islands of CdSe nanoparticles within Se nanofibers, was obtained in this particular case. The main objective was to explore and exploit the noble structural features of RTILs and the special features of electron beam irradiation technique in synthesizing and directing the self-assembly of NPs into well-defined structures of fundamental importance. In the normal chemical route, the synthesis was carried out at purely ambient conditions without perturbing the internal structure of the IL by external parameters such as temperature or any external solvents (for dilution)/stabilizing agent. Herein, the aim was to probe the role of the structural and the fluidic aspects of IL in influencing the morphology of nanoparticles grown *in situ*.

Based on the synthetic techniques, the work carried out in this part of the thesis has been divided and described under two sections i.e. (i) Radiation and (ii) Normal chemical routes for the synthesis of CdSe nano/microstructures in the host matrices of RTILs. The possible mechanism behind the as obtained nanomorphologies in both the cases has been proposed in the respective sections.

6.2. Radiation mediated synthesis

6.2.1. Materials and Methods

High purity chemicals, cadmium sulfate (CdSO_4), Sodium Selenite (Na_2SeO_3), sodium sulfite, *tert*-butanol were obtained from Sigma-Aldrich and used without further purification. Other chemicals such as ethanol and acetone used for subsequent cleaning and washing off the organic impurities from the precipitates were obtained from SDFCL, Mumbai, with highest purity. The IL, 1-Ethyl-3-methyl imidazolium ethylsulfate

Chapter 6

([EMIM][EtSO₄]) was obtained from Alfa Aesar (UK) with a purity of 99%. The water content in the IL was measured by coulometric Karl-Fischer method using a Metrohm 831 KF Coulometer and was determined to be very less (i.e. 20 ppm) to cause any considerable changes in the intrinsic structure of the IL.

It is to be mentioned here that same IL ([EMIM][EtSO₄]) was employed as the solvent for the synthesis of the nanoparticles in both the methodologies. Most commonly used RTILs containing PF₆ and BF₄ anions are vulnerable to hydrolysis in the presence of water and eventually lead to the formation of toxic and corrosive species.^{270b, 285b, 326} On the contrary, alkyl sulfate anion based ILs (e.g. as employed [EMIM][EtSO₄]) are halogen-free and relatively hydrolysis-stable, providing better alternative for industrial applications. The molecular structure of the IL has been shown in Fig.6.1 along with the denotations of various atoms of cation and the anion.

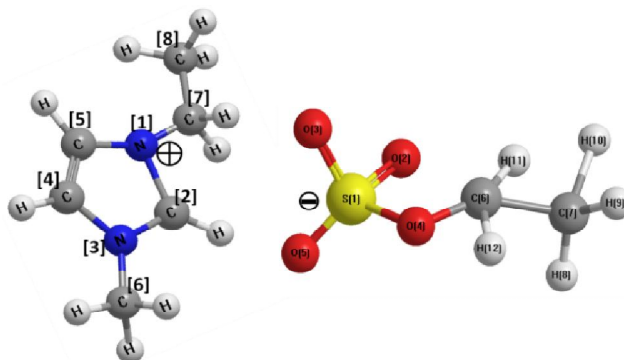


Fig.6.1. Structure of IL, 1-ethyl-3-methylimidazolium ethylsulfate ([EMIM][EtSO₄]).

The procedure for the preparation of sample solution containing the precursors has been described as follows. Cadmium sulfate (CdSO₄), 0.0156 gm and Sodium selenite (Na₂SeO₃), 0.0129 gm were dissolved in 1.5 ml of IL ([EMIM][EtSO₄]) by sonicating for 30-45 minutes. The resultant solution was nitrogen bubbled and irradiated with a 7 MeV

Chapter 6

electron beam having an FWHM (Full width at half maximum) of 2 μs from a LINAC. The absorbed dose per pulse was kept at 140 Gy and the samples were irradiated with repeated pulses at a rate of 12 pulses per second with a total absorbed dose of 10 kGy. After irradiation, the color of the solution changed to reddish orange, which is the primary indication of the formation of CdSe nanoparticles. The techniques for the nanoparticle characterization have been discussed in Chapter 2.

6.2.2. Results and Discussion

UV-Vis absorption spectrum of the electron beam irradiated solution clearly shows an excitonic peak at ~ 580 nm (Fig.6.2). The inset of Fig.6.2 shows the evolution of color in the IL containing precursors of Cd and Se on irradiation.

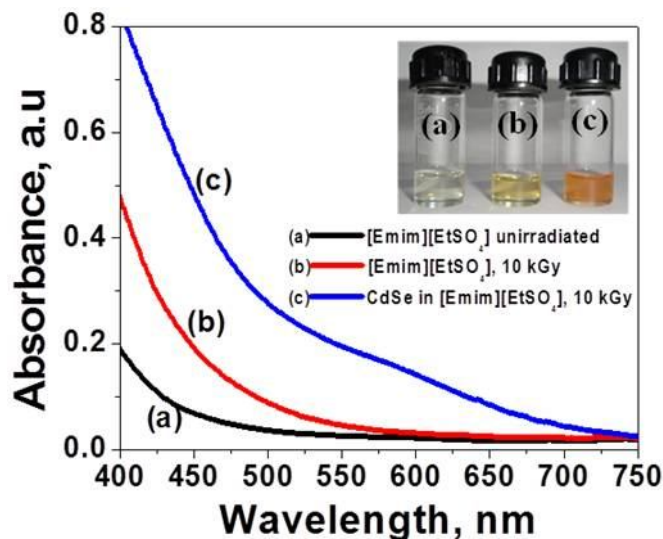


Fig.6.2. UV-Vis absorption spectra of CdSe nanoparticles synthesized in IL via electron beam irradiation, Dose = 10 kGy. Inset shows the camera ready picture of the unirradiated IL, (a); neat IL (10 kGy), (b); IL + CdSe (10 kGy), (c).

However, the neat IL also exhibited greenish yellow color on irradiation at similar radiation doses. This implies that the IL had undergone some degradation on irradiation.

Chapter 6

It is to be mentioned here that various studies have showed the high radiation stability of imidazolium based ILs even at a radiation dose of 500 kGy and only up to 1 mol% (or less) of the IL undergo degradation.^{75, 76, 78-83} The evolution of color has been attributed to the generation of oligomeric (having high molar extinction co-efficient) and possibly carbene related species.^{76, 79, 83} Apart from these, we have also investigated the extent and mechanism of radiation stability of the imidazolium based FAP ILs and the results obtained are in full agreement with the similar studies carried out earlier by various researchers.⁸⁴ As can be seen from Fig.6.2 that the unirradiated IL, [EMIM][EtSO₄] does not exhibit any significant absorption in the visible spectrum range of 400-700 nm. While, on irradiation to higher doses, the imidazolium based ILs display absorption mainly up to 480 nm. The similar features have been reported for irradiated imidazolium based ILs by various researchers.^{76, 79, 80, 83} Therefore, the peak at around 580 nm has been assigned to the formation of CdSe nanoparticles.

However, the excitonic peak corresponding to the CdSe nanoparticles is not well resolved. One of the possible reasons for such features could be the polydispersity in the size, shape or the mass distribution of the particles formed.³²⁷ As a matter of fact, the well established characteristic of RTILs i.e. microheterogeneity can cause such non-uniformity in any of the aforementioned structural features. The other probable reason could be the formation of other species having absorption near to the excitonic peak position of the CdSe nanoparticles. In this perspective, Se nanoparticles does exhibit similar absorption features as that of CdSe nanoparticles.³²⁸ To assess such possibility, Na₂SeO₃ was solely irradiated in the IL maintaining all other parameters exactly similar as in the case of the

Chapter 6

synthesis of CdSe nanoparticles. The color of the solution turned to brick red (indication of the formation of Se). Subsequently, the absorption spectrum of this sol was measured and two peaks at 435 and 625 nm were observed, as shown in Fig.6.3. To eliminate the possible absorption effects of the radiolytic products of the ILs, the precipitates were extracted from the sol and washed thoroughly using ethanol. The as obtained precipitates of Se exhibited similar absorption features, when re-dispersed in ethanol. The results suggest the possible formation of Se nanostructures along with the CdSe nanoparticles.

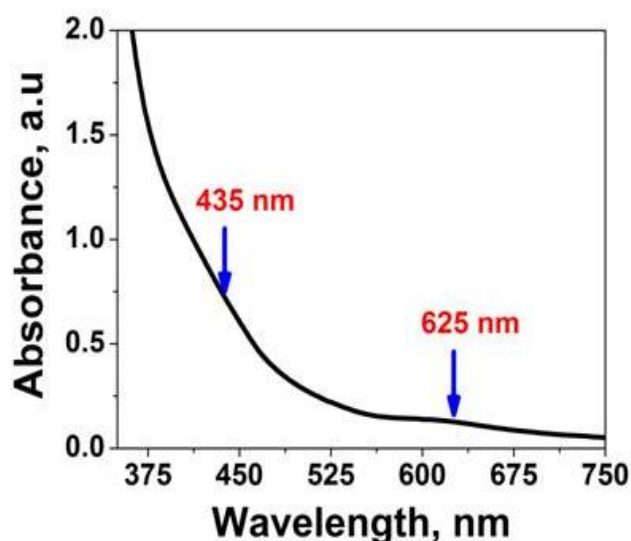


Fig.6.3. UV-Vis absorption spectra of Se nanoparticles synthesized in IL ([EMIM][EtSO₄]) via electron beam irradiation, Dose = 10 kGy.

In order to probe the morphology of as grown nanoparticles, the precipitates obtained from the irradiated solution (containing Cd and Se precursors in IL) were extracted and washed 5 to 6 times with ethanol to remove any impurities. These precipitates were used for further characterization studies. The TEM image of as grown nanoparticles showed an interesting leaf-like morphology (Fig.6.4a).

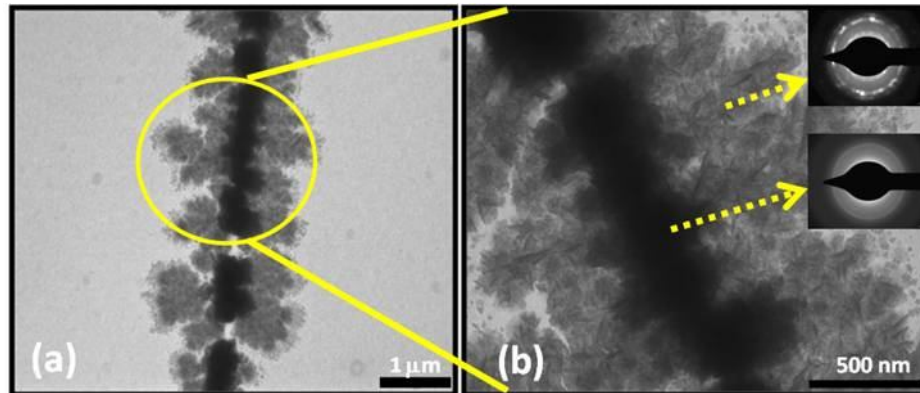


Fig.6.4. TEM image of the nanostructure synthesized in IL via electron beam irradiation, Dose = 10 kGy. Inset: SAED pattern of the fibrous and the thick black chunks.

The image gives an impression of a leaf, where large number of small veins creep out from the main vein. However, some fiber like morphology (Fig.6.4b) surrounding the thick black chunks partially segregated from each other appeared on going for the deeper insight of the encircled portion of the earlier image. The inset of Fig.6.4b shows the SAED pattern of the fibrous and the thick black chunk regions, which clearly indicates the semicrystalline and the predominantly amorphous (diffused rings) nature of these respective areas. From the TEM images, it appeared that the nanofiber like structure has been probably formed, but the nature of the thick black chunks could not be known. To further probe the as obtained morphology, SEM analysis of the precipitates were carried out on a silicon wafer. A unique highly porous appearing structure of entangled nanofibers surrounding the chunks (similar to those as observed in TEM image) within its network was obtained. The compositional analyses of the fiber region as well as of the chunks were carried out with EDS. The probed regions have been marked in the SEM image and the corresponding EDS spectra are shown in the right panel of Fig.6.5.

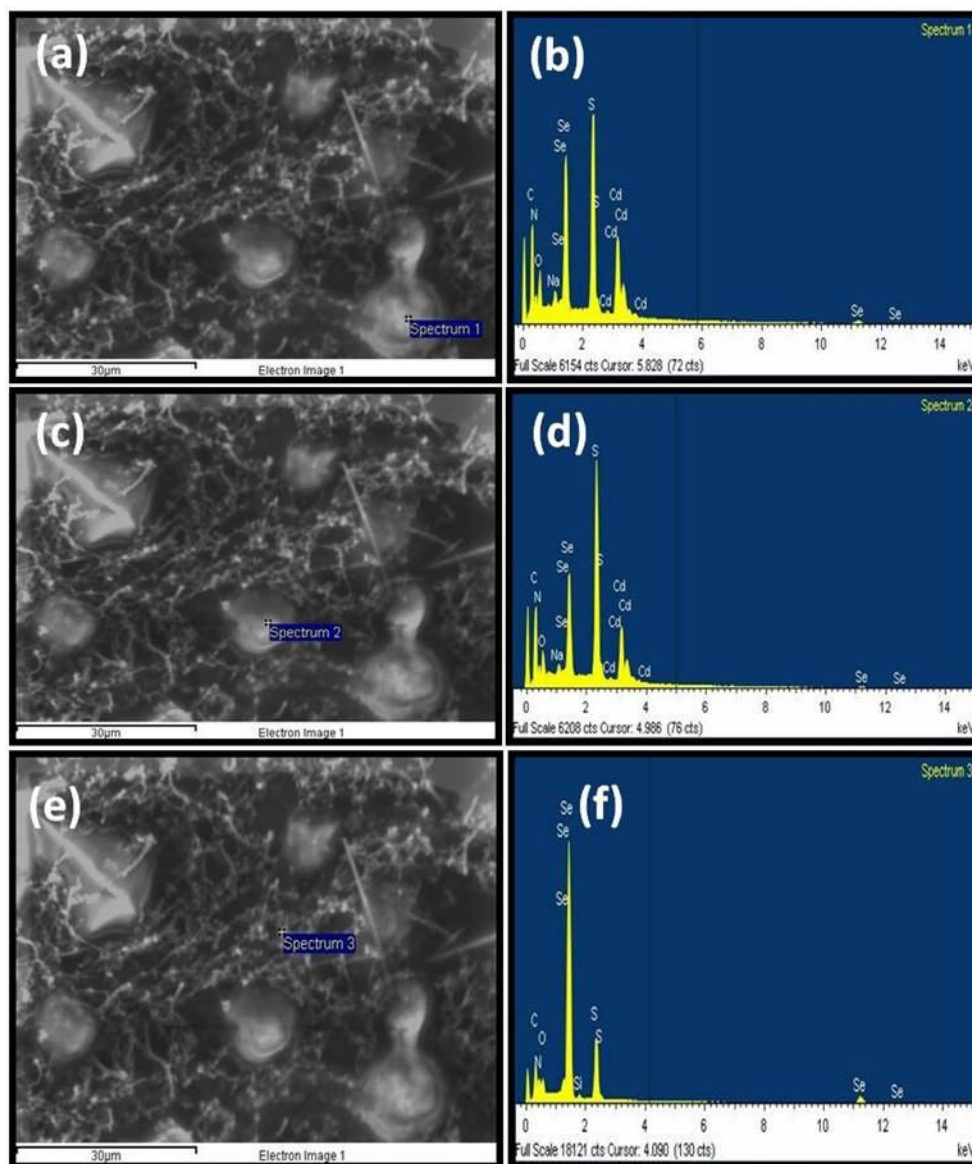


Fig.6.5. SEM images (a, c, e) of the nanostructures synthesized in IL ($[EMIM][EtSO_4]$) via electron beam irradiation at various regions. Adjacent images (b), (d), (f) corresponds to the EDS of the marked locations in the SEM images (a), (c) and (e) respectively.

The images showing the EDS (Fig.6.5 b, d and f) of the respected marked areas on the SEM images revealed some interesting compositional features. The EDS analysis of the chunk region marked as ‘spectrum 1’ and ‘spectrum 2’ (Fig.6.5 b and d) clearly showed

Chapter 6

the presence of Cd and Se. But, the presence of S (sulphur) along with Cd and Se signifies two possibilities. Presence of Sulphur could lead to the formation of ternary nanoparticles with composition as *CdSSe* or it could be present in the form of an impurity. There have been reports of the formation of such alloyed type nanocrystalline materials.³²⁹ While, the EDD of the fibrous region marked as ‘spectrum 3’ showed the presence of only Se (no Cd) along with S. The origin of Sulphur could be from the Cd precursor (CdSO_4) or from the IL itself as its anionic moiety i.e. ethyl sulphate contains S. However, the presence of S in the chunk areas as well as in the fibrous region raised a question of its being present in the alloyed form (as *CdSSe*).

To resolve this issue, Raman spectroscopy of the chunks and the fibrous region was carried out. In fact, Raman spectroscopy is a very powerful tool for characterization and conformational analysis of II-VI nanoparticles.³³⁰ Essentially, *CdSSe* is a ternary compound and is placed among the well-known ‘two-mode behaviour alloys,’ which displays simultaneous presence of optical phonon modes corresponding to CdS and CdSe.³³¹ Consequently, the formation of *CdSSe* would be associated with CdSe like LO1 (longitudinal optical phonon) peak at around 200 cm^{-1} (198.5^{329a} , 205^{332a} , 199^{331a} , 210^{332b}) and CdS like LO2 peak at around 300 cm^{-1} (298^{329a} , 290^{332a} , 292^{331a} , 302^{332b}) in its Raman spectra. Simultaneous appearance of TO1 (Transverse optical) modes of CdSe at around 175 cm^{-1} ^{330a, 333} and TO2 modes of CdS at around 228 cm^{-1} ³³⁴ can also be used as the indicators for the formation of *CdSSe* compound. However, Raman spectra of as obtained nanostructure measured at various regions (Fig.6.6) did not show any of these characteristic peaks of CdS. Thus, we can rule out the possibility of the formation of

Chapter 6

CdSSe compound. In fact, along with S, the peaks corresponding to the elements such as C, N, and O may be noticed, which signifies not only the efficient coating by the IL on the surface of as obtained nanostructure, but also excludes the possibility of the formation of any binary or ternary compound containing S.

Further, Raman spectra revealed the formation of a mixture of both amorphous selenium (a-Se) and trigonal crystalline selenium (t-Se), which substantiates the semicrystalline nature of the fibrous nanostructure, as earlier indicated by the SAED pattern. The peak observed at $\sim 256\text{ cm}^{-1}$ is quite broad and comprises of shoulders, which indicates the formation of a-Se, while the peak at 235 cm^{-1} has been assigned to t-Se.³³⁵ In fact, another crystalline form of Se, which is monoclinic in nature (m-Se) and exist as Se_8 ring structures also exhibit Raman peak at around 254 cm^{-1} ,³³⁶ similar to a-Se. This pattern signifies the co-existence of chains (in the form of t-Se) and rings (in the form of m-Se) along with a-Se in the final product. The Raman spectra (Fig.6.6 a & c) with peak at 204 cm^{-1} is the typical signature of the presence of CdSe nanoparticles and has been attributed to the LO1 mode, as mentioned earlier. The high frequency component at around 456 cm^{-1} (Fig.6.6 a & b) has been assigned to the second order spectra of t-Se³³⁶,³³⁷ and the low frequency component in the form of a shoulder at $\sim 175\text{ cm}^{-1}$ (Fig.6.6 b & d) appeared to be originated from the TO1 mode of the CdSe nanoparticles. However, most of the Se containing compounds does exhibit a significant intensity band at $\sim 173\text{ cm}^{-1}$, which has been attributed to the vibrating modes of Se.³³⁸

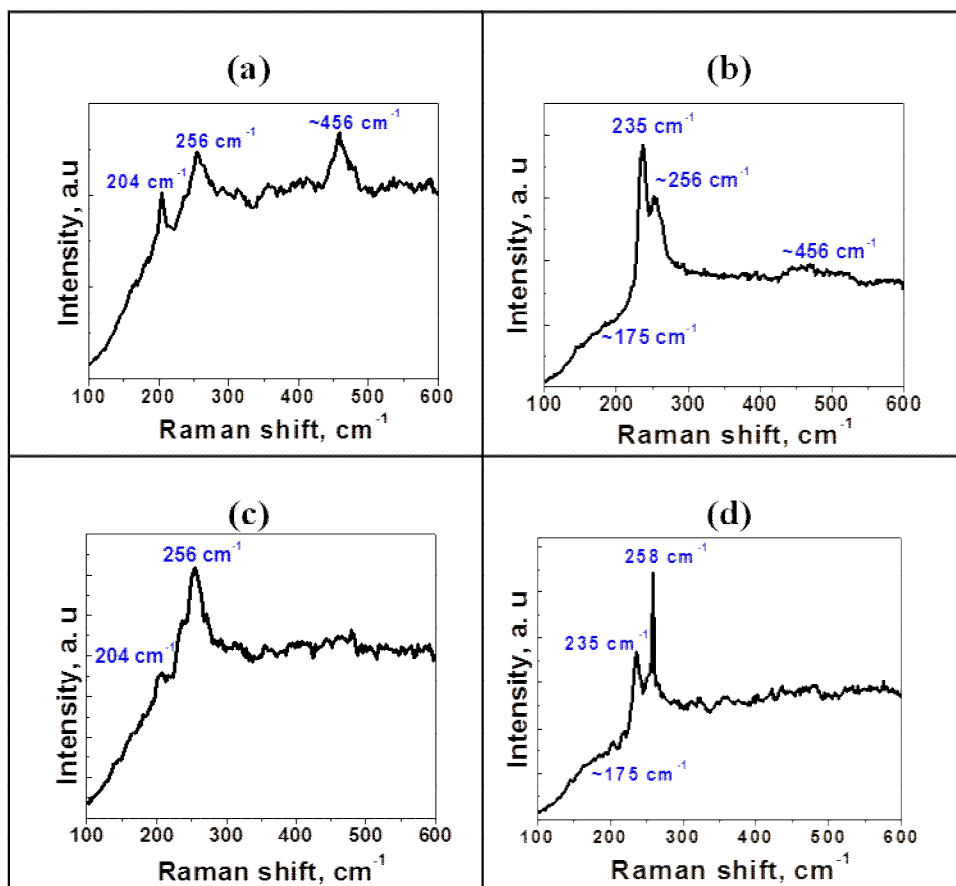


Fig.6.6. Raman spectra of the nanostructures synthesized in IL ([EMIM][EtSO₄]) via electron beam irradiation at various regions: (a) & (c) depicts the formation of CdSe nanoparticles, while (b) & (d) represents the fibrous regions (comprises of mainly Se) present in the sample.

Of late, a broad and low intensity band in the range of 50-175 cm⁻¹ has been reported by Edwards *et al.*³³⁹ for Germanium selenide glasses (similar to our case) and the same was assigned to the bending and rocking modes of Se atoms. Furthermore, Hartree–Fock *ab initio* Raman spectra calculations were performed by Lukács *et al.*³⁴⁰ on a-Se and a small shoulder peak at 179.4 cm⁻¹ has been assigned to the vibrating modes of interchain Se-Se atoms. Therefore, to resolve the issue about the origin of band near 175 cm⁻¹,

Chapter 6

Raman spectra of the precipitates of Se nanoparticles was recorded. Interestingly, analogous pattern of Raman bands were observed from the as obtained precipitates of Se nanoparticles (Fig.6.7).

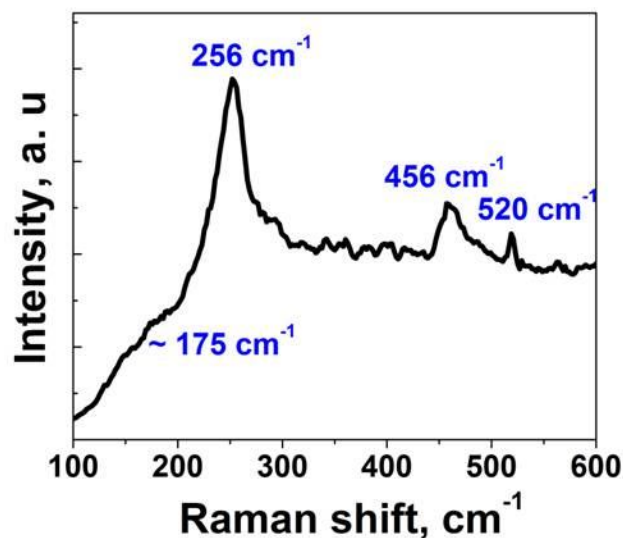


Fig.6.7. Raman spectrum of the Se nanoparticles synthesized in IL ([EMIM][EtSO₄]) via electron beam irradiation, Dose = 10 kGy.

The peak at $\sim 256 \text{ cm}^{-1}$ is broad and comprises of shoulders, which is a clear indication of the formation of chains and ring structures of Se. The peak at 520 cm^{-1} belongs to the Si wafer acting as a substrate for the sample. The broad and low intensity band at $\sim 175 \text{ cm}^{-1}$ was also observed here. These results signify that the similar band observed in earlier case (Fig.6.6) is plausibly not due to the TO1 mode of CdSe nanoparticles, but most likely originated from the vibrating modes of Se atoms present in the networking structure. Moreover, Fig.6.8 a and b shows the XRD spectrum of the as grown nanostructure before and after heating the sample at 230°C for 1 hour, respectively. In corroboration with the SEM and the Raman spectral studies, the signatures of CdSe formation along with the Se diffraction peaks could be observed in the XRD pattern,

Chapter 6

which became prominent after heating the sample. The peaks at 2θ values: 24.61° , 41.11° and 49.37° belong to the cubic phase (JCPDS Card No. 19-0191) of CdSe and have been marked along with their respective lattice planes.

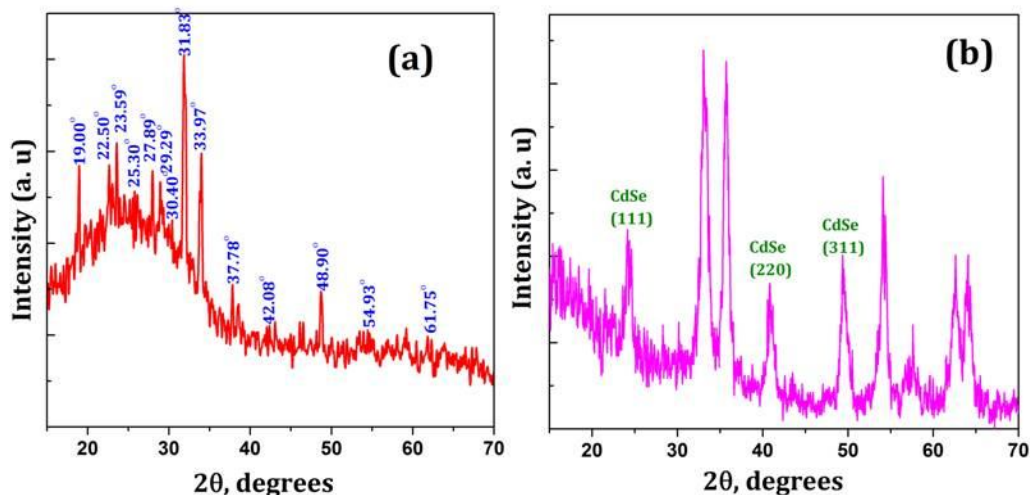


Fig.6.8. XRD spectrum of as grown nanostructure synthesized in IL ($[EMIM][EtSO_4]$) via electron beam irradiation before (a) and after heating the sample at 230°C for 1 hour (b). Dose = 10 kGy.

In fact, the direct synthesis of Se@CdSe nanocables has been reported by Jiang *et al.*³⁴¹, wherein the XRD pattern of unheated sample showed the similar signatory appearance of CdSe along with that of t-Se. Besides, analogous spectral features of amorphous CdSe nanoparticles (in case of unheated sample) have been observed earlier.³⁴² The SAED measurements (discussed earlier) also indicated the amorphous nature of the CdSe nanoparticles grown within the fibrous network of Se. The crystalline phase comprising the mixture of both the m-Se (JCPDS no. 24-1202) and the t-Se (JCPDS no. 06-362), could be realised from the appearance of the diffraction peaks characteristic of these mentioned phases of Se. Nonetheless, the aforementioned morphology i.e. islands of CdSe nanoparticles within the Se fibrous network gets further

Chapter 6

endorsement from these observations. Essentially, the IL (host matrix) and the electron beam are playing a major role in directing the as obtained unique nanomorphology.

The probable mechanism and the contribution of IL along with the peculiarities of the electron beam in guiding the as obtained morphology has been discussed further. For better explanation and to determine the individual roles of IL and the electron beam, SEM images of only the fibrous region were recorded and the same has been shown in Fig.6.9. It could be clearly noticed that predominantly the chains are having the diameter between 100-500 nm, but in some junctions, these chains appear to be stacked to form thicker structures of diameter up to 1 μm . Due to their higher diameters, we can call them as nanofibers instead of nanowires, because later ones usually have a lateral size of tens of nanometres or less.

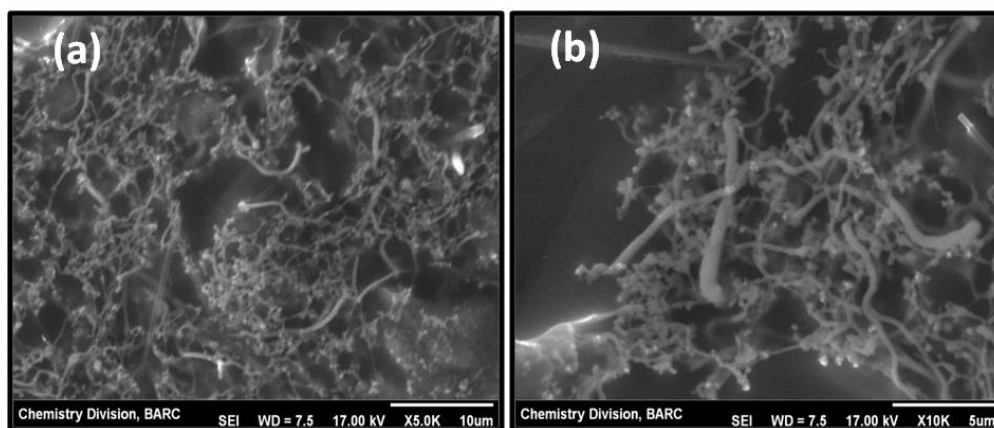


Fig.6.9. SEM image of the Se nanofibers synthesized in IL ($[\text{EMIM}][\text{EtSO}_4]$) via electron beam irradiation, Dose = 10 kGy.

Further, the chains can be seen interwoven into each other along with some welded joints at various junctions resulting into a 3-D network of nanofibers. The morphology appeared to be quite porous, thereby seems to possess high surface area as apparent from

Chapter 6

its highly entangled networking structure. This fibrous region is made of Se chains, as has been evident by EDS and Raman spectroscopy. Basically, Se being one of the major chalcogens possesses the inherent tendency to undergo catenation/polymerization. However, such tendency of Se to form chains by undergoing catenation persists only in its crystalline form. There are numerous reports^{337, 343} in which 1-D structures of crystalline Se nanomaterials have been synthesized by making use of its inherent anisotropic crystal property. On the other hand, the formation of spherical nanoparticles of Se is generally only possible/ favored, if it retains its amorphous form, which is thermodynamically unstable³⁴⁴ and some meticulous synthetic methods are required to obtain a-Se spheres. However, formations of spherical selenium nanoparticles by γ ³⁴⁵ and electron beam³⁴⁶ irradiations have been reported. One of the prominent features of as obtained morphology is the presence of beads, which can be noticed on a careful viewing of the SEM images (Fig.6.9). These beads appeared to be like the spherical globules and can be seen mostly at the ends of the fibers. The beaded joints are also clearly visible among the entangled chains. This signifies that the chains are formed as a result of beaded growth mechanism and most probably, the beads are acting as the seeds for the 3-D networking structure. Similar beaded growth mechanism of a-Se to t-Se nanowires has been reported earlier by Gates *et al.*³⁴⁷ Nonetheless, these spherical beads are the clear evidence of the formation of a-Se in the initial stage for the formation of the final nanostructure. As mentioned earlier that the a-Se is unstable in nature due to its higher free energy relative to t-Se and thus, spontaneously dissolve into the solution to re-crystallize with t-Se nuclei, which further grow into various 1-D nanostructures.

Chapter 6

Raman spectral data in the present study have clearly evidenced the formation of crystalline Se, mostly t-Se (Fig.6.6 b & d). Therefore, networking structure obtained here comprises of both amorphous and crystalline forms of Se. This co-existence of both the forms raises a question on the well established and the highly feasible process involving the phase transformation of a-Se into t-Se.³⁴³ This transformation requires ~ 5 hrs of ageing period³⁴⁷ in alcohol. The answer to this mystery lies probably within the physicochemical properties of the host matrix, IL. Since, the viscosity of the IL ([EMIM][EtSO₄]) is ~100 cP at 298 K,³⁴⁸ which is almost 100 times greater than ethanol (~ 1.26 cP at 298 K). Furthermore, only 40-80% conversion of a-Se to t-Se over the course of 1 week has been reported by Mayers *et al.*³⁴³ for solvents such as diethylene and triethylene glycol, generally regarded as the oligomers of ethylene glycol. Interestingly, this observation is in analogy with the case of ILs, where *in situ* oligomeric formation has been well reported on irradiation.^{76, 79, 80, 83} Thus, our experimental observations are in well agreement with the reported facts in the literature. In addition to this, the IL also seems to play a shape directing template. This can be envisaged from the fact that imidazolium based ILs comprises of non-covalent bonding interactions such as π - π stacked aromatic geometry among the cationic moieties.^{86, 89} Consequently, this feature along with the extended hydrogen bonding network (*hydrogen bond-co- π - π stacking mechanism*) has been regarded as the most probable shape directing mechanism for obtaining various anisotropic structures (tubes, wires, rods, sheets) of nanomaterials synthesized in imidazolium based ILs, by different techniques.^{90, 92-95, 349} The aforesaid argument is further substantiated from the similar type of experiments conducted earlier

Chapter 6

by our group, wherein the CdSe nanoparticles were synthesized in aqueous solutions (homogeneous in nature contrary to the ILs) *via* irradiation techniques (both electron beam and γ induced).^{165, 167} The CdSe nanoparticles did not exhibit any specific morphology, rather they were found to aggregate randomly (TEM images shown in Fig.6.10) and further had the tendency to decompose within 24 hours in ambient conditions.

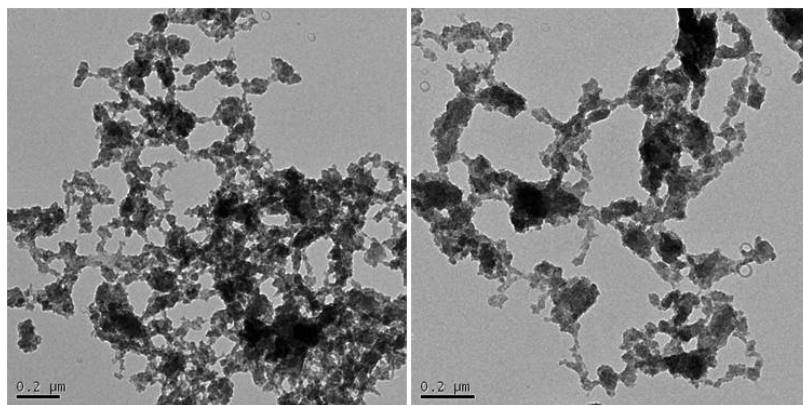


Fig.6.10. TEM images of bare CdSe nanoparticles synthesized in aqueous medium via electron beam irradiation.

In this perspective, we can say that IL is playing three roles simultaneously; as solvent, as a shape guiding template and as a stabilizer. However, we were not able to observe any 1-D anisotropic nanostructure as was expected; rather a 3-D randomly oriented fibrous structure containing islands of CdSe was obtained. The most probable reason for this could be the high dose rate involved in the electron beam irradiation technique.

To verify our hypothesis, another experiment was conducted (keeping all the parameters exactly similar as in case of electron beam irradiation technique), in which the

Chapter 6

sample solution was irradiated by γ -rays to an equivalent dose of 10 kGy. On irradiation, the sample colour turned to reddish orange, similar to that observed in the case of electron beam method. The precipitates were extracted and washed by following the similar method, as earlier mentioned. The SEM images of as obtained precipitates have been shown in Fig.6.11. As expected, 1-D anisotropic structures i.e. nanosheets (mainly) and some needle shaped features were observed in case of γ -irradiation method, which can be ascribed to the inherent π - π stacked geometry of imidazolium rings of the IL as well as the self-catenating property of Se (in crystalline form).

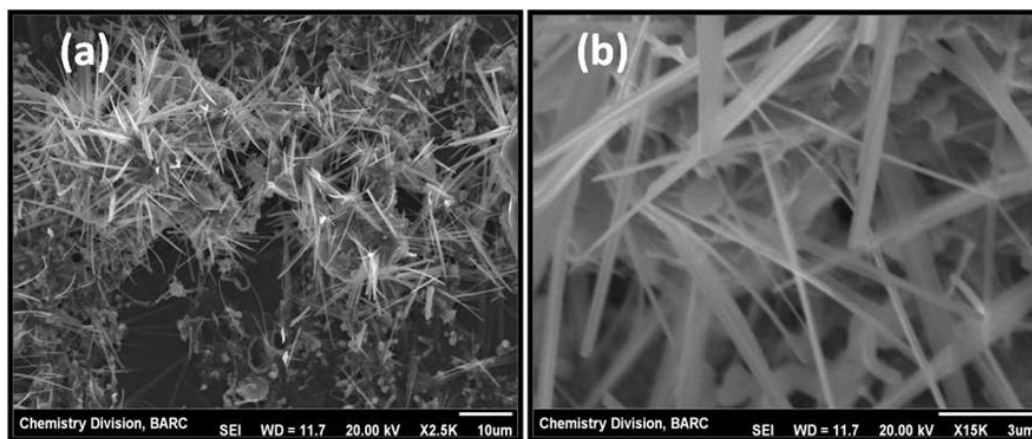


Fig.6.11. SEM images of as obtained nanostructures synthesized in IL ($[EMIM][EtSO_4]$) via γ -irradiation, Absorbed Dose = 10 kGy. Scale bar dimensions; 10 μ m (a) and 3 μ m (b).

The Raman spectra of the corresponding nanostructure (obtained by γ -irradiation method) have been shown in Fig.6.12. The peaks at 204 cm^{-1} and 410 cm^{-1} corresponds to the LO1 and 2LO1 (second order) phonon modes of CdSe nanoparticles. While, the Raman peaks at 256 cm^{-1} and 456 cm^{-1} has been attributed to the formation of Se based nanostructures, as previously discussed. The peak at 256 cm^{-1} is accompanied by the broadness and the presence of shoulders, which clearly indicates the presence of

Chapter 6

amorphicity in the structure. The broad peak at $\sim 377 \text{ cm}^{-1}$ is probably due to the TO + LO phonon mode of CdSe nanobelts and nanosheets as reported by Venugopal *et al.*^{333b}

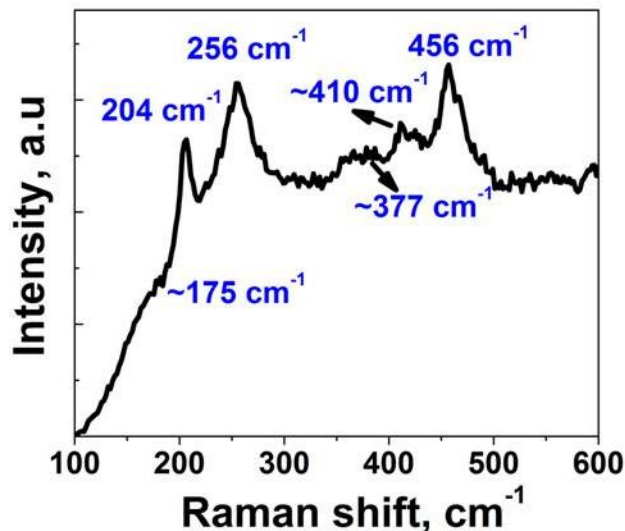


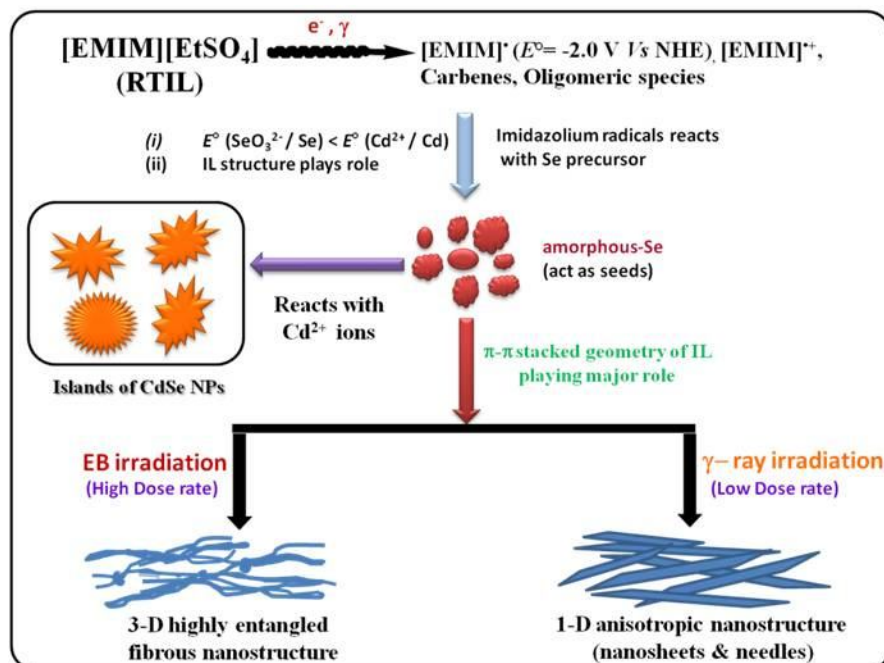
Fig.6.12. Raman spectrum of the nanostructure synthesized in IL ($[\text{EMIM}][\text{EtSO}_4]$) via γ -beam irradiation, Dose = 10 kGy.

More importantly, we could observe such a remarkable difference in the morphologies of as obtained nanostructures, even though all the experimental parameters were kept similar in both the methods (electron beam and γ -irradiation). Furthermore, it was noticed that the CdSe nanoparticles formed in the later method are distributed much more homogeneously along the entire sample. This observation is contrary to the case of electron beam irradiation technique, where the distribution of CdSe nanoparticles is significantly heterogeneous; thereby, such places were named as ‘islands’. Apparently, such morphological variations have been attributed due to the differences in the dose rate and the direction of energy deposition in the two techniques. In contrast to the directional nature of the electron beam method, the irradiation takes place uniformly with respect to the sample volume in the γ -ray method. However, initial dose rate dependent processes

Chapter 6

are most likely to play a dominant role (compared from directionality differences) in leading to the diverse final structures as obtained in the respective methods. It is pertinent to emphasize here that the dose rate involved in electron beam irradiation technique was estimated to be ~ 1.6 kGy/s, while that in case of γ -irradiation was ~ 0.4 Gy/s. Consequently, the high dose rate in case of electron beam method leads to the instantaneous dumping of large amount of energy in a very short time. This aspect of the electron beam most probably rendered the growth of the nanostructure in a highly random fashion, resulting into a highly porous 3-D fibrous like network.

On the basis of the microheterogeneous structural features of the IL and the peculiarities of the electron beam, a mechanism has been proposed for the formation of islands of CdSe nanoparticles (called nanoislands) within the Se nanofibers and has been illustrated schematically in Scheme 6.1. In general, most of the radiation assisted synthetic techniques of nanomaterials involve the formation of solvated (or aquated) electron, e^-_{sol} ($E^{\circ} = -2.9$ V V_s NHE) as the primary reducing species of the precursor compounds.^{91, 165, 167, 311, 312, 314} However, in imidazolium based ILs, the electron reacts very efficiently with the imidazolium cation before being solvated. The efficiency of the reaction can be envisaged from the fact that the bimolecular rate constant (k) for the reaction between the electron and the imidazolium cation is greater than that of diffusion-limited reactions ($k = 10^7$ - 10^{12} $M^{-1} s^{-1}$).^{86, 87, 89}



Scheme 6.1: Scheme showing the proposed mechanism for the nanomorphology i.e. Islands of CdSe nanoparticles within Se nanofibers obtained on electron beam irradiation of the IL ([EMIM][EtSO₄]) containing Cd and Se precursors. Dose = 10 kGy.

Nevertheless, the radiation chemical studies of the imidazolium based ILs have reported the formation of imidazolium related radicals.^{76, 79, 83, 271, 295} In fact, the imidazolium radicals are reducing in nature (E° = -2.0 V vs NHE). Therefore, the imidazolium radicals are probably carrying out the reduction of the precursor ions. Now, the feasibility of the reaction of imidazolium radicals with the selenite ions (SeO₃²⁻) appears to be comparatively more than the cadmium ions (Cd²⁺) due to two factors as follows. The presence of Cd²⁺ ions are expected to be near the anion part (EtSO₄) of the IL, whereas the SeO₃²⁻ might find its proximity near the EMIM cation (due to the electrostatic forces). Thus, the imidazolium radicals produced by the irradiation would possibly interact more with SeO₃²⁻ than with Cd²⁺. Secondly, the reduction potential of

Chapter 6

$\text{SeO}_3^{2-} / \text{Se}$ ($E^\circ = -0.37 \text{ V Vs SHE}$) is lower than that of $\text{Cd}^{2+} / \text{Cd}$ ($E^\circ = -0.40 \text{ V Vs SHE}$). Hence, the imidazolium radicals are expected to preferably react with the selenite ions.

As discussed earlier, formation of spherical globules of a-Se are the preliminary steps for the networking structure in case of electron beam method. Similar spherical beads can also be seen in the SEM images of the nanostructures obtained by γ -radiation method. The as formed Se nanospheres possess high chemical reactivity (high free energy³⁴⁴) which further react with Cd ions to form islands of CdSe nanoparticles. However, the main driving force behind the formation of islands of CdSe nanoparticles within the Se nanofibers is probably the lower reactivity of Cd ions, the microheterogeneous structure of the IL, and also due to the formation of instantaneously large concentration of initial species in the electron beam irradiation method. It is important to emphasize here that the self-catenating property of Se enables it to form polymeric chains leading to the formation of a variety of 1-D structures, such as nanoribbons, nanowires and nanorods. In such a situation, presence of a shape directing template guides these polymeric chains into various morphologies. In the present case, the π - π stacked structure of the IL is acting as a shape directing template, as discussed earlier. However, a 3-D fibrous networking structure was obtained in case of electron beam irradiation method, while 1-D anisotropic structure comprising of nanosheets and needles were obtained in case of γ -irradiation method. This signifies that the low dose rate in γ -irradiation method leads to a much orderly and directional oriented beaded growth of a-Se globules along with the assistance of π - π stacked geometry of as employed imidazolium based IL. On the basis of the evidences and results of the γ -irradiation experiment, the proposed mechanism

Chapter 6

appropriately explains the various structural and dynamical aspects of the fibrous structure obtained in case of electron beam irradiation method.

6.3. Normal chemical route

6.3.1. Materials and Methods

The precursors of Cd & Se and the IL employed in this study were same as mentioned in section 6.2.1. Other chemicals used for cleaning and washing off the organic impurities from the precipitates were also same as in the preceding work.

The procedure for the synthesis of CdSe nanoparticles in this part of the work has been mentioned as follows. CdSO₄, 0.0156 gm and Na₂SeO₃, 0.0129 gm were dissolved in 2.0 ml of IL, [EMIM][EtSO₄] by sonication for 30-45 minutes followed by magnetic stirring for nearly 30 minutes. Consecutively, 0.0076 gm of sodium borohydride (NaBH₄, SBH) was added to the above solution as a reducing agent, while stirring the same at 1500 rpm (rotations per minute). On mixing, the color of the IL turned to reddish orange within the first 2 minutes of the reaction, and then subsequently changed to yellowish green after 5 minutes, which remained stable for prolonged period of time. The precipitates of the nanoparticles were obtained by centrifugation of the sample at 9000 rpm followed by washing the same with ethanol and nanopure water for 3-4 times. The precipitates were utilized for carrying out compositional and morphological characterization studies.

6.3.2. Results and Discussion

The UV-Vis absorption spectrum of the yellowish green solution obtained upon mixing of the precursors and NaBH₄, has been provided in Fig.6.13, which clearly shows a shoulder

Chapter 6

like excitonic peak at ~ 400 nm, while no such spectral feature was observed in case of neat IL.

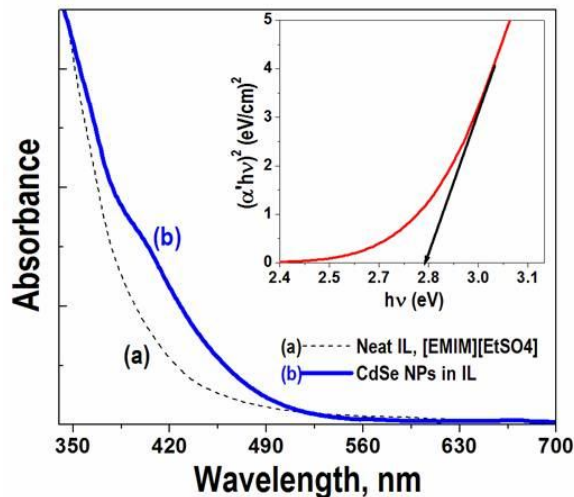


Fig.6.13. UV-Vis absorption spectra of neat IL (a) and CdSe nanoparticles synthesized in IL ([EMIM][EtSO₄]) (b). Inset: Tauc plot of $(\alpha \cdot h\nu)^2$ vs. $h\nu$ for the determination of band gap values (E_g).

However, the excitonic peak is quite broad and not very well resolved. The large difference between the onset and the shoulder indicates polydispersity in the size or in the shape distribution of the nanoparticles. Nonetheless, an estimation of the average nanoparticle size of CdSe was calculated using the simplified Brus equation (6.1):

$$E_g = E_g(0) + \alpha/d^2 \quad [6.1]$$

where, $\alpha = 3.7 \text{ eV nm}^2$, bulk band gap of CdSe i.e. $E_g(0) = 1.75 \text{ eV}$, d = nanoparticle size (nm) and E_g is the band gap value of nanoparticles in eV. The band gap (E_g) value was determined from the Tauc's plot (inset of Fig.6.13). The estimated average values of the band gap and the particle size were found to be 2.81 eV and 1.85 nm, respectively, which indicate strong quantum confinement effect exhibited by the CdSe nanoparticles. The

Chapter 6

probable reaction of Cd and the Se precursors with the reducing agent (NaBH₄) leading to the formation of CdSe nanoparticles can be formulated as follows:



The presence of Cd²⁺ ions are expected to be near the anion part (EtSO₄) of the IL whereas, SeO₃²⁻ ions might find its proximity near the EMIM cation (due to the electrostatic forces). Further, the reducing species (BH₄⁻) is also expected to be in the close immediacy of the imidazolium cation. Apart from that, the reduction potential of SeO₃²⁻ / Se (E° = -0.37 V Vs SHE) is lower than that of Cd²⁺ / Cd (E° = -0.40 V Vs SHE). These facts signify the feasibility and the high reactivity of the selenite ions (SeO₃²⁻) as compare to the cadmium ions (Cd²⁺), thereby supporting the proposed reactions for the formation of CdSe nanoparticles.

A typical XRD pattern obtained from the as prepared nanoparticles, before and after heating (at 230°C for 1 hour) has been shown in Fig.6.14. The unheated one shows a broad and noisy spectrum, which makes it difficult to identify the phase of the nanoparticles. However, the heat treatment would have led to the annihilation of various anticipated organic and inorganic impurities along with the fusion of plausible surface defects present in the form of grain boundaries. This is quite evident from the well-refined diffraction peaks consistent with the wurtzite structure of CdSe (Fig.6.14b). The lattice constants as determined are: a = 4.284 Å and c = 6.986 Å, which are little lower than the standard value of wurtzite phase of CdSe (a = 4.299 Å and c = 7.010 Å, JCPDS

Chapter 6

file No. 08-0459). This signifies tensile stress leading to lattice contraction. The peaks marked by the star sign (★) could probably be originated from presence of residual Se.

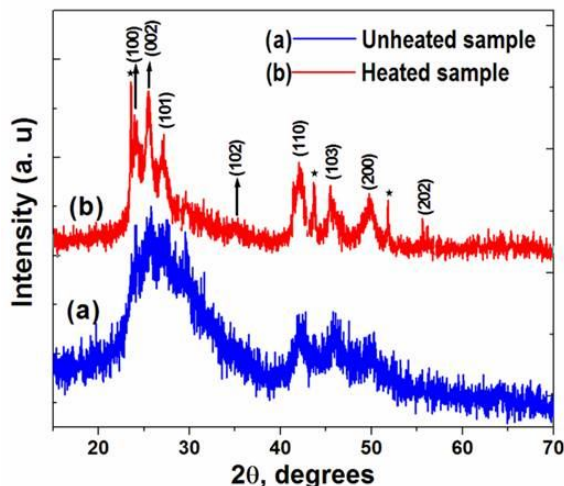


Fig.6.14. XRD spectrum of as grown nanoparticles synthesized in IL ([EMIM][EtSO₄]) before (a) and after heating the sample at 230 °C for 1 hour (b). The peaks marked by the star sign (★) has been identified as originated due to the presence of residual Se.

The TEM images of the as grown nanoparticles have been shown in Fig.6.15. The polydispersity in the particle size (2 to 5 nm) could be observed from the HRTEM image shown in Fig. 6.15b. However, average nanoparticle size was found to be ~ 2 nm, which matches well with that estimated from the absorption spectral studies. More interesting aspect revealed from the TEM studies is the self-assembling of the primary nanoparticles into some sort of superstructures (Fig.6.15a). Indeed, the formation of sheet like superstructures as a result of self-assembling can be realized from the images shown in Fig.6.16. However, the SAED pattern (inset of Fig.6.16d) rules out the formation of a single crystalline structures. The self-assembling behavior of the primary nanoparticles in RTILs has been demonstrated earlier by Zhou *et al.*³⁵⁰

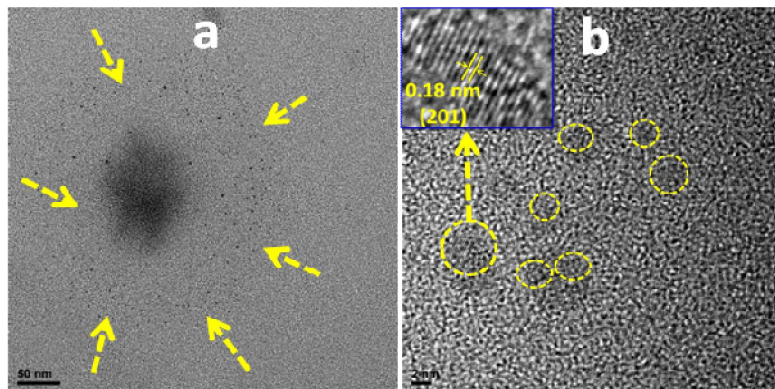


Fig.6.15. TEM (a) (Scale bar dimensions = 50 nm) and the HRTEM (b) image (Scale bar dimensions = 2 nm) of the CdSe nanoparticles synthesized in neat IL ([EMIM][EtSO₄]). Inset in the image (b) shows the lattice fringe pattern with the interplanar distance of 0.18 nm, which correspond to the (201) plane (standard value of the interplanar distance = 0.179 nm) of the hexagonal phase of CdSe.

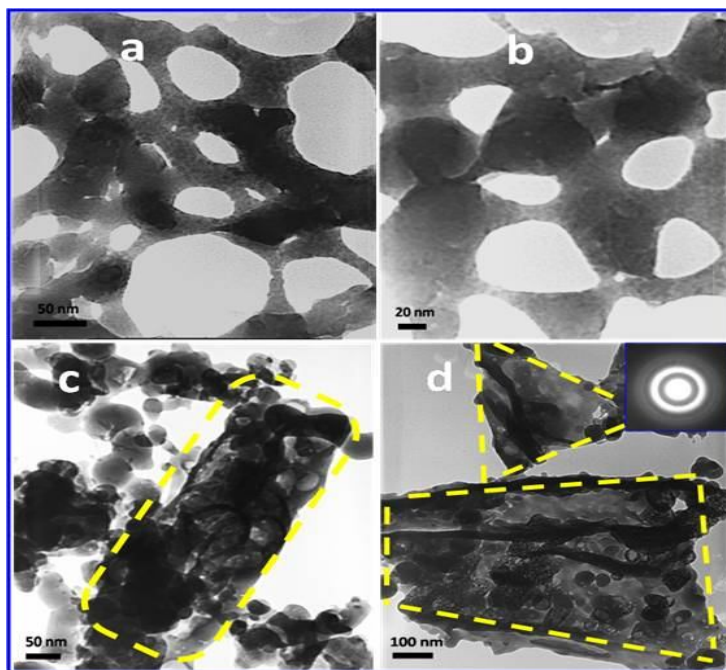


Fig.6.16. TEM images (a & b) showing the self-assembly of primary nanoparticles. Images (c) & (d) clearly illustrates the formation of sheet like superstructures as a result of self-assembly. Inset of image (d) shows the SAED pattern of the corresponding structure. The images were taken after 5 hours of the reaction.

Chapter 6

To further probe into the self-assembling of the primary nanoparticles, SEM images were recorded at different regions, shown in Fig.6.17. The composition was analysed by recording the EDS spectrum (inset of Fig.6.17a), which confirmed the formation of CdSe nanoparticles. The peak showing the presence of Si is originated from Silicon wafer used as a substrate for the sample analysis.

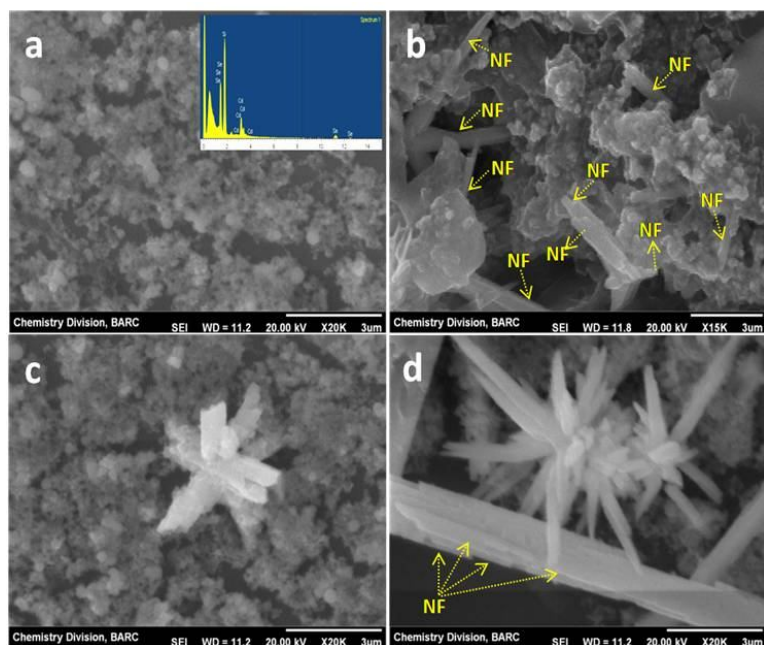


Fig.6.17. SEM images of as grown CdSe nanostructures after 5 hours of the reaction at different regions of the sample depicting the various transient stages as: globular like shape (a), nanoflake (NF) like structure (b), flower-like 3D pattern (c) and nanosheet like 2D structures (d). (Scale bar dimensions in all the images is 3 μm). Inset of image (a) shows the EDS spectrum confirming the formation of CdSe nanoparticles.

As indicated in Fig.6.17a, the primary nanoparticles were having nearly globular shape, which grow into nanoflake (NF) like structures and the formation of such features could be clearly seen (depicted by an arrow) in Fig.6.17b. Subsequently, the NFs self-assemble to form a mixture of nanosheets (2D) and nanoflower (3D) like structures. The

Chapter 6

formation of both of these anisotropic nanostructures could be clearly noticed in Fig. 6.17c & d as well as after 24 hours of the reaction (Fig.6.18). It is to be noted that, even after 24 hours of the reaction, the morphologies were stable as were found after 5 hours of the reaction. This clearly indicates that IL itself is acting as a good stabilizing agent in maintaining the nanomorphologies unperturbed even after 24 hours of the reaction.

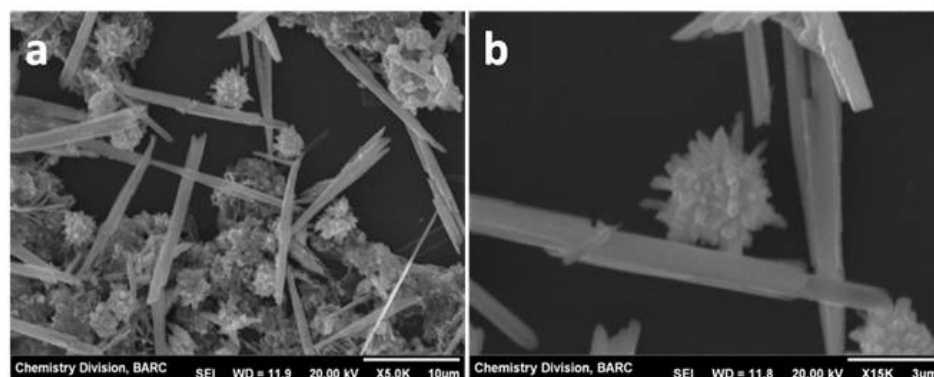


Fig.6.18. SEM images of as grown CdSe nanostructures after 24 hours, showing the dual co-existence of nanosheets and nanoflowers. Scale bar dimensions; 10µm(a) and 3µm(b).

From the SEM images, it can be noticed that the NFs assemble non-homogeneously due to their anticipated high surface area and eventually form the 2D (sheet like) and 3D (flower like) nano/micro-architectures. The sheets are formed due to the fusion of NFs at the end, edge and the front facets, thereby resulting into multilayered 2D structures (marked in Fig.6.17d) with length and width in the range of 10-15 µm and 1-2 µm, respectively. To the best of our knowledge, there has not been any earlier report on the formation and the co-existence of nano/micro-scaled sheets and flowers of CdSe in *neat* ILs. At this stage, it is imperative to recall some of the recent works regarding the synthesis of metal chalcogenide nanoparticles assisted by ILs. For instance, the preparation of ZnS nanoparticles,^{351a} flower like MoS₂,^{351b} PbS nanocubes,^{351c} ZnSe

Chapter 6

hollow microspheres^{351d} and CdSe hierarchical dendrites^{351e} have been reported with the aid of ILs. As could be noticed that predominantly single morphologies have been mentioned in these reports and none of these accounts for the simultaneous co-existence of different nanomorphologies as observed in the present case. Moreover, the synthetic protocols of these nano/microstructures involved conventional solvents for dilution purpose in addition to the employment of high temperature/pressure techniques (i.e. autoclaving). Presumably, the intrinsic networking structure of the IL would have perturbed in such conditions. Still, some of the nanostructures were found to be hierarchical (self-assembly of primary units) in nature, which have been explained rendering the influence/presence of the ILs employed therein. To provide a precise mechanism for the formation of anisotropic nanostructures as obtained in the present case may not be easy. However, a possible explanation might be given on the basis of the inherent structural and fluidic aspects of the IL (compared to the conventional solvents) in the initial phase of the reaction, i.e. up to the formation of nanoflakes. These nanoflakes with high energy surfaces are combined together to form nano/micro sheets and flower like structures, which are found to co-exist and stabilized by the rigid structure of IL. The viscosity of the IL, [EMIM][EtSO₄] is ~ 100.4 cP at 298.15 K,³⁵² which is at least 10 times higher as compared to usually employed conventional solvents (aqueous and organic) for the synthesis of nanoparticles. Such high viscosity would significantly slow down the diffusion of the reactant ions as well as the primary nanospecies. In other words, compared to the fast nucleation and aggregation in the conventional solvents, the primary CdSe nanospecies would be kinetically slower, thereby allowing them to have

Chapter 6

enough time to grow into hierarchical morphologies directed by the networking structure of the IL. Moreover, it has been mentioned earlier that RTILs display a high degree of self-organization and microheterogeneity in the liquid state,^{65, 66, 69, 353} and this feature along with the extended hydrogen bonding network (*hydrogen bond-co- π - π stacking mechanism*) has been regarded as the shape directing mechanism for obtaining various anisotropic structures (tubes, wires, rods, sheets) of nanomaterials synthesized in imidazolium based ILs.^{89, 90, 92, 94, 95} Apparently, the relative diffusion flux (in various domains of ILs; structural heterogeneity) complemented by the diffusion limited aggregation (fluidic aspect of the ILs) of the nanospecies formed at the initial stages could be regarded as the possible factors for their self-organization process. However, as the inherent heterogeneity of the IL is in nanoscale, it cannot be responsible for microstructures as obtained in the present case. It is a well-known fact that the thermodynamic processes often result in uniform growth of all crystal facets and subsequent formation of spherical or near spherical structures.³⁵⁴ Whereas, preferential and directional growth occurs in case of kinetically controlled process resulting into the formation of various anisotropic nanostructures. In other words, if the enthalpy gain from such oriented attachment dominates the entropy loss, the self-assembled 2D or the 3D nanostructures could become thermodynamically favorable.³⁵⁵ The driving force for such process is the elimination of the high energy surfaces, ultimately leading to a substantial reduction in the surface free energy. Thus, in the present case, the NFs self-assemble in different ways to generate the anisotropic structures.

Chapter 6

To supplement the proposed mechanism, some control experiments were carried out by diluting the IL with water, keeping other experimental parameters unchanged. In such two cases, mole fraction of water in the reaction mixtures were 0.35 and 0.91, and the respective morphologies of the CdSe nanoparticles were examined. At a mole fraction of (water) 0.35, the nanostructure as well as their distribution (Fig.6.19) is significantly different from the former case (*neat* IL). Interestingly, the 3D flower like morphology was formed predominantly due to the self-assembly of NFs (Fig.6.19c & d).

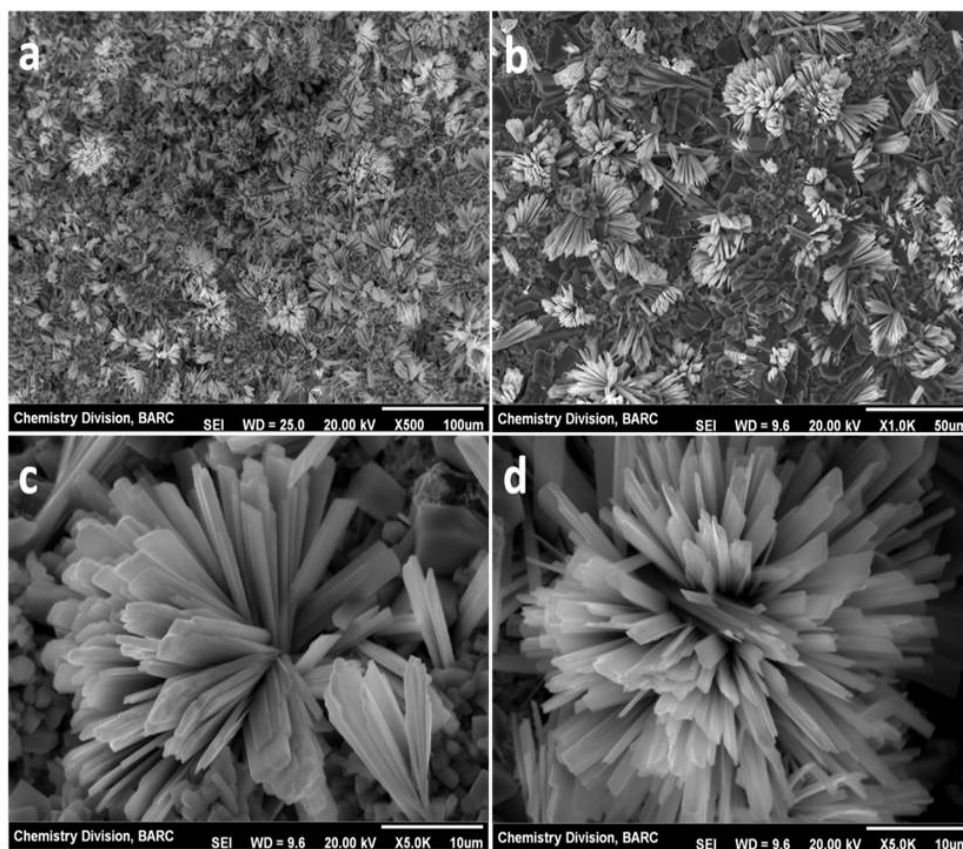


Fig.6.19. SEM images (at different regions with various nanoscale dimensions) of as grown CdSe nanostructures synthesized in IL ([EMIM][EtSO₄]) having 0.35 mole fraction of water. The images were taken after 5 hours of the reaction. Scale bar dimensions = 100 μm (a), 50 μm (b), 10 μm (c) and 10 μm (d).

Chapter 6

Furthermore, the large sheet like morphologies formed through the fusion of NFs (as in case of *neat* ILs) were not observed in this case. Instead, the small sheet-like units (NFs) having the length primarily in the range of 2-5 μm were found to fuse by their tails, while the other side remained free. This orientation gives the impression of the flower like morphology with petals comprising a bunch of well aligned NFs. On the contrary, the NFs (primary units) forming the flower like nano/microstructures in case of *neat* IL were found to orient randomly. After 24 hours of the reaction, the morphology of the CdSe nanostructures was re-examined and the SEM images are shown in Fig.6.20.

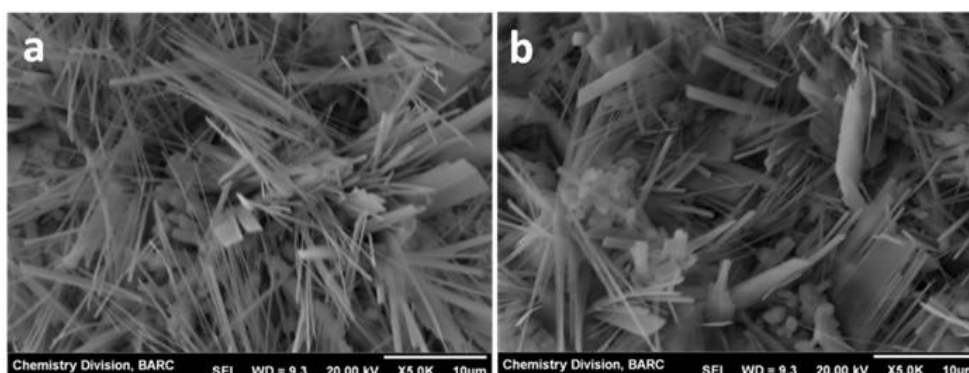


Fig.6.20. SEM images (at different regions with various nanoscale dimensions) of as grown CdSe nanostructures synthesized in IL ($[\text{EMIM}][\text{EtSO}_4]$) having 0.35 mole fraction of water. The images were taken after 24 hours of the reaction. Scale bar dimensions = 10 μm (a) and 10 μm (b).

Mainly nanoneedles accompanied by nanorods and nanosheets are visible, while no flower like architectures were noticed in this case. Indeed, this transformation of 3D nanomorphology into a mixture of 1D and 2D nanostructures was surprising. However, the plausible reason behind this transition could be the combined effect of structural defects present in the initial morphology as well as the decline in the stabilizing tendency

Chapter 6

of the host matrix i.e. IL with the presence of water. Images shown in Fig.6.19 indicate that the petals (NFs) are well aligned leading to the formation of a flower like geometry but some defects due to the minor distortion in their arrangements at some places could be noticed very clearly. Such defects may induce the instability in the structure and thus encourage its transformation to other morphologies.³⁵⁶ It is to be mentioned here that the presence of such structural defects cannot be denied in case of nanoflowers formed in neat IL. But, no such structural transition was observed in that case which could be due to the inherent rigidity present in the host matrix of IL.

Similar structural transformation with different nanomorphologies was observed on further dilution of the IL (mole fraction of water = 0.91). The nanoparticles formed in this case underwent coagulation followed by precipitation within few minutes of the reaction. Nonetheless, flower like morphologies were observed in various regions of the sample, as could be seen from the SEM images recorded after 5 hours of the reaction (Fig.6.21).

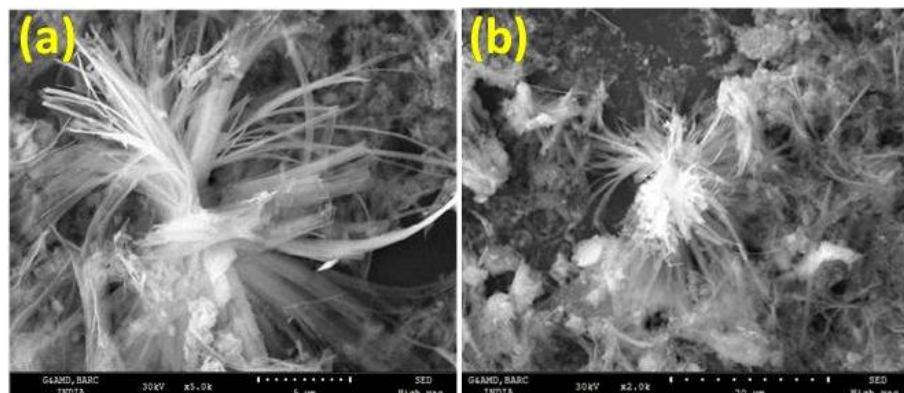


Fig.6.21. SEM image of as grown CdSe nanostructures synthesized in IL ([EMIM][EtSO₄]) having 0.91 mole fraction of water. The image were taken after 5 hours of the reaction. Scale bar dimensions = 5 μm (a) and 20 μm (b).

Chapter 6

It can be noticed that the irregular alignment and random fusion of NFs, needles and some fiber like nanoscale units actually gave the distorted flower like structures. These flower like morphologies were not predominant after 24 hours, rather the nanoscale units, i.e. NFs, rods and needles were present in a non-uniform and random manner (Fig.6.22). Furthermore, these anisotropic nanoscale units were not found to fuse into each other and primarily joined at their heads and tails. But, in case of *neat* IL, the NFs were fused into each other to form sheets of microscale dimensions, as already discussed.

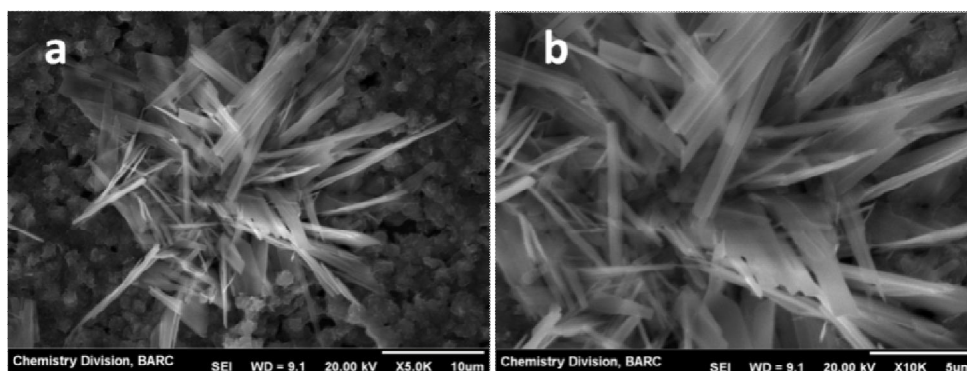


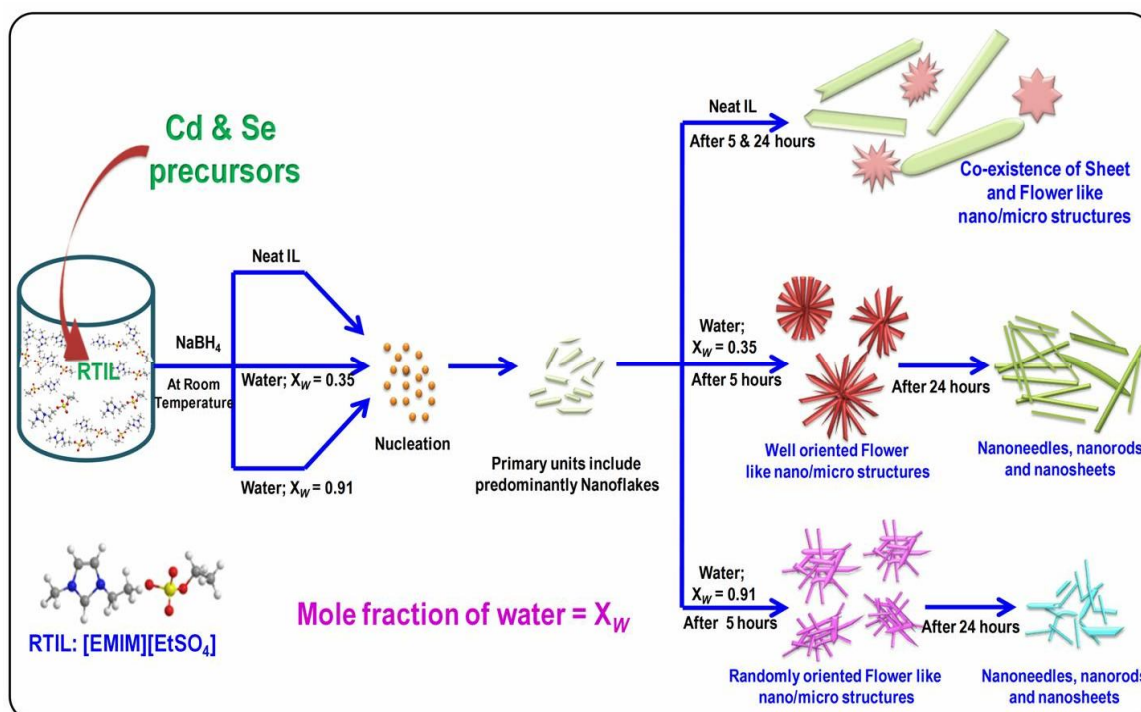
Fig.6.22. SEM images at different nanoscale dimensions of as grown CdSe nanostructures synthesized in IL ([EMIM][EtSO₄]) having 0.91 mole fraction of water. Scale bar dimensions = 10 μm (a) and 5 μm (b).

It is essential and worthwhile to mention here that the dimension of the anisotropic (1D or 2D) nano/micro-architectures decreases with the increase in the volume fraction of water. Unambiguously, the IL still influences the morphology of the CdSe nanoparticles, but its shape directing and stabilizing tendencies appeared to be considerably declined. The plausible reason for this is the perturbation in the internal structural organization of the IL, which leads to decrease in the extended ordering of nanoscale structures. In other

Chapter 6

words, the self-assembling tendency of the primary units is weakened with the dilution of the IL.

The formation of anisotropic nanomorphologies of CdSe along with the different intermediate stages in different set of experiments has been shown in scheme 6.2. The proposed scheme, based on the results obtained and the available literature appears to be reasonable at this point of time however, provides scope for refinement in future.



Scheme 6.2: Schematic representation showing the probable intermediate stages with different nano/micro-morphologies of CdSe synthesized in IL ([EMIM][EtSO₄]), at various time intervals and mole fractions of water.

Further characterization of the as grown CdSe nanoparticles was carried out by recording the Raman spectrum of the precipitates. Fig.6.23 shows the Raman spectrum of the precipitates with multi-Lorentzian fitting. As could be seen, the spectrum comprises

Chapter 6

of fundamental longitudinal optical (LO) phonon peak along with its overtone (2LO) peak at $\sim 205 \text{ cm}^{-1}$ and $\sim 408 \text{ cm}^{-1}$, respectively. A shoulder near 170 cm^{-1} can be noticed, which is attributed to the transverse optical (TO) phonon mode of CdSe nanoparticles.³⁵⁷ A small and broad peak at about 264 cm^{-1} is also apparent in the spectrum.

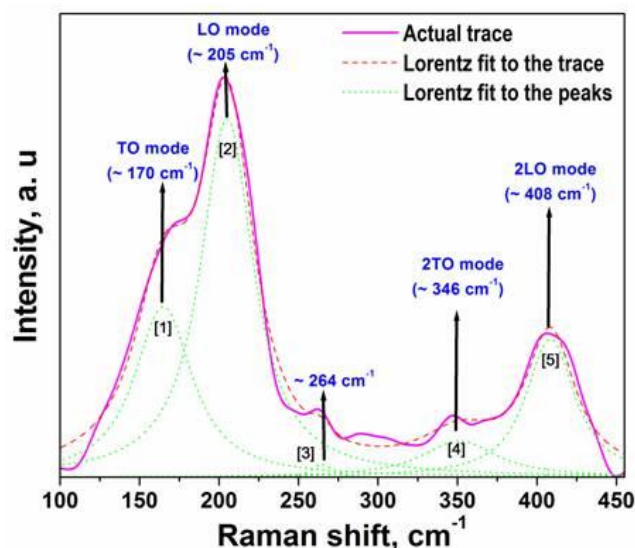


Fig.6.23. Multi-Lorentzian fitting Raman spectrum of CdSe nanoparticles synthesized in neat IL ([EMIM][EtSO₄]).

The appearance of surface optic (SO) modes has been reported earlier³⁵⁸ in case of small sized QDs (CdSe) accompanied by a peak near 250 cm^{-1} . And these SO modes originate due to the presence of more number of atoms on the surface as compared to the bulk in very small sized nanoclusters, behaving like molecules.³⁵⁸ Similar band was observed by Epifani *et al.*³⁵⁷ in case of CdSe nanoparticles at around 270 cm^{-1} and was assigned to the SO modes. Furthermore, the presence of amorphous-Se has also been reported to exhibit a Raman peak at around 264 cm^{-1} .^{344b, 359} The data obtained from the EDS analysis seems to corroborate well with the possibility of the existence of more number of Se atoms on the surface of the nanoparticles. Thus, the peak obtained at about

Chapter 6

264 cm^{-1} in the Raman spectrum of as grown CdSe nanoparticles has been attributed to the SO modes. This is further substantiated by the signatures of the Se-O bond formation (discussed later) in the Raman spectral analysis of IL containing CdSe. The peak at around 346 cm^{-1} could be ascribed to the 2TO phonon mode of the CdSe similar to that assigned by Venugopal *et al.*^{333b} for the 2TO phonon modes (at $\sim 356.8 \text{ cm}^{-1}$) of CdSe nanobelts. Besides, a red shift (down shift) of LO peak from its position for bulk CdSe (of 210 - 213 cm^{-1})^{330b, 360} was also observed. The reduction in size of various materials is mainly dominated by quantum confinement effects, but it is often accompanied by the dimensional effects, such as surface reconstruction and lattice contraction. These dimensional effects arise due to the variation in surface energy, which is a function of particle size. As a result of reduced dimensions, a competition between strain and confinement effects exists. Therefore, when a crystal with reduced dimensions experiences phonon confinement or tensile stress (strain effect), optical phonon modes undergo red shift with respect to their bulk values.^{330b} Considering this, the red shift observed in our case has been attributed due to the phonon confinement effect as the size of the primary nanoparticles were between 2 to 5 nm (from HRTEM), which is less than the bulk Bohr exciton radius of CdSe (5.6 nm).¹²⁹ Therefore, the down shift in the LO peak relative to the bulk value appears to be the combined effect of the phonon confinement and the strain leading to the tensile stress, as observed in XRD also.

FTIR spectral studies were carried out to probe the perturbations in the bonding interactions of the cationic and the anionic moieties of the IL pertaining to the formation

Chapter 6

of CdSe nanoparticles. The IR spectra of the neat as well as the IL containing CdSe have been shown in Fig.6.24.

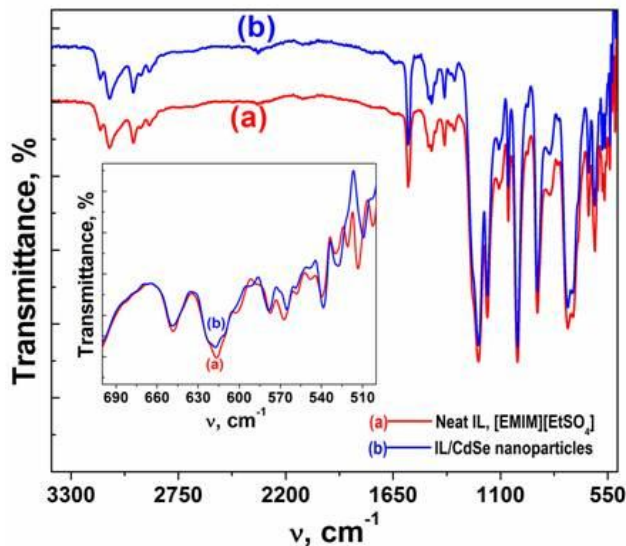


Fig.6.24. FT-IR spectra of neat IL (a) and IL + CdSe (b). Inset shows the IR spectra of the same in the region of 700-500 cm^{-1} .

It is to be mentioned here that the detailed vibrational studies (involving IR and Raman) of [EMIM][EtSO₄] have been reported earlier by Kiefer *et al.*^{303c} and other researchers.³⁶¹ The theoretical as well as experimentally determined vibrational frequencies of various bonds of the IL have been reported therein. In the present work, the IR spectra of IL and IL + CdSe do not exhibit any significant difference, especially in the region of 4000-700 cm^{-1} . However, in the range of 700-500 cm^{-1} (inset of Fig.6.24), considerable changes in the vibrational frequencies of the IL containing CdSe with respect to the relative intensities as well as in the peak positions were observed. The intensities of the peaks with wave numbers 648 cm^{-1} and 617 cm^{-1} representing the ring out-of-plane asymmetric bending vibrations^{303c} decrease in case of IL + CdSe as

Chapter 6

compared to the neat IL. Dhumal *et al.*³⁶¹ have assigned the peak at 648 cm^{-1} to the CN bond oscillation. Similar bending vibrations at $\sim 600\text{ cm}^{-1}$ were found to diminish considerably in case of IL + CdSe as compared to the *neat* one. Further, the peak position of the vibrational frequency at $\sim 565\text{ cm}^{-1}$ (due to the ring in-plane symmetric bending^{303c} for *neat* IL) was red shifted (change of $\sim 2\text{ cm}^{-1}$) in the presence of CdSe (i.e. IL + CdSe). All these signify the interaction prevailing between the imidazolium cation and the CdSe nanoparticles. In addition, the peak at $\sim 517\text{ cm}^{-1}$ (for *neat* IL) representing the bending vibrational mode of bond $\text{O}_{[3]}-\text{S}_{[1]}-\text{O}_{[5]}$ ³⁶¹ decreases significantly in case of IL + CdSe. These observations clearly indicate that both the imidazolium cation and the ethylsulfate anion are involved in the interaction with the CdSe nanoparticles. Some of the earlier studies related to the synthesis of various nanomaterials in ILs satisfactorily corroborate with our findings. For instance, Fonseca *et al.*³⁶² demonstrated that the interaction between the metal surface and the IL is through oxygen in case of triflate, CF_3SO_3 or through F (in case of anions i.e. $\text{BF}_4 / \text{PF}_6$) as anion. Zhou *et al.*⁸⁹ reported the synthesis of monolithic mesoporous silica with wormhole framework and attributed its formation mechanism to both the hydrogen bonds formed between the anionic moiety of the IL and the silano group of silica gel and the $\pi-\pi$ stacking interactions between the neighboring imidazolium rings. These interactions were confirmed by employing the FTIR spectroscopy.

Raman spectroscopy being a complementary technique to the IR spectroscopy was employed to examine the alterations in the vibrational frequencies of the IL in the

Chapter 6

presence of CdSe. Raman spectra of the *neat* IL and the IL + CdSe have been shown in Fig.6.25.

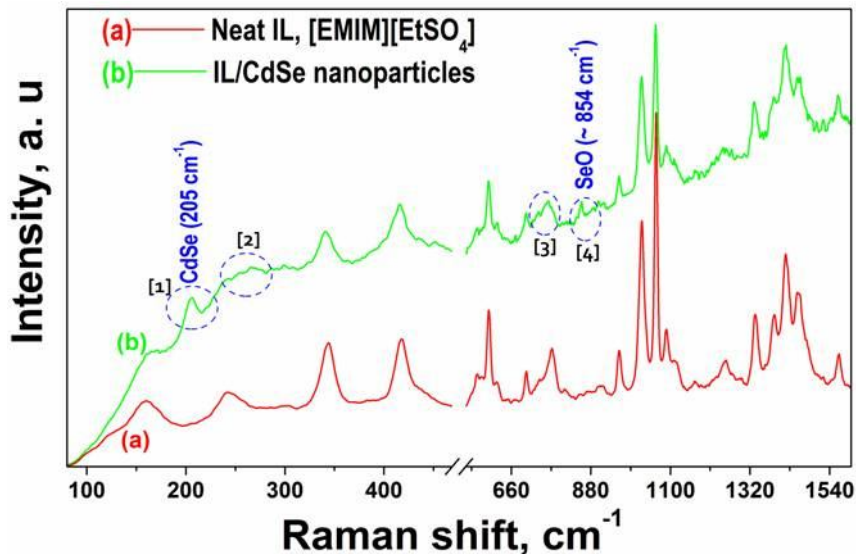


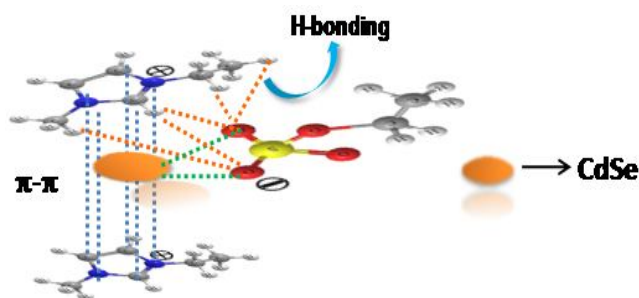
Fig.6.25. Raman spectra of neat IL (a) and IL + CdSe (b). The peaks marked have been described in the text.

The spectrum of the *neat* IL matches well with the earlier reports.^{303c, 361} The Raman spectra of the *neat* IL resembles closely with that of IL + CdSe with the appearance of some new peaks in the later case. No significant variation in the regions 1600-3200 cm⁻¹ could be observed in the Raman spectra of IL in the presence of CdSe. Nonetheless, the peak at ~ 205 cm⁻¹ (peak [1], IL + CdSe) (Fig.6.25b) have been assigned to the fundamental LO phonon mode of CdSe. Additional peak at 854 cm⁻¹ (shown as peak [4]) could be observed only in case of IL + CdSe and has been ascribed to the formation of a Se-O bond.³⁶³ The peaks present in the region 710-770 cm⁻¹ represents the C-C stretching and the ring HCCH symmetric bending modes of the *neat* IL,^{303c} which are altered and broadened in case of IL + CdSe (marked as [3]). Further, the peak appearing at ~ 250 cm⁻¹

Chapter 6

in case of *neat* IL (ascribed to the out-of-plane bending mode of the CH₃-(N) methyl group in the imidazolium cation³⁶⁴) is perturbed in case of IL + CdSe and seems to be embedded due to the appearance of a shoulder extending from 250-270 cm⁻¹ (marked as [2]). The presence of amorphous-Se might have contributed to the broadening in the said region as has been observed (Fig.6.23) in case of CdSe nanoparticles extracted from the IL. It is reasonable to confer that these variations in the intensities and the positions of the vibrational peak frequencies clearly indicate the involvement of π - π stacked aromatic geometry (among the cationic moieties) and the hydrogen bonding network (between the cation and the anion) is responsible for the as obtained nanomorphologies.

A pictorial representation of the interactions among the cationic and the anionic moieties of the IL with CdSe have been shown in scheme 6.3 on the basis of the vibrational studies.



Scheme 6.3 Diagrammatic representation of the possible interactions of the cationic and the anionic moieties of the IL with the as grown CdSe nanoparticles.

6.4. Conclusions

In the present work, we have demonstrated the influence of the inherent structure of the RTIL on the morphology of CdSe nanoparticles. In either of the synthetic methodologies, it was observed that IL played multiple roles, i.e. a solvent, stabilizing agent and a shape

Chapter 6

directing template. The fluidic aspects of the IL in conjunction with its *hydrogen bond-co- π - π stacking* mechanism enabled it to perform a function of a diffusion controller and an anisotropic growth director, respectively. The part of the work related to the normal chemical synthetic route (for the synthesis of CdSe nanoparticles in the IL), on one hand categorically demonstrates and emphasizes the fundamental role of water in creating the perturbations/distortions in the networking structure of the IL, but also reflect the potential to manipulate the morphologies (*vis-à-vis* their properties and applications) of the nanomaterials by precisely controlling the presence of water in the host matrix of the IL.

While, in case of radiation chemical synthesis, the peculiar properties of the electron beam induced nucleation and the subsequent growth process directed by the templated matrix of the IL leads to a unique nanomorphology. The proposed mechanism for the obtained 3D anisotropic nanomorphology may provide an intuitive protocol for better understanding and development of such complicated nanomaterials employing ILs as templates. The applications of such morphology of islands of quantum dots can be envisaged from its 3-D highly porous networking structure, as the nanostructures with high surface area and porosity exhibits tremendous potential in sensing and catalysis.

Chapter 7

Self-assembled CdSe quantum dots functionalized with β -cyclodextrin: Reduced cytotoxicity and band gap engineering

7.1. Introduction

In the realm of nanoscience and nanotechnology, researchers are paying more attention towards developing environmentally friendly and economically viable methodologies for the synthesis of nanomaterials.^{365, 366} Most of the passivating agents and some nanomaterials (for example CdSe) themselves are highly toxic in nature and the challenge lies in search of capping agents, which are biocompatible, provide desired aqueous solubility and also reduce the cytotoxicity of the nanoparticles. Furthermore, apart from the traditional research on the synthesis and morphological control of nanoparticles, we are now going through a stage of bottom-up nanofabrication in which nanoparticles spontaneously organize or self-assemble into ordered structures directed by using agents, external fields, or templates.³⁶⁷ In the recent times, the directed self-assembling of primary nanoparticles into superstructures has attracted tremendous interest, because they can reveal fundamentally interesting collective physical properties with enhanced efficiencies.³⁶⁸

Chapter 7

In this pretext, biomolecules such as cyclodextrins (CDs) and its derivatives have been used as a host matrix for the synthesis of various organized assemblies of predominantly metal nanoparticles.^{112, 369} CDs, as discussed in Chapter 1, are one of the well-known members of the family of supramolecular assemblies and comprises of glucose units (i.e. six (α -CD), seven (β -CD), or eight (γ -CD)) connected by α -1, 4 glycosidic linkages to form a series of oligosaccharide rings. One of the most important features exhibited by CDs is the structural microheterogeneity⁹⁹ in the sense that the hydrophilic -OH groups occupy both rims of the cone, while inside of the cavity is hydrophobic in character. These features have been reported to be responsible for the stabilization as well as the directed self-assembly of the nanoparticles through the hydrogen-bonding interactions between the exposed secondary -OH groups which eventually facilitate the threading of neighboring CDs.^{112, 115}

Considering this, we have demonstrated a simple, rapid and one step method mediated by electron beam irradiation technique for the synthesis as well as *in situ* functionalization of CdSe QDs with β -CD. The unique features of β -CD over other CDs as well as the advantageous aspects of electron beam mediated synthetic technique have been discussed in Chapter 1. Nevertheless, it was found that the β -CD molecules cap the as grown CdSe QDs by forming a non-inclusion complex. Detailed investigations were carried out to identify the forces and the binding sites involved in the complex formation between CD molecules and the QDs. Also, the effect of experimental parameters i.e. precursor and ligands (β -CD) concentration, absorbed dose and dose rate on the morphology and photophysical behavior of CdSe QDs were investigated. X-ray

Chapter 7

photoelectron spectroscopy (XPS) and pulse radiolysis studies were carried out to elucidate the role of β -CD in influencing the morphology and the formation mechanism of CdSe nanoparticles, respectively. Furthermore, the cytotoxicity effect of CdSe QDs was also monitored keeping in view of the bio-compatibility of β -CD.³⁷⁰

7.2. Experimental

High purity chemicals, β -CD, cadmium sulfate (CdSO_4), selenium (Se) powder, sodium sulfite (Na_2SO_3), were obtained from Sigma-Aldrich and used as received. The reagents, *tert*-butanol and ammonia solution were purchased with highest purity available from SDFCL, Mumbai. For preparing the precursor solutions, nanopure water from Millipore water purifying system was used. It is to be noted that equimolar concentrations of Cd and Se precursors were used to prepare the reaction mixture for the synthesis of CdSe nanoparticles. The freshly prepared Na_2SeSO_3 solution⁴⁰⁻⁴³ was added to the ammoniated CdSO_4 solution followed by *tert*-butanol to scavenge the $\cdot\text{OH}$ radicals generated during the radiolysis of aqueous solution. The scavenging of $\cdot\text{OH}$ radicals would allow only the e_{aq}^- to react with the precursors, thus inducing the reaction to proceed. β -CD was added to the reaction mixture just prior to irradiation. It is to be mentioned here that the concentration of β -CD employed in the reaction mixture matters a lot, because it is a well established fact that β -CD in water self-assembles even at concentrations as low as 3 mM, whereas no aggregates has been found to present in solution at lower concentrations.^{106, 107, 371} On exceeding the concentration of β -CD (in water) beyond 3 mM, initially a broad size distribution of clusters is formed, which is followed by the cluster-cluster and cluster-particle interactions.^{106, 107, 371} Taking these facts into account, the concentration of β -CD

Chapter 7

in the present work was kept constant at 2 mM, while the precursor solutions were varied to obtain various molar ratios (i.e. $[\beta\text{-CD}]: [\text{QD}] = 1:1, 2:1, 1:2$) and the same have been described in the following sections to investigate their impact on the morphology and the optical properties of as grown CdSe nanoparticles. It is to be noted that the concentration of the precursors solutions were very low, and no chemical reaction (leading to the formation of CdSe) was observed either in the absence or in the presence of $\beta\text{-CD}$ without irradiation.

The aforementioned reaction mixture was irradiated with a 7 MeV electron beam having an FWHM of 2 μs from a LINAC (described in Chapter 2) at a repetition rate of 12 pulses per second. However, the dose per pulse (Grey (Gy) per pulse, GPP) was varied from 10–140 Gy to investigate the dose rate effect. Also, the total absorbed dose imparted to the samples was ranged from 1 to 40 kGy to determine the dose effect. On irradiation, the color of the solution turned to greenish-yellow or reddish-orange, depending on the experimental parameters and this was the primary indication for the formation of CdSe nanoparticles. For convenience, the $\beta\text{-CD}$ coated CdSe QDs have been written as $\beta\text{-CD/CdSe QDs}$.

Pulse radiolysis experiments were carried out with a 7 MeV LINAC coupled with a kinetic spectrometer. The details of the set up are provided in Chapter 2. The FWHM of the electron pulse in these experiments were kept at 100 ns and absorbed dose was kept at 21 Gy/pulse. The time-resolved absorption spectra for the intermediate species produced during the radiolysis were obtained. The samples were N_2 bubbled for about 5-10 minutes prior to the irradiation.

Chapter 7

Cytotoxicity studies

Cell Cultures: INT 407, human intestinal epithelial cell line was maintained in Dulbecco's modified Eagle's medium (DMEM) (Himedia, India) supplemented with 10% fetal bovine serum (FBS), 100 units/ml penicillin and 100 $\mu\text{g/ml}$ streptomycin (Himedia, India). The cells were incubated in 5% CO_2 humidified at 37°C for growth.

The cytotoxicity of β -CD/CdSe QDs was carried out in human intestinal cell line, INT 407 cell (derived from human embryonic jejunum and ileum). In brief, cells (6×10^3) were seeded in a 96 well plate in DMEM supplemented with 10 % fetal bovine serum and antibiotics (100 units/ml penicillin and 100 $\mu\text{g/ml}$ streptomycin) and kept overnight in a CO_2 incubator (5% CO_2 and 95% humidity at 37°C) for attachment. The next day old medium was replaced with fresh medium with various concentrations of β -CD, bare CdSe QDs and β -CD/CdSe QDs. Changes in the cell morphology was monitored 24 hour post treatment. The corresponding morphological changes in INT 407 cells after incubation were visualized using an inverted microscope (Carl Zeiss, Axiovert 40 CFL, Germany) equipped with CCD camera. Representative images of the respective cases were captured and have been shown in the text along with their analysis.

Various photophysical studies (i.e. UV-Vis, Photoluminescence (PL), FTIR, Raman and PL lifetime) and nanoparticle characterization techniques (TEM, SEM and XRD) employed in this work have been explained in Chapter 2. To further substantiate the binding interaction mechanism between β -CD molecules and the QDs, the X-ray photoelectron spectroscopy (XPS) studies were performed using Mg K_α (1253.6 eV)

Chapter 7

source and a MAC-2 electron analyzer. The XPS-analysis chamber has a base vacuum of 10^{-9} mbar. The XPS binding energy scale was calibrated to C-1s line at 284.5 eV.

7.3. Results and Discussion

7.3.1. Morphology and structural characterization

On irradiation the color of the solution containing the reaction mixture turned to greenish-yellow or reddish-orange depending on the experimental parameters. This was considered as the primary indication for the formation of the CdSe nanoparticles. Fig.7.1 shows the TEM images of bare as well as β -CD/CdSe QDs grown *via* electron beam irradiation method. The SAED pattern (shown in the inset of Fig. 7.1a) indicates the polycrystalline nature of these nanoparticles. Besides, the particles display more or less spherical shapes as could be observed from their TEM images.

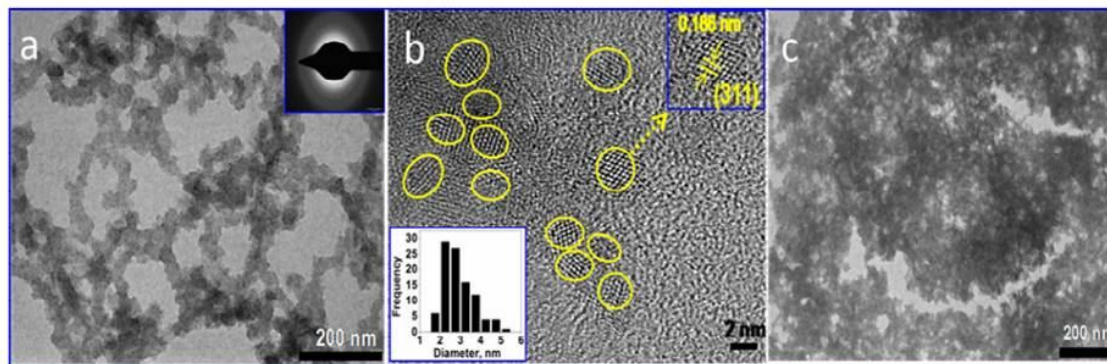


Fig.7.1. TEM (a) and HRTEM (b) images of β -CD/QD with molar ratio of 2:1. Inset in the image (b) shows the particle size distribution. The average size was found to be ~ 2.2 nm. TEM image of β -CD/QD with molar ratio of 1:1 (c), synthesized via electron beam irradiation (Absorbed dose = 25 kGy @ 140 GPP).

The HRTEM image (bar scale = 2 nm) have been provided in Fig.7.1b, wherein the lattice fringes could be clearly seen and the measured interplanar distance ($d = 0.186$ nm)

Chapter 7

closely matches with the standard 'd' value of 0.183 nm for lattice plane (311) of the cubic phase of CdSe. Also, the particle size distribution plot has been shown in the inset of Fig.7.1b. The average size of the QDs was found to be $\sim 2.2 \pm 0.3$ nm; hence the polydispersity in the size distribution was calculated to be ~ 14 %.

In the absence of β -CD, the CdSe nanoparticles agglomerated and formed a complex network with no well defined structure/pattern, as has been reported earlier.^{165, 167} While, β -CD/CdSe QDs appeared to form an array like network in which small beads are joined together to give a pearl necklace shape (Fig.7.1a). The most probable reason for such a shape could be the intermolecular hydrogen bonding between the -OH groups of the β -CD molecules adsorbed on the surface of the nanoparticles. The adsorption phenomenon has also been evidenced in the FTIR spectral and XPS studies (discussed later). It appears that, β -CD being the linker molecule, drives the self-assembly of the CdSe nanoparticles leading to necklace shaped superstructure. However, it is to be noted that such pattern was observed only in case of β -CD to precursor molar ratio of 2:1. At a molar ratio of 1:1 of β -CD to precursor, the density of as grown nanoparticles increases in conjunction with the formation of a complex network (Fig.7.1c). In other words, at precursor concentrations greater than or equal to that of β -CD, the corresponding increase in the density of CdSe nanoparticles hinders the rearrangement process. Thus, multiple interactions among the β -CD coated QDs lead to a complex network. Nevertheless, no agglomeration of nanoparticles was observed here, unlike in the case of bare nanoparticles.

Chapter 7

The structure, phase and size of as grown nanoparticles were determined from the XRD pattern. The XRD spectrum of as synthesized nanoparticles with molar ratio, 2:1 ([β -CD]: [Precursor]) has been provided as a representative diffraction pattern in Fig.7.2. Along with the β -CD coated QDs, the XRD pattern of bare CdSe nanoparticles is also illustrated for comparative studies. The diffraction pattern of the nanoparticles has been found to be in good agreement with the standard JCPDS card no. 19-0191, corresponding to the cubic structure of CdSe. The diffraction peaks of β -CD/CdSe QDs appeared at 2θ (degree) values of 25.97, 42.43, 49.49 and are related to the lattice planes (111), (220), (311), respectively. All the diffraction peaks comprised of considerable broadening, which might have arisen due to the diffraction uncertainties related to the polycrystalline nature, small particle size and strain. The nanoparticles size (or diameter, D) has also been determined by using Scherrer formula:

$$D = \frac{0.9 \lambda}{\beta \cos(\theta)} \quad [7.1]$$

where, λ is the wavelength of X-ray used (1.54 Å), β is the FWHM (in radians) and θ is the diffraction angle. The particle size of CdSe QDs in the presence of β -CD was obtained to be ~ 1.6 nm, while the same was found to be ~ 2 nm for bare QDs. The possibility of the strain developed on the as grown QDs was determined by calculating the lattice constant (a) in the equation relating the interplanar distance (d) with the miller indices of cubic crystal i.e. $d = a / (h^2 + k^2 + l^2)^{\frac{1}{2}}$. The lattice constant (a) for β -CD/CdSe QDs and bare ones were obtained as 5.92 Å and 6.02 Å, respectively, while the standard value of 'a' for cubic CdSe is 6.07 Å. Therefore, it is evident that significant

Chapter 7

amount of strain is present in β -CD/CdSe QDs, while it is very less in case of bare ones. These observations were further substantiated by the Raman spectral studies discussed below.

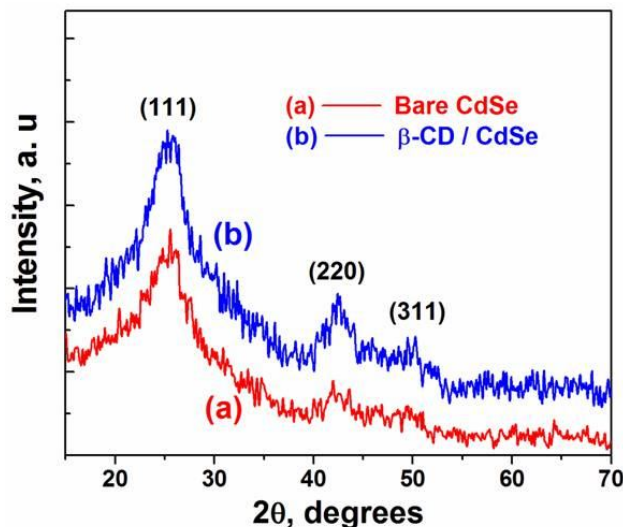


Fig.7.2. XRD patterns of bare CdSe nanoparticles (a), β -CD/CdSe QD with molar ratio of 2:1 (b), synthesized via electron beam irradiation (Dose = 25 kGy @ 140 GPP).

Raman spectra of as grown β -CD/CdSe QDs comprise of fundamental longitudinal optical (LO) phonon peak along with its overtone (2LO) peak at 205 and 407 cm^{-1} , respectively (Fig.7.3). While the bare CdSe QDs exhibit LO and 2LO peaks at 207 and 409 cm^{-1} , respectively. A shoulder occurring in both the cases (bare CdSe and β -CD /CdSe) at around 168 cm^{-1} can also be noticed, which has been attributed to the transverse optical (TO) phonon mode.³⁵⁷ A small diffused and broad peak at $\sim 250 \text{ cm}^{-1}$ is apparent in the Raman spectra of bare CdSe, which is reduced in case of β -CD coated QDs. Essentially, appearance of surface optic (SO) modes have been reported earlier^{357, 358} in case of small sized QDs (CdSe), accompanied by a peak near 250 cm^{-1} . And these SO

Chapter 7

modes originates due to the presence of more number of atoms on the surface as compare to the bulk in very small sized nanoclusters, behaving like molecules.³⁵⁸ Thus, the peak obtained at $\sim 250 \text{ cm}^{-1}$ in the Raman spectra of as grown bare as well as β -CD/CdSe QDs has been attributed to the SO modes. From these results, it can be inferred that β -CD effectively passivate the CdSe QDs along with the substantial reduction in the amount of surface states. Besides, there is a red shift (down shift) of LO peak in both the cases (bare CdSe as well as β -CD/CdSe) from its position for bulk CdSe i.e. $210 - 213 \text{ cm}^{-1}$.^{330b, 360} The red shift of LO peak with respect to the bulk CdSe in case of β -CD/CdSe QDs (205 cm^{-1}) is more compared to that of bare QDs (207 cm^{-1}). Since, the shifts in the fundamental LO peaks in nanomaterials is primarily dominated by the quantum confinement effects, but it is often accompanied by the dimensional effects such as surface reconstruction and lattice contraction.^{330d, 372-374}

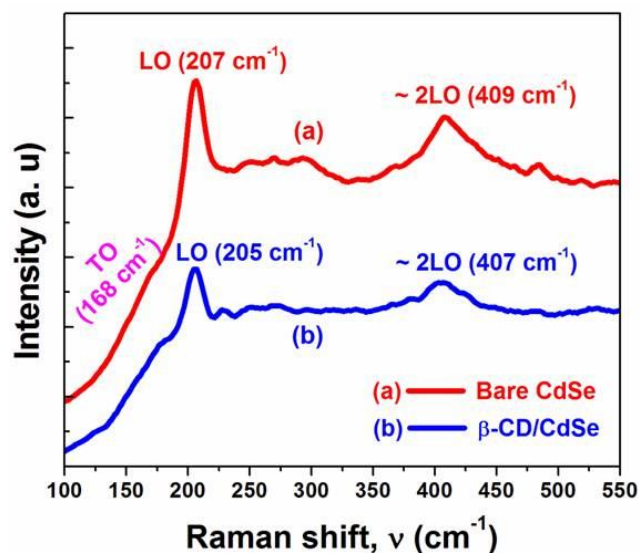


Fig.7.3. Raman spectra of bare CdSe nanoparticles (a), β -CD/QDs with molar ratio of 2:1 (b), synthesized via electron beam irradiation (Dose = 25 kGy @ 140 GPP).

Chapter 7

The surface morphological and chemical composition studies of as grown QDs were further carried out by SEM and EDS measurements, respectively. Fig.7.4a shows the SEM image of as grown β -CD/CdSe QDs. An interesting morphology was observed just like a 'dry river bed'. It appeared that the QDs formed are embedded in the planar domains of sheets, which underwent rupturing at certain stage due to some kind of strain. The EDS measurements (Fig.7.4b) confirmed the formation of CdSe. The high intensity peak showing the presence of silicon (Si) is originated from the Si wafer used as a substrate for the sample analysis. The chemical composition mapping of the region (depicted in Fig.7.4a) was carried out, which further supports the presence of Cd (image 4c) and Se (image 4d) in the same chunk areas.

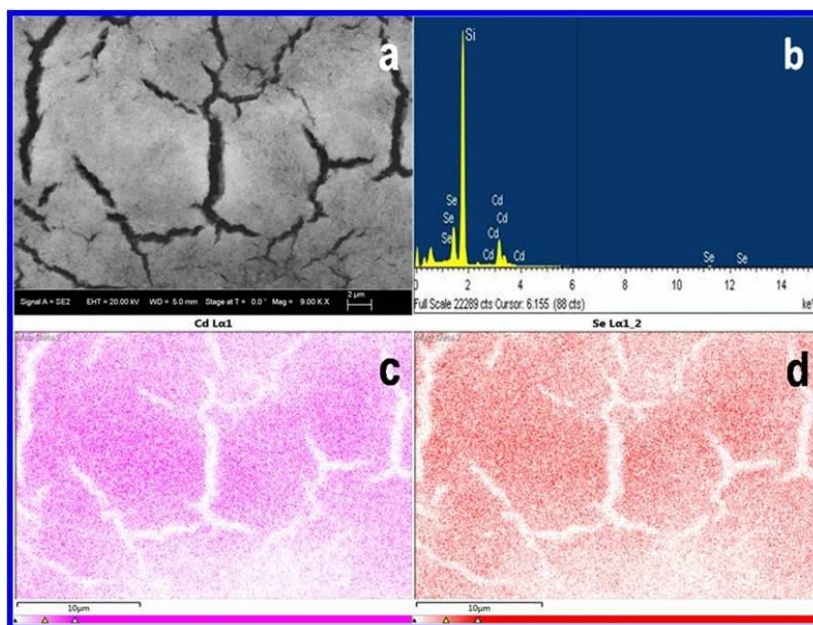


Fig.7.4. SEM image (a) and the corresponding EDS (b) of β -CD/CdSe nanoparticles with molar ratio of 2:1, synthesized via electron beam irradiation (Dose = 25 kGy @ 140 GPP). Images (c) & (d) show the presence of Cd and Se, respectively during the chemical composition mapping of the region in image (a).

Chapter 7

To ensure the reproducibility of as obtained morphology, same experiment was repeated 3 times and each time similar features were noticed. Earlier, we have also reported the citric acid mediated synthesis of CdSe nanoparticles *via* similar technique and under similar experimental conditions; however, sea urchin like morphology was observed therein.¹⁶⁴ This indicates a significant influence of β -CD molecules in the formation of above mentioned morphological features shown in the SEM image (Fig.7.4a). Although the exact reason for the obtained sheet like morphology is not known precisely, however, it could be due to the hydrogen bond network present among the molecules of β -CD. Further, the concentration of β -CD was kept at as low as 2 mM in the present study, which should exclude any possibility of the aggregate formation. Moreover, it is well recognized fact that β -CD among its CD family behaves most mysteriously in the sense that the molecules of β -CD in aqueous solution undergo restructuring to form different morphologies, which basically depends on its concentration. For instance, Bonini *et al.*¹⁰⁶ have reported the formation of large sheet like domains of β -CD, when its concentration is increased up to 6 mM. Furthermore, rupturing of such sheets was also reported due to the shear stress developed during the blotting step in the sample preparation process. And, this effect was ascribed owing to the fragile nature of the cohesive forces present in the aggregates/clusters of CDs. Keeping these facts into account, it is suspected that the evaporation (of solvent, water) process during the sample preparation might have lead to some amount of aggregation on the Silicon wafer (as a sample substrate). Eventually, that could have resulted into the

Chapter 7

formation of sheet like structure embedding CdSe nanoparticles in it and, further rupturing of these sheets due to the reason already mentioned.

Evidence for the functionalization of β -CD with CdSe QDs

Our group has earlier reported the formation of bare CdSe nanoparticles *via* electron beam irradiation technique in aqueous solution.¹⁶⁵ However, the nanoparticles were found to be highly unstable and undergo decomposition within 2-3 hours. Further, the bare nanoparticles were feebly fluorescent. Therefore, first and the foremost evidence for the functionalization of CdSe QDs with β -CD is the enhancement of their stability from few hours to approximately 1 month at ambient conditions. In addition, the β -CD coated QDs showed strong emission (discussed later), which can be regarded as an indirect indication of passivation of the surface of QDs with β -CD.

Apart from these, FTIR spectra could provide the direct evidence of the *in situ* adsorption or functionalization of β -CD on the surface of as grown CdSe QDs. The FTIR spectra of bare CdSe QDs have been shown along with that of β -CD and β -CD/CdSe QDs in Fig.7.5. It can be clearly seen that β -CD and β -CD/QDs show very similar spectral features and peak positions for several vibrational modes. It is to be mentioned here that because the sizes of nanoparticles determined from the TEM, XRD and absorption measurements are much larger than the diameter of the β -CD cavity (inner diameter \sim 6-8 Å), therefore the possibility of formation of inclusion complexes has been ruled out. Nevertheless, the strong resemblance between their IR spectra indicates a successful anchoring of β -CD onto the surface of CdSe QDs. Further evidences can be realised from the decrease in the relative intensity of the transmittance bands corresponding to the

Chapter 7

skeletal vibrations in the region $700\text{-}1300\text{ cm}^{-1}$, especially involving α -1, 4 linkage at 946 cm^{-1} and ring ‘breathing’ vibration at 756 cm^{-1} of free β -CD molecules.^{369f} The peak at 1645 cm^{-1} is due to the moisture absorption. Interestingly, a doublet at around 2356 cm^{-1} and 2333 cm^{-1} accompanied by a broad peak at $\sim 2080\text{ cm}^{-1}$ can be noticed in the IR spectra of bare CdSe and β -CD/CdSe QDs. These peaks have been ascribed to the presence of CO_2 present in the sample chamber, which might have adsorbed on the sample surface. A peak was observed at $\sim 950\text{ cm}^{-1}$ in the IR spectra of bare CdSe QDs, which have been assigned to the Se-O bond.

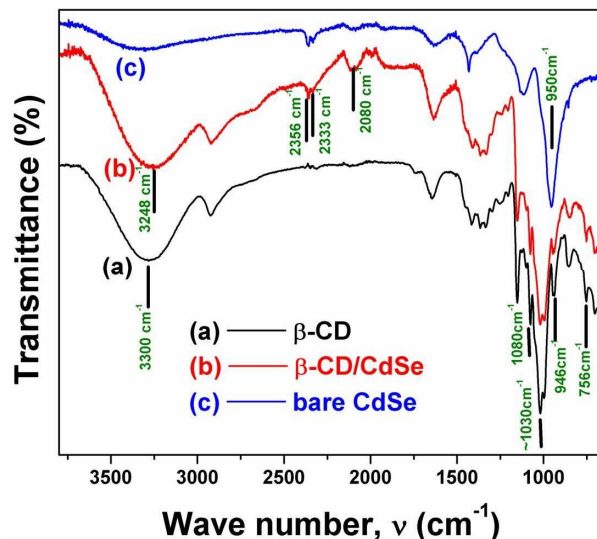


Fig.7.5. FTIR spectra of β -CD (a), β -CD/CdSe with molar ratio of 2:1 (b). Absorbed Dose = 25 kGy @ 140 GPP.

As mentioned earlier also that the uncapped CdSe QDs were found to be highly unstable and decomposed quickly.^{165, 167} This was attributed to the presence of unsatisfied Se valencies which react with oxygen to form SeO_2 and other related species. However, peak corresponding to Se-O bond is not visible in the IR spectra of β -CD/CdSe QDs,

Chapter 7

which indicates the strong passivation by the β -CD molecules. Apart from this, there is a red shift accompanied by broadening of the peak in the O-H stretching frequency of β -CD/CdSe QDs ($\sim 3248 \text{ cm}^{-1}$) compared to that of β -CD ($\sim 3300 \text{ cm}^{-1}$). This signifies a sort of bond formation between -OH groups of β -CD and the QDs. Now, the question arises here is regarding the identification of the -OH groups (primary, 1^0 or secondary, 2^0) involved in the bond formation with the QDs. The ν (C-O) stretching frequency of the 2^0 -OH groups (present on the secondary face) lies at 1080 cm^{-1} , while that of ν (C-O) stretching frequency of the 1^0 -OH groups (present on the primary face) lies at $\sim 1030 \text{ cm}^{-1}$.^{369b} Since, the IR peak corresponding to 1^0 -OH groups were much more dampened than that for 2^0 -OH groups which indicates that the bonding is preferably taking place with the 1^0 -OH groups of β -CD molecules. Moreover, the 1^0 -OH groups of β -CD molecule are more flexible and have higher reach as compared to that of 2^0 -OH groups,³⁷¹ due to which a reactivity difference arises between the two types of -OH groups. Thus, it can be inferred on the basis of FTIR spectral analysis that β -CD molecules are most probably undergoing chemisorption through the 1^0 -OH groups, followed by the formation of a non-inclusion complex thereby, coating the surface of the QDs.

Further, XPS measurements were carried out to investigate the constituting elements involved in the bonding interactions between the QDs and β -CD molecules. The core level spectra of Cd 3d, Se 3d, and O 1s are shown in Fig.7.6.

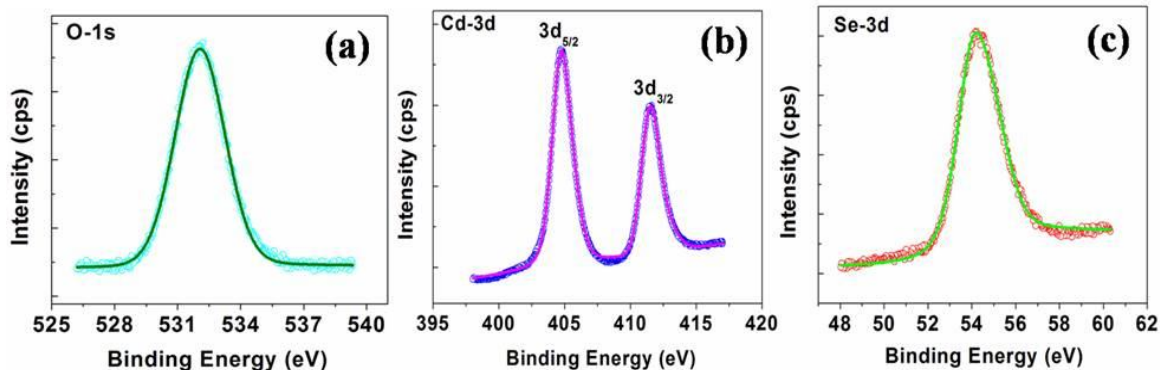


Fig.7.6. Core level XPS spectra of (a) O 1s, (b) Cd 3d, and (c) Se 3d.

The appearance of O 1s peak at 532 eV (Fig.7.6a) indicates its presence in the form of -OH group.^{375a} The pair of peaks located at ~ 405 eV and ~ 411.5 eV has been assigned to Cd 3d_{5/2} and 3d_{3/2}, respectively.^{375b} The presence of Se 3d peak at a binding energy of 54.2 eV confirms the presence of CdSe phase only.^{375b} The existence of Se oxides gives a peak between 58-59 eV,^{375c} which was not found in the XPS of these QDs. The possible formation of CdO also can be rejected because of the absence of both the O 1s peak at 530 eV^{375a} and Cd 3d_{5/2} peak at ~ 404.0 eV.^{375a, c} However, the XPS peak for Cd (3d_{5/2}) present in the form of Cd(OH)₂ appears at 405.1 eV,^{375a, c} which is very close to the binding energy of Cd (3d_{5/2}) existing in the CdSe phase. Thus, the XPS measurements clearly suggest the bonding of the -OH groups of the β -CD molecules predominantly with the Cd atoms present on the surface of the QDs. Similar observations were reported by Liu *et al.*³⁷⁶ in which various ligands such as TOPO, thiophenol, α -toluenethiol, and p-hydroxythiophenol were found to bind much strongly to the Cd atoms than to the Se atoms of the CdSe QDs.

Chapter 7

7.3.2. Optical studies

7.3.2.1. Molar ratio effect

The optical absorption measurements of the sample solutions were carried out before and after the electron beam irradiation. The unirradiated solutions containing the precursors (equimolar) and β -CD exhibited no absorption in the range from 350 to 700 nm (Fig.7.7). On the contrary, the irradiated solutions showed absorption with clear excitonic peaks in the range of 400-500 nm. The absorption spectra of the corresponding sols with different molar ratios of β -CD and precursor (represented as β -CD: QD) at a fixed dose of 25 kGy @ 140 GPP have been shown in Fig.7.7.

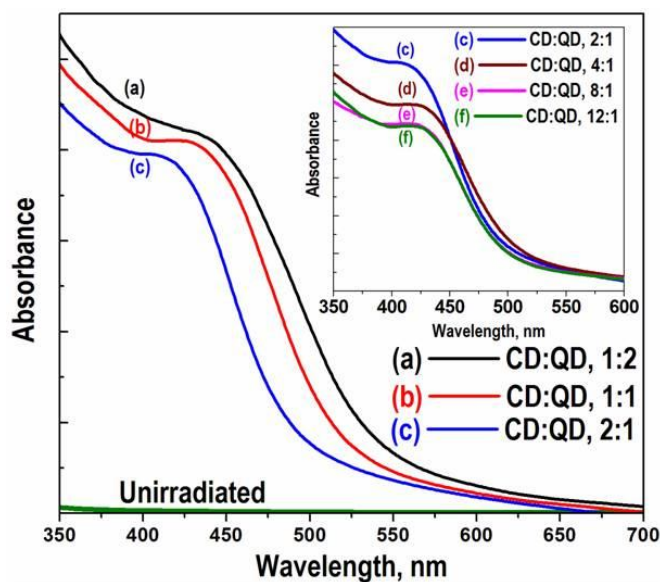


Fig.7.7. UV-Vis absorption spectra of β -CD/CdSe QDs with molar ratios (β -CD: QD); 1:2 (a), 1:1 (b), 2:1 (c). Inset shows the spectra with higher molar ratios (β -CD: QD); 4:1 (d), 8:1 (e), 12:1 (f). Absorbed Dose = 25 kGy @ 140 GPP.

The excitonic peak of β -CD/CdSe QDs with molar ratio of 2:1 appeared at \sim 420 nm, which is significantly blue-shifted from the bulk CdSe having peak at \sim 716 nm. This

Chapter 7

illustrates the quantum confinement effect governing the optical properties of β -CD/CdSe QDs. However, a red shift in the excitonic peak position was observed on varying the β -CD: QD from 1:1 (~ 432 nm) to 1:2 (~ 443 nm). At higher molar ratios i.e. 4:1, 8:1 and 12:1, no noticeable shift in the excitonic peak positions was observed relative to that in case of molar ratio 2:1 (inset of Fig.7.7). Thus, optimum molar ratio of β -CD and the precursors is 2:1 for effectively coating and restricting the size of as grown CdSe QDs. This was further supported by the PL measurements of β -CD/CdSe QDs with different molar ratios of β -CD and precursors.

Fig.7.8 shows the trend for the variation of PL intensity (at 525 nm with $\lambda_{\text{ex}} = 420$ nm) of β -CD/CdSe QDs with different molar ratios at a fixed dose of 25 kGy @ 140 GPP. The QDs with molar ratio 2:1 (β -CD: QD) displayed the highest PL intensity followed by the ratios 1:1 and 1:2, respectively. Therefore, the trend of the PL intensities clearly indicates the inappropriate capping of the CdSe QDs by β -CD molecules at lower concentrations. As a result of which, number of trap/defect states on the surface of the CdSe QDs increases, thus leading to the occurrence of the non-radiative carrier relaxation processes. Further, the QDs synthesized with molar ratios of 1:1 and 1:2 were less stable. This is probably due to the reaction of oxygen with the surface exposed unsatisfied valencies (mostly Se) leading to the formation of their oxides (i.e. SeO_2), and thereby paving the way for the decomposition of CdSe QDs.

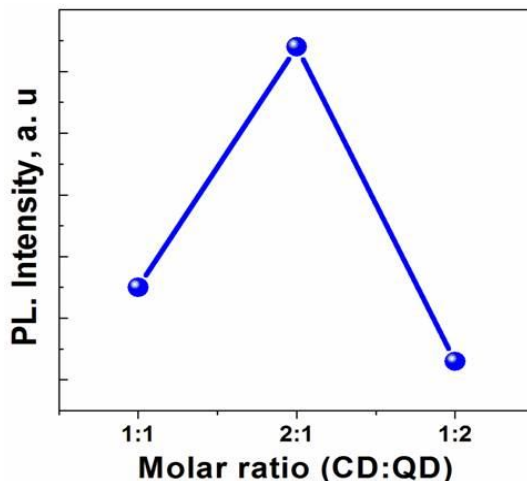


Fig.7.8. Trend showing PL intensity of β -CD/CdSe QDs with various molar ratios (β -CD: QD) at 525 nm. $\lambda_{ex} = 420$ nm. Absorbed dose = 25 kGy @ 140 GPP.

The estimated size of the primary CdSe QDs functionalized with β -CD at various molar ratios were calculated from the absorption spectra by using the modified Brus equation (7.2):

$$E_g = E_g(0) + \alpha/d^2 \quad [7.2]$$

where, $\alpha = 3.7 \text{ eV nm}^2$, $E_g(0) = 1.75 \text{ eV}$, $d =$ particle size (nm) and $E_g =$ band gap value in eV. The band gap (E_g) values were determined from the Tauc plot of $(\alpha' h\nu)^2$ vs. $h\nu$, as this is a direct band gap semiconductor. The symbol ' α ' represents the absorption coefficient multiplied with the concentration of the CdSe QDs and is equivalent to the relation $(2.303A/l)$, where ' A ' is the absorbance and ' l ' is the optical path length of the cell (10 mm). The term ' $h\nu$ ' represents the photon energy. The estimated sizes of the QDs synthesized under various experimental conditions are listed in Table 7.1. The size of QDs synthesized with molar ratio of 2:1 is in good concurrence with that determined from the XRD and the TEM analysis.

Chapter 7

Table 7.1: The band gap values (E_g , eV) and the size of the CdSe QDs (nm) synthesized via electron beam irradiation with different molar ratios of β -CD and precursor concentrations, absorbed dose and dose rates.

Molar ratio (β -CD : QD)	Dose, kGy	Dose rate, Gy/pulse	Band gap energy, E_g (eV)	Particle size (nm)
2:1	10	140	2.31	2.31
	15	140	2.47	2.25
	25	140	2.54	2.10
	25	50	2.42	2.33
	25	80	2.45	2.28
1:2	25	140	2.40	2.36
1:1	25	140	2.46	2.26

7.3.2.2. Absorbed dose effect

To investigate the effect of dose on the morphology of as grown QDs, the reaction mixtures (with molar ratio β -CD: QD, 2:1) were irradiated with different absorbed doses (@ 140 GPP) and the absorption spectra of the corresponding sols have been shown in Fig.7.9. The optimization of dose imparted is an essential step in the radiation induced synthesis of nanomaterials. CDs are made of saccharides, which are vulnerable to decomposition at higher radiation doses. However, it has been reported earlier¹¹⁹⁻¹²¹ that the presence of water acts as a protector and insignificant radiation decomposition of β -CD has been observed at a dose more than 25 kGy.^{122, 123} Thus, our approach was to study the effect of absorbed dose on the nanomorphology of β -CD/CdSe QDs.

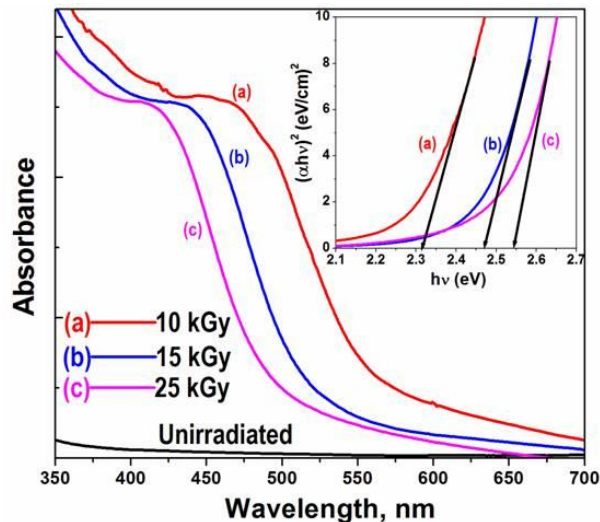


Fig.7.9. UV-Vis absorption spectra of β -CD/CdSe QDs with molar ratio (β -CD: QD, 2:1) at various doses (@ 140 GPP); 10 kGy (a), 15 kGy (b), 25 kGy (c). Inset: Tauc plot of $(\alpha' h\nu)^2$ vs. $h\nu$ for the determination of band gap values (E_g).

The optimization of dose was carried out on the basis of stability, absorption and emission characteristics of the QDs at various doses. As can be seen from Fig.7.9, the excitonic peak undergoes blue shift with the increase in dose. This indicates that the size of β -CD/CdSe QDs decreases with the increase in dose. The observed trend can be explained on the basis that at higher absorbed doses, the number of nucleation centers formed are more and lead to the retardation of growth process. Subsequently, coalescence of these very small nanoparticles is prevented by the efficient capping of the β -CD molecules. Similar results regarding the effect of dose on the size of the nanoparticles have been observed by various researchers.^{251, 252} The estimated size of the primary β -CD/CdSe QDs at various radiation doses were determined from the absorption spectra and are listed in Table 7.1.

Chapter 7

The PL intensity of β -CD/CdSe QDs were measured at various absorbed doses keeping the molar ratio (β -CD: QD) and dose rate fixed at 2:1 and 140 GPP, respectively (Fig.7.10). Interestingly, the PL intensity was found to be highest at an absorbed dose of 25 kGy, after which it decreases drastically. At lower doses, (especially at ≤ 10 kGy) the PL intensity was found to be very less. Consequently, the dose of 25 kGy was found to be optimized in terms of maximum PL intensity exhibited by the QDs as well as keeping in view of the radiolytic degradation of β -CD.

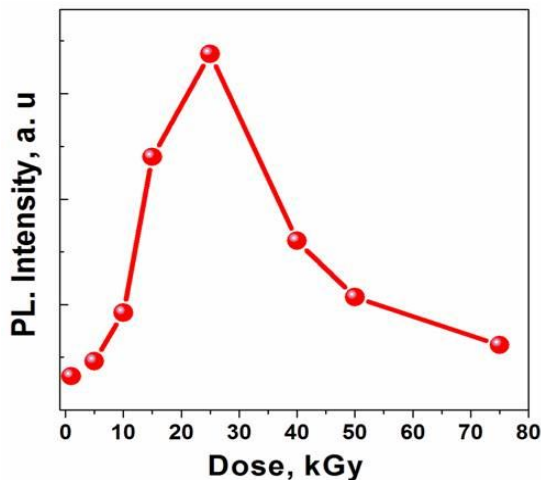


Fig.7.10. Trend showing PL intensity of β -CD/CdSe QDs vs. absorbed dose with molar ratio (β -CD: QD) of 2:1 at 525 nm and λ_{ex} of 420 nm. Dose rate = 140 GPP.

Typical room temperature absorption and emission spectra of β -CD/CdSe QDs grown under these optimum experimental conditions are shown in Fig.7.11A, at different excitation wavelengths. It is observed that the PL spectra is quite broad and extends from 450-700 nm region. Such broadening in the PL spectra of QDs is generally rationalized by: (i) polydispersity in the size distribution of the nanoparticles²⁵⁴ or (ii) polydispersity in the density and the nature of distribution of trap/defect states leading to various

Chapter 7

recombination paths for the photogenerated carriers in the nanoparticles.^{253b, 255} Since, the as grown CdSe QDs exhibit excitation wavelength independent (in terms of peak shifts) emission spectra; it can be regarded as an indication of a narrow size distribution.³⁷⁷ Further, the particle size distribution as determined from the TEM measurements was found to be only about 14 %. Therefore, the main reason for the broadening in the emission spectrum (of β -CD/CdSe QDs) can be ascribed to the polydispersity in the density and the nature of distribution of trap/defect states.

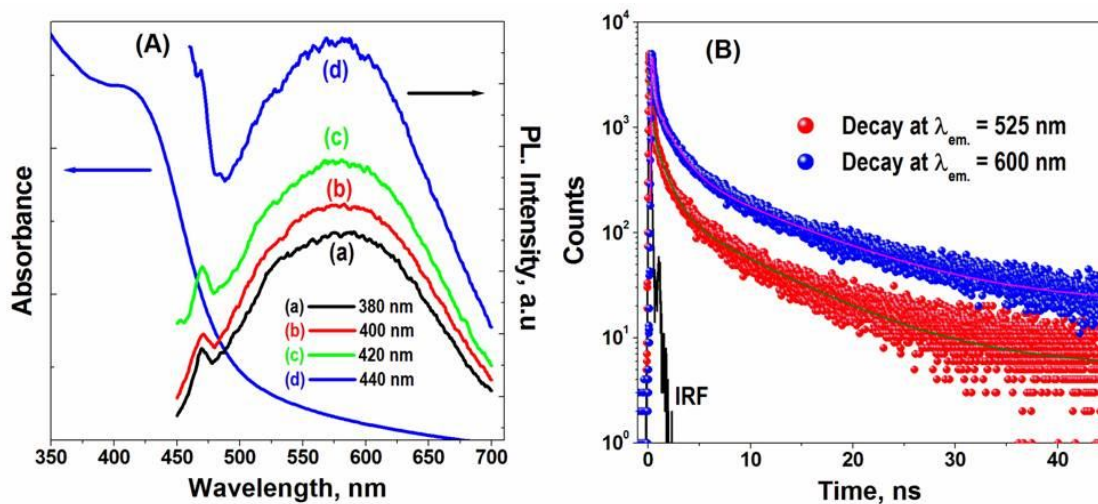


Fig.7.11. Room temperature PL spectra (A) and the PL Lifetime decay curve ($\lambda_{ex} = 374$ nm) (B) of β -CD/CdSe QDs with molar ratio (β -CD: QD) of 2:1 at an absorbed dose of 25 kGy @ 140 GPP.

The PL spectrum appeared to be a convolution of two regions, a shoulder at ~ 525 nm and a noticeable peak at ~ 600 nm. The PL band with a shoulder at ~ 525 nm has been assigned to the band gap emission (BGE) due to its close proximity with the excitonic peak position. The PL band with the peak at ~ 600 nm has been designated to the trap state emission (TSE) due to its large Stokes shift relative to the excitonic absorption peak.

Chapter 7

The time resolved PL decay studies (shown in Fig.7.11B) further substantiate the above denotation of the peaks at two emission wavelengths i.e. 525 nm (BGE) and 600 nm (TSE). In general, the shorter life-time is accredited to the band gap (intrinsic) recombination, while the longer lifetime is attributed to the involvement of surface states in the carrier recombination process.³⁷⁸ In concurrence to this, the average lifetime ($\langle\tau\rangle$) obtained by analyzing and fitting the decay traces at BGE and TSE are 3.8 and 5.5 ns, respectively. The corresponding χ^2 values for the former and the later decay traces are 1.2 and 1.3, respectively. The PL decay curves of as synthesized CdSe QDs exhibited multi-exponential (tri-exponential) behavior, which were analyzed and fitted using equation (7.3):

$$I(t) = a_1 e^{-t/\tau_1} + a_2 e^{-t/\tau_2} + a_3 e^{-t/\tau_3} \quad [7.3]$$

where, $I(t)$ is the time-dependent emission intensity, 'a' is the amplitude, and τ is the lifetime. The average PL lifetime ($\langle\tau\rangle$) values were deduced using equation (7.4):

$$\langle\tau\rangle = \frac{\tau_1 a_1 + \tau_2 a_2 + \tau_3 a_3}{a_1 + a_2 + a_3} \quad [7.4]$$

Such multi-exponential behavior of the CdSe nanoparticles is widely known and has been reported by various researchers earlier.^{256a-c} Although, most of these reports generally attribute such behavior to the diverse recombination paths owing to the varying degree of size, shape, surface defects/energy traps between the individual nanocrystals. Still, the origin and the explanation for this multi-exponential emission dynamics are not very clear and is currently a subject of debate.

Chapter 7

Furthermore, the excitonic dynamics and the nature of distribution of surface/trap states of as grown CdSe QDs at various absorbed doses can be realized from their time-resolved PL decay traces as shown in Fig.7.12.

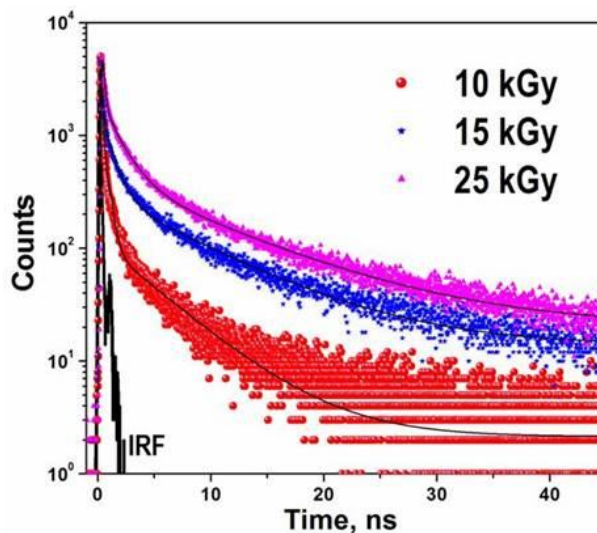


Fig.7.12. Room temperature time resolved PL decay curve ($\lambda_{ex} = 374$ nm and $\lambda_{em} = 600$ nm) of β -CD/CdSe QDs with molar ratio (β -CD: QD) of 2:1 at various absorbed doses @ 140 GPP.

In the following set of experiment, the molar ratio (β -CD: QD) and the dose rate were kept fixed at 2:1 and 140 GPP, respectively. Table 7.2 shows the time constant values with their relative amplitudes (in %) and the average life time values at various absorbed doses. The highest excitonic recombination lifetime was observed for QDs synthesized at an absorbed dose of 25 kGy, which was further declined with the decrease in the imparted dose. It was revealed in our experiments that the PL intensity increased with increase in dose up to 25 kGy, while the size of the as grown QDs was found to vary conversely with the dose.

Chapter 7

Table 7.2: Emission lifetime values of β -CD/CdSe QDs synthesized via electron beam irradiation at different absorbed doses with fixed molar ratio of 2:1 and dose rate at 140 GPP ; $\lambda_{ex} = 374$ nm and $\lambda_{em} = 600$ nm.

Dose, kGy	τ_1 (a ₁)	τ_2 (a ₂)	τ_3 (a ₃)	Average lifetime ($\langle\tau\rangle$), ns
10	4.0E-10 (15 %)	5.1E-09 (15 %)	6.4E-12 (70 %)	1.0
15	1.6E-09 (30 %)	9.8E-09 (47 %)	2.0E-10 (23 %)	5.1
25	1.8E-09 (32 %)	1.0E-08 (48 %)	2.6E-10 (20 %)	5.5

Essentially, these trends reflect a sort of correlation with the trend noticed in the lifetime values with the dose. It is known that the photo-excitation of CdSe QDs lead to the promotion of an electron to the conduction band which relaxes quickly to the bottom of the conduction band giving rise to BGE and contributes to the fastest lifetime decays. Considering this, the time constant, τ_3 is the fastest component (for the dose of 10 kGy) and thus most probably originated from the intrinsic recombination (band gap) of charge carriers. Further, the time constants, τ_1 and τ_2 are originated from the surface states/trap states. It signifies that the trap states comprises of both the shallow as well as the deep states. In fact, it has been reported that the shallow trap states exhibit lower lifetime than the deep trap states, depending on the chemical nature and crystal structure of the QDs.^{379,}
³⁸⁰ Therefore, the constant τ_1 having lower lifetime of 0.40 ns can be assigned to recombination time involving the shallow trap states, while the constant τ_2 with higher lifetime of 5.13 ns has been attributed to be originated due to the presence of deep trap states. Similar assignments can be made to the time constants obtained in case of QDs

Chapter 7

synthesized at radiation doses of 15 and 25 kGy. On careful examination of the time constant values and their relative amplitudes (Table 7.2), it is noticed that the contribution of the slowest component i.e. τ_2 in all the cases increases with the dose imparted. Interestingly, this trend is in synchronization with that of the PL intensity, which increased with the increase in the amount of dose imparted up to 25 kGy (explained earlier). Therefore, it can be stated that the increase in the PL lifetime of as grown β -CD/CdSe QDs is associated with an increase in the PL intensity. This enhancement in the PL intensity is primarily originated from an increase in the contribution from the radiative carrier recombination at the surface states. In fact, the as observed surface states related influence on the lifetime of the excitonic recombination has been reported by various researchers also,^{261, 262, 381} wherein the increase of the PL quantum efficiency of the QDs under photoactivation was found to be associated with an increase in the average PL lifetime values. The reason behind the faster recombination dynamics observed in QDs synthesized at lower radiation doses (i.e. 10 kGy) have been ascribed to their bigger size. Apparently, the increase in the interior trap states such as crystal defects can be realized from the diminution of the lifetime values. This statement gets further support from the earlier studies,^{236a, 382, 383} wherein the faster dynamics in the larger size nanoparticles was attributed to the non-radiative relaxation of the charge carriers to underlying trap states. Furthermore, Rao *et al.*³⁸⁴ had also reported the faster PL decay in the bigger size nanoparticles and explained it on the basis of the volume recombination of the carriers, as the surface to volume ratio decreases with the size of the nanoparticles.

Chapter 7

7.3.2.3. Dose rate effect

The effect of dose rate on the morphology of β -CD/CdSe QDs was investigated by varying the dose per pulse as well as the irradiation time. The reaction mixture with a molar ratio (β -CD: QD) of 2:1 was irradiated with a fixed absorbed dose of 25 kGy at different dose rates ranging from 50 to 140 GPP. The absorption spectra of the corresponding colloidal sols have been shown in Fig.7.13.

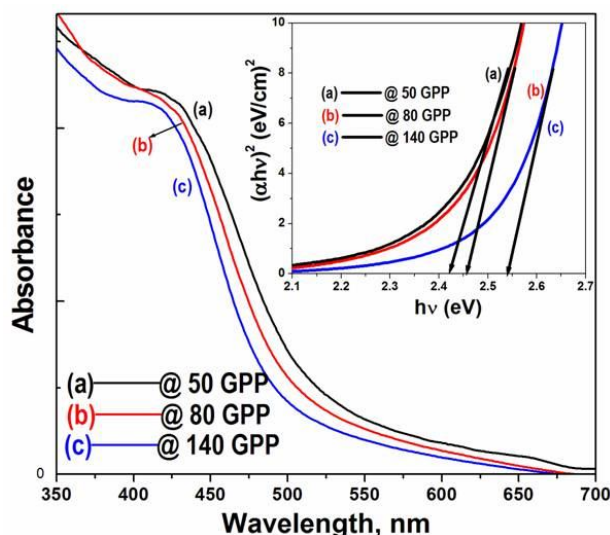


Fig.7.13. UV-Vis absorption spectra of β -CD/CdSe QDs with molar ratio (β -CD: QD, 2:1) at various dose rates (GPP); 50 (a), 80 (b), 140 (c). Absorbed dose = 25 kGy. Inset: Tauc plot of $(\alpha h\nu)^2$ vs. $h\nu$ for the determination of band gap values (E_g).

The excitonic absorption peak underwent red shift with the decrease in the dose rate. It signifies that the size of as grown nanoparticles increased with the decrease in the dose rate. Furthermore, the excitonic peak appeared to be well defined and sharp or in other way, the difference between the onset and the shoulder peak positions decreases at higher dose rates. This reflects the narrow size distribution of the nanoparticles with increase in the dose rates. Similar observations have been reported by Remita *et al.*³⁸⁵ and other

Chapter 7

researchers,^{166, 385-387} wherein the particles were found to become smaller and less dispersed in size as the dose rate was increased. The reason behind this trend lies in the fact that electron beam dumps large amount of energy in a very small time leading to the creation of large number of nucleation centers at the same instant, followed by the growth process. The band gap (E_g) values and the nanoparticle sizes at different dose rates were determined and have been provided in Table 7.1.

Fig.7.14 shows the trends in the intensities of BGE ($\lambda_{em} = 525$ nm) and TSE ($\lambda_{em} = 600$ nm) displayed by β -CD/CdSe QDs at various dose rates i.e. 50, 80 and 140 GPP. The as observed PL measurements were conducted at a fixed molar ratio (β -CD: QD) of 2:1, while the absorbed dose was also kept constant during the experiment. For instance, the QDs were synthesized with aforementioned dose rates by regulating the irradiation time and the dose per pulse, while keeping the total absorbed dose constant, as shown in Fig.7.14A (dose fixed at 15 kGy) and Fig.7.14B (dose fixed at 25 kGy). The ratio of the intensities of BGE and TSE at various dose rates has been shown in the inset of Fig.7.14A & 14B. It could be clearly seen from these trends that the BGE is favored at low dose rates, while there is substantial increase in the intensity of TSE at higher dose rates as well as at higher absorbed dose. However, at 80 GPP the intensities of both the BGE and TSE reach at an equivalence point for both the absorbed doses (15 kGy and 25 kGy). At higher dose rates (140 GPP) and high dose (25 kGy), the PL spectra becomes very broad covering the region from 450-700 nm which is predominantly due to the polydispersity in the density and nature of the surface states.

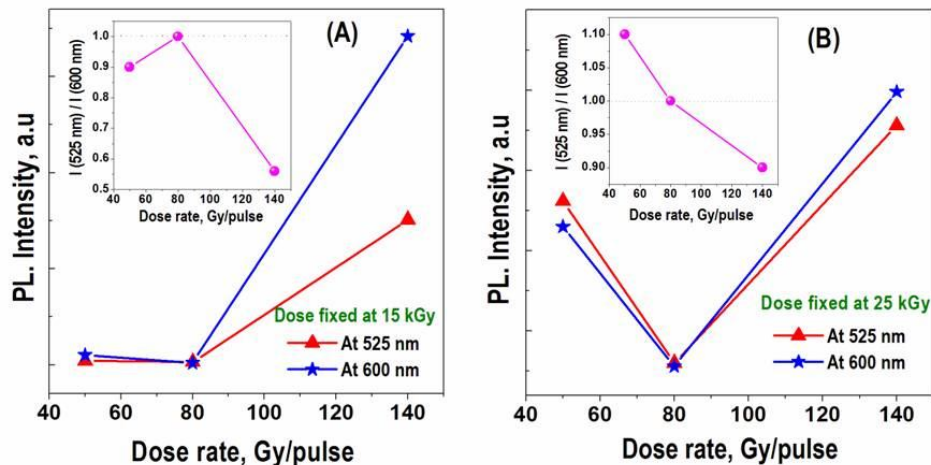


Fig.7.14. Trends showing variations in the intensities of BGE ($\lambda_{em} = 525 \text{ nm}$) and TSE ($\lambda_{em} = 600 \text{ nm}$) displayed by β -CD/CdSe QDs at various dose rates i.e. 50 GPP, 80 GPP and 140 GPP, keeping absorbed dose fixed as 15 kGy (A) and 25 kGy (B). Molar ratio (β -CD: QD) = 2:1. Inset shows the ratio of the intensities of BGE and TSE.

Nevertheless, it can be envisaged from these observations that the PL properties of as grown β -CD/CdSe QDs could be tuned in terms of the intensities of BGE and TSE. Moreover, the position of the PL peaks can also be controlled by controlling experimental parameters. Fig.7.15 shows the room temperature PL spectrum of as grown QDs with the molar ratio (β -CD: QD) of 2:1 at an absorbed dose of 1 kGy @ 10 GPP. The excitonic peak appears at $\sim 520 \text{ nm}$, while PL peak position can be noticed at $\sim 550 \text{ nm}$. Due to the close proximity of the emission and the excitonic peak position, the observed PL can be ascribed to the intrinsic recombination (BGE) of charge carriers. However, the TSE, which in this case generally appears at $\lambda \geq 600 \text{ nm}$, is very less. Conversely, a convolution of BGE and TSE was observed in case of QDs synthesized with an absorbed dose of 25 kGy @ 140 GPP, with the dominant contribution from the later one (Fig.7.11).

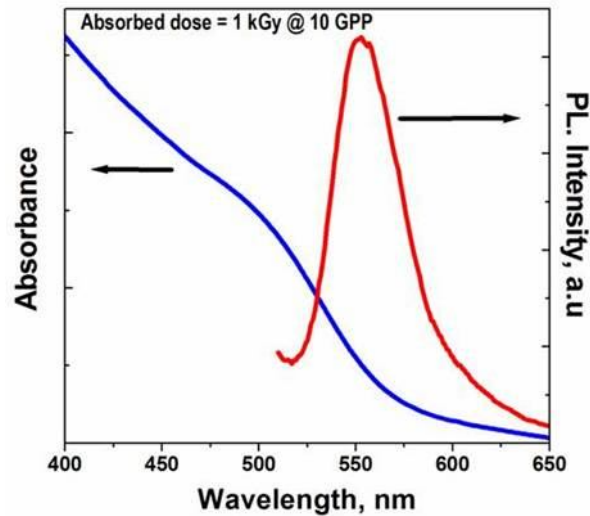


Fig.7.15. Room temperature PL spectra ($\lambda_{ex} = 480 \text{ nm}$) of $\beta\text{-CD/CdSe}$ nanoparticles with molar ratio ($\beta\text{-CD: QD}$) of 2:1 at an absorbed dose of 1 kGy @ 10 GPP.

Finally, the tunability in the optical properties of these QDs could be visualized from the different CIE chromaticity x , y co-ordinates displayed by these particles at various experimental parameters, listed in Table 7.3.

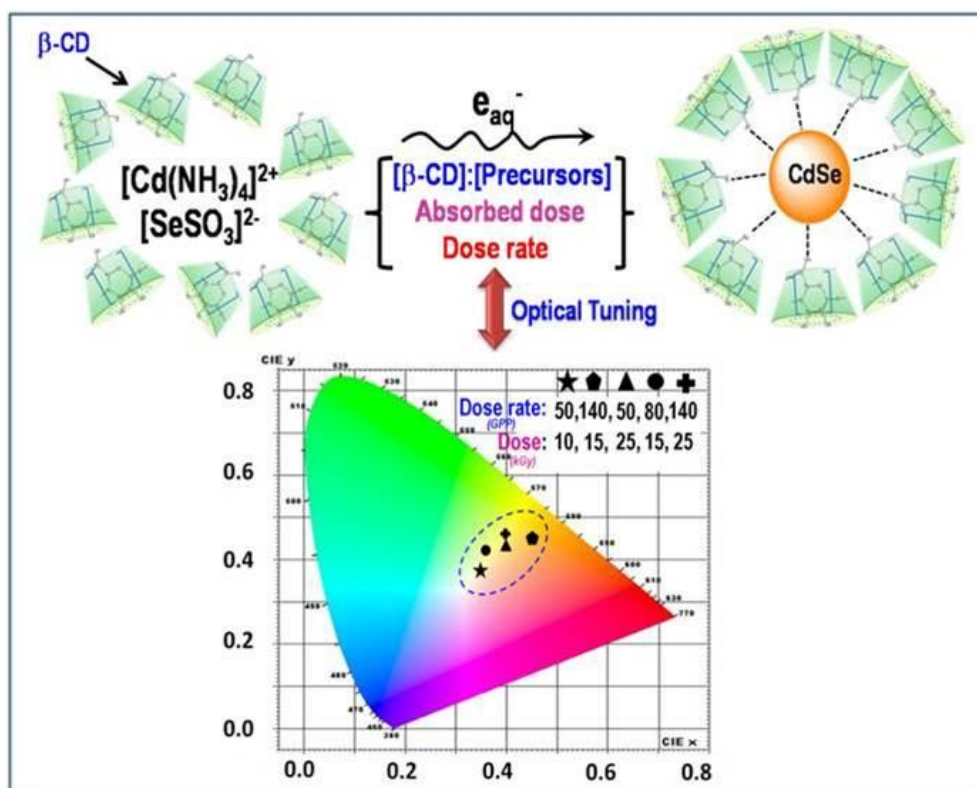
Table 7.3: CIE Chromaticity x , y co-ordinates of as grown $\beta\text{-CD/CdSe}$ QDs with molar ratio ($\beta\text{-CD: QD}$) of 2:1 at various experimental conditions.

Dose	Dose rate	CIE x , y co-ordinates	Remarks
10 kGy	50 GPP	0.36, 0.37	White light
10 kGy	80 GPP	0.45, 0.42	Orange light
15 kGy	50 GPP	0.39, 0.40	Yellowish orange light
15 kGy	80 GPP	0.38, 0.40	Yellowish orange light
15 kGy	140 GPP	0.47, 0.41	Orange light
25 kGy	50 GPP	0.40, 0.42	Yellowish orange light
25 kGy	80 GPP	0.39, 0.42	Yellow light
25 kGy	140 GPP	0.40, 0.44	Yellow light

Chapter 7

Interestingly, the QDs synthesized by employing the experimental conditions as: Molar ratio of 2:1, dose = 10 kGy @ 50 GPP were found to exhibit CIE x, y co-ordinates (0.36, 0.37), which are quite close to those exhibited by white light emitting sources.^{253b} It indicates towards the potential application of these QDs in white light emitting devices.

The electron beam mediated synthesis of β -CD functionalized CdSe QDs has been represented in Scheme 7.1 along with the chromaticity diagram illustrating the optical tunability achieved by varying the different experimental parameters.



Scheme 7.1 Electron beam mediated synthesis and the optical tunability (shown in the chromaticity diagram) displayed by β -CD/CdSe nanoparticles at various experimental conditions.

Chapter 7

7.3.3. Pulse radiolysis study

Pulse radiolysis is one of the most important techniques which have been employed to carry out the mechanistic studies regarding the formation of nanoparticles^{178, 388} and nanoclusters.^{389, 390} Our group has earlier reported the dynamics of the radiation induced synthesis of CdSe nanoparticles in aqueous solutions by electron pulse radiolysis.¹⁷⁸ In that study, the transient intermediate species formed during the radiolytic processes were investigated under various experimental conditions, for getting a clear understanding of the reaction mechanism and the formation of these nanoparticles. In the present work, the pulse radiolysis studies were carried out with the aqueous solutions containing equimolar (1 mM) concentration of both the precursors along with 2 mM β -CD and 1 M *tert*-butanol in order to investigate the dynamics of formation of the CdSe nanoparticles. The solutions were de-aerated by purging with N₂, just prior to experiments. It is expected that under these experimental conditions, the precursors will react with the hydrated electrons, e_{aq}⁻ as *tert*-butanol will scavenge H[•] and [•]OH radicals, which are produced upon the radiolysis of water. The transient absorption spectra recorded at different time scales is shown in Fig.7.16. The transient intermediate species formed upon the reaction of the e_{aq}⁻ with the precursors were found to exhibit two distinct absorption peaks at ~ 380 and ~ 510 nm, which were assigned as Band-I and Band-II, respectively. The intensity of the Band-II is higher as compared to that of the Band-I. These observations matches well with the previous report on the dynamics of radiolytic formation of CdSe nanoparticles in pure aqueous solution.¹⁷⁸

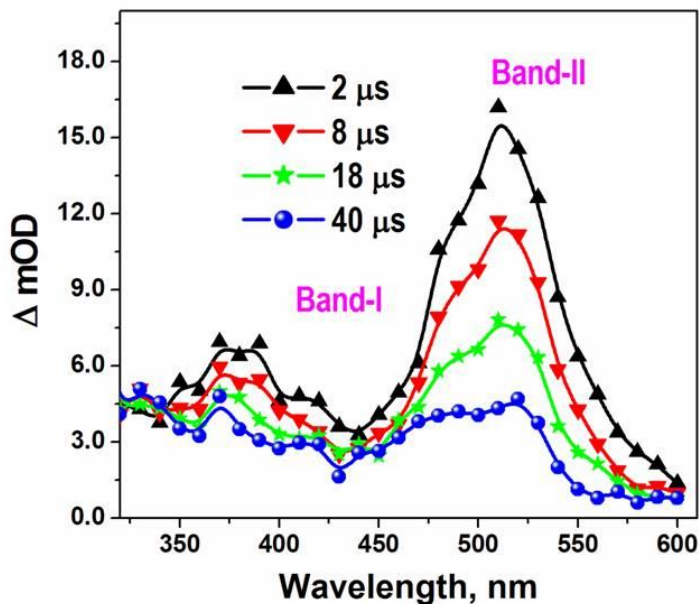
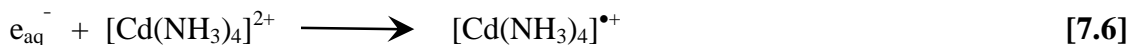


Fig.7.16. Transient absorption spectra obtained from the pulse radiolysis studies of the aqueous solutions containing Cd and Se precursors along with β -CD at following experimental conditions: $[Precursor] = 1 \text{ mM}$; $[\beta\text{-CD}] = 2\text{mM}$; Pulse duration = 100 ns; Dose = 21 Gy.

Based on the results of previous studies and the present experimental observations, the probable reactions leading to the formation of CdSe nanoparticles in aqueous solutions upon electron beam irradiation are summarized as:



The transient species generated during the formation of these nanoparticles are actually very complex and may be attributed to the formation of following intermediates i.e. $[\text{Cd}(\text{NH}_3)_4]^{\bullet+}:\text{[SeSO}_3]^{2-}$, $[\text{Cd}(\text{NH}_3)_4]^{2+}:\text{Se}\cdot^-$ and $[\text{Cd}(\text{NH}_3)_4]^{\bullet+}:\text{Se}\cdot^-$, similar to those

Chapter 7

reported in our previous study.¹⁷⁸ It appears that β -CD molecules do not play any role in the formation of these nanoparticles; however they provide stability by adsorbing on the surface of these particles during their growth processes.

7.3.4. Cytotoxicity study

It has been reported that cadmium-based QDs are toxic to cells due to the release of Cd^{2+} ions and generation of reactive oxygen species (ROS).^{391, 392} Due to this, the utilization of CdSe QDs has been limited in spite of their tremendous potential applications in bio-labeling. However, the cytotoxicity of QDs is greatly dependent on their surface molecules/ligands.³⁹³ Therefore, an attempt was made to investigate the effectiveness of capping ability of β -CD *vis-à-vis* its potential in decreasing the cytotoxicity of the CdSe QDs. As it has been mentioned in the experimental section that microscopic examination of the morphology of INT 407 cells exposed to β -CD, bare CdSe QDs and β -CD/CdSe QDs was performed 24 hour post treatment. The normal morphology of INT 407 cells was adherent while toxicity causes significant changes in its morphology leading to cell-shrinkage, non-adherence and round shape transformation. It is clearly evident from Fig.7.17 that the treatment of cells with β -CD alone did not exhibit any cytotoxicity up to a concentration of 200 μM whereas it showed slight toxicity at 400 μM . Further, exposure of cells to bare CdSe QDs had toxic effect at all the tested concentrations i.e. 25, 50 and 100 μM . The cells treated with β -CD/CdSe QDs have better cell morphology compared to bare CdSe QDs at all the concentrations. This finding shows that the cytotoxicity of the CdSe QDs significantly reduces on capping with β -CD.

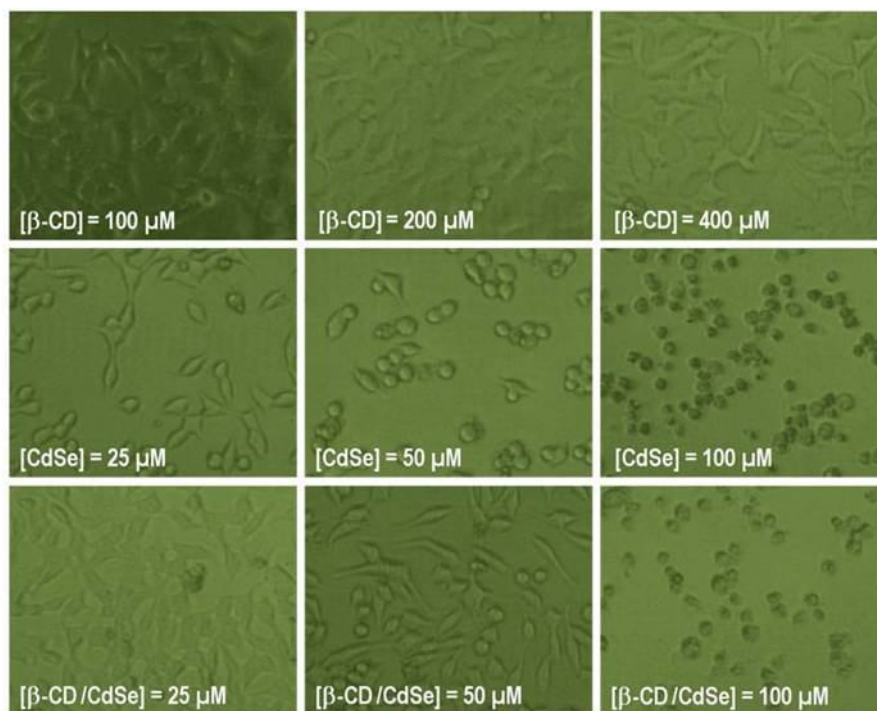


Fig.7.17. Representative Images showing the changes in the morphology of INT 407 cells exposed to β -CD, bare CdSe QDs and β -CD/CdSe QDs, respectively. The cells were incubated and monitored 24 hour post treatment using an inverted microscope.

Lastly, it is worthwhile to mention about the good correlation between the XPS and the cytotoxicity studies in the sense that the former indicated towards the bonding of the -OH groups (of β -CD) predominantly with Cd, thereby hindering the release of Cd^{2+} ions and hence resulted in reduced cytotoxicity of CdSe QDs.

7.4. Conclusions

A simple, rapid and one step method assisted by electron beam irradiation technique has been demonstrated for the synthesis as well as *in situ* functionalization of CdSe QDs with β -CD in aqueous solution. It was observed that the β -CD molecules cap the as grown CdSe nanoparticles by forming a non-inclusion complex. This complex formation was

Chapter 7

plausibly ascribed to the chemisorption of β -CD molecules on the surface of nanoparticles by their primary hydroxyl groups. Tuning of the PL properties of QDs was illustrated with respect to the intensities and the peak positions of BGE and TSE. This can also be envisaged from their CIE chromaticity x, y co-ordinates, which varied accordingly with the experimental parameters. Lifetime measurements revealed the domination of surface state originated carrier relaxation processes in the overall PL decay dynamics of as grown QDs at higher doses and dose rates. The employment of β -CD like supramolecular assemblies in the synthesis of QDs ensures their fairly good colloidal stability, water dispersibility, low cytotoxicity and most essential is the *template free self-assembling* tendency. The potential application of these β -CD/CdSe QDs in white light emitting devices has also been demonstrated.

Chapter 8

Summary and outlook

The present thesis is an attempt to carry out an exposition of the radiation and photochemical investigation of three microheterogeneous systems i.e. microemulsions, room temperature ionic liquids, and cyclodextrins, which are entirely different from each other with respect to their structure, nature of heterogeneity, composition and fluidic aspects. It is of fundamental interest as well as quite intriguing to probe the primary processes (such as electron solvation, electron transfer, free radical reactions etc.) in these media taking into account of their dissimilarities from the homogeneous systems. Subsequently, the influence of the inherent compartmentalized structural organization of these media on the morphology and the photoluminescent properties of the QDs were explored. The summary of the important findings of the work described in chapters 3, 4, 5, 6, and 7 and their outlook have been consecutively presented here.

In chapter 3, an attempt was made to comprehend the solvated electron properties in a cationic surfactant based quaternary w/o microemulsion (i.e. CTAB/H₂O/n-butanol/cyclohexane). It was observed that almost half of the dry electrons get solvated in the interface, while rest could escape the interface to be hydrated in the water core. Thus, the interface of the microemulsion actually impedes the solvation process and the signature of which is visible even up to few microseconds. The electrons are more stabilized in the interface as compared to that in the water core. The physical nature of the

Chapter 8

interface becomes comprehensible with the observation of effect of W_0 on the lifetime of the electrons solvated at the interface. At higher W_0 , solvated electrons at the interface become more mobile to interact amongst themselves and also gather higher probability to escape to water core and interact with hydrated electrons in addition to the other species if present. The presence of counter ions in microemulsions has not been seriously considered in earlier studies on radiation chemical as well as dynamical studies. The formation of counter ion radical i.e. $\text{Br}_2^{\bullet-}$ could be observed and characterized. Consequently, a two phase reaction between inorganic radicals produced in the aqueous core and a molecule that is completely insoluble in water has also been demonstrated. The spinoff of this particular part is a significant improvement in the well established kinetic protocol for free radical scavenging and antioxidant activity assay, which can now be applicable to molecules soluble in solvents with wide polarity assortment.

In chapter 4, CTAB based w/o microemulsions were employed as a template for the synthesis of CdSe QDs by normal chemical and radiation chemical route. It was observed that the dimensions of water pool in CTAB microemulsions have poor correlation with the size of the QDs. However, photoluminescent properties of the nanoparticles were found to vary with the W_0 values of the CTAB microemulsions. And, it was attributed to the probable variation in the shape of the nanoparticles. The nanoparticles exhibited excitation wavelength dependent PL spectra and the ratio of BG-PL and the TS-PL could be tuned by varying the precursor concentrations and the W_0 values. On the contrary, the PL properties displayed by CdSe nanoparticles synthesized in CTAB based microemulsions *via* electron beam irradiation technique were predominantly originated

Chapter 8

from the trap states. A comparative study was conducted to investigate the fundamental role of the structural dynamics, interfacial fluidities and the chemical nature of the water pool of cationic (CTAB) and the anionic (AOT) surfactant based microemulsions in governing the morphology and various photophysical properties of QDs. Interestingly, profound and contrasting results were observed, for example, the average PL lifetime values and the quantum yields of the QDs grown in case of CTAB microemulsions were found to be at least 3 times lower as compared to that in AOT microemulsions. These results emphasize the necessity of judicial selection of the host matrix (or the template) in the synthesis of QDs. Furthermore, the inherent property of electron beam to dump large amount of energy in a small time scale leads to the formation of unsatisfied vacancies on the surface of the QDs. However, an attempt has been made to tap this feature in conjunction with the controlled induction of the surface/trap states to manipulate the band gap and the surface composition of the QDs. Evidently, the PL lifetime values could be increased from ~18 ns to as high as ~74 ns (in case of AOT microemulsions). This interesting aspect can contribute to the better understanding of the role of trapping sites on the dynamics of charge recombination processes, which eventually governs the efficiency of solar cell devices. By optimizing various experimental parameters, stable bluish-white light emitting ultrasmall CdSe QDs were obtained and the band gap of the QDs was engineered to achieve tunable broadband light emission extending from 450 to 750 nm. Such characteristics are essentially desirable for WLED applications. The methodology of combining the advantageous properties of electron beam irradiation technique with the templated synthesis of microemulsion method is relatively new for

Chapter 8

semiconductor nanomaterial synthesis and renders unique conditions to achieve a much finer control over the composition, morphology and size of the QDs.

Owing to the high hydrolytic stability of FAP based imidazolium ILs, an assortment of characterization and qualitative studies were performed to explore their radiation stabilities and the same has been presented in chapter 5. The insignificant variations in the physicochemical properties even at high radiation doses clearly indicated the hidden potential of FAP based imidazolium ILs to be a good solvent for various applications involving high radiation fields. The color evolution in the post-irradiated ILs attributed due to the formation of oligomeric and multiple bond order group containing radiolytic products as indicated from the mass and vibrational studies, respectively. Besides, the hydrogen gas yields of FAP ILs were found to be comparable to that of a radiolytically stable aromatic compound, benzene. The significant radiation resistance put forth by FAP ILs has been correlated well with the fractional stopping power of the FAP anion, which clearly implicates it as an effective protector/shield (among various other fluoroanion based ILs) to the cation. However, the influence of the introduction of a hydroxyl group (in the alkyl side chain of the imidazolium moiety) on the radiation resistance of the IL was found to be detrimental, as it resulted into significant changes in the properties (of the IL) such as thermal stability, conductivity and electrochemical window. The transient spectroscopic studies carried out to delineate the radiolytic sensitization effects of the hydroxyl group on the reaction mechanistic pathways clearly showed a marked difference (from the non-hydroxyl IL) in the reactivity, reaction center and the nature of the radiolytic products. Furthermore, photophysical investigations of post-irradiated FAP ILs

Chapter 8

showed considerable changes in the orientations and the molecular rearrangements of the ionic moieties. Moreover, such studies would be helpful in gaining the microscopic insight of the radiation induced mutations in the structure-property relationships and the nature of various interactions existing in ILs. However, for the practical applications of ILs in industrial and other areas involving high radiation fields, a lot of important aspects need to be probed. These are electron solvation and scavenging mechanisms in conjunction with various relaxation processes such as radiative, non-radiative and dissociative pathways of energy dissipation.

Chapter 6 demonstrates the application of RTILs as a novel media for the synthesis of self-assembled superstructures of nanomaterials. CdSe nanoparticles were grown in *neat* imidazolium based IL *via* radiation as well as normal chemical route. In either of the synthetic methodologies, it was observed that IL played multiple roles, i.e. a solvent, stabilizing agent and a shape directing template. In case of radiation chemical synthesis, the electron beam induced nucleation and the subsequent growth process directed by the matrix of IL leads to a unique nanomorphology, i.e. islands of CdSe within the Se nanofibers. The applications of such morphology can be envisaged from its 3-D highly porous networking structure, as the nanostructures with high surface area and porosity exhibits tremendous potential in sensing and catalysis. Furthermore, the dose rate was found to influence the growth mechanism, i.e. 3-D structure was obtained in the electron beam induced case, while 1-D structures were observed in γ -ray assisted synthesis. The mechanism proposed for the obtained nanostructures may provide an intuitive protocol for the development of such complicated nanomorphologies by employing ILs as

Chapter 8

templates. In the normal chemical synthetic route, co-existence of anisotropic 2D sheet and flower-like 3D nanostructures was evident. The fluidic aspects of the IL in conjunction with its *hydrogen bond-co- π - π stacking* mechanism enabled it to perform a function of a diffusion controller and an anisotropic growth director, respectively. Accordingly, a possible mechanism for the formation of self-assembled anisotropic nanostructures has been provided. The fundamental role of water in creating a perturbation/distortion in the networking structure of the IL has been demonstrated. These results reflect the potential to maneuver the morphologies of the nanomaterials by precisely controlling the presence of water in the host matrix of the IL. However, further investigations are necessary for the better understanding of the role of intrinsic microheterogeneity prevailing in the RTILs, so that these media could be used in fine tuning the morphology of the nanoparticles *vis-à-vis* their properties and applications.

In chapter 7, a simple, rapid and one step method assisted by electron beam irradiation technique has been demonstrated for the synthesis as well as *in situ* functionalization of CdSe QDs with β -CD in aqueous solution. Through transient absorption studies, the possible mechanism for the formation of β -CD/CdSe nanoparticles was elucidated and it was inferred that β -CD do not interfere in the dynamics of radiolytic formation of CdSe nanoparticles, rather it acts as a capping or stabilizing agent. Some interesting orientation patterns of the QDs (i.e. pearl necklace shaped) were observed and attributed to the directional nature of forces of interaction between the β -CD molecules coating the QDs surface. Another important physical aspect of the present work is the tuning of optical properties of the QDs, which could be achieved by optimizing various experimental

Chapter 8

parameters. Since, electron beam irradiation of the solutions could be carried out in the common industrial accelerator plants (generally used for sterilizing medical kits and other items); therefore this methodology could find promising applications in the large scale and cheaper production of QDs. In addition, this technique is attractive from the view point of clean chemistry (no external reducing agent is involved) and ensuring reproducibility in the synthetic protocol. The employment of supramolecular assemblies such as β -CD makes this method more advantageous, as can be realized from the following points. It was observed that the β -CD molecules cap the as grown CdSe QDs by forming a non-inclusion complex. Therefore, the individual QDs self-aligns in the form of chains through the hydrogen bonding between the -OH groups of β -CD molecules chemisorbed on their surface. Apparently, it could be anticipated that the interactions between the individual nanospheres would be significantly enhanced. And, this could have considerable impact on the optoelectronic properties of such QDs, as the self-alignment can eventually boost the charge transport carrier efficiencies. Nevertheless, this could be a topic of further investigation. Furthermore, the bio-compatibility of β -CD is well proven and holds the potential in decreasing the toxicity of CdSe QDs, as has been observed from the cytotoxicity studies. Hence, the present methodology not only provide a rapid and one step approach to synthesize QDs but the employment of β -CD like supramolecular assemblies ensures fairly good colloidal stability, water dispersible, low cytotoxicity and most essential is the *template free self-assembling* tendency. The potential application of these β -CD/CdSe QDs in white light emitting devices has also been demonstrated.

Chapter 8

Future perspective

As discussed earlier, microheterogeneity is one of the basic and versatile features of many natural systems, and plays a vital role in directing/influencing the fundamental processes such as electron, charger transfer and other free radical reactions. An in-depth understanding of these processes is pertinent for variety of societal applications. The investigations presented in the thesis may contribute toward this endeavor. For instance, the study of two phase reactions in CTAB based w/o microemulsions may significantly improve the existing protocol for free radical scavenging and antioxidant activity assay. This method now can be applicable to molecules soluble in solvents with wide polarity assortment. In radiation chemical studies of imidazolium ionic liquids, it was clearly demonstrated that even a diminutive alteration in the molecular structure of these fluids might cause marked differences in the reactivity, reaction center and the nature of the radiolytic products, which eventually lead to the significant changes in their physicochemical properties. Such findings can be of immense importance considering the potential applications of room temperature ionic liquids in high radiation fields such as space and nuclear fuel cycle.

The influence of the structure, dynamics and fluidic aspects of the microheterogeneous systems in conjunction with the inherent features of the radiation techniques was explored in directing the morphology and the photophysical properties of the CdSe nanoparticles. The mechanism behind the formation of self-assembled nanoarchitectures has been provided. Such information can be useful in synthesizing unique superstructures of other nanomaterials as well, which are important from the

Chapter 8

fundamental point of view. Finally, the self-effacing inference here is that, attempts have been made to resolve important issues, which have been raised in the introduction of the thesis through systematic investigations. However, there is ample scope for future research in understanding the heterogeneous structural features of room temperature ionic liquids through radiation and photochemical techniques.

REFERENCES

1. (a) M. Grätzel and K. Kalyanasundaram, *Kinetics and Catalysis in Microheterogeneous Systems*, CRC Press, New York, 1991; (b) K. Kalyanasundaram, *Photochemistry in microheterogeneous systems*, Academic press Inc., London, 1987; (c) J. R. Lakowicz, *Principles of Fluorescence Spectroscopy*, Springer Science, New York, 3rd editio., 2006.
2. (a) D. M. Vriezema, M. C. Aragonès, J. A. A. W. Elemans, J. J. L. M. Cornelissen, A. E. Rowan, and R. J. M. Nolte, *Chem. Rev.*, 2005, **105**, 1445–1489; (b) M. M. Safont-Sempere, G. Fernández, and F. Würthner, *Chem. Rev.*, 2011, **111**, 5784–5814.
3. (a) D. Cahen and I. Lubomirsky, *Mater. Today*, 2008, **11**, 16–20; (b) A. Regalado, *Sci. Am.*, 2010, **303**, 86-89.
4. (a) A. V. Barzykin, K. Seki, and M. Tachiya, *Adv. Colloid Interface Sci.*, 2001, **89**, 47–140; (b) D. M. Shin, K. S. Schanze, and D. G. Whitten, *J. Am. Chem. Soc.*, 1989, **111**, 8494–8501; (c) J. H. Fendler, *J. Phys. Chem.*, 1980, **84**, 1485–1491; (d) S. P. Moulik and B. K. Paul, *Adv. Colloid Interface Sci.*, 1998, **78**, 99–195.
5. (a) S. P. Moulik and A. K. Rakshit, *Surf. Sci.*, 2006, **22**, 159–186; (b) V. T. Liveri, *Controlled Synthesis of Nanoparticles in Microheterogeneous Systems*, Springer Science, New York, 2006; (c) M. Fanun, *Microemulsions: Properties and Applications*, CRC Press (Taylor & Francis Group), 2009.
6. (a) Farhahaziz and M. A. J. Rodger, *Radiation Chemistry: Principles and Applications*, VCH, New York, 1987; (b) J. W. T. Spinks and R. J. Woods, *An Introduction to Radiation Chemistry*, John Wiley and Sons, New York, 3rd edn.,

REFERENCES

- 1990; (c) A. J. Swallow, *Radiation chemistry: An Introduction*, Prentice Hall Press, 1973.
7. (a) W. R. Leo, *Techniques for Nuclear and Particle Physics Experiments*, Springer-Verlag, Germany, 2nd rev., 1994; (b) G. F. Knoll, *Radiation Detection and Measurement*, John Wiley & Sons, USA, 4th edn., 2010.
8. (a) A. O. Allen, *The Radiation Chemistry of Water and Aqueous Solutions*, Van Nostrand, New Jersey, 1961; (b) I. G. Draganic and Z. D. Draganic, *The Radiation Chemistry of Water*, Academic Press, New York-London, 1971.
9. (a) Y. Yoshida, S. Tagawa, and Y. Tabata, *Pulse Radiolysis*, CRC Press, 1990; (b) J. H. Baxendale and F. Busi, Eds., *The Study of Fast Processes and Transient Species by Electron Pulse Radiolysis*, Springer Netherlands, Dordrecht, Holland, 1982; (c) A. Hummel, *Adv. Radiat. Chem.*, 1974, **4**, 1-102; (d) Y. Yoshida, S. Tagawa, and Y. Tabata, *Radiat. Phys. Chem.*, 1984, **23**, 279-285.
10. (a) Y. Katsumara, Y. Tabata, and S. Tagawa, *Radiat. Phys. Chem.*, 1982, **19**, 267-276; (b) L. H. Luthjens, H. D. K. Codee, H. C. D. Leng, A. Hummel, and G. Beck, *Radiat. Phys. Chem.*, 1983, **21**, 21-26.
11. N. J. Turro, *Modern Molecular Photochemistry*, Benjamin, New York, 1978.
12. (a) T. P. Hoar and J. H. Schulman, *Nature*, 1943, **152**, 102-103; (b) J. H. Schulman, W. Staerkenius, and L. M. Prince, *J. Phys. Chem.*, 1959, **63**, 1677-1680.
13. M. P. Pileni, *J. Phys. Chem.*, 1993, **97**, 6961-6973.
14. (a) M. A. López-Quintela, C. Tojo, M. C. Blanco, L. García Rio and J R. Leis, *Curr. Opin. Colloid Interface Sci.*, 2004, **9**, 264-278; (b) M. López-Quintela, M. B. J.

REFERENCES

- Rivas, and C. Tojo, in *Nanoscale Materials*, eds. L. M. Liz-Marzán and P. V. Kamat, Springer, 2003, 135–155; (c) A. K. Ganguli, A. Ganguly, and S. Vaidya, *Chem. Soc. Rev.*, 2010, **39**, 474–485.
15. V. Uskoković and M. Drogenik, *Surf. Rev. Lett.*, 2005, **12**, 239–277.
16. (a) M. Wong, M. Grätzel and J. K. Thomas, *Chem. Phys. Lett.*, 1975, **30**, 329–333; (b) J. L. Gebicki and P. Bednarek, *J. Mol. Structure*, 2000, **555**, 227–234; (c) J. L. Gebicki, L. Gebicka and J. Kroh, *J. chem. soc. Faraday Trans.*, 1994, **90**, 3411–3414; (d) M. P. Pileni, B. Hickel, C. Ferradini and J. Pucheault, *Chem. Phys. Lett.*, 1982, **92**, 308–312; (e) J. L. Gebicki and M. Maciejewska, *Radiat. Phys. Chem.*, 2003, **67**, 257–261.
17. S. M. Hubig and M. A. J. Rodgers, *J. Phys. Chem.*, 1990, **94**, 1933–1936.
18. G. Wu, Y. Katsumura, N. Chitose, and Z. Zuo, *Radiat. Phys. Chem.*, 2001, **60**, 643–650.
19. S. Adhikari, R. Joshi, and C. Gopinathan, *J. Colloid Interface Sci.*, 1997, **191**, 268–271.
20. R. Joshi and T. Mukherjee, *Radiat. Phys. Chem.*, 2003, **66**, 397–402.
21. A. Guleria, A. K. Singh, S. K. Sarkar, T. Mukherjee, and S. Adhikari, *J. Phys. Chem. B*, 2011, **115**, 10615–10621.
22. B. K. Paul and S. P. Moulik, *Curr. Sci.*, 2001, **80**, 990–1001.
23. I. Capek, *Adv. Colloid Interface Sci.*, 2004, **110**, 49–74.
24. M. Boutonnet, J. Kizling, P. Stenius, and G. Maire, *Colloids Surf.*, 1982, **5**, 209–225.
25. G. L. Li and G. H. Wang, *Nanostructured Mater.*, 1999, **11**, 663–668.

REFERENCES

26. C. Okoli, M. Sanchez-Dominguez, M. Boutonnet, S. Järås, C. Civera, C. Solans, and G. R. Kuttuva, *Langmuir*, 2012, **28**, 8479–8485.
27. D. Sarkar, S. Tikku, V. Thapar, R. S. Srinivasa, and K. C. Khilar, *Colloids Surfaces A Physicochem. Eng. Asp.*, 2011, **381**, 123–129.
28. N. Castillo, L. Díaz Barriga, R. Pérez, M. J. Martínez-Ortiz, and A. C. Gallardo, *Rev. Adv. Mater. Sci.*, 2008, **18**, 720-724.
29. D. H. Chen and C. J. Chen, *J. Mater. Chem.*, 2002, **12**, 1557–1562.
30. H. M. Chen, R. S. Liu, L. Y. Jang, J. F. Lee, and S. F. Hu, *Chem. Phys. Lett.*, 2006, **421**, 118–123.
31. N. Pinna, K. Weiss, H. Sack-Kongehl, W. Vogel, J. Urban, and M. P. Pileni, *Langmuir*, 2001, **17**, 7982–7987.
32. C. Petit, P. Lixon, and M.P. Pileni, *J. Phys. Chem.*, 1990, **94**, 1598–1603.
33. J. Eastoe and M. Warne, *Curr. Opin. Colloid. Interf. Sci.*, 1996, **1**, 800–805.
34. B. H. Robinson, T. F. Towey, S. Zourab, A. J. W. G. Visser, and A. Van Hoek, *Colloid. Surf.*, 1991, **61**, 175–188.
35. P. Kumar, V. Pillai, and D. O. Shah, *Appl. Phys. Lett.*, 1993, **62**, 765-768.
36. V. Pillai, P. Kumar, M. J. Hou, P. Ayyub, and D. O. Shah, *Adv. Colloid Interface Sci.*, 1995, **55**, 241–269.
37. E. E. Carpenter, C. J. O. Connor, and V.G. Harris, *J. Appl. Phys.*, 1999, **85**, 5175–5177.
38. F. Agnoli, W. L. Zhou, and C. J. O. Connor, *Adv. Mater.*, 2001, **13**, 1697–1699.
39. G. Guo, Y. Sun, Z. Wang, and H. Guo, *Ceram. Int.*, 2005, **31**, 869–872.

REFERENCES

40. A. Guleria, S. Singh, M. C. Rath, A. K. Singh, S. Adhikari, and S. K. Sarkar, *J. Lumin*, 2012, **132**, 652–658.
41. S. Singh, A. Guleria, M. C. Rath, A. K. Singh, S. Adhikari, and S. K. Sarkar, *Mater. Lett.*, 2011, **65**, 1815.
42. S. Singh, Apurav Guleria, M. C. Rath, A. K. Singh, S. Adhikari, and S. K. Sarkar, *Adv. Mat. Lett.*, 2013, **4**, 449-453.
43. S. Singh, Apurav Guleria, A. K. Singh, M. C. Rath, S. Adhikari, and S. K. Sarkar, *J. Colloid Interface Sci.*, 2013, **398**, 112–119.
44. (a) T. Welton, *Chem. Rev.*, 1999, **99**, 2071–2083; (b) V. I. Pârvulescu and C. Hardacre, *Chem. Rev.*, 2007, **107**, 2615–2665; (c) J. P. Hallett and T. Welton, *Chem. Rev.*, 2011, **111**, 3508–3576; (d) P. Hapiot and C. Lagros, *Chem. Rev.* 2008, **108**, 2238–2264.
45. P. Walden, *Bull. Acad. Imp. Sci. St. Petersburg*, 1914, **8**, 405-422.
46. D. F. Evans, A. Yamauchi, R. Roman, and E. Z. Casassa, *J. Colloid Interface Sci.*, 1982, **88**, 89-96.
47. (a) Z. J. Karpinski and R. A. Osteryoung, *Inorg. Chem.*, 1984, **23**, 1491-1494; (b) T. A. Zawodzinski, Jr. and R. A. Osteryoung, *Inorg. Chem.*, 1990, **29**, 2842-2847; (c) R. A. Mantz, P. C. Trulove, R. T. Carlin, and R. A. Osteryoung, *Inorg. Chem.*, 1995, **34**, 3846-3847.
48. J. S. Wilkes, J. A. Levisky, R. A. Wilson, and C. L. Hussey, *Inorg. Chem.*, 1982, **21**, 1263-1264.

REFERENCES

49. (a) J. S. Wilkes and M. J. Zaworotko, *J. Chem. Soc., Chem Commun.*, 1992, 965-967;
(b) J. Fuller, R. T. Carlin, H. C. De Long, and D. Haworth, *J. Chem. Soc., Chem Commun.*, 1994, 299-300.
50. N.V. Plechkova and K.R. Seddon, *Chem. Soc. Rev.*, 2008, **37**, 123-150.
51. P. M. Dean, J. M. Pringle, and D. R. MacFarlane, *Phys. Chem. Chem. Phys.*, 2010, **12**, 9144-9153.
52. T. L. Greaves and C. J. Drummond, *Chem. Soc. Rev.*, 2013, **42**, 1096-1120.
53. J. N. C. Lopes, K. Shimizu, A. A. H. Pádua, Y. Umebayashi, S. Fukuda, K. Fujii, and S. Ishiguro, *J. Phys. Chem. B*, 2008, **112**, 1465–1472.
54. C. Hardacre, J. D. Holbrey, C. L. Mullan, M. Nieuwenhuyzen, T. G. A. Youngs, and D. T. Bowron, *J. Phys. Chem. B*, 2008, **112**, 8049–8056.
55. E. W. Castner Jr., C. J. Margulis, M. Maroncelli, and J. F. Wishart, *Annu. Rev. Phys. Chem.*, 2011, **62**, 85-105.
56. F. Castiglione, M. Moreno, G. Raos, A. Famulari, A. Mele, G. B. Appetecchi, and S. Passerini, *J. Phys. Chem. B*, 2009, **113**, 10750–10759.
57. M. L. P. Le, F. Alloin, P. Strobel, J. C. Leprêtre, C. P. del Valle, and P. Judeinstein, *J. Phys. Chem. B*, 2010, **114**, 894–903.
58. K. Iwata, H. Okajima, S. Saha, and H. Hamaguchi, *Acc. Chem. Res.*, 2007, **40**, 1174–1181.
59. G. L. Burrell, I. M. Burgar, F. Separovic, and Noel F. Dunlop, *Phys. Chem. Chem. Phys.*, 2010, **12**, 1571–1577.
60. D. F. Kennedy and C. J. Drummond, *J. Phys. Chem. B*, 2009, **113**, 5690–5693.

REFERENCES

61. Y. Wang, W. Jiang, T. Yan, and G. A. Voth, *Acc. Chem. Res.*, 2007, **40**, 1193–1199.
62. E. J. Maginn, *Acc. Chem. Res.*, 2007, **40**, 1200–1207.
63. L. J. A. Siqueira and M. C. C. Ribeiro, *J. Phys. Chem. B*, 2009, **113**, 1074–1079.
64. S. G. Rajua and S. Balasubramanian, *J. Mater. Chem.*, 2009, **19**, 4343–4347.
65. J. Habasaki and K. L. Ngai, *J. Chem. Phys.*, 2008, **129**, 194501-15.
66. Z. Hu and C. J. Margulis, *Proc. Natl Acad. Sci.*, 2006, **103**, 831-836.
67. P. G. Debenedetti and F. H. Stillinger, *Nature*, 2001, **410**, 259-267.
68. Z. Hu and C. J. Margulis, *Acc. Chem. Res.*, 2007, **40**, 1097–1105.
69. A. Samanta, *J. Phys. Chem. B*, 2006, **110**, 13704–13716.
70. P. Wasserscheid and W. Keim, *Angew. Chem. Int. Ed.*, 2000, **39**, 3772–3789.
71. R. Sheldon, *Chem. Commun.*, 2001, 2399–2407.
72. X. Sun, H. Luo, and S. Dai, *Chem. Rev.*, 2012, **112**, 2100–2128.
73. S. H. Ha, R. N. Menchavez, and Y. M. Koo, *Korean J. Chem. Eng.*, 2010, **27**, 1360-1365.
74. I. A. Shkrob, S. D. Chemerisov, and J. F. Wishart, *J. Phys. Chem. B*, 2007, **111**, 6878–6886.
75. D. Allen, G. Baston, A. E. Bradley, T. Gorman, A. Haile, I. Hamblett, J. E. Hatter, M. J. F. Healey, B. Hodgson, R. Lewin, K. V. Lovell, B. Newton, W. R. Pitner, D. W. Rooney, D. Sanders, K. R. Seddon, H. E. Sims, and R. C. Thied, *Green Chem.*, 2002, **4**, 152–158.
76. L. Berthon, S. I. Nikitenko, I. Bisel, C. Berthon, M. Faucon, B. Saucerotte, N. Zorz, and P. Moisy, *Dalton Trans.*, 2006, 2526–2534.

REFERENCES

77. E. Bossé , L. Berthon , N. Zorz , J. Monget , C. Berthon , I. Bisel , S. Legand, and P. Moisy, *Dalton Trans.*, 2008, 924–931.
78. M. Y. Qi, G. Z. Wu, S. M. Chen, and Y. D. Liu, *Radiat. Res.*, 2007, **167**, 508–514.
79. L. Yuan, J. Peng, M. Zhai, J. Li, and G. Wei, *Radiat. Phys. Chem.*, 2009, **78**, 737–739.
80. M. Y. Qi, G. Z. Wu, Q.M. Li, and Y. S. Luo, *Radiat. Phys. Chem.*, 2008, **77**, 877–883.
81. G. Le Rouzo, C. Lamouroux, V. Dauvois, A. Dannoux, S. Legand, D. Durand, P. Moisy, and G. Moutiersc, *Dalton Trans.*, 2009, 6175–6184.
82. Ch. Jagadeeswara Rao, K. A. Venkatesan, B. V. R. Tata, K. Nagarajan, T. G. Srinivasan, and P. R. Vasudeva Rao, *Radiat. Phys. Chem.*, 2011, **80**, 643–649.
83. L. Yuan, J. Peng, L. Xu, M. Zhai, J. Li , and G. Wei, *Radiat. Phys. Chem.*, 2009, **78**, 1133–1136.
84. A. Guleria, A. K. Singh, S. Adhikari, and S. K. Sarkar, *Dalton Trans.*, 2014, **43**, 609–625.
85. (a) N.V. Ignatev, U. Welz-Biermann, A. Kucheryna, G. Bissky, and H. Willner, *J. Fluorine Chem.*, 2005, **126**, 1150–1159; (b) S. Sowmiah, V. Srinivasadesikan, M. C. Tseng, and Yen-Ho Chu, *Molecules*, 2009, **14**, 3780-3813; (c) A. V. Plakhotnyka, L. Ernst, and R. Schmutzler, *J. Fluorine Chem.*, 2005, **126**, 27–31.
86. L. Wu, J. Lian, G. Sun, X. Kong, and W. Zheng, *Eur. J. Inorg. Chem.*, 2009, 2897–2900
87. Z. Ma, J. Yu, and S. Dai, *Adv. Mater.*, 2010, **22**, 261–285.

REFERENCES

88. Z. Li, Z. Jia, Y. Luan, and T. Mu, *Curr. Opin. Solid State Mater. Sci.*, 2008, **12**, 1–8.
89. Y. Zhou, J. H. Schattka, and M. Antonietti, *Nano Lett.*, 2004, **4**, 477–481.
90. Y. J. Zhu, W. W. Wang, R. J. Qi, and X. L. Hu, *Angew. Chem. Int. Ed.*, 2004, **43**, 1410–1414.
91. Y. Wang and Hong Yang, *J. Am. Chem. Soc.*, 2005, **127**, 5316–5317.
92. K. Biswas and C. N. R. Rao, *Chem. Eur. J.*, 2007, **13**, 6123–6129.
93. Y. Jiang, Y. J. Zhu, and G. F. Cheng, *Cryst. Growth Des.*, 2006, **6**, 2174–2176.
94. Y. Sun and W. Zheng, *Dalton Trans.*, 2010, **39**, 7098–7103.
95. L. Wang, L. X. Chang, B. Zhao, Z. Y. Yuan, G. S. Shao, and W. J. Zheng, *Inorg. Chem.*, 2008, **47**, 1443–1452.
96. A. Guleria, A. K. Singh, M. C. Rath, S. Adhikari, and S. K. Sarkar, *Dalton Trans.*, 2013, **42**, 15159–15168.
97. A. Guleria, A. K. Singh, M. C. Rath, S. K. Sarkar, and S. Adhikari, *Dalton Trans.*, 2014, **43**, 11843–11854.
98. M. Antonietti, D. Kuang, B. Smarsly, and Y. Zhou, *Angew. Chem. Int. Ed.*, 2004, **43**, 4988–4992.
99. (a) Jozsef Szejtli, *Chem. Rev.*, 1998, **98**, 1743–1753; (b) E.M. Martin Del Valle, *Process Biochem.*, 2004, **39**, 1033–1046.
100. A. R. Hedges, *Chem. Rev.*, 1998, **98**, 2035–2044.
101. C. Baudin, C. Pean, B. Perly, and P. Gosselin, *Int. J. Environ. Anal. Chem.*, 2000, **77**, 233–242.

REFERENCES

102. R. Koukiekolo, V. Desseaux, Y. Moreau, G. M. Mouren, and M. Santimone, *Eur. J. Biochem.*, 2001, **268**, 841-848.
103. T. Loftsson and M. E. Brewster, *J. Pharm. Sci.* 1996, **85**, 1017-10125.
104. J. W. Steed and J. L. Atwood, *Supramolecular Chemistry*, John Wiley & Sons, UK, 2 nd., 2009.
105. Y. He, P. Fu, X. Shen, and H. Gao, *Micron*, 2008, **39**, 495–516.
106. M. Bonini, S. Rossi, G. Karlsson, M. Almgren, P. L. Nostro, and P. Baglioni, *Langmuir*, 2006, **14**, 1478-84.
107. A. W. Coleman, I. Nicolis, N. Keller, and J. P. Dalbiez, *J. Incl. Phen. Mol. Recogn.*, 1992, **13**, 139-143.
108. G. G. Gaitano and Wyn Brown, *J. Phys. Chem. B*, 1997, **101**, 710–719.
109. G. G. Gaitano, P. Rodríguez, J. R. Isasi, M. Fuentes, G. Tardajos, and M. Sánchez, *J. Inclusion Phenom. Mol. Recognit. Chem.*, 2002, **44**, 101–105.
110. T. Ogoshi and A. Harada, *Sensors*, 2008, **8**, 4961-4982.
111. Y. L. Liu, K. B. Male, P. Bouvrette, and J. H. T. Luong, *Chem. Mater.*, 2003, **15**, 4172-4180.
112. T. Huang, F. Meng, and L. M. Qi, *J. Phys. Chem. C*, 2009, **113**, 13636-13642.
113. J. Liu, S. Mendoza, E. Roman, M. J. Lynn, R. L. Xu, and A. E. Kaifer, *J. Am. Chem. Soc.*, 1999, **121**, 4304-4305.
114. J. Liu, W. Ong, E. Roman, M. J. Lynn, and A. E. Kaifer, *Langmuir*, 2000, **16**, 3000-3002.
115. C. H. B. Ng, J. X. Yang, and W. Y. Fan, *J. Phys. Chem. C*, 2008, **112**, 4141-4145.

REFERENCES

116. I. Willner and D. Mandler, *J. Am. Chem. Soc.*, 1989, **111**, 1330-1336.
117. J. Z. Xu, S. Xu, J. Geng, G. X. Li, and J. J. Zhu, *Ultrason. Sonochem.*, 2006, **13**, 451-454.
118. L. Li, X. Sun, Y. Yang, N. Guan, and F. Zhang, *Chem. Asian J.*, 2006, **1**, 664-668.
119. G. O. Phillips and M. Young, *J. Chem. Soc.*, 1966, 383-387.
120. G. O. Phillips and M. Young, *J. Chem. Soc. (A)*, 1966, 393-400.
121. U. K. Misra, J. C. Picken, and D. French, *Radiat. Res.*, 1961, **14**, 775-778.
122. E. M. Bilensoy and A. A. Hincal, *Int. J. Pharm.*, 2006, **311**, 203-208.
123. Q. Chen, X. Shen, and Hongcheng Gao, *Adv. Colloid Interface Sci.* 2010, **159**, 32-44.
124. A. I. Ekimov and A. A. Onushchenko, *Sov. Phys. Semicond.*, 1982, **16**, 775-778.
125. A. I. Ekimov, Al. L. Efros, and A. A. Onushchenko, *Solid State Commun.*, 1985, **56**, 921-924.
126. *Nanotechnology Timeline* by National Nanotechnology Initiative, Web: www.nano.gov
127. M. A. Reed, J. N. Randall, R. J. Aggarwal, R. J. Matyi, T. M. Moore, and A. E. Wetsel, *Phys. Rev. Lett.* 1988, **60**, 535-537.
128. (a) A. P. Alivisatos, *Science*, 1996, 933-937; (b) A. Andreev, Ed., *Theory of Semiconductor Quantum Dots: Band Structure, Optical Properties and Applications*, World Scientific Publishing Co Pte Ltd, 2006; (c) A. Tartakovskii, Ed., *Quantum Dots: Optics, Electron Transport and Future Applications*, Cambridge University Press, 2012; (d) V. I. Klimov, Ed., *Nanocrystal Quantum Dots*, CRC Press, Taylor and Francis Group, LLC., 2nd., 2010.

REFERENCES

129. R. W. Meulenberg, J. R. I. Lee, A. Wolcott, J. Z. Zhang, L. J. Terminello, and T. Van Buuren, *ACS Nano*, 2009, **3**, 325–330.
130. L. E. Brus, *J. Chem. Phys.* 1984, **80**, 4403–4409.
131. G. Schmid, M. Bäuml, M. Geckens, I. Heim, C. Osemann, and T. Sawitowski, *Chem. Soc. Rev.*, 1999, **28**, 179-185.
132. V. I. Klimov, A. A. Mikhailovsky, S. Xu, A. Malko, J. A. Hollingsworth, C. A. Leatherdale, H. J. Eisler, and M. G. Bawendi, *Science*, 2000, **290**, 314-317.
133. M. Kazes, D. Y. Lewis, Y. Ebenstein, T. Mokari, and U. Banin, *Adv. Mater.*, 2002, **14**, 317-321.
134. H. J. Eisler, V. C. Sunder, M. G. Bawendi, M. Walsh, H. I. Smith, and V. I. Klimov, *Appl. Phys. Lett.*, 2002, **80**, 4614-4617.
135. (a) W. U. Huynh, J. J. Dittmer, and A. P. Alivisatos, *Science*, 2002, **295**, 2425-2427;
(b) P. V. Kamat, *J. Phys. Chem. C*, 2008, **112**, 18737–18753.
136. N. Ganesh, W. Zhang, P. C. Mathias, E. Chow, J. A. N. T. Soares, V. Malyarchuk, A. D. Smith, and B. T. Cunningham, *Nat. Nanotechnol.* 2007, **2**, 515-520.
137. S. Coe, W. K. Woo, M. G. Bawendi, and V. Bulovic, *Nature*, 2002, **420**, 800-803.
138. V. L. Colvin, M. C. Schlamp, and A. P. Alivisatos, *Nature*, 1994, **370**, 354-357.
139. K. E. Sapsford, T. Pons, Igor. L. Medintz, and H. Mattoussi, *Sensors*, 2006, **6**, 925-953.
140. P. C. Ray, *Chem. Rev.* 2010, **110**, 5332–5365.
141. R. Freeman and I. Willner, *Chem. Soc. Rev.* 2012, **41**, 4067-4085.

REFERENCES

142. M. Bruchez Jr., M. Moronne, P. Gin, S. Weiss, and A. P. Alivisatos, *Science*, 1998, **281**, 2013-2016.
143. I. L. Medintz, H. T. Uyeda, E. R. Goldman, and H. Mattoussi, *Nat. Mater.*, 2005, **4**, 435-446.
144. W. C. W. Chan and S. Nie, *Science*, 1998, **281**, 2016-2018.
145. D. Beydoun, R. Amal, G. Low, and S. McEvoy, *J. Nanoparticle Res.*, 1999, **1**, 439–458.
146. X. Liu, C. Ma, Y. Yan, G. Yao, Y. Tang, P. Huo, W. Shi, and Y. Yan, *Ind. Eng. Chem. Res.*, 2013, **52**, 15015–15023.
147. (a) N. Salah, S.S. Habib, Z. H. Khan, A. Memic, A. Azam, E. Alarfaj, N. Zahed, and S. A. Hamed, *Int. J. Nanomedicine*, 2011, **6**, 863–869; (b) S. H. Yun, B. H. Sohn, J. C. Jung, W. C. Zin, M. Ree, and J. W. Park, *Nanotechnology*, 2006, **17**, 450-454; (c) D. Bera, L. Qian, T. K. Tseng, and P. H. Holloway, *Materials*, 2010, **3**, 2260-2345.
148. L. Spanhel, M. Haase, H. Weller, and A. Henglein, *J. Am. Chem. Soc.*, 1987, **109**, 5649–5655.
149. J. Bang, H. Yang, and P. H. Holloway, *Nanotechnology*, 2006, **17**, 973–978.
150. D. Bera, L. Qian, S. Sabui, S. Santra, and P. H. Holloway, *Opt. Mater.*, 2008, **30**, 1233–1239.
151. A. Sashchiuk, E. Lifshitz, R. Reisfeld, T. Saraidarov, M. Zelner, and A. Willenz, *J. Sol-Gel Sci. Technol.*, 2002, **24**, 31–38.
152. C. B. Murray, D. J. Norris, and M. G. Bawendi, *J. Am. Chem. Soc.*, 1993, **115**, 8706–8715.

REFERENCES

153. Y. Bae, N. Myung, and A. J. Bard, *Nano Lett.*, 2004, **4**, 1153–1161.
154. M. A. Hines and P. Guyot-Sionnest, *J. Phys. Chem. B*, 1998, **102**, 3655–3657.
155. L. Bakueva, S. Musikhin, M.A. Hines, T.W.F. Chang, M. Tzolov, G.D. Scholes, and E. H. Sargent, *Appl. Phys. Lett.*, 2003, **82**, 2895–2897.
156. D. Battaglia and X.G. Peng, *Nano Lett.* 2002, **2**, 1027–1030.
157. J. J. Zhu, Y. Koltypin, and A. Gedanken, *Chem. Mater.*, 2000, **12**, 73–78.
158. Yi Xie , Ghafar Ali, Seung Hwa Yoo, and Sung Oh Cho, *ACS Appl Mater Interfaces.*, 2010, **2**, 2910-4.
159. Y. T. Kim, J. H. Han, B. H. Hong, and Y. U. Kwon, *Adv. Mater.*, 2010, **22**, 515-518.
160. D. V. Freitas, J. M. M. Dias, S. G. B. Passos, G. C. S. de Souza, E. T. Neto, and M. Navarro, *Green Chem.*, 2014, **16**, 3247-3254.
161. C. M. Gonzalez, W. C. Wu, J. B. Tracy, and B. Martin, *Chem. Commun.*, 2015, **51**, 3087-3090.
162. M. Liu, H. Zhao, S. Chen, H. Wang, and X. Quan, *Inorg. Chim. Acta*, 2012, **392**, 236–240.
163. Y. Hu and J. F. Chen, *J. Clust. Sc.*, 2007, **18**, 371-387.
164. S. Singh, A. Guleria, M. C. Rath, A. K. Singh, S. Adhikari, and S. K. Sarkar, *J. Nanosci. Nanotechnol.*, 2013, **13**, 5365-5373.
165. S. Singh, M. C. Rath, A. K. Singh, T. Mukherjee, O. D. Jayakumar, A. K. Tyagi, and S. K. Sarkar, *Rad. Phys. Chem.* 2011, **80**, 736-741.
166. M. Mostafavi, Y. P. Liu, P. Pernot, and J. Belloni, *Rad. Phys. Chem.* 2000, **59**, 49-59.

REFERENCES

167. S. Singh, M. C. Rath, A. K. Singh, S. K. Sarkar, and T. Mukherjee, *Mater. Chem. Phys.* 2010, **124**, 6–9.
168. Z. Li, L. Peng, Y. Fang, Z. Chen, D. Pan, and M. Wu, *Rad. Phys. Chem.*, 2011, **80**, 1333-1336.
169. J. Biswal, S. Singh, M. C. Rath, S. P. Ramnani, S. K. Sarkar, and S. Sabharwal, *Int. J. Nanotechnol.*, 2010, **7**, 1013 – 1026.
170. S. Q. Chang, Y. D. Dai, B. Kang, W. Han, and D. Chen, *J. Nanosci. Nanotechnol.* 2009, **9**, 5693-700.
171. D. Leonard, M. Krishnamurthy, C. M. Reaves, S. P. Denbaars, and P. M. Petroff, *Appl. Phys. Lett.*, 1993, **63**, 3203–3205.
172. S. H. Xin, P. D. Wang, A. Yin, C. Kim, M. Dobrowolska, J. L. Merz, and J. K. Furdyna, *Appl. Phys. Lett.*, 1996, **69**, 3884–3886.
173. J. R Heine, J. R. Viejo, M. G Bawendi, and K. F Jensen, *J. Cryst. Growth*, 1998, **195**, 564–568.
174. M. Danek, K. F. Jensen, C. B. Murray, and M. G. Bawendi, *J. Cryst. Growth*, 1994, **145**, 714–720.
175. Z. Hai, C. Zhu, J. Huang, H. Liu, and J. Chen, *Inorg. Chem.*, 2010, **49**, 7217–7219.
176. J. Biswal, S. P. Ramnani, R. Tewari, G. K. Dey, and S. Sabharwal, *Radiat. Phys. Chem.* 2010, **79**, 441–445.
177. A. Abedini, A. R. Daud, M. A. A. Hamid, N. K. Othman, and E. Saion, *Nanoscale Res. Lett.*, 2013, **8**, 474.
178. S. Singh, M. C. Rath, and S. K. Sarkar, *J. Phys. Chem. A*, 2011, **115**, 13251-8.

REFERENCES

179. N. M. Dimitrijević, *J. Chem. Soc., Faraday Trans.* 1987, **83**, 1193-1201.
180. H. Zhu and T. Lian, *Energy Environ. Sci.*, 2012, **5**, 9406-9418.
181. A. J. Nozik and R. Memming, *J. Phys. Chem.*, 1996, **100**, 13061–13078.
182. S. A. Hilli and M. Willander, *Sensors*, 2009, **9**, 7445-7480.
183. B. Smaller, J. R. Remko, and E. C. Avery, *J. Chem. Phys.*, 1968, **48**, 5174-5181.
184. K. H. Schmidt and W. L. Buck, *Science*, 1966, **151**, 70-71.
185. Y. Tabata, *Pulse Radiolysis of Irradiated Systems*, CRC Press, 1991.
186. G. V. Buxton and C. R. Stuart, *J. Chem. Soc. Faraday Trans.*, 1995, **91**, 279-281.
187. J. V. Davies and J. Law, *Phys. Med. Biol.*, 1963, **8**, 91-96.
188. K. Shih, Ed., *X-Ray Diffraction: Structure, Principles and Applications*, Nova Science, 2013.
189. A. R. West, *Basic Solid State Chemistry*, John Wiley & Sons, 2nd editio., 1999.
190. U. Holzwarth and N. Gibson, *Nat. Nanotechnol.*, 2011, **6**, 534-534.
191. B. Fultz and J. Howe, *Transmission Electron Microscopy and Diffractometry of Materials*, Springer, 2007.
192. R. Egerton, *Physical principles of electron microscopy*, Springer, 2005.
193. E. Kirkland, *Advanced computing in Electron Microscopy*, Springer, 1998.
194. D. McMullan, *Scanning*, 2006, **17**, 175-185.
195. P. Echlin, D. C. Joy, C. Fiori, and E. Lifshin, *Goldstein, G. I., Newbury, D. E., Scanning electron microscopy and x-ray microanalysis*, Plenum Press, New York, 1981.

REFERENCES

196. K. K. Rohatgi-Mukherjee, *Fundamentals of Photochemistry*, Wiley Eastern Ltd: India, 1986.
197. D. A. Skoog, F. J. Holler, and S. R. Crouch, *Principles of Instrumental Analysis*, Belmont, CA: Thomson Brooks/Cole, 6th ed., 2007.
198. M. Y. Berezin and S. Achilefu, *Chem. Rev.*, 2010, **110**, 2641–2684.
199. D. V. O'Connor and D. Phillips, *Time-Correlated Single-Photon Counting*, Academic Press, London, 1984.
200. B. C. Smith, *Fundamentals of Fourier Transform Infrared Spectroscopy*, CRC Press, Second Edi., 2011.
201. B. H. Stuart, *Infrared Spectroscopy: Fundamentals and Applications*, Wiley, 2004.
202. R. White, *Chromatography/Fourier Transform Infrared Spectroscopy and its Applications*, CRC Press, Ist editio., 1989.
203. F. M. Mirabella, *Practical Spectroscopy Series; Internal reflection spectroscopy: Theory and applications*, CRC Press, 1992.
204. Technical note on FTIR spectroscopy, PerkinElmer.
205. J. R. Ferraro, *Introductory Raman Spectroscopy*, Academic Press Inc, 2nd editio., 2002.
206. B. Schrader, *Infrared and Raman Spectroscopy*, VCH Publishers Inc., New York, 1995.
207. A. B. Myers and R. A. Mathies, *Biological Applications of Raman Spectroscopy: Resonance Raman Spectra of Polyenes and Aromatics*, John Wiley and Sons, New York, 1987.

REFERENCES

208. P. Larkin, *Infrared and Raman Spectroscopy; Principles and Spectral Interpretation*, Elsevier Science Publishing Co Inc, 2011.
209. H. Krister, *Eur. J. Org. Chem.*, 2007, 731–742.
210. G. S. Dimitry and B. S. Gleb, *Adv. Mater.*, 2004, **16**, 671-682.
211. (a) Z. Jian, J. Fang, and F. Peng, *J. Chem. Tech. Biotech.*, 2010, **85**, 860–865; (b) H. Gröger, C. Kind, P. Leidinger, M. Roming, and C. Feldmann, *Materials*, 2010, **3**, 4355-4386.
212. S. M. Johann and S. Katrin, *Chem. Rev.*, 1995, **95**, 849-864.
213. (a) S. S. Atik and J. K. Thomas, *J. Am. Chem. Soc.*, 1981, **103**, 4367- 4371; (b) M. P. Pileni, P. Brochette, B. Hickel, and B. J. Lerebouis, *J. Colloid Interface Sci.*, 1984, **98**, 549-554; (c) R. Wolf and P. Luisi, *Biochem. Biophys. Res. Commun.*, 1979, **89**, 209-217.
214. S. Adhikari, S. K. Kapoor, S. Chattopadhyay, and T. Mukherjee, *Biophys. Chem.*, 2000, **88**, 111–117.
215. A. Swami, G. Espinosa, S. Guillot, E. Raspaud, F. Boue, and D. Langevin, *Langmuir*, 2008, **24**, 11828-11833.
216. E. M. Corbeil and N. E. Levinger, *Langmuir*, 2003, **19**, 7264-7270.
217. (a) M. Giustini, G. Palazzo, G. Colafemmina, M. Della Monica, M. Giomini, and A. Ceglie, *J. Phys. Chem.*, 1996, **100**, 3190-3198; (b) G. Palazzo, F. Lopez, M. Giustini, G. Colafemmina, and A. Ceglie, *J. Phys. Chem. B*, 2003, **107**, 1924-1931.
218. P. K. Das and A. Chaudhuri, *Langmuir*, 1999, **15**, 8771-8775.

REFERENCES

- 219.** (a) O. A. El Seoud, *J. Mol. Liq.*, 1997, **72**, 85-103; (b) I. M. Cuccovia, L. G. Dias, F. A. Maximiano, and H. Chaimovich, *Langmuir*, 2001, **17**, 1060-1068.
- 220.** K. S. Mali and G. B. Dutt, *J. Chem. Phys.*, 2009, **131**, 1747081-1747088.
- 221.** (a) M. Wong, M. Gratzel, and J. K. Thomas, *J. Am. Chem. Soc.*, 1976, **98**, 2391-2397; (b) V. Calvo-Perez, G. S. Beddard, and J. H. J. Fendler, *Phys. Chem.*, 1981, **85**, 2316-2319; (c) P. Brochette, T. Zemb, P. Mathis, and M. P. Pileni, *J. Phys. Chem.*, 1987, **91**, 1444-1450; (d) G. Bakale, G. Beck, and J. K. Thomas, *J. Phys. Chem.*, 1992, **96**, 2328-2334; (e) S. Adhikari, R. Joshi, and C. Gopinathan, *Int. J. Chem. Kinet.*, 1998, **30**, 699-705; (f) J. L. Gebicki, E. S. Pietek, L. Gebicka, *Properties and reactions of radiation induced transients*; PWN, Warsaw, 1999, 151-176; (g) S. Adhikari and T. Mukherjee, *Proc. React. Kinet. Mech.*, 2001, **26**, 301-336; (h) J. Fendler and L. K. Patterson, *J. Phys. Chem.*, 1970, **74**, 4608-4609.
- 222.** C. Petit, P. Brochette, and M. P. Pileni, *J. Phys. Chem.*, 1986, **90**, 6517-6521.
- 223.** (a) S. Chauhan, M. S. Chauhan, D. Kaushal, V. K. Syal, and J. Jyoti, *J. Solution Chem.*, 2010, **39**, 622-638; (b) R. H. Arain, J. S. Shukla, and G. S. Misra, *Die Makromol. Chem.*, 1970, **134**, 179-192.
- 224.** M. Gratzel, J. K. Thomas, and L. K. Paterson, *Chem. Phys. Lett.*, 1974, **29**, 393-396.
- 225.** P. K. Das, G. V. Srilakshmi, and A. Chaudhuri, *Langmuir*, 1999, **15**, 981-987.
- 226.** (a) D. Zehavi and J. Rabani, *J. Phys. Chem.*, 1972, **76**, 312-319; (b) M. S. Matheson, W. A. Mulac, J. L. Weeks, and J. Rabani, *J. Phys. Chem.*, 1966, **70**, 2092-2099.
- 227.** A. J. Frank, M. Gratzel, and J. J. Kozak, *J. Am. Chem. Soc.*, 1976, **98**, 3317-3321.
- 228.** B. H. Milosavljevic and J. A. LaVerne, *J. Phys. Chem. A*, 2005, **109**, 165-168.

REFERENCES

- 229.** (a) R. Re, N. Pellegrini, A. Protegente, A. Panala, M. Yang, and C. Rice-Evans, *Free Radic. Biol. Med.*, 1999, **26**, 1231–1237; (b) B. Nitha, S. De, S. Adhikari, T. P. A. Devasagayam, and K. K. Janardhanan, *Pharm. Biol.*, 2010, **48**, 453-460; (c) R. B. Walker and J. D. Everette, *J. Agric. Food Chem.*, 2009, **57**, 1156–1161; (d) G. Miliauskasa, P. R. Venskutonisa, and T. A. van Beek, *Food Chem.*, 2004, **85**, 231–237; (e) B. W. Lee, J. H. Lee, S. W. Gal, Y. H. Moon, and K. H. Park, *Biosci. Biotechnol. Biochem.*, 2006, **70**, 427-432; (f) M. Mohammadi, S. Khole, T. P. A. Devasagayam, and S. S. Ghaskadbi, *Drug Discov Ther.*, 2009, **3**, 151-161; (g) S. Chatterjee, Z. Niaz, S. Gautam, S. Adhikari, P. S. Variyar, and A. Sharma, *Food Chemistry*, 2007, **101**, 515–523.
- 230.** B. S. Wolfenden and R. L. Willson, *J. Chem. Soc. Perkin Trans. II*, 1982, 805-812.
- 231.** J. L. Gebicki and M. Maciejewska, *J. Phys. Chem. A*, 2007, **111**, 2122-2127.
- 232.** S. L. Scott, W. J. Chen, B. Andreja, and J. H. Espenson, *J. Phys. Chem.*, 1993, **97**, 6710-6714.
- 233.** R. Arbain, M. Othman, and S. Palaniandy, *Miner. Eng.*, 2011, **24**, 1-9.
- 234.** E. P. Tijerina, M. G. Pinilla, S. M. Rosales, U. O. Méndez, A. Torres, and M. J. Yacamán, *Faraday Discuss.*, 2008, **138**, 353-362.
- 235.** M. A. Lopez-Quintela, *Curr. Opin. Coll. Int. Sci.*, 2003, **8**, 137-144.
- 236.** (a) C. Burda, X. Chen, R. Narayanan, and M. A. El-Sayed, *Chem Rev.*, 2005, **105**, 1025-1102; (b) A. M. Smith and S. Nie, *Acc. Chem. Res.*, 2010, **43**, 190–200; (c) K. Grieve, P. Mulvaney, and F. Grieser, *Curr. Opin. Colloid Interface Sci.*, 2000, **5**, 168–172.

REFERENCES

237. (a) L. F. Xi and Y.M. Lam, *J. Colloid Interface Sci.*, 2007, **316**, 771-8; (b) N. Chandrasekharan and P. V. Kamat, *Res. Chem. Intermed.*, 2002, **28**, 847-856; (c) L. F. Xi, Y. M. Lam, Y. P. Xu, and L. J. Li, *J. Colloid Interface Sci.*, 2008, **320**, 491-500.
238. J. Eastoe, M. J. Hollamby, and L. Hudson, *Adv. Colloid Interface Sci.*, 2006, **128-130**, 5-15.
239. M. C. Rath, J. A. Mondal, D. K. Palit, T. Mukherjee, and H. N. Ghosh, *J. Nanomaterials*, 2007, **2007**, Art ID 36271.
240. Y. Mei, Y. Han, Y. Li, W. Wang, and Z. Nie, *Mater. Lett.*, 2006, **60**, 3068-3072.
241. A. Agostiano, M. Catalano, M. L. Curri, M. Della Monica, L. Manna, and L. Vasanelli, *Micron*, 2000, **31**, 253-258.
242. L. E. Brus, *J. Phys. Chem.*, 1986, **90**, 2555-2560.
243. (a) D. J. Norris and M. G. Bawendi, *Phys. Rev. B*, 1996, **53**, 16338-16346; (b) Y. Z. Hu, M. Lindberg, and S. W. Koch, *Phys. Rev. B*, 1990, **42**, 1713-1723; (c) W. Que, *Phys. Rev. B*, 1992, **45**, 11036-11041.
244. J. Zhang, L. Sun, C. Liao, and C. Yan, *Solid State Commun.*, 2002, **124**, 45-48.
245. M. L. Curri, A. Agostiano, L. Manna, M. D. Monica, M. Catalano, L. Chiavarone, V. Spagnolo, and M. Lugara, *J. Phys. Chem. B*, 2000, **104**, 8391-8397.
246. P. V. Kamat, N. M. Dimitrijevic, and R. W. Fessenden, *J. Phys. Chem.*, 1987, **91**, 396-401.
247. (a) H. Yu and S. L. Brock, *ACS Nano.*, 2008, **2**, 1563-1570; (b) X. Peng, L. Manna, W. Yang, J. Wickham, E. Scher, A. Kadavanich, and A. P. Alivisatos, *Nature*, 2000, **404**, 59-61; (c) M. B. Mohamed, C. Burda, and M. A. El-Sayed, *Nano Lett.*, 2001, **1**,

REFERENCES

- 589-593; (d) C. F. Landes, S. Link, M. B. Mohamed, B. Nikoobakht, and M. A. El-Sayed, *Pure Appl. Chem.*, 2002, **74**, 1675-1692.
- 248.** X. Li, T. Li, C. Wu, and Z. Zhang, *J. Nano Res.*, 2007, **9**, 1081-1086.
- 249.** (a) G. Cantele, D. Ninno, and G. Iadonisi, *J. Phys. Condens. Matter.*, 2000, **12**, 9019-9036; (b) G. Cantele, D. Ninno, and G. Iadonisi, *Nano Lett.*, 2001, **1**, 121-124.
- 250.** L. Qi, in *Encyclopedia of Surface and Colloid Science*, ed. P. Somasundaran, Taylor & Francis, New York, 2006.
- 251.** E. Gharibshahi and E. Saion, *Int. J. Mol. Sci.*, 2012, **13**, 14723–14741.
- 252.** E. Saion, E. Gharibshahi, and K. Naghavi, *Int. J. Mol. Sci.*, 2013, **14**, 7880–7896.
- 253.** (a) A. D. Dukes III, M. A. Schreuder, J. A. Sammons, J. R. McBride, N. J. Smith, and S. J. Rosenthal, *J. Chem. Phys.*, 2008, **129**, 121102–121104; (b) A. D. Dukes III, P. C. Samson, J. D. Keene, L. M. Davis, J. P. Wikswo, and S. J. Rosenthal, *J. Phys. Chem. A*, 2011, **115**, 4076–4081.
- 254.** (a) T. R. Ravindran, A. K. Arora, B. Balamurugan, and B. R. Mehta, *NanoStructured Mater.*, 1999, **11**, 603–609; (b) E. M. Chan, C. Xu, A. W. Mao, G. Han, J. S. Owen, B. E. Cohen, and D. J. Milliron, *Nano Lett.*, 2010, **10**, 1874–1885; (c) J. Choi, N. S. Wang, and V. Reipa, *Langmuir*, 2007, **23**, 3388–3394.
- 255.** A. V. Katsaba, S. A. Ambrozevich, A. G. Vitukhnovsky, V. V. Fedyanin, A. N. Lobanov, V. S. Krivobok, R. B. Vasiliev, and I. G. Samatov, *J. Appl. Phys.*, 2013, **113**, 184306-6.
- 256.** (a) B. R. Fisher, H. J. Eisler, N. E. Stott, and M. G. Bawendi, *J. Phys. Chem. B*, 2004, **108**, 143–148; (b) A. Al Salman, A. Tortschanoff, G. Van der Zwan, F. Van Mourik,

REFERENCES

- and M. Chergui, *Chem. Phys.*, 2009, **357**, 96–101; (c) A. Van Driel, I. Nikolaev, P. Vergeer, P. Lodahl, D. Vanmaekelbergh, and W. L. Vos, *Phys. Rev. B*, 2007, **75**, 035329; (d) E. S. Barnard, E. T. Hoke, S. T. Connor, J. R. Groves, T. Kuykendall, Z. Yan, E. C. Samulon, E. D. Bourret-Courchesne, S. Aloni, P. J. Schuck, C. H. Peters, and B. E. Hardin, *Sci. Rep.*, 2013, **3**, Article number: 2098.
- 257.** M. A. Schreuder, J. R. McBride, A. D. Dukes III, J. A. Sammons, and S. J. Rosenthal, *J. Phys. Chem. C*, 2009, **113**, 8169–8176.
- 258.** (a) S. Kudera, M. Zanella, C. Giannini, A. Rizzo, Y. Li, G. Gigli, R. Cingolani, G. Ciccarella, W. Spahl, W. J. Parak, and L. Manna, *Adv. Mater.*, 2007, **19**, 548–552; (b) M. Zanella, A. Z. Abbasi, A. K. Schaper, and W. J. Parak, *J. Phys. Chem. C*, 2010, **114**, 6205–6215.
- 259.** (a) M. J. Bowers, J. R. McBride, M. D. Garrett, J. A. Sammons, A. D. Dukes, M. A. Schreuder, T. L. Watt, A. R. Lupini, S. J. Pennycook, and S. J. Rosenthal, *J. Am. Chem. Soc.*, 2009, **131**, 5730–5731; (b) M. J. Bowers, J. R. McBride, and S. J. Rosenthal, *J. Am. Chem. Soc.*, 2005, **127**, 15378–15379; (c) L. Qian, D. Bera, and P. H. Holloway, *Nanotechnology*, 2008, **19**, 285702.
- 260.** X. F. Zhang, I. Zhang, and L. Liu, *Photochem. Photobiol.*, 2010, **86**, 492–498.
- 261.** X. Wang, L. Qu, J. Zhang, X. Peng, and M. Xiao, *Nano Lett.*, 2003, **3**, 1103–1106.
- 262.** V. Biju, R. Kanemoto, Y. Matsumoto, S. Ishii, S. Nakanishi, T. Itoh, Y. Baba, and M. Ishikawa, *J. Phys. Chem. C*, 2007, **111**, 7924–7932.
- 263.** W. Z. Lee, G. W. Shu, J. S. Wang, J. L. Shen, C. A. Lin, W. H. Chang, R. C. Ruaan, W. C. Chou, C. H. Lu, and Y. C. Lee, *Nanotechnology*, 2005, **16**, 1517–1521.

REFERENCES

- 264.** (a) M. H. Hatzopoulos, J. Eastoe, P. J. Dowding, and I. Grillo, *J. Colloid Interface Sci.*, 2013, **392**, 304–310; (b) M. J. Lawrence and G. D. Rees, *Adv. Drug Deliv. Rev.*, 2000, **45**, 89–121; (c) M. P. Pileni, *Nat. Mater.*, 2003, **2**, 145–150; (d) R. Angelico, G. Palazzo, G. Colafemmina, P. A. Cirkel, M. Giustini, and A. Ceglie, *J. Phys. Chem. B*, 1998, **102**, 2883–2889.
- 265.** P. Wasserscheid and W. Keim, *Angew. Chem. Int. Ed.*, 2000, **39**, 3773–3789.
- 266.** A. M. Funston, T. A. Fadeeva, J. F. Wishart, and E. W. Castner Jr., *J. Phys. Chem. B*, 2007, **111**, 4963–4977.
- 267.** P. Tarábek, S. Liu, K. Haygarth, and D. M. Bartels, *Radiat. Phys. Chem.*, 2009, **78**, 168–172.
- 268.** S. B. Dhiman, G. S. Goff, W. Runde, and J. A. LaVerne, *J. Phys. Chem. B*, 2013, **117**, 6782–6788.
- 269.** L. Yuan, C. Xu, J. Peng, L. Xu, M. Zhai, J. Li, G. Wei, and X. Shen, *Dalton Trans.*, 2009, 7873–7875.
- 270.** (a) A. V. Plakhotnyka, L. Ernst, and R. Schmutzler, *J. Fluorine Chem.*, 2005, **126**, 27–31; (b) S. Keskin, D. Kayrak-Talay, U. Akman, and O. HortaÇsu, *J. of Supercritical Fluids*, 2007, **43**, 150–180; (c) B. Özmen-Monkul and M. M. Lerner, *Carbon*, 2010, **N48**, 3205–3210; (d) D. Bejan, N. Ignat'ev, and H. Willner, *J. Fluorine Chem.*, 2010, **131**, 325–332.
- 271.** (a) D. Behar, C. Gonzalez, and P. Neta, *J. Phys. Chem. A*, 2001, **105**, 7607–7614; (b) K. Takahashi, T. Sato, Y. Katsumura, J. Yang, T. Kondoh, Y. Yoshida, and R. Katoh,

REFERENCES

- Radiat. Phys. Chem.*, 2008, **77**, 1239-1243; (c) H. Y. Fu, Z. G. Xing, X. Y. Cao, and G. Z. Wu, *Chin. Sci. Bull.*, 2012, **57**, 2752-2758.
- 272.** I. A. Shkrob, *J. Phys. Chem. B*, 2010, **114**, 368–375.
- 273.** (a) D. Minehan, K. A. Marx, and S. K. Tripathy, *Polymer Preprints -- Papers Presented At the Boston, Massachusetts Meeting* - 1990, **31**, 390-391; (b) J. Yin and R. L. Elsenbaumer, *J. Org. Chem.*, 2005, **70**, 9436-9446.
- 274.** J. W. Kamplain and C. W. Bielawski, *Chem. Commun.*, 2006, 1727–1729.
- 275.** R. Katoh, *Chem. Lett.*, 2007, **36**, 1256-1257.
- 276.** T. Cremer, C. Kolbeck, K. R. J. Lovelock, N. Paape, R. Woelfel, P. S. Schulz, P. Wasserscheid, H. Weber, J. Thar, B. Kirchner, F. Maier, and H. Steinrueck, *Chem.-Eur. J*, 2010, **16**, 9018–9030.
- 277.** J. Jacquemin, R. Ge, P. Nancarrow, D. W. Rooney, M. F. C. Gomes, A. A. H. Pádua, and C. Hardacre, *J. Chem. Eng. Data*, 2008, **53**, 716–726.
- 278.** (a) J. G. Huddleston, Ann E. Visser, W. M. Reichert, H. D. Willauer, G. A. Broker and R. D. Rogers, *Green Chem.*, 2001, **3**, 156–164; (b) M. Tariq, P. A. S. Forte, M. F. C. Gomes, J. N. C. Lopes, and L. P. N. Rebelo, *J. Chem. Thermodynamics*, 2009, **41**, 790–798; (c) K. Shimizu, M. Tariq, M. F. Costa Gomes, L. P. N. Rebelo, and J. N. Canongia Lopes, *J. Phys. Chem. B*, 2010, **114**, 5831–5834; (d) S. G. Kazarian, B. J. Briscoe, and T. Welton, *Chem. Commun.*, 2000, 2047–2048; (e) Y. F. Hu, Z. C. Liu, C. M. Xu, and X. M. Zhang, *Chem. Soc. Rev.*, 2011, **40**, 3802–3823; (f) J. L. Anthony, J. L. Anderson, E. J. Maginn, and J. F. Brennecke, *J. Phys. Chem. B*, 2005, **109**, 6366-6374.

REFERENCES

- 279.** (a) M. A. Iglesias-Otero, J. Troncoso, E. Carballo, and L. Romani, *J. Chem. Thermodynamics*, 2008, **40**, 949–956; (b) M. Deetlefs, K. R. Seddon, and M. Shara, *Phys. Chem. Chem. Phys.*, 2006, **8**, 642–649; (c) B. Hasse, J. Lehmann, D. Assenbaum, P. Wasserscheid, A. Leipertz, and A. P. Froba, *J. Chem. Eng. Data*, 2009, **54**, 2576–2583; (d) M. Larriba, S. García, J. N. García, J. S. Torrecilla, and F. Rodríguez, *J. Chem. Eng. Data*, 2011, **56**, 3589–3597.
- 280.** (a) H. Tokuda, K. Hayamizu, K. Ishii, M. A. B. H. Susan, and M. Watanabe, *J. Phys. Chem. B*, 2004, **108**, 16593–16600; (b) S. V. Dzyuba and R. A. Bartsch, *Chem. Phys. Chem.*, 2002, **3**, 161–166; (c) Z. Y. Gu and J. F. Brennecke, *J. Chem. Eng. Data*, 2002, **47**, 339–345.
- 281.** (a) G. Singh and A. Kumar, *Indian J. Chem.*, 2008, **47A**, 495–503; (b) C. P. Fredlake, J. M. Crosthwaite, D. G. Hert, S. N. V. K. Aki, and J. F. Brennecke, *J. Chem. Eng. Data*, 2004, **49**, 954–964.
- 282.** (a) Q. S. Liu, J. Tong, Z. C. Tan, U. Welz-Biermann, and J. Z. Yang, *J. Chem. Eng. Data*, 2010, **55**, 2586–2589; (b) S. Seki, N. Serizawa, K. Hayamizu, S. Tsuzuki, Y. Umebayashi, K. Takei, and H. Miyashiro, *J Electrochem Soc.*, 2012, **159**, A967–A971.
- 283.** P. R. Vasudeva Rao, K. A. Venkatesan, A. Rout, T. G. Srinivasan, and K. Nagarajan, *Sep. Sci. Technol.*, 2012, **47**, 204–222.
- 284.** H. L. Ngo, H. L. Compte, L. Hargens, and A. B. McEwen, *Thermochim. Acta*, 2000, **357**, 97–102.

REFERENCES

- 285.** (a) M. Kosmulski, J. Gustafsson, and J. B. Rosenholm, *Thermochim. Acta*, 2004, **412**, 47–53; (b) F. Endres and S. Z. E. Abedin, *Phys. Chem. Chem. Phys.*, 2006, **8**, 2101–2116.
- 286.** (a) V. Kamavaram and R. G. Reddy, *Int. J. Therm. Sci.*, 2008, **47**, 773–777; (b) B. K. M. Chan, N. H. Chang, and M. R. Grimmett, *Aust. J. Chem.*, 1977, **30**, 2005–2013.
- 287.** N. S. Choi, Z. Chen, S. A. Freunberger, X. Ji, Y. K. Sun, K. Amine, G. Yushin, L. F. Nazar, J. Cho, and P. G. Bruce, *Angew. Chem. Int. Ed.*, 2012, **51**, 9994 – 10024.
- 288.** A. G. Glenn and P. B. Jones, *Tetrahedron Lett.*, 2004, **45**, 6967–6969.
- 289.** (a) R. T. Carlin, H. C. De Long, J. Fuller, and P. C. Trulove, *J. Electrochem. Soc.*, 1998, **145**, 1598–1607; (b) V. R. Koch, L. A. Dominey, C. Nanjundiah, and M. J. Ondrechen, *J. Electrochem. Soc.*, 1996, **143**, 798–803.
- 290.** R. Hagiwara and Y. Ito, *J. Fluorine Chem.*, 2000, **105**, 221–227.
- 291.** M. Buzzeo, C. Hardacre, and R. Compton, *Chem. Phys. Chem.*, 2006, **7**, 176–180.
- 292.** N. J. Bridges, A. E. Visser, M. J. Williamson, J. I. Mickalonis, and T. M. Adams, *Radiochim. Acta*, 2010, **98**, 243–247.
- 293.** S. Zhang, X. Qi, X. Ma, L. Lu, Q. Zhang, and Y. Deng, *J. Phys. Org. Chem.*, 2012, **25**, 248–257.
- 294.** (a) J. L. Dimicoli, A. Renaud, and J. Bieth, *Eur J. Biochem.*, 1980, **107**, 423–432; (b) J. J. Kampa, J. W. Nail, and R. J. Lagow, *Angew. Chem., Int. Ed. Engl.*, 1995, **34**, 1241–1244; (c) S. K. Alley Jr. and R. L. Scott, *J. Chem. Eng. Data*, 1963, **8**, 117–119.
- 295.** I. A. Shkrob, T. W. Marin, S. D. Chemerisov, J. L. Hatcher, and J. F. Wishart, *J. Phys. Chem. B*, 2011, **115**, 3889–3902.

REFERENCES

- 296.** S. Wang, J. Liu, L. Yuan, Z. Cui, J. Peng, J. Li, M. Zhai, and W. Liu, *Phys. Chem. Chem. Phys.*, 2014, **16**, 18729–18735.
- 297.** J. A. LaVerne and R. H. Schuler, *J. Phys. Chem.*, 1984, **88**, 1200-1205.
- 298.** *Radiation Chemistry of Hydrocarbons*, G. Foldiak, Elsevier Scientific Pub., Amsterdam, 1981.
- 299.** (a) J. F. Wishart, A. M. Funston, T. Szreder, A. R. Cook and M. Gohdo, *Faraday Discuss.*, 2012, **154**, 353-363; (b) J. F. Wishart, *J. Phys. Chem. Lett.*, 2010, **1**, 3225-3231.
- 300.** A. René, D. Hauchard, C. Lagrost, and P. Hapiot, *J. Phys. Chem. B*, 2009, **113**, 2826–2831.
- 301.** (a) A. Paul, P. K. Mandal, and A. Samanta, *J. Phys. Chem. B*, 2005, **109**, 9148–9153; (b) P. K. Mandal, M. Sarkar, and A. Samanta, *J. Phys. Chem. A*, 2004, **108**, 9048–9053; (c) A. Paul and A. Samanta, *J. Chem. Sci.*, 2006, **118**, 335–340; (d) A. Paul, P. K. Mandal, and A. Samanta, *Chem. Phys. Lett.*, 2005, **402**, 375–379; (e) A. Ghosh, T. Chatterjee, and P. K. Mandal, *Chem. Commun.*, 2012, **48**, 6250–6252; (f) S. Cha, T. Shim, Y. Ouchi, and D. Kim, *J. Phys. Chem. B*, 2013, **117**, 10818–10825.
- 302.** (a) J. Coates, in *Encyclopedia of Analytical Chemistry*, ed. R. A. Meyers, John Wiley & Sons Ltd, Chichester, 2000, pp. 10815–10837; (b) G. Socrates, *Infrared and Raman characteristic group frequencies: Tables and Charts*, John Wiley & Sons, 2004; (c) L. J. Bellamy, *Infrared Spectra of Complex Molecules*, Chapman & Hall, New York, USA, Vol. 1, 1975.

REFERENCES

- 303.** (a) K. P. Huang, P. Lin, and H. C. Shih, *J. Appl. Phys.*, 2004, **96**, 354–360; (b) A. M. Moschovia, S. Ntais, V. Dracopoulos, and V. Nikolakis, *Vibrational Spectroscopy*, 2012, **63**, 350–359; (c) J. Kiefer, J. Fries, and A. Leipertz, *Appl. Spectrosc.*, 2007, **61**, 1306–1311.
- 304.** N. E. Heimer, R. E. D. Sesto, Z. Meng, J. S. Wilkes, and W. R. Carper, *Journal of Molecular Liquids*, 2006, **124**, 84 – 95.
- 305.** E. R. Talaty, S. Raja, V. J. Storhaug, A. Dölle, and W. R. Carper, *J. Phys. Chem. B*, 2004, **108**, 13177–13184.
- 306.** S. A. Katsyuba, M. V. Vener, E. E. Zvereva, Z. Fei, R. Scopelliti, G. Laurency, N. Yan, E. Paunescu, and P. J. Dyson, *J. Phys. Chem. B*, 2013, **117**, 9094–9105.
- 307.** C. Janiak, *Z. Naturforsch.*, 2013, **68b**, 1059 – 1089.
- 308.** F. Endres, M. Bukowski, R. Hempelmann, and H. Natter, *Angew. Chem. Int. Ed. Engl.*, 2003, **42**, 3428–30.
- 309.** S. Zein El Abedin, N. Borissenko, and F. Endres, *Electrochem. commun.*, 2004, **6**, 510–514.
- 310.** J. F. Huang and I. W. Sun, *Adv. Funct. Mater.*, 2005, **15**, 989–994.
- 311.** J. F. Huang and Sun I. Wen, *Chem. Mater.*, 2004, **16**, 1829–1831.
- 312.** H. G. Zhu, J. F. Huang, Z. W. Pan, and S. Dai, *Chem. Mater.*, 2006, **18**, 4473–4477.
- 313.** Y. Wang and H. Yang, *Chem. Commun.*, 2006, 2545–2547.
- 314.** X. Zhou, Z. X. Xie, Z. Y. Jiang, Q. Kuang, S. H. Zhang, T. Xu, R. B. Huang, and L. S. Zheng, *Chem. Commun.*, 2005, 5572–5574.

REFERENCES

315. S. Dai, Y. H. Ju, H. J. Gao, J. S. Lin, S. J. Pennycook, and C. E. Barnes, *Chem. Commun.*, 2000, 243–244.
316. T. Nakashima and N. Kimizuka, *J. Am. Chem. Soc.*, 2003, **125**, 6386–6387.
317. E. K. Goharshadi, Y. Ding, M. N. Jorabchi, and P. Nancarrow, *Ultrason. Sonochem.*, 2009, **16**, 120–123.
318. T. Tsuda, T. Sakamoto, Y. Nishimura, S. Seino, A. Imanishi, and S. Kuwabata, *Chem. Commun.*, 2012, **48**, 1925–1927.
319. T. Tsuda, T. Sakamoto, Y. Nishimura, S. Seino, A. Imanishi, K. Matsumoto, R. Hagiwara, T. Uematsu, and S. Kuwabata, *RSC Adv.*, 2012, **2**, 11801–11807.
320. A. Imanishi, T. Masaaki, and S. Kuwabata, *ChemComm*, 2009, 1775–1777.
321. S. Chen, Y. Liu, and G. Wu, *Nanotechnology*, 2005, **16**, 2360–2364.
322. M. E. Meyre, M. Tréguer-Delapierre, and C. Faure, *Langmuir*, 2008, **24**, 4421–5.
323. Z. Li, Z. Liu, J. Zhang, B. Han, J. Du, Y. Gao, and T. Jiang, *J. Phys. Chem. B*, 2005, **109**, 14445–8.
324. Q. F. Zhang, T. P. Chou, B. Russo, S. A. Jenekhe, and G. Cao, *Angewandte Chemie*, 2008, **47**, 2402–2406.
325. Q. F. Zhang, T. P. Chou, B. Russo, S. A. Jenekhe, and G. Z. Cao, *Adv. Funct. Mater.*, 2008, **18**, 1654–1660.
326. J. H. Porada, M. Mansueto, S. Laschat, and C. Stubenrauch, *Soft Matter*, 2011, **7**, 6805–6810.
327. (a) R. Rossetti, J. L. Ellison, J. M. Gibson, and L. E. Brus, *J. Chem. Phys.*, 1984, **80**, 4464–4469; (b) Z. Li and X. Peng, *J. Am. Chem. Soc.*, 2011, **133**, 6578–6586.

REFERENCES

- 328.** (a) K. Mondal and S. K. Srivastava, *Mat. Chem. Phys.*, 2010, **124**, 535–540; (b) S. C. Singh, S. K. Mishra, R. K. Srivastava, and R. Gopal, *J. Phys. Chem. C*, 2010, **114**, 17374–17384.
- 329.** (a) P. Verma, L. Gupta, S. C. Abbi, and K. P. Jain, *J. Appl. Phys.*, 2000, **88**, 4109–4116; (b) C. I. Ratcliffe, K. Yu, J. A. Ripmeester, Md. Badruz Zaman, C. Badarau, and S. Singh, *Phys. Chem. Chem. Phys.*, 2006, **8**, 3510–3519; (c) A. Pan, H. Yang, R. Yu, and B. Zou, *Nanotechnology*, 2006, **17**, 1083–1086.
- 330.** (a) V. Dzhagan, M. Valakh, N. Mel'nik, O. Rayevska, I. Lokteva, J. Kolny-Olesiak, and D. R. T. Zahn, *Int. J. Spectrosc.*, 2012, **2012**, Article ID 532385; (b) Robert W. Meulenberg, T. Jennings, and G. F. Strouse, *Phys. Rev. B*, 2004, **70**, 235311–235315; (c) E. S. F. Neto, N. O. Dantas, S. W. da Silva, P. C. Morais, and M. A. Pereira da Silva, *J. Raman Spectrosc.*, 2010, **41**, 1302–1305; (d) Jia-Yu Zhang, Xiao-Yong Wang, M. Xiao, L. Qu, and X. Peng, *Appl. Phys. Lett.*, 2002, **81**, 2076–2081.
- 331.** (a) A. Roy and A. K. Sood, *Phys. Rev. B*, 1996, **53**, 12127–12132; (b) M. Ivanda, K. Babocsi, C. Dem, M. Schmitt, M. Montagna, and W. Kiefer, *Phys. Rev. B*, 2003, **67**, 235329–235338.
- 332.** (a) S. Chaure, N. B. Chaure and R. K. Pandey, *J. Nanosci. Nanotechnol.*, 2006, **6**, 731–737; (b) A. M. Alcalde, A. A. Ribeiro, N. O. Dantas, D. R. Mendes Jr., G.E. Marques, and C. Trallero-Giner, *J. Non-Crystalline Solids*, 2006, **352**, 3618–3623.
- 333.** (a) Y. N. Hwang, S. H. Park, and D. Kim, *Phys. Rev. B*, 1999, **59**, 7285–7288; (b) R. Venugopal, P. I. Lin, C. C. Liu, and Y. T. Chen, *J. Am. Chem. Soc.*, 2005, **127**, 11262–11268.

REFERENCES

- 334.** (a) B. Tell, T. C. Damen, and S. P. S. Porto, *Phys. Rev.*, 1966, **144**, 771-774; (b) J. M. Ralston, R. L. Wadsack, and R. K. Chang, *Phys. Rev. Lett.*, 1970, **25**, 814-818; (c) C. M. Dai and Der San Chuu, *J. Appl. Phys.*, 1992, **71**, 3056-3058.
- 335.** (a) P. J. Carroll and J. S. Iannin, *Solid State Commun.*, 1981, **40**, 81-84; (b) S. N. Yannopoulos and K. S. Andrikopoulos, *J. Chem. Phys.*, 2004, **121**, 4747-4758.
- 336.** G. Lucovsky, A. Mooradian, W. Taylor, G. B. Wright, and R. C. Keezer, *Solid State Commun.*, 1967, **5**, 113-117.
- 337.** H. Chen, D. W. Shin, J. G. Nam, K. W. Kwon, and J. B. Yoo, *Mater. Res. Bull.*, 2010, **45**, 699-704.
- 338.** (a) C. Rincón and F. J. Ramírez, *J. Appl. Phys.*, 1992, **72**, 4321-4324; (b) C. M. Xu, X. L. Xu, J. Xu, X. J. Yang, J. Zuo, N. Kong, W. H. Huang, and H. T. Liu, *Semicond. Sci. Technol.*, 2004, **19**, 1201-1206.
- 339.** T. G. Edwards and S. Sen, *J. Phys. Chem. B*, 2011, **115**, 4307-4314.
- 340.** R. Lukács, M. Veres, K. Shimakawa, and S. Kugler, *J. Appl. Phys.*, 2010, **107**, 073517-5.
- 341.** X. Jiang, B. Mayers, T. Herricks, and Y. Xia, *Adv. Mater.*, 2003, **15**, 1740-1743.
- 342.** J. P. Ge, Y. D. Li, and G. Q. Yang, *Chem Commun.*, 2002, 1826-1827.
- 343.** B. T. Mayers, K. Liu, D. Sunderland, and Y. Xia, *Chem. Mater.*, 2003, **15**, 3852-3858.
- 344.** (a) U. Jeong, P. H. C. Camargo, Y. H. Lee, and Y. Xia, *J. Mater. Chem.*, 2006, **16**, 3893-3897; (b) L. Liu, Q. Peng, and Y. Li, *Nano Res.*, 2008, **1**, 403-411.
- 345.** Y. Zhu, Y. Qian, H. Huang, and M. Zhang, *Mat. Lett.*, 1996, **28**, 119-122.

REFERENCES

346. S. Adhikari, T. Mukherjee, and E. Janata, *Res. Chem. Intermed.*, 2005, **31**, 227-234.
347. B. Gates, B. Mayers, A. Grossman, and Y. Xia, *Adv. Mater.*, 2002, **14**, 1749-1752.
348. J. Esser, P. Wasserscheid, and A. Jess, *Green Chem.*, 2004, **6**, 316-322.
349. Y. Sun, C. Li, and W. Zheng, *Cryst. Growth Des.*, 2010, **10**, 262-267.
350. Y. Zhou and M. Antonietti, *J. Am. Chem. Soc.*, 2003, **125**, 14960-14961.
351. (a) Y. Wu, X. Hao, J. Yang, F. Tian, and M. Jiang, *Mater. Lett.*, 2006, **60**, 2764-2766; (b) H. Li, W. Li, L. Ma, W. Chen, and J. Wang, *J. Alloys Compd.*, 2009, **471**, 442-447; (c) X. L. Zhao, C. X. Wang, X. P. Hao, J. X. Yang, Y. Z. Wu, Y. P. Tian, X. T. Tao, and M. H. Jiang, *Mater. Lett.*, 2007, **61**, 4791-4793; (d) X. Liu, J. Ma, P. Peng, and W. Zheng, *Mater. Sci. Eng. B*, 2008, **150**, 89-94; (e) X. Liu, R. Liu, S. Chen, and B. Liang, *Mater. Lett.*, 2012, **66**, 264-266.
352. G. Yu, X. Li, X. Liu, C. Asumana, and X. Chen, *Ind. Eng. Chem. Res.*, 2011, **50**, 2236-2244.
353. (a) T. Ichikawa, M. Yoshio, A. Hamasaki, T. Mukai, H. Ohno, and T. Kato, *J. Am. Chem. Soc.*, 2007, **129**, 10662-10663; (b) T. Gutel, J. Garcia-Antón, K. Pelzer, K. Philippot, C. C. Santini, Y. Chauvin, B. Chaudret, and J.-M. Basset, *J. Mater. Chem.*, 2007, **17**, 3290-3292; (c) L. V. Zherenkova and P. G. Khalatur, *Russ. J. Phys. Chem. A*, 2010, **84**, 1097-1103; (d) Y. Wang and G. A. Voth, *J. Am. Chem. Soc.*, 2005, **127**, 12192-3; (e) H. Jin, X. Li, and M. Maroncelli, *J. Phys. Chem. B*, 2007, **111**, 13473-8; (f) S. G. Raju and S. Balasubramanian, *Indian J. Chem.*, 2010, **49A**, 721-726; (g) S. S. Sarangi, W. Zhao, F. Müller-Plathe, and S. Balasubramanian, *Chemphyschem*,

REFERENCES

- 2010, **11**, 2001–10; (h) S. Patra and A. Samanta, *J. Phys. Chem. B*, 2012, **116**, 12275–83.
- 354.** P. R. Sajanlal, T. S. Sreepasad, A. K. Samal, and T. Pradeep, *Nano Rev.*, 2011, **2**, 1–62.
- 355.** R. Thiruvengadathan, V. Korampally, A. Ghosh, N. Chanda, K. Gangopadhyay, and S. Gangopadhyay, *Rep. Prog. Phys.*, 2013, **76**, 066501.
- 356.** J. Ning, K. Men, G. Xiao, L. Wang, Q. Dai, B. Zou, B. Liu, and G. Zou, *Nanoscale*, 2010, **2**, 1699–1703.
- 357.** M. Epifani, E. Pellicer, J. Arbiol, N. Sergent, T. Pagnier, and J. R. Morante, *Langmuir*, 2008, **24**, 11182–8.
- 358.** B. K. Rai, H. D. Bist, R. S. Katiyar, M. T. S. Nair, P. K. Nair, and A. Mannivannan, *J. Appl. Phys.*, 1997, **82**, 1310–1319.
- 359.** B. Gates, B. Mayers, B. Cattle, and Y. Xia, *Adv. Funct. Mater.*, 2002, **12**, 219–227.
- 360.** A. Tanaka, S. Onari, and T. Arai, *Phys. Rev. B*, 1992, **45**, 6587–6592.
- 361.** N. R. Dhumal, H. J. Kim, and J. Kiefer, *J. Phys. Chem. A*, 2011, **115**, 3551–3558.
- 362.** G. S. Fonseca, G. Machado, S. R. Teixeira, G. H. Fecher, J. Morais, M. C. M. Alves, and J. Dupont, *J. Colloid Interface Sci.*, 2006, **301**, 193–204.
- 363.** G. Lefèvre, *Adv. Colloid Interface Sci.*, 2004, **107**, 109–123.
- 364.** A. Wulf, K. Fumino, R. Ludwig, and P.F. Taday, *ChemPhysChem*, 2010, **11**, 349–53.
- 365.** A. G. Ingale and A. N. Chaudhari, *J. Nanomed Nanotechol*, 2013, **4**, 1-7.
- 366.** J. M. Patete, X. Peng, C. Koenigsmann, Y. Xu, B. Karn, and S. S. Wong, *Green Chem.*, 2011, **13**, 482-519.

REFERENCES

- 367.** M. Grzelczak, J. Vermant, E. M. Furst, and L. M. Liz-Marzan, *ACS Nano*, 2010, **4**, 3591–3605.
- 368.** (a) A. K. Boal, F. Ilhan, J. E. DeRouchey, T. T. Albrecht, T. P. Russell, and V. M. Rotello, *Nature*, 2000, **404**, 746-748; (b) J. Shi, Z. Xiao, N. Kamaly, and O. C. Farokhzad, *Acc Chem Res.* 2011, **18**, 1123-34.
- 369.** (a) K. Palaniappan, C. Xue, G. Arumugam, S. A. Hackney, and J. Liu, *Chem. Mater.* 2006, **18**, 1275-1280; (b) J. D. Senra, L. F. B. Malta, M. E. H. M. da. Costa, R. C. Michel, L. C. S. Aguiar, A. B. C. Simas, and O. A. C. Antunes, *Adv. Synth. Catal.* 2009, **351**, 2411–2422; (c) H. Kochkar, M. Aouine, A. Ghorbel, and G. Berhault, *J. Phys. Chem. C* 2011, **115**, 11364–11373; (d) X. Sun, C. Zheng, F. Zhang, L. Li, Y. Yang, G. Wu, and N. Guan, *J. Phys. Chem. C* 2008, **112**, 17148–17155; (e) N. Depalo, R. Comparelli, M. Striccoli, M. L. Curri, P. Fini, L. Giotta, and A. Agostiano, *J. Phys. Chem. B* 2006, **110**, 17388-17399; (f) Y. Huang, D. Li, and J. Li, *Chem. Phys. Lett.* 2004, **389**, 14–18.
- 370.** (a) M. Stojanov, H. M. Nielsen, and K. L. Larsen, *Int. J. Pharm.*, 2012, **422**, 349–355; (b) F. L. Callari, A. Mazzaglia, L. M. Scolaro, L. Vallid, and S. Sortino, *J. Mater. Chem.*, 2008, **18**, 802-805.
- 371.** M. Messner, S. V. Kurkov, P. Jansook, and T. Loftsson, *Inter. J. Pharm.* 2010, **387**, 199–208.
- 372.** W. Robert, J. Meulenberg, R. I. Lee, W. Abraham, Z. Jin, J. Louis, and B. Tony, *ACS Nano* 2009, **3**, 325-330.

REFERENCES

- 373.** V. M. Dzhagan, M. Y. Valakh, A. E. Raevskaya, A. L. Stroyuk, S. Y. Kuchmiy, and D. R.T. Zahn, *Nanotechnology* 2007, **18**, 285701-7.
- 374.** V. M. Dzhagan, M. Y. Valakh, A. E. Raevskaya, A. L. Stroyuk, S. Y. Kuchmiy, and D. R. T. Zahn, *Nanotechnology* 2008, **19**, 305707-6.
- 375.** (a) S. J. Kerber, J. J. Bruckner, K. Wozniak, S. Seal, S. Hardcastle, and T. L. Barr, *J. Vac. Sci. Technol.*, A. **1996**, **14**, 1314-1320; (b) S. Azoz, J. Jiang, G. Keskar, C. McEnally, A. Alkas, F. Ren, N. Marinkovic, G. L. Haller, S. I-Beigi, and L. D. Pfefferle, *Nanoscale.*, 2013, **5**, 6893-6900; (c) Y. S. Park, Y. Okamoto, N. Kaji, M. Tokeshi, and Y. Baba, *J. Nanoparticle Res.*, **2011**, **13**, 5781-5798.
- 376.** I. S. Liu, H. H. Lo, C. T. Chien, Y. Y. Lin, C. W. Chen, Y. F. Chen, W. F. Su, and Sz C. Liou, *J. Mater. Chem.*, 2008, **18**, 675-682.
- 377.** Y. Wu, G. P. Lopez, L.A. Sklar, and T. Buranda, *Anal Biochem.*, 2007, **364**, 193-203.
- 378.** J. Z. Zhang, *J. Phys. Chem. B* 2000, **104**, 7239-7253.
- 379.** S. Karan, M. Majumder, and B. Mallik, *Photochem. Photobiol. Sci.*, 2012, **11**, 1220-1232.
- 380.** J. Z. Zhang and C. D. Grant, *Ann. Rev. Nano Res.*, 2008, **2**, 1-61.
- 381.** M. Hamada, E. S. Shibu, T. Itoh, M. S. Kiran, S. Nakanishi, M. Ishikawa, and V. Biju, *Nano Rev.*, 2011, **2**, 6366.
- 382.** I. Yagi, K. Mikami, K. Ebina, M. Okamura, and K. Uosaki, *J. Phys. Chem.B*, **2006**, **110**, 14192-7.
- 383.** R. Sarkar, A. K. Shaw, S. S. Narayanan, C. Rothe, S. Hintschich, A. Monkman, and S. K. Pal, *Opt. Mater.*, 2007, **29**, 1310-1320.

REFERENCES

- 384.** K. V. S. Rao, B. Srinivas, and M. Subrahmanyam, *Research Signpost* 31, ISBN-8177362267 (2004).
- 385.** H. Remita, I. Lampre, M. Mostafavi, E. Balanzat, and S. Bouffard, *Rad. Phys. Chem.*, 2005, **72**, 575-586.
- 386.** A. Datta, A. Priyam, S. Chatterjee, A. K. Sinha, S. N. Bhattacharyya, and A. Saha, *Colloids Surf. A: Physicochem. Eng. Aspects*, 2007, **301**, 239-245.
- 387.** J. Belloni, *Catalysis Today*, 2006, **113**, 141-156.
- 388.** A. H. Souici, N. Keghouche, J. A. Delaire, H. Remita, and M. Mostafavi, *Chem. Phys. Lett.*, 2006, **422**, 25-29.
- 389.** J. Belloni, M. Mostafavi, H. Remita, J. L. Marignier, and M. O. Delcourt, *New. J. Chem.*, **1998**, 1239-1255.
- 390.** V. Swayambunathan, D. Hayes, K. H. Schmidt, Y. X. Liao, and D. Meisel, *J. Am. Chem. Soc.*, 1990, **112**, 3831-3837.
- 391.** C. Kirchner, T. Liedl, S. Kudera, T. Pellegrino, A. Muñoz Javier, H. E. Gaub, S. Stölzle, N. Fertig, and W. J. Parak, *Nano Lett.*, 2005, **5**, 331-338.
- 392.** S. J. Cho, D. Maysinger, M. Jain, B. Röder, S. Hackbarth, and F.M. Winnik, *Langmuir*, 2007, **23**, 1974-1980.
- 393.** L. Wang, D. K. Nagesha, S. Selvarasah, M. R. Dokmeci, and R. L. Carrier, *J. Nanobiotechnology.*, 2008, **6**:11.